Modelling of Traumatic Spinal Cord Injury In Vitro

Trang Kim Nguyen

Submitted in accordance with the requirements for the degree
of Doctor of Philosophy

The University of Leeds

Institute of Medical and Biological Engineering
School of Mechanical Engineering

November 2020

Declaration

The candidate confirms that the work submitted is her own and that appropriate credit has been given where reference has been made to the work of others.

This copy has been supplied on the understanding that it is copyright material and that no quotation from the thesis may be published without proper acknowledgement.

The right of Trang Kim Nguyen to be identified as Author of this work has been asserted by her in accordance with the Copyright, Designs and Patents Act 1988.

Acknowledgements

From quite early on, I knew I wanted to do a PhD. Little did I know, I was about to embark on a turbulent journey in life which could not have been possible without the people who took the time to support me, both personally and professionally. It has been a privilege to work with a team of encouraging supervisors: James, Joanne, Richard, and Jessica. Thank you for your unwavering support, patience, expertise, and for reviewing my thesis. I would also like to acknowledge the EPSRC for funding this research.

I would like to thank everyone who has helped me within the iMBE lab in FBS. Special mentions to Katie for sharing my cells and gels pain, and Georgina for escaping the lab with me to drink copious amounts of coffee. I have worked in a few laboratories in my time, none of which were supported so heavily by an amazing manager, Dan. Your office door will forever have my knuckle dents in it. Much appreciation and gratitude also goes to Phil, Dave, and Andrew in iMBE for your support and quick turnaround in the design and manufacture of the distraction moulds.

I would like to thank my CDT cohort for being such a caring group of people. It was a comfort knowing that I was not alone on this journey. Jack and Danny, I especially enjoyed all those Old Bar trips where you made me temporarily forget my PhD woes, or at least revel in them with me. Thank you to my friends for encouraging me to achieve my goals, keeping me sane, and for always being there when I finally emerged from the dark depths of the confocal microscopy suite.

This thesis is dedicated to my family: to my parents, Kim and Chung, who are always supportive of me even if you do not quite understand my research (mostly due to my incompetent translational skills). To my sister, Thu, I highly doubt I would be where I am today if it was not for the competitiveness we shared. Thank you for the countless times you have supported me, especially with all those free holidays!

As an isolating experience as writing this thesis was, this was compounded by an unprecedented global pandemic and lockdown period. My heart goes out to those who struggled during this time. I hope to look back in many years' time and remember my PhD experience with laughter and gratitude.

Abstract

Traumatic spinal cord injury arises from varied primary mechanisms, leaving individuals with significant long-term disability. Mechanically distinct secondary damage patterns have been observed *in vivo*; however, there remains a lack of consensus on how biomechanical parameters, such as displacement and velocity, influences secondary pathology. Astrocytes are key responders to mechanical insult, thus the aim of this project was to evaluate the effects of varied displacement and velocity parameters of contusion and distraction injury on primary astrocyte reactivity *in vitro*.

A 3D culture model with astrocytes embedded in a collagen hydrogel (5×10^5 cells.ml^{-1}) was used to simulate the CNS environment. Using the BOSE Electroforce BioDynamic 5110, contusion was modelled at 100 and 1000 mm.s^{-1} to depths of 25, 50, and 75% gel thickness. Distraction was simulated at 100 mm.s^{-1} to 10, 20, and 30% of the gauge length. Increasing displacement and velocity resulted in an increase in energy applied, resulting in astrogliotic alterations: hypertrophy, ramification, loss of individual domains, increased glial fibrillary acidic protein volume, and increased chondroitin sulfate proteoglycan deposition. Increased astrocyte reactivity was observed with increasing contusion depth at 100, but not 1000 mm.s^{-1}. Distraction injury also induced astrogliotic changes, but with temporal differences in GFAP volume and CSPG expression. Further, distraction length had no effect on injury severity from Day 7 onwards, suggesting injury mechanism influences astrocyte reactivity in different ways.

In vitro models of contusion and distraction injury were developed, but with scope for adapting them to use different neural cell types and increase cellular complexity in a controlled manner. This may enable the user to evaluate the biomechanical thresholds of different cell populations and the influence of cell-cell interactions on secondary pathophysiology. These preclinical models may also be useful for early stage testing of therapeutic interventions and refinement of animal experiments.

Contents

List of Figures

List of Tables

List of Equations

List of Abbreviations

2D	Two-dimensional
3D	Three-dimensional
3R's	Reduction, Replacement, Refinement
ANOVA	Analysis of variance
ATP	Adenosine triphosphate
BSA	Bovine serum albumin
BSCB	Blood spinal cord barrier
ChABC	Chondroitinase ABC
CNS	Central nervous system
CSPG	Chondroitin sulfate proteoglycan
DAPI	4',6-diamidino-2-phenylindole
DNA	Deoxyribonucleic acid
DMEM	Dulbecco's modified Eagle's medium
ECM	Extracellular matrix
EngNT	Engineered neural tissue
FIJI	FIJI is just ImageJ
GFAP	Glial fibrillary acidic protein
MEM	Minimum essential medium
MMP	Matrix metalloproteinase
PBS	Phosphate buffered saline
PEEK	Polyether ether ketone
PFA	Paraformaldehyde
ROS	Reactive oxygen species
SCI	Spinal cord injury
SD	Standard deviation
SEM	Standard error of the mean
TGFβ-1	Transforming growth factor beta-1
TSCI	Traumatic spinal cord injury
v/v	Volume per volume
w/w	Weight per weight
w/v	Weight per volume

Outputs

Conference Presentations

NGUYEN, T.K., Phillips, J.B., Hall, R.M., and Kwok, J.C.F. 2019. Interaction Between Contusion Velocity and Depth Influences Astrocyte Reactivity in an In Vitro Model of Traumatic Spinal Cord Injury. *TERMIS EU 27th – 31st June 2019, Rhodes, Greece.*

NGUYEN, T.K., Phillips, J.B., Hall, R.M., and Kwok, J.C.F. 2018. Biomechanically Controlled Simulation of Traumatic Spinal Cord Injury In Vitro Using a 3D Hydrogel Model. *BioMedEng, 6th – 7th September 2018, London, United Kingdom.*

Conference Posters

NGUYEN, T.K., Phillips, J.B., Hall, R.M., and Kwok, J.C.F. 2019. A Non-Linear Relationship Between Contusion Velocity and Displacement Depth and Astrocyte Reactivity in an In Vitro Model of Spinal Cord Injury. *Scandinavian Society for Biomaterials Conference 12th – 14th June 2019, Helsinki, Finland.*

NGUYEN, T.K., Kwok, J.C.F., Phillips, J.B., Hall, R.M., and Tipper, J.L. 2018. Development of a biomechanical simulation model of traumatic spinal cord injury. *Tissue and Cell Engineering Society 2018 Conference, 2nd – 4th July, Keele University.*

NGUYEN, T.K., Ichiyama, R.M., Phillips, J.B., Hall, R.M., and Tipper, J.L. 2018. Characterising the displacement and speed capabilities of the BOSE Electroforce 5110 BioDynamic for simulating traumatic spinal cord injuries using an in vitro hydrogel model. *Biomaterials & Tissue Engineering Group 19th Annual White Rose Work in Progress Meeting, 18th December, University of Leeds.*

NGUYEN, T.K., Ichiyama, R.M., Phillips, J.B., Hall, R.M., and Tipper, J.L. 2017. Development of an impaction model of traumatic spinal cord injury using the BOSE Electroforce 5110. *University of Leeds Engineering CDT Joint Conference, 24th May 2017, Leeds, United Kingdom.*

NGUYEN, T.K., Phillips, J.B., Hall, R.M., and Tipper, J.L. 2016. Realistic modelling of traumatic spinal cord injury in vitro. *EPSRC and MRC CDT TERM Joint Conference, 8th July 2016, University of Manchester.*

Chapter 1

Introduction

1.1 Overview

Traumatic spinal cord injury (TSCI) refers to damage to the spinal cord which results from high energy events, such as motor vehicle accidents or falls from a height. TSCI arises from failure of the vertebral column, the structure which houses and protects the spinal cord. These injuries create a large long-term physical, financial and socioeconomic burden on those affected. The current state of TSCI research has provided a toolbox of experimental techniques and models both *in vitro* and *in vivo*, which have contributed greatly to our understanding of the mechanisms of injury and pathophysiological events which follow. *In silico* models are increasingly useful supplementary models for providing predictions of the evolution of injury and resultant strain and stress patterns, which are difficult to measure instantaneously due to the unexpected nature of injury and timeframe in the order of milliseconds (Wilcox *et al.*, 2002).

Despite this wealth of knowledge, which has led to the development of numerous clinical trials, an effective treatment has yet to be developed which leads to a robust and complete functional recovery for the patient. Heterogeneity exists due not only to the mechanism, severity, and level of vertebral column failure leading to spinal cord damage but also heterogeneity in the population who receive the injury. The age, gender, health, and socioeconomic status of an individual also influences their recovery. This diversity is not reflected in the preclinical models and clinical trials which may be impeding the search for effective treatment(s).

More recent research has highlighted the importance of injury mechanism in determining the progression of primary and secondary injury, thus influencing the behavioural outcomes *in vivo*. The injury mechanism, encompassing the mechanism of vertebral column failure and spinal cord damage, is also defined by the extent of cord displacement and velocity. Researchers at the University of British Columbia have provided evidence for mechanism-specific distinct strain and biological damage patterns through developing a custom electromagnetic injury device - The University of British Columbia (UBC) multimechanism device - which is capable of modelling contusion, distraction and dislocation SCI with independent control of displacement and velocity (Chen *et al.*, 2016; Choo *et al.*, 2008, 2007).

However, how injury biomechanics, such as displacement and velocity, influences the pathophysiological outcomes of individual populations of cells, and what the biomechanical thresholds for injury activation are for these populations has been difficult to elucidate *in vivo* due to the complexity of the native CNS. There is also a lack of consensus on which biomechanical parameter(s) is/are dominant in determining the severity of injury *in vivo*. Therefore, three-dimensional *in vitro* models provide a useful tool for which these questions can be probed. Further, the tailorability of these models provides scope to better reflect the heterogeneity of TSCI. The work in this thesis explores the effects of contusion and distraction injury with independent control of displacement and velocity in an *in vitro* three-dimensional model, composed of primary neonatal cortical astrocytes seeded into collagen hydrogels. The motivation for this research is to determine whether and how these parameters influence astrocyte reactivity at a single cell population level.

1.2   Anatomy of the Spine and Spinal Cord

The vertebral column is the central support structure of the body, providing structural support, stability and flexibility alongside soft tissues, such as ligaments and intervertebral discs. The vertebral column is divided into vertebral segments, of which there are 24 in humans: seven cervical (C1 – C7), twelve thoracic (T1 – T12), and five lumbar (L1 – L5). Below the lumbar spine is the sacrum and coccyx, each of which are formed through the fusing of five sacral (S1 – S5) and three to five coccygeal vertebrae, respectively (Figure 1.1).

One of the main functions of the spine is to protect the spinal cord, which runs through its central canal. As one of two structurally distinct nervous systems in the human body, the central nervous system (CNS) comprises the brain and the spinal cord. The spinal cord receives, integrates, and relays information to and from the brain and spinal cord to the rest of the body, via tracts of neurons and glial cells organised throughout the spinal cord. In humans, the spinal cord occupies the upper two-thirds of the spinal canal, typically ending between the L1 and L2 vertebra; although it can end anywhere between T12 and L3 (Barson, 1970). The spinal cord is ovoid in shape and is typically wider in the transverse plane (5 – 13 mm) compared to the anteroposterior plane (4 – 8 mm) (Frostell *et al.,* 2016).
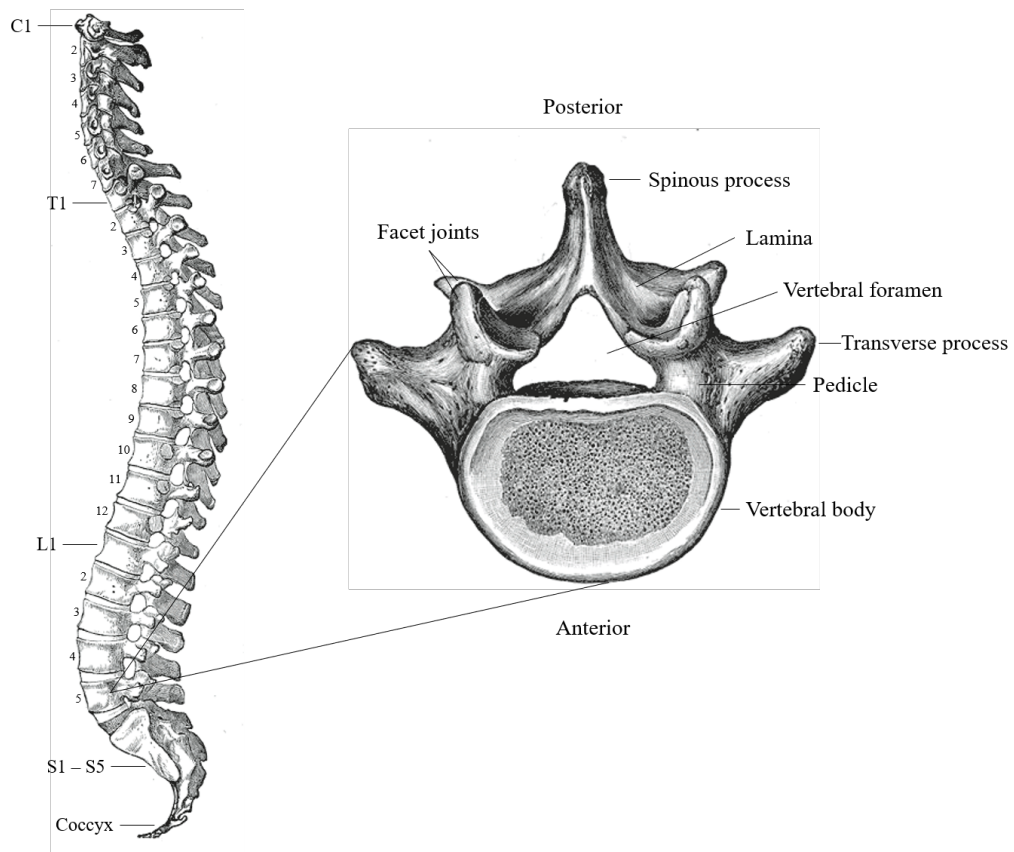
Figure 1.1: Anatomy of the human vertebral column and vertebrae. The human vertebral column can be divided into cervical, thoracic, lumbar, sacral, and coccygeal regions (left). A typical vertebra comprises several structures as annotated (right). Through the vertebral foramen is where the spinal cord runs. Image adapted and modified from Gray (1985).

Similar to the vertebral column, the spinal cord is divided into segments based on the pairs of spinal nerves which are located on each side of the cord, and each spinal nerve is formed from two pairs of nerve roots (Figure 1.2). Spinal nerves conduct motor, sensory, and autonomic information between the spinal cord and the body, with each individual spinal nerve innervating a specific area of the body, called a dermatome (de Campos *et al.,* 2017; Greenberg, 2003). There are 31 pairs of spinal nerves in humans, which are numbered according to the vertebrae above which they emerge: eight cervical (C1 – C8), twelve thoracic (T1 – T12), five lumbar (L1 – L5), five sacral (S1 – S5) and one coccygeal nerve (Co1). There are two major enlargements of the spinal cord: a cervical enlargement associated with the origin of spinal nerves C5-T1 innervating the upper limbs; and a lumbosacral enlargement associated with the origins of spinal nerves L2-S3 innervating the lower limbs (Purves *et al.,* 2001).

The protective meninges of the spinal cord extends from the foramen magnum, at the base of the skull, to approximately the level of the intervertebral disc between L1 and L2, and comprises the outer dura mater, arachnoid mater, and inner pia mater (Figure 1.2) (Nógrádi and Vrbová, 2006). Cerebrospinal fluid (CSF) bathes the inner and outer surfaces of the spinal cord to biomechanically protect the spinal cord, through supporting the weight of the tissue and absorbing shock (Sakka *et al.,* 2011). CSF also

provides immunological support and enables the transport of nutrients and removal of waste products from CNS metabolism. Experimental studies on bovine cord and finite element studies have demonstrated the protective role of CSF against SCI, by reducing cord deformation during impact (Persson *et al.*, 2009).
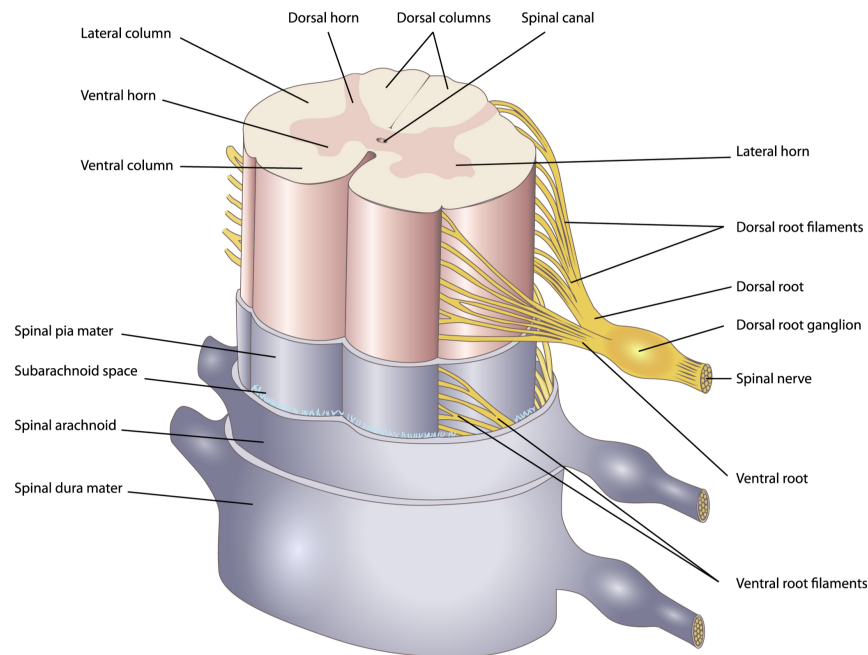
Figure 1.2: Anatomy of the human spinal cord. The spinal cord is housed in the vertebral foramen of the spine and is protected by three layers of membranous tissue (dura mater, arachnoid mater, pia mater) which form the meninges. Additional mechanical and immunological protection is provided by the cerebrospinal fluid (CSF) which occupies the subarachnoid space, between the arachnoid mater and pia mater, and central spinal cord canal. Image adapted and modified from Shutterstock.

A transverse section of the spinal cord reveals the grey and white matter of the spinal cord, with white matter surrounding the grey matter and forming a characteristic butterfly shape (Figure 1.2). The grey matter is predominantly comprised of nerve cell bodies, glial cells, dendrites, and unmyelinated axons, forming longitudinal columns along the cord (Purves *et al.*, 2001). The white matter is rich in myelinated nerve cell processes, with few nerve cell bodies, hence its white-like colour. These nerves form large bundles, or tracts, that ascend and descend throughout the spinal cord, connecting cell bodies from the grey matter and transmitting electrical signals to and from the brain (Watson *et al.*, 2009).

1.2.1   Spinal Cord Cytoarchitecture

The vertebrate spinal cord is comprised of two major classes of cells: neurons and glia (Table 1.1). Neurons are electrically excitable cells responsible for transmitting all signals to and from the brain to the rest of the body. As highly specialized nerve cells, neurons can relay different types of information depending on their specific function. Neurons can be functionally classified into three types: sensory, motor, or interneurons (Mancall and Brock, 2011).

Collectively termed neuroglia or glial cells, non-neuronal cells exist alongside neuronal

cells in the CNS but do not directly facilitate signal transmission. Glia were historically described as the support cells, or glue, holding nervous tissue together. However, research has since revealed the cellular complexity and functions of glial cells in the CNS (Purves *et al.,* 2001; Sofroniew and Vinters, 2010). Glia are the most abundant cells within the spinal cord, outnumbering neurons by approximately 3:1 (Simons and Trajkovic, 2006). In general, there are three main types of glia: astrocytes, microglia, and oligodendrocytes. Ependymal cells are a fourth minor type of glial cell. Glia and neurons are highly organised within the spinal cord from the developmental program that begins with the neural plate in the embryo (Watson *et al.,* 2009).

Table 1.1: Cell types of the central nervous system. The cells which comprise the CNS and thus spinal cord encompass neuronal and neuroglial subtypes, each of which possess distinct functions. CNS = central nervous system; CSF = cerebrospinal fluid.

Cell Type	Functions
Neurons	
Sensory	Receive sensory signals from sensory organs and transmit them to the CNS (afferent).
Motor	Conduct motor signals from the cortex to the spinal cord, or from the spinal cord to the effector organs, such as muscles (efferent).
Interneuron	Residing entirely within the CNS, interneurons receive and integrate information from sensory neurons, and generate a response via the motor neuron.
Neuroglia	
Astrocytes	Maintain homeostatic activities, such as synaptic function and metabolism; respond to pathological insults through numerous repair activities.
Microglia	Resident macrophage cells of the CNS acting to clear cellular debris and dead and/or damaged neurons; respond to infectious agents.
Oligodendrocytes	Myelinating cells of the CNS, producing the myelin sheath that envelops and provides insulation and support to axons.
Ependymal cells	Located in the central canal of the spinal cord and involved in the production of CSF.

Astrocytes, also known as astroglia, are the most abundant cells in the CNS and have been proposed to perform many functions: they are the support cells that regulate the formation of new synapses, with the absence of astrocytes being reported to limit the ability of neurons to form mature and functional synapses (Ullian *et al.,* 2001). Astrocytes also regulate the functions of endothelial cells at the blood brain barrier, provide nutrients, and maintain a wide range of homeostatic activities due to the broad range of neurotransmitter receptors and ion channels that they possess, which can remove molecules from the synaptic cleft (Kerstetter and Miller, 2012; Miller, 2002).

Astrocytes have historically been categorised into two main subtypes: fibrous and protoplasmic astrocytes, based on their morphology and anatomical location, as depicted

in Figure 1.3 (Cajal, 1909). However, heterogeneity in astrocytes extends beyond just morphological differences, and increasing evidence is being presented for genetic and functional astrocyte heterogeneity (Miller, 2018).

Fibrous   Protoplasmic
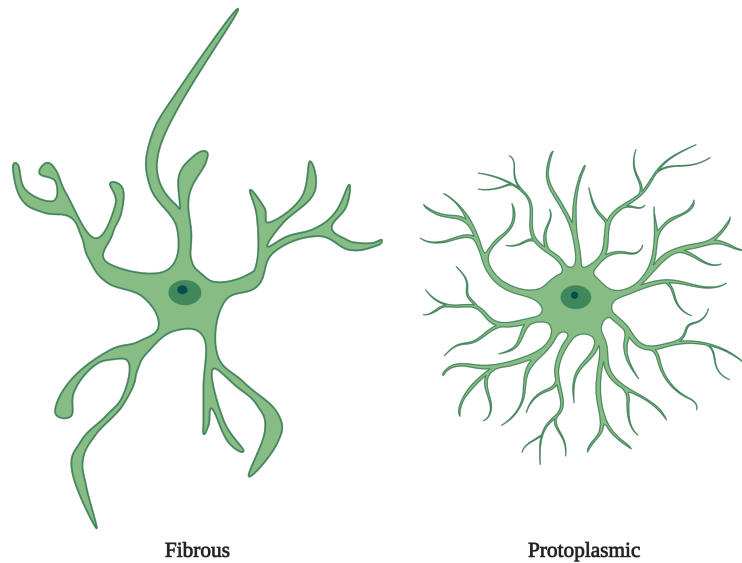
Figure 1.3: Morphology of fibrous and protoplasmic astrocytes. Fibrous astrocytes are predominantly located in the white matter and are characterised by their sparse and long processes which are thicker and less finely branched. Protoplasmic astrocytes are located in the grey matter and possess many finely branched processes which extend radially, giving it a 'brush' like structure. Figure created using Biorender.

Under physiological conditions, astrocytes are said to be in a resting, or 'non-reactive' state. Exposure to an injury stimulus, such as cellular perturbation via a spinal cord injury, results in the release of a variety of molecules. These molecules include inflammatory mediators like TNF-α, reactive oxygen species (ROS), and glutamate and can be released by multiple cell types within the CNS (Sofroniew, 2009). These molecules trigger astrogliosis, the process whereby astrocytes respond to damage in a graded manner by increasing in number and size (hypertrophy), upregulating glial fibrillary acid protein (GFAP) expression, extending their processes, and altering their gene expression (Eng and Ghirnikar, 1994; Faulkner *et al.,* 2004; Sofroniew, 2009). One major consequence of astrogliosis is the formation of a mechanical and chemical barrier to axon regeneration called the glial scar, of which reactive astrocytes contribute. Examples of genes upregulated during astrogliosis include, GFAP, vimentin, and nestin. Typical immunohistochemical identification of astrocytes utilises the expression of GFAP, a cytoskeletal intermediate filament element; although it has been reported that some healthy astrocytes may not express detectable levels of GFAP, compared to injured astrocytes undergoing astrogliosis (Sofroniew, 2009; Sofroniew and Vinters, 2010).

Microglia are the resident immunocompetent cells of the CNS, acting as the primary form of immune defence against injury and infection (Aloisi, 2001). Resting microglia exhibit small cell bodies and are highly ramified, with elaborate thin processes extending in all directions. Their processes continuously scan the surrounding microenvironment thus are able to detect and respond to insults rapidly (Zhou *et al.,* 2014). Damage or

infection induces microglia to exhibit a reactive 'macrophage' phenotype, characterised by the retraction of processes and transition from a ramified to a rod-like morphology. This enables them to perform phagocytic functions by migrating to areas of injury and expressing inflammatory molecules.

Oligodendrocytes are the myelinating glia of the CNS, ensheathing axons in compacted spirals of lipid-rich plasma membrane (Miller, 2002; Simons and Trajkovic, 2006). This enables neurons to conduct action potentials rapidly, and also support their survival through the production of trophic molecules, such as brain-derived neurotrophic factor (BDNF) (Kassmann and Nave, 2008; Lappe-Siefke *et al.,* 2003). Demyelination of axons, as a result of SCI, typically results in remyelination by the generation of new mature oligodendrocytes from the OPC pool distributed throughout the CNS (Malas and Panayiotou, 2013). Remyelination appears to be triggered by factors derived from activated microglia and astrocytes, such as IL-1α, and IFNγ (Rhodes *et al.,* 2006).

A fourth, often less discussed type of neuroglial cell are ependymal cells. Ependymal cells line the central canal of the spinal cord and are thought to be involved in the directed movement of cerebrospinal fluid (CSF) throughout the CNS (Barnabé-Heider *et al.,* 2010). Movement of CSF allows nutrient delivery to neurons, and removal of waste substances (Sakka *et al.,* 2011). Ependymal cells have been demonstrated to exhibit stem cell-like behaviour *in vitro*, resulting in interest in isolating these cells for regenerative purposes (Barnabé-Heider *et al.,* 2010; Meletis *et al.,* 2008).

1.2.2   The Extracellular Matrix Environment of the Spinal Cord

Extracellular matrix (ECM) is a bioactive scaffold comprised of a complex network of numerous proteins, such as fibrous proteins (collagen, elastin, fibronectin), adhesion proteins (integrin), growth factors (FGF, VEGF), cytokines, chemokines, and proteoglycans (aggrecan) expressed by cells (Frantz *et al.,* 2010). The mature CNS ECM consists of the basement membrane (BM), interstitial space (IS), and specialised ECM called perineuronal nets (PNNs) (Carulli *et al.,* 2006; Haggerty *et al.,* 2017). ECM composition differs between different tissues, offering tissue-specific regulation of structure, biological and biomechanical behaviour, and is reported to contribute to 20% of the total volume of the adult CNS (Sobel, 1998).

Whereas fibrous proteins, such as collagen, laminin and fibronectin are enriched in the ECM of peripheral tissue, the opposite is the case in CNS tissue. The ECM of the spinal cord comprises mostly of glycosaminoglycans (GAGs) and proteoglycans (DeQuach *et al.,* 2011; Rauch, 2007). GAGs are long unbranched polysaccharides of a variable number of repeating disaccharide units, and hyaluronan (HA) is the most abundant GAG and ECM structural component in the CNS. Due to their polyanionic properties, HA attracts positively charged cations, such as sodium ions and water. Its large water retaining capacity results in a highly hydrated ECM and contributes to the low stiffness of the spinal cord. Proteoglycans are composed of a protein core with GAG side chains. Chondroitin sulfate proteoglycans (CSPG) are an important group of

proteoglycans within the spinal cord ECM and include aggrecan, versican, neurocan, and brevican. In the healthy CNS, proteoglycans mediate activities, such as cell adhesion, growth, migration, and receptor binding (Rhodes and Fawcett, 2004). The GAG chains of proteoglycans can form a matrix of varying pore size, which can serve as a regulator of cell migration, for instance.

In response to mechanical damage, the composition of the ECM at the lesion site and glial scar is altered with the increased expression of matrix metalloproteinases (MMP) and deposition of ECM molecules which are inhibitory to neurite outgrowth (Fitch and Silver, 2008; Volpato *et al.,* 2013). For instance, increased expression of neurocan, brevican, phosphacan, and versican has been shown to persist for up to two months after spinal cord injury *in vivo*, and has been shown to inhibit axonal regeneration (Jones *et al.,* 2003). It is thought that the CS-GAG chains are particularly inhibitory to neurite outgrowth and possible mechanisms of inhibition include binding to membrane-bound receptors mediating inhibition, and blocking the functions of growth-promoting molecules such as laminins (Sharma *et al.,* 2012). This knowledge of ECM alterations following injury has been exploited to develop tissue engineered constructs to enhance or deposit growth promoting ECM factors, for instance (Volpato *et al.,* 2013).

1.3   Biomechanical Properties of the Spinal Cord

Biomechanics is the study of the responses of the body and tissues to mechanical loading, and defining the biomechanical properties of tissues is important for understanding their native function and discerning their tolerance to mechanical loading. Thus, determining the effects of different injury mechanisms on the cellular responses in the spinal cord may provide more effective strategies for treatment. Modulus, a commonly measured biomechanical property of tissues, is defined as the tendency of a material to deform along an axis upon application of a force, and is typically measured in units of Pascals (Pa). Modulus can be determined under shear, compressive, or tensile loading, which has led to variability in reported data for the spinal cord, as reviewed by (Bartlett *et al.,* 2016b).

Biological tissues, such as the spinal cord exhibit viscoelastic behaviour: both viscous and elastic properties under stress and deformation (Bilston, 2011). This behaviour is time-dependent; thus, the moduli calculated will depend on the strain rate applied to the tissue. Albeit not the predominant mechanism of injury in humans, uniaxial tensile testing is the most common biomechanical test to determine the relationship between force and tensile deformation (Cheng *et al.,* 2008). Studies pertaining to the stress-strain response of spinal cord tissue to tensile forces is summarised in Table 1.2. The values reported are in fact pseudo-moduli as they are derived from the gradient of the linear region of a stress-strain curve. The inherent cylindrical-like nature of the spinal cord makes specimen loading onto the apparatus more convenient (Bilston, 2011). However, securing soft tissues, such as the spinal cord, into grips proves difficult due to the risk of tissue damage at the clamping point.

Variables, such as tissue origin, segment of the spinal cord tested, age of the tissue, testing environment, boundary conditions, mode of testing, and preconditioning have contributed to variable data between groups. There is yet no consensus on the appropriate parameters and sample preparation procedures, resulting in a lack of standardised protocols. The lack of a standardised testing protocol is evident, resulting in tensile modulus values ranging from 0.012 MPa to 1.98 MPa (Table 1.2). The earlier tensile studies were performed *in vivo* thus the environmental conditions differed significantly from *ex vivo* studies (Hung and Chang, 1981; Hung *et al.,* 1981a,b). For instance, the spinal cord *in vivo* is under tensile pre-strain and this has been suggested to contribute to the more linear stress-strain relationship observed, compared to the J-shaped response in *ex vivo* studies by Bilston and Thibault (1995), Fiford and Bilston (2005) and Oakland *et al.,* (2006).

Further, the presence or absence of some or all of the meningeal components have contributed to the varied results as the meninges has been shown to contribute significantly to the stiffness of the spinal cord (Mazuchowski, Thibault, *et al.,* 2003; Ozawa *et al.,* 2004; Ramo *et al.,* 2018). Another limitation of these studies is that the strain rates used are not comparable to those experienced during a traumatic SCI event, which is in the order of milliseconds. However, a study by Mazuchowski, Thibault, *et al.,* (2003) showed that the spinal cord appears to be rate insensitive in the axial direction at higher rates (0.2, 1, 10 s^{-1}), with a reported Young's modulus of ~1.40 MPa which is within the range of moduli reported by Bilston and Thibault (1995).

The compressive properties of the spinal cord has been less studied despite being a prominent mechanism of SCI and the majority of experimental injury models utilise compression/contusion (Sharif-Alhoseini *et al.,* 2017). Karimi *et al.,* (2017) performed an *ex vivo* study on the compressive properties of male human cervical spinal cord and calculated the elastic modulus to be 40.12 kPa (5 mm.min^{-1} to failure). This is lower than the moduli reported for human spinal cord under tensile loading (Table 1.2) highlighting the anisotropy of the spinal cord. Further, the spinal cord is a complex cellular structure, with its highly organised cytoarchitecture contributing to its viscoelastic and non-linear anisotropic properties (Koser *et al.,* 2015; Shreiber *et al.,* 2009). For instance, the orientation of axons in the white matter along the craniocaudal direction could contribute to the tensile strength of the spinal cord.

Despite a wide range of tools available to evaluate the mechanical properties of the spinal cord (as reviewed by Bartlett *et al.,* (2016b) and Cheng *et al.,* (2008)) the lack of consensus and standardised protocol for specimen acquisition, setup and testing parameters has led to the variability in moduli reported. There is also a discrepancy in the level of experimental detail reported, which impedes the comparison of data between studies. However, this data has led to the development of useful *in silico* models for predicting stresses and strains in response to simulated injury, and continues to inform research into applications where the design of tissue engineered therapies requires the incorporation of desirable mechanical properties for the host.

Table 1.2: Tensile testing studies involving measurement of the biomechanical properties of the spinal cord. Summary of the studies involving tensile testing of the spinal cord, including the species used, properties of the sample, and mechanical testing parameters. The region from which the spinal cord sample was taken refers to the vertebral segments. Reported moduli values are pseudo-moduli, which is the gradient of the linear region of the stress-strain curve. * = unless stated otherwise. Stretch ratio $(\lambda) = L/L_0$, where L is the instantaneous length of the specimen and L_0 is original length of specimen hanging under its own weight. NR = Not Reported.

Reference	Species	Region	Sample Length (mm)	Strain rate (s^{-1})*	Maximum Strain (%)*	Modulus (MPa)
(Luna *et al.,* 2013)	Sea lamprey	Whole	$30-50$	$0.5-2$ mm at a time using manipulator	18	$0.015-0.5$
(Oakland *et al.,* 2006)	Cow	NR	$130-180$	0.24	~ 8.5	1.19
(Fiford and Bilston, 2005)	Rat ($\sim$230 g)	C1 – L4	NR	0.002, 0.02, 0.2	5	$1.14-1.98$
(Mazuchowski, Thibault, *et al.,* 2003)	Human (59 – 81 yrs)	Whole	50	+ pia mater: 0.2, 1, 10; – pia mater: 0.1, 1, 10	+ pia mater: $\lambda = 1.06-1.20$; – pia mater: $\lambda = 1.5$	+ pia mater = 1.40; – pia mater = 0.089
(Bilston and Thibault, 1995)	Human (30 – 84 yrs)	Cervical Thoracic	$30-45$	0.048, 0.120, 0.225	~ 10	1.02, 1.17, 1.37
(Hung and Chang, 1981)	Puppy (3 – 5 kg)	L1 – L2	8	0.003	1.70	0.265
(Hung *et al.,* 1981b)	Cat	T8 – T11	25	0.0008	$8-12$	0.4
(Hung *et al.,* 1981a)	Cat	L1 – L12	7	0.002	1, 16	0.252, 0.295
(Tunturi, 1978)	Dog	NR	120	Quasi-static (5 g increments)	19 (failure)	$0.012-0.017$

1.4   The Spinal Cord under Physiological Conditions

The spinal cord and vertebra experiences constant loading through everyday physiological activities, such as walking and lifting objects where flexion, extension and rotational movements occur. The vertebral column, together with associated ligaments, muscles, and intervertebral discs (IVD) results in a structure which can support and distribute compressive loading repetitively whilst also encasing and protecting the spinal cord. For instance, Cappozzo (1983) predicted the L3-L4 forces during various speeds of gait in five young males to range from 0.2 to 2.5 times body weight throughout the gait cycle.

The spinal cord itself must also tolerate dynamic loads under physiological conditions, particularly the cervical spinal cord due to the movements of the head and neck. The anteroposterior diameter of the cervical spinal cord has been shown to be up to 0.5 mm larger in extension and smaller in flexion, compared to the neutral position (Kuwazawa *et al.,* 2006). The spinal cord occupies up to approximately 45% of the vertebral canal at the C2 – T1 level with little change in canal occupation under flexion or extension; thus, the cord is able to deform in a relatively unconfined manner without resulting in damage (Sayıt *et al.,* 2015). Another observation in that study was that during extension at the C4 – C6 level, the diameter of the spinal canal was at its smallest, with maximum disc bulging and ligamentum flavum thickness. This makes this region more susceptible to compression and this knowledge may contribute to the design of injury risk prevention tools.

Ageing and diseases can reduce the load-bearing capacity of the vertebra, resulting in weakened support and increased risk of fracture, exposing the spinal cord to damage. In a society where the mean life expectancy is increasing, the population at risk of fractures and spinal cord injuries grows, which has implications for the individual, and health and social care services. Further, an increase in load above the physiological threshold can also result in spinal cord injury with or without vertebral column failure, which often occurs following high velocity and energy traumatic events.

1.5   Traumatic Spinal Cord Injury

Traumatic spinal cord injury (TSCI) results from the acute lesion of the neural components of the spinal cord, above its physiological threshold, resulting in temporary or permanent sensory and/or motor loss below the level of injury. Trauma may involve failure of ligamentous support to the spinal cord, or dynamic interactions between the spinal cord and vertebral column (Szwedowski and Walecki, 2014). Non-traumatic spinal cord injury differs in that deformation of the cord is degenerative and occurs over a longer time period of up to years (David *et al.,* 2019).

Global incidences (the number of new cases per year) of TSCI vary widely, with one systematic review reporting a range of 3.6 to 195.4 patients per million, across 41 individual countries (Jazayeri *et al.,* 2015). This creates an enormous burden, not only on the

mental and physical welfare of the patient themselves, but also on the socioeconomic environment. It is estimated that the annual cost of treating and managing spinal cord injury is £1 billion, in the UK (McDaid *et al.,* 2019). The severity of TSCI depends on the level, mechanism, and extent of injury, but includes permanent locomotor and sensory deficits, and may lead to neuropathic pain, spasticity, urinary and respiratory dysfunction, metabolic problems as well as psychological problems (Watson *et al.,* 2009).

1.5.1   Biomechanics of Traumatic Spinal Cord Injury

TSCI results from a number of diverse causes, including falls, motor vehicle accidents (MVA), sports-related incidents, and violence. Globally, MVAs and falls are the most common causes of TSCI, although the incidence of falls in the elderly is increasing due to the increasing ageing population (Center *et al.,* 2015; Singh *et al.,* 2014). These events cause a wide variety of injuries to the vertebral column and spinal cord. Common mechanisms of TSCI involving the vertebral column include, burst fracture, distraction or and dislocation (Oxland *et al.,* 2010; Panjabi and White, 1990). Injuries most frequently occur at the cervical level, which poses a larger problem due to the increased severity and number of functional deficits at this level (Singh *et al.,* 2014). This is likely due to the increased range of motion around the head and neck, along with the smaller size of the cervical vertebrae making this region more vulnerable to forces which surpass the physiological threshold (Sekhon and Fehlings, 2001).

A burst fracture type injury may result from high speed motor vehicle accidents, resulting in vertebral fracture and secondary retropulsion of bony fragments into the spinal cord at high velocity. Approximately $15 - 30\%$ of all acute SCIs arise from this type of trauma (Denis, 1983; Sekhon and Fehlings, 2001). This leads to a contusion and/or compression mechanism of SCI. Although velocities of burst fractures, and other injury mechanisms, cannot be measured directly in clinical scenarios, *ex vivo* experiments using bovine and human cadaveric vertebral segments have shown that velocities of $1 - 10$ m.s^{-1} were achieved (Panjabi *et al.,* 1994; Wilcox *et al.,* 2003). Further, maximum canal occlusion has been shown to be achieved during the dynamic injury, which is under-represented in post-injury radiographs and may lead to an underestimation of the severity of the initial injury (Wilcox *et al.,* 2003, 2002).

Dislocation involves the relative translation of two adjacent vertebra, exerting a combination of compressive, tensile, and shear forces on the spinal cord (Russell *et al.,* 2012). Thus, it is typically an unstable injury, meaning further mechanical and biological damage is likely without appropriate intervention to stabilise the injury. Dislocation injury may occur with or without fracture and is the most commonly observed injury mechanism, occurring in roughly $32 - 58\%$ of SCI cases (Sekhon and Fehlings, 2001; Tator *et al.,* 1987; Tator, 1983; Wilson *et al.,* 2013). Ivancic *et al.,* (2007) modelled a frontal sled impact on human cadaveric vertebral segments to produce a dislocation injury, and the mean velocity was reported to be 0.23 m.s^{-1}.

Distraction injuries arise when adjacent vertebrae are pulled apart, with the spinal cord

being stretched in the axial plane, and is commonly observed in motor vehicle accidents where rapid deceleration can cause hyperflexion, or sudden backwards acceleration leads to hyperextension leading to a combination of compressive and tensile forces acting on the cord (Dumont *et al.,* 2001). The role of distraction in TSCI is more difficult to define and correlate with SCI outcomes because distraction usually occurs in concert with other mechanisms, such as flexion (Vaccaro *et al.,* 2005). It is important to understand the relationship between the structure and function of the vertebral column, with respect to the spinal cord, in order to understand how the consequent injury evolves during a TSCI.

1.6 Pathophysiology of Traumatic Spinal Cord Injury

The pathophysiological events following trauma are complex, heterogeneous, and involve many cell types and molecules. The events following the initial trauma evolve over time and can manifest itself in many ways depending on the location and severity of the injury, and the cells affected. Therefore, each patient will present unique pathologies, and treating them with the same strategy is unlikely to yield the same results.

1.6.1 Primary Injury

The primary response to injury is concurrent with the mechanical load on the cord and occurs within the order of milliseconds. A combination of the initial impact and persistent compression after injury (resulting commonly in burst fracture and fracture-dislocation) is most typical of TSCI, giving rise to local cell death, ischaemia, and disruption of the blood spinal cord barrier (BSCB) (Dumont *et al.,* 2001). Other morphologies of primary injury include impact alone with transient compression, distraction, and laceration/transection (Oyinbo, 2011). The cytoarchitecture of the spinal cord is altered dramatically: damage of nerve fibre pathways in the white and grey matter means that spinal segments below the level of the injury cannot receive nor transmit signals to the brain, and disruption to the blood spinal cord barrier typically occurs (Norenberg *et al.,* 2004). Blood-borne immune cells also begin to infiltrate the injury site to initiate the inflammatory process alongside the activation of resident microglia and astrocytes, which evolves and becomes amplified in the secondary phase of pathology. Downstream events following the primary injury involve a complex cascade of cellular and immunological events- the secondary injury- culminating in a degenerative microenvironment which is inhibitory to neuroregeneration.

1.6.2 Secondary Injury

The primary injury triggers a secondary reactive phase which comprises a cascade of numerous systemic and cellular events initiated within minutes following the primary injury. This process can last for days, weeks, or even years (Bareyre and Schwab, 2003; Oyinbo, 2011). Common events occurring during this phase include, inflammation, astrogliosis, axon degeneration, free-radical production, and formation of a glial scar and cystic cavity (Fleming *et al.,* 2006). A summary of common events which occur during the secondary pathophysiological response to SCI can be seen in Table 1.3. For the scope of this thesis, the events of astrogliosis will be described in more detail. As a result of continued degeneration, the lesion can expand radially and longitudinally leading to

further damage to the spinal cord in areas which were not affected by the initial impact (Schwab *et al.,* 2006; Zhou *et al.,* 2014).

Table 1.3: Common characteristics of the secondary pathophysiological response to traumatic spinal cord injury. AAD = acute axonal degeneration. CSPG = chondroitin sulfate proteoglycan. ECM = extracellular matrix. GFAP = glial fibrillary acidic protein. MAI = myelin associated inhibitor. MMP = matrix metalloproteinase. NO = nitric oxide.

Characteristic	Description	Reference(s)
Glial scar	Astrocytes undergo astrogliosis: increased GFAP expression, hypertrophy, proliferation, and formation of a compact glial scar- composed predominantly of fibroblasts and inflammatory cells bordered by reactive astrocytes.	(Sofroniew, 2015)
Cell death & excitotoxicity	Hypoxic conditions lead to widespread necrosis and apoptosis, release of free radicals e.g. NO, neurotransmitters, and calcium ions, which signals excitotoxicity to neighbouring cells.	(Dong *et al.,* 2009)
Inflammation	Infiltration of blood-borne immune cells and activation of innate microglia mediate clearance of debris and release of pro-inflammatory cytokines e.g. IL-6, TNF-α, IL-1β and IFN-γ. M1 macrophage response can persist for months following initial injury resulting in an imbalance of pro- and anti-inflammatory processes.	(Pineau and Lacroix, 2007; Schwartz, 2003; Zhou *et al.,* 2014)
Neurodegeneration	AAD and Wallerian degeneration occurs in damaged axons. Myelin debris results in the release of MAIs.	(Kerschensteiner *et al.,* 2005)
ECM alterations	Upregulation of MMPs and collagenases; deposition of ECM components e.g. CSPGs, laminin, vimentin, and collagen	(Bradbury and Burnside, 2019; Didangelos *et al.,* 2016)

1.6.2.1 Astrogliosis and Glial Scar Formation

One major mechanical and chemical barrier to regeneration is the formation of the glial scar and fluid-filled cystic cavity where debris has been cleared by macrophages and microglia (Fitch and Silver, 2008). Formation of the glial scar is primarily mediated by reactive astrocytes, in concert with glia, neurons and other non-neuronal cells, such as pericytes (Burda and Sofroniew, 2014). Astrocytes in particular respond to CNS insult by triggering a gradated response to injury through the process of astrogliosis, or reactive gliosis (Sofroniew, 2015). Astrogliosis encompasses a spectrum of molecular, structural and functional alterations in astrocytes which are regulated in a context and severity-dependent manner (Figure 1.4).
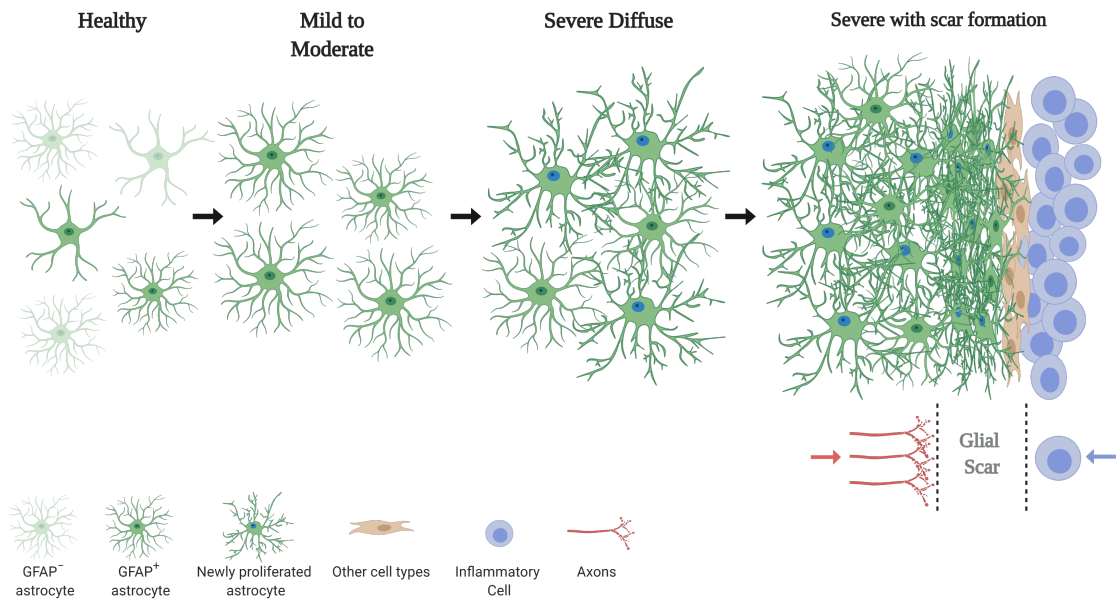
Figure 1.4: Astrogliosis is a spectrum of heterogeneous molecular, cellular and functional changes. Astrocytes in the healthy CNS express little GFAP and there is little overlap of individual astrocyte domains. In response to a mild or moderate insult, variable alterations in GFAP expression and cellular hypertrophy occur depending on the injury type and severity. Astrocyte domains remain distinct and do not overlap. Severe diffuse astrogliosis is characterised by overlapping of astrocyte processes and proliferation over a more widespread area. Severe astrogliosis with glial scar formation sees the formation of a glial scar composed of reactive and proliferating scar-forming astrocytes, other cell types such as fibroblasts and meningeal cells, as well as an altered ECM microenvironment with increased deposition of collagen and CSPGs. This creates a barrier against axons and inflammatory cells. Adapted and modified from Sofroniew and Vinters (2010) using Biorender.

The glial scar exhibits altered ECM with increased deposition of chondroitin sulfate proteoglycans (CSPGs) by reactive astrocytes around the lesion site, which has been shown to inhibit neurite outgrowth (Jones *et al.,* 2003; Siebert *et al.,* 2014; Snow *et al.,* 1990). Other components of the glial scar include myelin-associated inhibitors (MAIs), a class of neurite growth inhibitors produced by oligodendrocytes in the CNS. Prototypical MAIs include Nogo, myelin associated glycoprotein (MAG), Semaphorin 4D (Sema4D), and oligodendrocyte myelin glycoprotein (OMgp) (Chen *et al.,* 2000; Kottis *et al.,* 2002; McKerracher *et al.,* 1994). Although the glial scar creates a physical barrier for regeneration, it has also been shown to also be beneficial, limiting the spread of further damage (Faulkner *et al.,* 2004). Studies where glial scar formation was inhibited through ablating reactive astrocytes showed worsening of functional outcome in animals, and it is thought reactive astrocytes also play roles in repairing the blood-spinal cord barrier and secretion of anti-inflammatory cytokines after injury (Faulkner *et al.,* 2004; Sofroniew, 2005).

1.7   Treatment Strategies for Spinal Cord Injury

A complex injury brings with it complex treatment strategies. Given the unexpected nature of TSCI and the primary injury, maintaining proper breathing and

immobilisation of the spine typically take precedence over repairing the damage to the cord itself. Therefore, therapeutic intervention has more commonly been directed towards mediating the secondary pathological reactions. However, treatment strategies also vary with the extent of secondary injury, that is the acute, subacute or chronic stage, where major temporal differences in cellular activity, gene expression, and inflammation exist. Despite the vast number of therapeutic targets and clinical trials that have been identified and initiated over the years, this has not translated into treatments which effectively restore sensorimotor function to the patients. A brief overview of the current treatment strategies for SCI is presented in Table 1.4.

Table 1.4: Current treatment strategies for SCI. A non-exhaustive list of treatment strategies for SCI, broadly categorised into four groups.

Intervention	Examples	Comments
Non-pharmacological	Surgical decompression/ stabilisation, CSF drainage, rehabilitation, epidural electrical stimulation	Primary aim is to maintain breathing and stabilise the patient; uncertainty over optimal timing of decompressive surgery (Badhiwala *et al.*, 2020)
Pharmacological	Corticosteroids (methylprednisolone), NSAIDs (ibuprofen), neuroprotection (riluzole, minocycline)	Reduce swelling and inflammation; methylprednisolone has been shown to not be associated with short- or long-term benefits (Sultan *et al.*, 2020)
Cell Therapies	iPSC, BM-MSC, PBSC, NSC, OEC	Directly replace or induce repair of damaged cells through indirect secretion of neurotrophic factors and cytokines (Li and Lepski, 2013)
Biomaterials	NGC, NeuroRegen scaffold with BMMCs and hUCB-MSCs (Zhao *et al.*, 2017)	No commercially approved biomaterial product yet; commonly used in combination with cells, drugs, or growth factors (Ashammakhi *et al.*, 2019)

BM-MSCs = bone marrow-derived mesenchymal stem cells; BMMC = bone marrow mononuclear cells; CSF = cerebrospinal fluid; hUCB-MSCs = human umbilical cord blood-derived mesenchymal stem cells; iPSC = induced pluripotent stem cells; NGC = nerve guidance conduit; NSAID = non-steroidal anti-inflammatory drugs; OEC = olfactory ensheathing cells; PBSC = peripheral blood stem cells; NSC = neural stem cells

Many factors affect the progression of secondary injury and neural regeneration, including the glial scar, CSPGs, demyelination and inflammation; thus, a combinatorial approach to address multiple different aspects of injury are likely to be more effective. However, it is clear that the understanding of the pathophysiology of SCI in humans is still limited, and increasing weight is being placed upon the appropriateness of preclinical models to reflect injury in humans. The research in this thesis will hopefully highlight the critical importance of modelling human injury biomechanics and how it can

affect cellular behaviour *in vitro* which, in turn, may lead to the development of preclinical models which are better informed.

1.8 Models of Traumatic Spinal Cord Injury

Spinal cord injury models have become extremely useful tools for discerning the biomechanics and pathophysiology of traumatic spinal cord injury, and for the testing of interventions aimed at improving functional recovery following injury. The injury models encompass *in vitro*, *in vivo* and *in silico* techniques, all of which have been designed with the aim to faithfully replicate one or more aspects of human SCI.

1.8.1 *In vivo* Models

Animal models provide an alternative complex system in which to study SCI since it is practically and ethically difficult to experiment using human participants. They have played a vital role in discerning injury mechanisms and for the development of therapies. However, the positive effects commonly observed in these preclinical models are usually not reflected in human trials. It has been shown that species, size, anatomical, and pathophysiological differences in animals contribute to the significant barriers of translation of treatments into humans (Cheriyan *et al.,* 2014).

Rats are the most frequently utilised animal model as they are relatively inexpensive to acquire and care for, thus can be studied in large numbers (Zhang *et al.,* 2014). Pathophysiologically, rats are similar to humans in that they develop glial scars and fluid-filled cystic cavities at the injury site following SCI (Kjell and Olson, 2016). Functional assays and endpoints are also well established for studying the effects of TSCI in rats, such as the widespread reporting of the BBB (Basso Beattie Bresnahan) Locomotor Rating score (Basso *et al.,* 1995). However, it is yet unclear how these endpoint measurements translate to humans, if possible, which is impeding clinical translation of SCI therapies.

The biomechanics of TSCI have becoming increasingly important in understanding how the spinal cord comes to be damaged and the influence of mechanical deformation on the progression of secondary injury. For the scope of this thesis, it will be important to examine the current literature for information regarding the biomechanical parameters used in SCI models, including the output measurements in order to discuss the relationship between injury biomechanics and biological outcomes. A summary of biomechanical studies of TSCI with reported input and output kinetic parameters is presented in Table 1.5. Non-biomechanical SCI models, such as chemically-induced SCI do not incorporate the element of biomechanical control so will not be discussed here. A number of apparatus capable of simulating any one or multiple mechanisms of injury have been developed and refined since the first weight drop contusion model was developed in 1911 by Allen (1911). The most commonly utilised biomechanical models of TSCI comprise contusion, compression, dislocation, and distraction mechanisms of injury. Transection models, although frequently utilised *in vivo*, will not be discussed as they are not often observed clinically.

Table 1.5: In vivo biomechanical models of traumatic spinal cord injury. In vivo models of TSCI.

Reference	Species	Apparatus	Mechanism	Location	Input Parameter(s)	Output Biomechanical Data Reported
(Fournely et al., 2018)	Female C57BL/6 mice 17 – 30 wk 20.1 – 23.5 g	IH impactor	Unilateral contusion	C4	Tip $\varnothing$= 0.6 mm Force = 30 kDyn Dwell = 0 s	Displacement = 0.31 ± 0.03 mm Peak velocity = 120 mm.s^{-1} Impact force = 31.0 ± 1.2 kDyn (Mean ± SD)
(Bhatnagar et al., 2016)	Male SD rats 300 g	Custom	Contusion Dislocation	C5/6	*Contusion* Displacement = 1.1 mm (mild); 1.8 mm (severe) *Dislocation* Displacement = 1.7 mm (mild); 2.5 mm (severe)	*Contusion* Displacement = 0.94 ± 0.24 mm (mild); 1.55 ± 0.19 mm (severe) *Dislocation* Displacement = 0.70 ± 0.08 mm (mild); 1.67 ± 0.65 mm (severe) (Mean ± SD)
(Salegio et al., 2016)	Adult male NHPs (*Macaca mulatta*)	BOSE TestBench™ system	Unilateral contusion	C6/7	Tip $\varnothing$= 4 mm *Waveform:* 200 ms dwell 1000 mm.s^{-1} ramp to 2.0, 3.0 or 4.0 mm 20 ms dwell 1000 mm.s^{-1} ramp to 0 mm	Displacement range = 1.71 – 3.72 mm Peak velocity range = 270 – 580 mm.s^{-1} Time to peak displacement = 20 ms Impact force range = -3.27 – -23.19 N Force at peak displacement = -0.16 – 19.10 N

Continued on next page

Table 1.5 – *Continued from previous page*

Reference	Species	Apparatus	Mechanism	Location	Input Parameter(s)	Output Biomechanical Data Reported
(Wu *et al.*, 2016)	Male Japanese white rabbits 4 – 5 mths 2.5 – 3.0 kg	Custom	Uniaxial distraction	L1 – L3	Displacement = 10, 20, 30% 1 turn = 2.5 mm; 5 mm dwell for each turn Dwell = 10 min	NR
(Chen *et al.*, 2016)	Male SD rats 17 – 282 g	UBC multimechanism	Contusion Dislocation Distraction	C5/6	Velocity = 1000 mm.s^{-1} *Contusion* Tip $\varnothing$ = 2.0 mm Displacement = 1.6 mm *Dislocation* Displacement = 1.8 mm *Distraction* Displacement = 5.6 mm (All mechanisms defined as moderate)	*Contusion* Displacement = 1.59 $\pm$ 0.01 mm Peak velocity = 1206 $\pm$ 78 mm.s^{-1} Impact force = 2.57 $\pm$ 0.53 N *Dislocation* Displacement = 1.84 $\pm$ 0.02 mm Peak velocity = 870 $\pm$ 11 mm.s^{-1} Impact force = 18.0 $\pm$ 1.9 N *Distraction* Displacement = 5.64 $\pm$ 0.10 mm Peak velocity = 1298 $\pm$ 40 mm.s^{-1} Impact force = 52.2 $\pm$ 2.9 N (Mean $\pm$ SD)

Table 1.5 – *Continued from previous page*

Reference	Species	Apparatus	Mechanism	Location	Input Parameter(s)	Output Biomechanical Data Reported
(Lam *et al.,* 2014)	Male SD rats 300 g	UBC multimechanism	Contusion	C5/6	Tip $\varnothing$= 2.0 mm Displacement = 0.9, 1.5 mm Velocity = 8, 80, 800 mm.s^{-1} Dwell = 0 s	Displacement range = $0.880 \pm 0.003 - 0.896 \pm 0.002$ mm $1.459 \pm 0.006 - 1.471 \pm 0.032$ mm Peak velocity range = $8.263 \pm 0.928 - 8.797 \pm 1.003$ mm.s^{-1} $83.800 \pm 1.112 - 83.868 \pm 1.396$ mm.s^{-1} $838.272 \pm 2.921 - 840.555 \pm 1.696$ mm.s^{-1} Impact force range = $0.637 \pm 0.106 - 2.134 \pm 0.266$ N Energy range = $0.250 \pm 0.038 - 1.775 \pm 0.209$ mJ (Mean $\pm$ SD)
(Sjovold *et al.,* 2013)	Male Wistar rats (mean 314 g)	UBC multimechanism	Contusion-compression	T9	Tip $\varnothing$= 2 mm Velocity = 700 mm.s^{-1} Displacement = 1 mm Residual compression = 0, 40, 90% Dwell = 60 min	Displacement = 1 mm Peak velocity = 700 mm.s^{-1}

Table 1.5 – *Continued from previous page*

Reference	Species	Apparatus	Mechanism	Location	Input Parameter(s)	Output Biomechanical Data Reported
(Lau *et al.,* 2013)	Male SD rats Infant (30 g); adult (250 g)	Lateral dislocation device (Fiford *et al.,* 2004)	Lateral dislocation	T12 – L1	*Infant* Displacement = 1.6, 2.8, 4.0 mm Velocity = 40, 80, 100 mm.s^{-1} *Adult* Displacement = 4, 7, 10 mm Velocity = 100, 200, 250 mm.s^{-1} Dwell = 1 s	NR
(Lee *et al.,* 2013)	Female Yucatan miniature pigs 20 – 25 kg	Custom weight drop	Contusion	T10 – 11	Tip ⌀ = 9.53 mm Tip mass = 50 g Drop height = 5, 10, 20, 30, 40 cm Dwell = 5 min (+ 100 g)	Peak velocity range = 1830 ± 20 – 2670 ± 30 mm.s^{-1} Impact force range = 11.1 ± 1.2 – 66.6 ± 7.8 N Dural displacement range = 2.1 ± 0.4 – 3.2 ± 0.3 mm (Mean ± SE)
(Yang *et al.,* 2013)	Farm pigs 51.6 ± 2.5 kg	Custom	Distraction	T9	Displacement = 1 mm intervals until TES-MEP recordings decreased by > 80% Dwell = 60 s every 3 mm; 90 s at SCI	NR

Table 1.5 – *Continued from previous page*

Reference	Species	Apparatus	Mechanism	Location	Input Parameter(s)	Output Biomechanical Data Reported
(Lee *et al.,* 2012)	Male SD rats 300 – 350 g	IH impactor	Unilateral contusion	C5	Tip $\varnothing$= 15 mm Force = 150 kDyn	Displacement = 1512.72 ± 27.86 µm Peak velocity = 120.24 ± 0.52 mm.s^{-1} Impact force = 155.55 ± 0.73 kDyn (Mean ± SD)
(Agrawal *et al.,* 2010)	Female Fischer rats 200 g	NYU MASCIS	Contusion	T8	Tip $\varnothing$= 2.0 mm Tip mass = 10 g Impact height = 6.25 mm (mild); 12.50 mm (moderate); 25.00 mm (severe); 50.00 mm (very severe)	NR
(Dunham *et al.,* 2010)	Male SD rats 275 – 300 g	IH Impactor	Hemicontusion	C5	Tip $\varnothing$= 0.8 mm Force = 100 kDyn (mild); 200 kDyn (moderate); 300 kDyn (severe)	Displacement = 679.3 ± 19.0; 1226.2 ± 25.5; 1614.6 ± 23.9 µm Peak velocity[†] = 118.5 ± 1.1; 124.5 ± 1.5; 118.7 ± 1.0 mm.s^{-1} Impact force = 103.4 ± 1.0; 213.6 ± 2.8; 312.6 ± 3.0 kDyn (Mean ± SEM) [†]Standard used with E of rodent spinal cord

Continued on next page

Table 1.5 – *Continued from previous page*

Reference	Species	Apparatus	Mechanism	Location	Input Parameter(s)	Output Biomechanical Data Reported
(Anderson *et al.*, 2009)	Female SD rats 200 – 230 g	IH Impactor	Contusion	C5	Tip $\varnothing$= 3.5 mm Force = 200 kDyn (mild); 250 kDyn (moderate) Dwell = 0 s	Impact force range = 208 – 231; 250 – 287 kDyn Peak velocity = 113 $\pm$ 1.7; 120.3 $\pm$ 7.3 mm.s^{-1} (Mean $\pm$ SD) Data from Experiment 3 of the study
(Choo *et al.*, 2009)	Male SD rats 311 $\pm$ 26 g	UBC multimechanism	Contusion Dislocation Distraction	Contusion = C4/5 Dislocation = C4/5 Distraction = C3/4 – C5/6	Velocity = 1000 mm.s^{-1} *Contusion:* Tip $\varnothing$= 2.0 mm Displacement = 1.1 mm *Dislocation:* Displacement = 2.3 mm (50%); 3.7 mm (100%)† *Distraction:* Displacement = 5.1 – 6.1 mm; 4.1 – 4.6 mm $\pm$ flexion Dwell = 1 s †Percentage canal occlusion	*Contusion:* Displacement range = 1.1 $\pm$ 0.02 mm Peak velocity range = 978 $\pm$ 37 mm.s^{-1} Impact force range = 2.1 $\pm$ 0.5 N *Dislocation:* Displacement range = 2.3 – 3.7 mm Peak velocity range = 753 – 1026 mm.s^{-1} Impact force range = 13.2 – 30.9 N *Distraction:* Displacement range = 4.1 – 6.1 mm Peak velocity range = 856 – 968 mm.s^{-1} Impact force range = 24.1 – 43.9 N (Mean $\pm$ SD for contusion)

Continued on next page

Table 1.5 – *Continued from previous page*

Reference	Species	Apparatus	Mechanism	Location	Input Parameter(s)	Output Biomechanical Data Reported
(Kim *et al.*, 2009)	Female C57BL/6 mice 18 – 20 g 10 wks	Custom	Contusion	T8/9	Tip $\varnothing$= 1.3 mm Displacement = 0.8 mm Velocity = 100, 200, 400 mm.s^{-1} Dwell = 20 ms	Data represented by graphs. No raw data.
(Persson *et al.*, 2009)	Cattle < 24 mths	Custom	Contusion	NR	Pellet area = 78.5, 157, 314 mm^2 Pellet mass = 7.0 g Velocity = 4.5 m.s^{-1}	NR
(Sparrey *et al.*, 2008)	Male SD rats 210 – 320 g	Modified OSU Impactor	Contusion	T10	Tip $\varnothing$= 2.0 mm Displacement = 1 mm Velocity = 3, 300 mm.s^{-1}	Displacement = 0.90 $\pm$ 0.03; 1.03 $\pm$ 0.10 mm Peak velocity = 2.69 $\pm$ 0.43; 307 $\pm$ 5.8 mm.s^{-1} Impact force = 0.54 $\pm$ 0.05; 2.37 $\pm$ 0.30 N Energy = 2.6 x 10^{-4} $\pm$ 1.7 x 10^{-5}; 1.4 x 10^{-3} $\pm$ 2.1 x 10^{-4} J Stiffness = 0.61 $\pm$ 0.07; 2.4 $\pm$ 0.28 N.mm^{-1} (Mean $\pm$ SD)

Table 1.5 – *Continued from previous page*

Reference	Species	Apparatus	Mechanism	Location	Input Parameter(s)	Output Biomechanical Data Reported
(Choo *et al.*, 2008)	Male SD rats 347 ± 28 g	UBC multimechanism	Contusion Dislocation Distraction	Contusion = C4/5 Dislocation = C4/5 Distraction = C3/4 – 5/6	See (Choo *et al.*, 2009)	*Contusion:* Displacement = 1.1 ± 0.02 mm Peak velocity = 998 ± 37 mm.s^{-1} Impact force = 1.5 ± 0.4 N *Dislocation:* Displacement = 2.5 ± 0.12 mm Peak velocity = 956 ± 32 mm.s^{-1} Impact force = 24.7 ± 5.7 N *Distraction:* Displacement = 4.1 ± 0.03 mm Peak velocity = 1112 ± 35 mm.s^{-1} Impact force = 37.9 ± 5.4 N (Mean ± SD)

Continued on next page

Table 1.5 – *Continued from previous page*

Reference	Species	Apparatus	Mechanism	Location	Input Parameter(s)	Output Biomechanical Data Reported
(Choo *et al.*, 2007)	Male SD rats 347 ± 28 g	UBC multimechanism	Contusion Dislocation Distraction	Contusion = C4/5 Dislocation = C4/5 Distraction = C3/4 – 5/6	See (Choo *et al.*, 2009)	*Contusion:* Displacement = 1.1 ± 0.06 mm Peak velocity = 967 ± 48 mm.s^{-1} Impact force = 2.0 ± 0.5 N *Dislocation:* Displacement = 2.5 ± 0.16 mm Peak velocity = 951 ± 95 mm.s^{-1} Impact force = 20.7 ± 6.5 N *Distraction:* Displacement = 4.1 ± 0.01 mm Peak velocity = 919 ± 29 mm.s^{-1} Impact force = 38.6 ± 3.0 N (Mean ± SD)
(Nishi *et al.*, 2007)	Female C57Bl/6 mice 8 wks	IH Impactor	Contusion	T9	Tip ⌀= 1.25 mm Force = 30 kDyn (mild); 50 kDyn (moderate); 70 kDyn (severe)	Data represented by graphs. No raw data.

Continued on next page

Table 1.5 – *Continued from previous page*

Reference	Species	Apparatus	Mechanism	Location	Input Parameter(s)	Output Biomechanical Data Reported
(Gensel *et al.*, 2006)	Female Long-Evans rats 217 g	Modified NYU MASCIS	Unilateral contusion	C5	Tip ⌀= 2.0 mm; Tip mass = 10 g; Drop height = 6.25 mm (mild); 12.5 mm (moderate)	Displacement = 2.11 ± 0.24 mm; 2.66 ± 0.24 mm; Peak velocity = 350 ± 10 mm.s^{-1}; 490 ± 10 mm.s^{-1}; Displacement rate = 0.28 ± 0.02 mm.s^{-1}; 0.39 ± 0.01 mm.s^{-1} (Mean ± SD)
(Dabney *et al.*, 2004)	Female Long-Evans rats 260 − 290 g	Harrington distractor	Distraction	T9/11	Displacement = 3 mm (mild); 5 mm (moderate); 7 mm (severe); Velocity = 1, 5, 10 mm.s^{-1}; Dwell = 0, 5, 10 s	NR
(Ghasemlou *et al.*, 2005)	Female BALB/c mice 16 − 18 g 6 − 8 wks	IH Impactor	Contusion	T10	Force = 30 kDyn (mild); 50 kDyn (moderate); 70 kDyn (severe)	Displacement range = 176 − 405 µm; 370 − 687 µm; 282 − 846 µm
(Pearse *et al.*, 2005)	Female Fischer rats 180–200 g	OSU ESCID	Contusion	C5	Tip ⌀= 4.0 mm; Displacement = 0.80 mm (mild); 0.95 mm (moderate); 1.10 mm (severe)	NR

Continued on next page

Table 1.5 – *Continued from previous page*

Reference	Species	Apparatus	Mechanism	Location	Input Parameter(s)	Output Biomechanical Data Reported
(Fiford *et al.*, 2004)	Female SD rats 200 – 250 g	Lateral dislocation device	Dislocation	T12 – L2	Displacement = 1 – 20 mm Velocity = 50 – 150 mm.s^{-1} Dwell = 1 s	Displacement range = 3.2 – 7.5 mm Velocity range = 57 – 127 mm.s^{-1} Force range = 17 – 27 N
(Scheff *et al.*, 2003)	Female SD rats 200 – 225 g	IH Impactor	Contusion	T10	Tip ⌀ = 2.5 mm Force = 100 kDyn (mild); 150 kDyn (moderate); 200 kDyn (severe)	Peak velocity = 122 ± 3.6 mm.s^{-1} Impact displacement and force data represented as graphs. No raw data. (Mean ± SEM)
(Stokes and Jakeman, 2002)	C57Bl/6 mice	OSU ESCID-2000	Contusion	T9	Displacement = 0.3, 0.5, 0.8 mm Dwell = 12 – 14 ms	Data represented by graphs. No raw data.
(Ma *et al.*, 2001)	Female C57Bl/6 mice 19 – 24 g 10-15 wks	OSU ESCID	Contusion	T9	Tip ⌀ = 1.35 mm Displacement = 0.3, 0.5, 0.8 mm Dwell = 12 – 14 ms	Impact displacement = 0.284 ± 0.001; 0.498 ± 0.002; 0.792 ± 0.003 mm Peak force = 51.5 ± 5.0; 102.4 ± 9.5; 185.4 ± 13.9 kDyn Impulse momentum = 0.613 ± 0.069; 1.045 ± 0.158; 1.634 ± 0.204 (Mean ± SEM)

Continued on next page

Table 1.5 – *Continued from previous page*

Reference	Species	Apparatus	Mechanism	Location	Input Parameter(s)	Output Biomechanical Data Reported
(Jakeman *et al.*, 2000)	Female Balb/C, C57Bl/6 ± B10/PL mice	OSU ESCID	Contusion	T9	Tip $\varnothing$= 1.3, 1.4 mm Displacement = 0.5, 0.7, 0.9 mm Dwell = 10 ms	Peak displacement = 0.50 ± 0.001; 0.70 ± 0.001 mm Peak force = 100 ± 3; 143 ± 6 kDyn Peak velocity = 14.80 ± 0.21; 17.94 ± 0.20 mm.s^{-1} Peak energy = 3.3 x $10^{-3} \pm$ l x 10^{-4}; 5.9 x $10^{-3} \pm 2$ x 10^{-4} kDyn.cm^{-1} (Mean ± SEM) 0.9 mm data excluded in study
(Kuhn and Wrathall, 1998)	Female C57Bl/6 mice 18-22 g 7 wks	Modified rat rig (Noble and Wrathall, 1989)	Contusion	T8	Tip $\varnothing$= 1.5 mm Mass of tip = 1, 2, 3 g Drop height = 2.5, 5.0 cm	NR

Continued on next page

Table 1.5 – *Continued from previous page*

Reference	Species	Apparatus	Mechanism	Location	Input Parameter(s)	Output Biomechanical Data Reported
(Bresnahan *et al.*, 1987)	Female albino rats 136 – 325 g	OSU ESCID	Contusion	T6	Tip $\varnothing$ = 2.0 mm *Group II:* Maximum force = 12 – 147 kDyn Dwell = 4 – 16 ms *Group III:* Displacement = 2 mm Dwell = 10 ms	*Group II:* Displacement range = 0.38 – 2.48 mm Force range = 12 – 147 kDyn Velocity range = 80 – 540 mm.s^{-1} Work range = 0.33 – 25.30 kDyn.cm^{-1} *Group III:* Displacement range = 0.17 – 0.184 mm Force range = 65 – 100 kDyn Velocity range = 400 – 460 mm.s^{-1} Work range = 1.7 – 6.7 kDyn.cm^{-1}

E = Young's Modulus; NR = Not Reported; NYU MASCIS = New York University Multicenter Animal Spinal Cord Injury Study impactor; OSU ESCID = Ohio State University Electromagnetic Spinal Cord Injury Device; SD rats = Sprague-Dawley rats; UBC = University of British Columbia; TES-MEP = Transcranial Electrical Stimulation Motor Evoked Potential; Output data listed in order of mild, moderate, severe where indicated in the input parameters column.

1.8.1.1   Contusion

Given velocities of up to 10 m.s^{-1} have been measured in *ex vivo* models of spinal cord injury (Section 1.5.1), reflecting this in *in vivo* animal models, which are much smaller in scale, has proved difficult due to practical limitations, including with the rigs available. Contusion models are designed to inflict a transient bruising injury to the spinal cord. Contusion is the most common mechanism of injury modelled *in vivo*, representing 43% of animal studies (Sharif-Alhoseini *et al.,* 2017). It is clinically relevant due to its prevalence in human cases (Section 1.5.1). Force feedback-controlled contusion devices, such as the Infinite Horizons Impactor, comprise a stepper motor capable of producing a stroke length at a relatively constant velocity and the impacting tip is automatically withdrawn once the target force is registered. Varying forces have been used to inflict graded cervical and thoracic injuries in rats and mice, ranging from mild to moderate to severe, as measured by various behavioural parameters (Anderson *et al.,* 2009; Dunham *et al.,* 2010; Ghasemlou *et al.,* 2005; Lee *et al.,* 2012; Nishi *et al.,* 2007; Scheff *et al.,* 2003). However, due to limited sensor feedback the velocity is restricted in order to prevent an overshoot in force. The requirements for a greater velocity means a greater distance is required in order to stop once the target force has been achieved with impact velocities of less than 130 mm.s^{-1} being achieved in literature (Table 1.5).

The Ohio State University (OSU) Electromagnetic Spinal Cord Injury Device (ESCID) is similar to the IH impactor in that it utilises a feedback-controlled electromagnetic impactor; however, displacement can be controlled using this device and does not result in bouncing as observed with other devices, such as the NYU MASCIS, because the impactor tip is actively withdrawn from the cord. The OSU ESCID has been used to model thoracic contusion injury in mice (Jakeman *et al.,* 2000; Ma *et al.,* 2001; Stokes and Jakeman, 2002) and both cervical and thoracic contusion in rats (Bresnahan *et al.,* 1987; Pearse *et al.,* 2005). Impact velocities have not been reported in all studies, but available data shows values of up to 460 mm.s^{-1} being achieved.

The New York University (NYU)/Multicentre Animal Spinal Cord Injury Study (MASCIS) impactor utilises the transfer of energy from a weight (typically a 10 g rod) dropped from a predetermined height onto the spinal cord (Gruner, 1992). An increase in mass of the weight and/or the height at which it is dropped results in an increase in injury severity due to the greater energy and displacement applied to the cord. The impact velocity is also inherently increased so these parameters cannot be decoupled using these types of devices. One limitation with this device is the potential for introduction of a second contusion event due to the weight bouncing off the cord from the initial contusion (Cheriyan *et al.,* 2014).

The University of British Columbia (UBC) multimechanism device was developed more recently to enable the modelling of contusion, dislocation and distraction SCI in rats (Choo *et al.,* 2007). The advantage of this device is that both displacement and velocity can be controlled independently and has the versatility of being able to inflict different mechanisms of SCI, the only device currently available to do so. It has mainly been used to

model cervical contusion injury in rats to evaluate the primary and secondary pathologies and behavioural changes up to eight weeks post-injury (Chen *et al.,* 2016; Choo *et al.,* 2008, 2007). A variety of displacement and velocities (up to 1 m.s^{-1}) have also been modelled to investigate the relative importance of each parameter in influencing injury outcomes (Lam *et al.,* 2014).

1.8.1.2   Compression

Compression models involve the persistent compression of the cord over a relatively longer period of time, as opposed to the transient nature of contusion injuries. This mode of injury is more commonly observed in non-traumatic SCI, where injury to the spinal cord is not caused by a sudden high energy impact, but rather lower velocity injury which progresses over a time period up to years in length. Examples of causes of non-traumatic SCI include bacterial infections, spinal stenosis, and tumour compression. Contusion-compression models, where a contusion injury is followed by sustained compression is a more common TSCI scenario, particularly resulting from burst fractures where bone fragments impinge on the cord and remain compressing the cord for a period of time. Few studies have modelled contusion-compression where the acute contusion injury has been modelled with clinically relevant impact velocities. Sjovold *et al.,* (2013) modelled a thoracic contusion-compression injury in rats using UBC multimechanism device. Contusion at 700 mm.s^{-1} and 1 mm displacement followed by residual compression (40 or 90%) for 60 minutes was simulated. Results showed that increased residual compression resulted in significantly increased haemorrhage and loss of neuronal nuclei in the grey matter, suggesting residual compression leads to more severe tissue damage and this is not being reflected in pure contusion models.

Common tools available to inflict a compression injury include a modified aneurysm clip, calibrated forceps and inflatable balloons (Cheriyan *et al.,* 2014). The clip or forceps are used to compress the exposed spinal cord to a defined force or width, respectively. Inflatable balloons attached to catheters have been implanted into the epidural or subdural space of multiple species, including rats and dogs (Fukuda *et al.,* 2005; Vanický *et al.,* 2001). By varying inflation volume, rate of inflation and duration, graded injuries have been produced. Despite these methods being inexpensive, relatively simple, and adaptable for use at different spinal regions they do not reproduce the biomechanical loads that result from an acute traumatic impact in humans.

1.8.1.3   Dislocation

Despite being the most prevalent mechanism of TSCI observed in humans, dislocation injury is not frequently modelled *in vivo*, representing only 1% of animal studies when combined with distraction model studies (Sharif-Alhoseini *et al.,* 2017). This is likely due to the increased complexity of the injury, requiring external clamps to grip onto adjacent vertebrae, and increased instability of the vertebral column (Section 1.5.1). Unlike contusion models which typically expose the spinal cord via a dorsal laminectomy, dislocation models are typically closed column, maintaining the integrity of the spine and spinal components. Fiford *et al.,* (2004) developed an electromagnetic

feedback-controlled lateral dislocation device which consisted of two horizontal beams, of which one was fixed and the other laterally displaced the caudal vertebrae to a defined displacement (1 – 20 mm) and maximum velocity of 150 mm.s^{-1}. The data showed that larger displacements resulted in an increase in injury severity, as characterised by ligamentous failure and fracture. Choo *et al.,* (2009) used the UBC multimechanism device to model cervical anterior fracture-dislocation, with displacements representing 50 and 100% canal occlusion. Peak velocities ranged from 750 – 1 m.s^{-1}, with the higher velocities achieved at the larger displacements.

1.8.1.4   Distraction
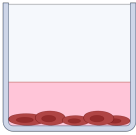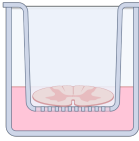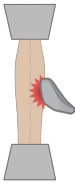
Distraction models involve axial stretching of the spinal cord, representing the tensile forces experienced by the spinal cord during flexion and hyperextension injuries. Distraction injuries are infrequently modelled compared to contusion injury. As previously mentioned distraction represents only 1% of the total proportion of *in vivo* studies when combined with dislocation (Sharif-Alhoseini *et al.,* 2017). Dabney *et al.,* (2004) performed a laminectomy in order to place modified Harrington hooks under the laminae of adjacent vertebrae in rats and inflicted injury using a computer-controlled stepping motor. Mild, moderate, and severe injury were modelled by varying the distraction length and velocity, which was limited to 10 mm.s^{-1}. The UBC multimechanism device utilises clamps which are wedged beneath the transverse processes of the vertebrae and also has the option of incorporating flexion to better mimic human flexion-distraction injuries (Choo *et al.,* 2009). A uniaxial distraction was applied to the cervical spinal cord of rats by distracting the caudal clamp to a defined displacement.

1.8.2   *In vitro* Models

In vivo models remain a preferred model to many scientific communities due to their similarities in biological complexity and (patho)physiology to humans. The requirement for more representative animal models, particularly larger animals, is becoming increasingly considered as an important intermediary for the translation of successful small animal preclinical trials into humans. However, there is a push by some communities to reduce the usage of animals in SCI research where the likelihood of causing pain, distress, suffering and lasting harm is greater. Further, it can be difficult to isolate specific aspects of TSCI pathology due to the high degree of biological complexity and interactions within the CNS.

Consequently, *in vitro* models have been developed as an alternative to overcome issues pertaining to the practical and ethical use of *in vivo* models, and support the principles of the 3Rs (Replacement, Reduction, Refinement). They can permit the study of cell-cell interactions and single cell population experiments in a more controlled environment and the knowledge gained can be used to complement and/or inform animal studies (Abu-Rub *et al.,* 2010). *In vitro* models are available in the form of numerous two- (2D) and three-(3D) dimensional formats (Table 1.6).

Table 1.6: Two-dimensional and three-dimensional formats for modelling spinal cord injury *in vitro*. A description of the most common types of models used to investigate SCI *in vitro*, including their advantages and disadvantages. Figures created using Biorender.

Model	Description	Advantages	Disadvantages	Reference(s)
Two-dimensional				
Cell culture	• Dissociated cells • Monolayer culture	• Simple • Inexpensive • Can generate isolated or co-cultures	• Altered cell-cell and cell-matrix interactions • Surface functionalisation required for neuronal attachment • Cannot mimic biomechanical aspects of TSCI e.g. displacement	(Slovinska *et al.,* 2016)
Three-dimensional				
Organotypic slice	• 150–400 µm slices • Transverse, longitudinal, or saggital • Commonly cultured at air-liquid interface	• Retains cytoarchitecture and connections • High throughput due to the number of slices available	• Damage to cells • Target innervation lost due to axotomy	(Abu-Rub *et al.,* 2010)
Ex vivo	• Dissection of SC from animal e.g. rodents, bovine	• Native tissue used	• SC not under in situ conditions • Degradation after dissection which alters biomechanical properties	(Mazuchowski, Thibault, *et al.,* 2003; Oakland *et al.,* 2006; Zhang *et al.,* 2010b)
Natural hydrogel	• Highly hydrophilic polymeric networks • Derived from natural sources e.g. collagen from rat tail	• Mimics aspects of ECM • Bioactive ligands facilitate cell attachment	• Less mechanically tuneable • Does not mimic complete ECM • Variability between batches	(Hopkins *et al.,* 2015; Perale *et al.,* 2011)
Synthetic hydrogel	• Prepared from synthetic materials e.g. polycaprolactone (PCL)	• Tuneable mechanical properties • Reduced immunogenicity	• Lack bioactivity	(Hopkins *et al.,* 2015; Lutolf and Hubbell, 2005)

Two-dimensional models of SCI have involved plating dissociated cells onto the surface of rigid materials, such as plastic, glass coverslips, membranes, or hydrogels. Boomkamp *et al.,* (2014) cultured astrocytes on the surface of plated dissociated mixed spinal cord cells isolated from rats and used a scalpel to create a lesion across the culture. They found a lack of neurite outgrowth and reactive astrocyte migration around the lesion, which is in agreement with results from *in vivo* models. Neural cell gene expression, growth, and function is greatly influenced not just by the culture conditions, but also the microenvironment in which they reside. Cells cultured in 2D generally only receive nutrients and support from the surface; whereas cells cultured in 3D are able to receive nutrients in all dimensions (Cukierman *et al.,* 2001; Pedersen and Swartz, 2005). Further, cell-cell and cell-matrix interactions are not replicated in 2D, which are important for a variety of functions including cell differentiation, proliferation, viability, and responsiveness to stimuli (Baker and Chen, 2012).

Cells cultured in 3D adopt more physiological morphologies, compared to 2D, where the cells are forced to adhere to a rigid surface and adopt a flattened morphology (Friedl and Bröcker, 2000; Pedersen and Swartz, 2005). Astrocytes cultured in 3D in softer collagen hydrogels exhibited small and round morphologies with few stress fibres (Georges *et al.,* 2006). In contrast, on stiffer surfaces, such as the edges of the hydrogel in contact with the walls of tissue culture plastic, astrocytes exhibited highly spread morphologies and more stress actin fibres, typical of reactive glia (East *et al.,* 2009; Georges *et al.,* 2006). This makes it difficult to investigate the effects of external factors on astrogliosis as the cells are already reactive without the experimental treatment. The aim of developing 3D *in vitro* models is to better recreate this unique microenvironment of the spinal cord and provide an intermediary between 2D monolayer cultures and *in vivo* systems.

Organotypic slice culture models involve culturing slices of the spinal cord (150 – 400 µm) typically on semi-porous membranes at the air-liquid interface (Stoppini *et al.,* 1991). This retains the native cytoarchitecture and neural connectivity of the native spinal cord, and does not require the dissociation of cells. Pandamooz *et al.,* (2019) simulated a weight drop contusion injury to 400 µm thick slices of adult lumbar rat spinal cord slices and observed maximal cell death at Day 1, an increase in GFAP expression and proliferation, which is in line with the pathophysiological events observed following SCI *in vivo*. Weightman *et al.,* (2014) generated 350 µm thick longitudinal spinal cord slices from mice and applied a lesion using a scalpel. Evidence of astrogliosis (increased GFAP expression and hypertrophy) and microglial infiltration into the lesion was observed at 12 days post-injury, mimicking the pathological features of SCI *in vivo*. Limitations of the use of organotypic slices include the loss of target innervation due to axotomy, particularly in transverse slices, and the damage caused to cells through the slicing process.

Hydrogels have been a popular choice of substrate for 3D cell culture and biomaterial for tissue engineering applications. Hydrogels are highly hydrophilic 3D networks of

crosslinked polymer chains capable of holding large amounts of water (Perale *et al.,* 2011). As a result, they exhibit mechanical properties similar to native soft tissues and can support cell adhesion, survival and proliferation (Caliari and Burdick, 2016). Hydrogels can be prepared from both natural and synthetic sources, which have their advantages and disadvantages (Table 1.6). In the CNS, laminins and collagens have been shown to promote neural attachment and neurite outgrowth (Barros *et al.,* 2011).

Collagen hydrogels have been used to model SCI *in vitro* using mechanical and chemical methods. Bar-Kochba *et al.,* (2016) encapsulated primary rat cortical neurons in type I collagen hydrogels (2.2 mg.mL^{-1}) and applied compressive strains at strain rates of 10.s^{-1} and 75.s^{-1} to evaluate neuronal pathology. East *et al.,* (2009) encapsulated primary cortical astrocytes in type I collagen hydrogels (2 mg.mL^{-1}, First Link UK) and modelled astrogliosis using the chemical, transforming growth factor–beta 1 (TGF-β1). Research at The University of Leeds has also utilised type I collagen (2 mg.mL^{-1}, First Link UK) to model focal contusion injuries using the IH impactor and BOSE Electroforce BioDynamic 5110 materials testing device (Kirk, 2018; Smith, 2016).

A disadvantage associated with natural hydrogels is that they are mechanically unstable due to their highly hydrated nature and the loss of some structural and chemical organisation during the extraction process (Tronci *et al.,* 2015). A summary of studies pertaining to the mechanical properties of collagen hydrogels is presented in Table 1.7. These values are lower than moduli reported for the spinal cord (Table 1.2) which has potential implications for the design of hydrogel-based scaffolds for SCI repair and influences on cell behaviour (Perale *et al.,* 2011). Variability exists in the mechanical testing methods and parameters used, and even collagen source and preparation has been shown to affect mechanical properties (Antoine *et al.,* 2014; Parenteau-Bareil *et al.,* 2011). Tensile tests have been most commonly used to evaluate the mechanical properties of SC tissues, whereas compression has been mostly used for hydrogels. Despite this, collagen hydrogels have already been used in neural tissue engineering applications, demonstrating successful neural cell attachment, proliferation and survival (East *et al.,* 2007, 2009; Georgiou *et al.,* 2013; Phillips *et al.,* 2005).

Many naturally-derived hydrogels utilise only one ECM component, such as collagen or laminin. As the ECM is composed of numerous types of proteins and molecules, there is a lack of complexity in these biomaterials, which may affect cellular behaviour. Therefore, a number hydrogels have been developed using methods to assemble hydrogels using multiple ECM components or prepare hydrogels from decellularised tissues (Tukmachev *et al.,* 2016; Uriel *et al.,* 2009). Synthetic hydrogels have become increasingly popular, due to their reduced immunogenicity, reduced batch-to-batch variation, and increased mechanical tuneability. However, they lack bioactivity thus are less conducive for cell attachment and survival and require modification to incorporate cell attachment motifs (Rao and Winter, 2009).

Table 1.7: Mechanical properties of type I collagen hydrogels. Studies which evaluated the mechanical properties of collagen type I hydrogels were summarised as they are pertinent to the hydrogels used in the research in this thesis. E_c = bulk compressive modulus. H_A = aggregate modulus. * = gels were functionalised.

Test	Source	Concentration	Specimen dimensions	Testing parameters	Modulus	Reference
Oscillatory rheology	Rat tail type I (First Link UK)	2 mg.mL^{-1}	$\varnothing$ = 24 well plate Volume = 500 ul	Strain = 1% Frequency = 1 Hz	48.66 Pa	(Smith, 2016)
Compression	Rat tail type I in-house	0.25 wt%	$\varnothing$ = 8 mm discs	Loading rate = 3 mm.min^{-1} to failure	E_c = 30 – 168 kPa *	(Tronci *et al.*, 2015)
Compression	Rat tail type I in-house	4–10 mg.mL^{-1}	$\varnothing$ = 9.5 mm Thickness = 8.5 mm	Strain rate = 0.1%.s^{-1} Strain = 0–20%	538 – 10 691 Pa	(Antoine *et al.*, 2015)
Compression	Rat tail type I in-house	0.2–0.4 w/v	$\varnothing$ = 16 mm Volume = 1 mL Mean thickness = 4.79 mm	Strain rate = 0.5%.s^{-1} Strain = 5%	H_A = 850 – 1200 Pa	(Busby *et al.*, 2013)
Oscillatory rheology	Rat tail type I (BD Biosciences)	2 mg.mL^{-1}	$\varnothing$ = 12 mm	Strain = 0.5% Frequency = 0.1 Hz	4 – 62 Pa	(Miron-Mendoza *et al.*, 2010)
DMA	Rat tail type I (First Link UK)	2 mg.mL^{-1}	Thickness = 0.1 mm Width = 1 mm strips Plastically Compressed	Strain = 5 – 30%	1057 – 2305 kPa	(Hadjipanayi *et al.*, 2009)
DMA	Rat tail type I (First Link UK)	2 mg.mL^{-1}	$\varnothing$ = 1.7 mm Length = 13 mm spiral constructs Plastically compressed	Loading rate = 200 mN.min^{-1} to failure	1.5 MPa	(Brown *et al.*, 2005)

1.8.2.1   Methods for Simulating SCI *In Vitro*

With the variety of culture formats available for modelling SCI, different methods for generating the injury itself have been developed (Table 1.8). In some studies, a specific aspect of SCI is investigated, such as formation of the glial scar or hypoxia-mediated cell death. This is achieved by manipulating the environment through culturing samples in a hypoxic chamber, for instance.

Table 1.8: Methods of inducing SCI or replicating specific aspects of SCI pathophysiology *in vitro*. Examples of methods used to induce SCI or aspects of SCI include chemical, mechanical, and environmental methods. TGF-β1 = transforming growth factor-β1. H_2O_2 = hydrogen peroxide.

Method	Examples	Advantages	Disadvantages	References
Chemical	• TGF-β1 • H_2O_2 • Kainite	• Specific aspects of TSCI modelled e.g. astrogliosis, oxidative injury, excitotoxicity	• Biomechanics of TSCI not replicated	(East *et al.*, 2009; Feeney *et al.*, 2008; Mazzone and Nistri, 2014)
Ischaemia/ Hypoxia	• Oxygen-glucose medium deprivation • Anoxic chambers	• Model hypoxia-related cytotoxicity	• Biomechanics of TSCI not replicated	(Frantseva *et al.*, 1999; Sundstrom *et al.*, 2005)
Mechanical	• Scratch model • Stretch model • SCI apparatus e.g. IH impactor	• Can model e.g. glial scar, axonal transection • Different deformation patterns e.g. shear, contusion, compression • Biomechanics of TSCI considered	• Biomechanical parameters not always clinically relevant • Increased complexity due to need to verify and validate parameters e.g. velocity, displacement	(Boomkamp *et al.*, 2014; Cullen *et al.*, 2007; Krassioukov *et al.*, 2002)

Transforming growth factor-β1 (TGFβ1)-mediated chemical induction of astrogliosis has been used to develop and validate 3D culture models, (East *et al.*, 2009). TGFβ1 has been shown to regulate the formation of the glial scar through multiple activities, such as activation of astrocytes and microglia and promoting matrix deposition (Logan *et al.*, 1994). It has also been utilised as a positive control of astrogliosis alongside the

development of biomechanical models of TSCI using novel apparatus, such as the BOSE Electroforce BioDynamic materials testing systems (Cullen *et al.,* 2007; Kirk, 2018). Despite the advantages associated with chemical inducers of SCI, they lack the important factor of incorporating the biomechanics of TSCI.

Mechanical methods encompass those with and without controllable biomechanical parameters, such as velocity and displacement. Scratch models employ scalpels or pipettes to scrape across the surface of cell-seeded surfaces or organotypic slices to model a lesion devoid of cells. Astrocytes and microglia migrate towards the lesion and mediate scar formation representing the process *in vivo* (Slovinska *et al.,* 2016; Weightman *et al.,* 2014). However, this model does not recapitulate the primary damage associated with a TSCI, which is caused by a high impact event and which is now known to influence the progression of secondary injury (Mattucci *et al.,* 2019). Mechanical models which have implemented biomechanical characteristics of a TSCI include Cullen *et al.,* (2007) who utilised a custom-built electromagnetic shearing device to inflict high strain rate shear deformation to primary rat cortical neuron-astrocyte co-cultures encapsulated in Matrigel hydrogels. Strain and strain rate were independently controlled: up to 0.50 strain and $30.s^{-1}$ strain rate.

Materials testing machines, such as the BOSE group of machines (TA Instruments), are capable of decoupling velocity and displacement, thus have the potential to be adapted for inflicting high velocity contusive and/or tensile injuries *in vitro.* Busby *et al.,* (2013) used the BOSE Electroforce 3200 Test Instrument to evaluate the mechanical properties of rat type I collagen hydrogels, using a strain of 5% and strain rate of $0.5\%.s^{-1}$ (Table 1.7). With a mean gel thickness of 4.79 ± 0.06 mm, this is equivalent to a rate of 0.024 mm.s^{-1}. Koivisto *et al.,* (2017) used the BOSE Electroforce BioDynamic 5100 to evaluate the mechanical properties of bioamine crosslinked gellan gum (GG) hydrogels for neural tissue engineering applications. Gels were tested under compression, with a strain rate of 10 mm.min^{-1} to a maximum strain of 65% of the original gel height (6.5 mm). These strain rates are not reflective of the rates used in *in vivo* TSCI models, nor observed clinically but are typical for mechanical testing.

Salegio *et al.,* (2016) used the BOSE TestBench™system apparatus *in vivo* to inflict a cervical unilateral contusion injury in Macaca mulatta (non-human primates) using an input velocity of 1000 mm.s^{-1} and a displacement depth range of 2.0 – 4.0 mm. A limitation of that study was that variable output velocities were measured- 270 – 580 mm.s^{-1}- which were below the target input. Kirk (2018) used the BOSE Electroforce BioDynamic 5110 to model focal contusion injuries in astrocyte-seeded collagen type I hydrogels, using an input velocity of 3000 mm.s^{-1} and a range of displacement depths up 100% of the total gel thickness. The output velocity was not reported but these parameters are within the range of velocities used *in vivo* and measured from biomechanical studies of burst fracture *ex vivo* (Wilcox *et al.,* 2003). This study has combined the biomechanical aspects of modelling from *in vivo* studies and the simplicity of *in vitro* systems to investigate a variety of research questions, including how matrix mechanical

properties affects neural cell behaviour and their responses to controlled high velocity focal contusion at defined displacement depths. However, verification and validation of these materials testing machines is required, particularly at the higher strain rates required to accurately model traumatic injuries.

1.9 Therapeutic Strategies

1.10 Summary and Aims

1.10.1 Summary

Traumatic spinal cord injury is a complex and heterogeneous series of events which affects a large and heterogeneous population. Given the complexity of human SCI, no one model can encompass all aspects of injury. The histopathological and behavioural differences observed across contusion, dislocation and distraction by Choo *et al.,* (2008) and Chen *et al.,* (2016) highlights the importance of considering and implementing biomechanical parameters into a model which reflects the stresses and strains observed clinically. It also presents an area of research for the stratification of patients based on injury mechanism and where the development and application of therapeutic interventions could be targeted more selectively. For instance, due to the larger extent of neuronal damage following dislocation injury, interventions which promote axon outgrowth may be most effective for contusion injury.

Although previous studies using *in vitro* and *in vivo* models have reported robust characteristic responses to SCI, the relationship between biomechanical inputs and secondary responses are less well understood. In particular, it is not known whether different neural cell populations respond to mechanical injury which is proportional to injury severity, whether there is a dominant parameter which influences cell responses, and what the thresholds are for injury activation in these different populations. It is difficult to isolate cell specific responses to injury *in vivo* due to the complex interactions between different neural cell types, thus an *in vitro* 3D model would be beneficial where single cell populations can be isolated and studied. In order to begin investigating these research gaps, an appropriate injury model needs to be developed which enables the independent control of displacement and velocity, is capable of modelling velocities reflective of traumatic injuries, and is capable of modelling multiple mechanisms of TSCI.

The BOSE Electroforce BioDynamic 5110 (BOSE) is a commercially available materials testing machine which possesses numerous features that make it appropriate for simulating TSCI. Most importantly, displacement and velocity can be independently controlled. Further, the apparatus can be configured to apply tensile strains by changing the compression platens for tensile grips, thus two mechanisms of injury can potentially be modelled. The BOSE group of apparatus has been used in limited TSCI contexts, modelling contusion injuries *in vivo* (Salegio *et al.,* 2016) and *in vitro* (Kirk, 2018). Therefore, in depth verification of the displacement and velocity parameters will be

evaluated under parameters which represent clinical injuries. The use of a 3D-seeded collagen hydrogel with primary rat cortical astrocytes was selected as this hydrogel provides a permissive environment for long-term neural cell survival which approximates that of the spinal cord. As key contributors to astrogliosis and the glial scar, primary astrocytes were selected to be experimented on in isolation to probe cellular thresholds. Astrocyte viability and reactivity will be assessed following contusion and distraction injury and discussed alongside the kinetic outputs measured: peak displacement, impact velocity, peak velocity, load, and energy applied.

1.10.2   Aim and Objectives

The aim of this project is to evaluate the effects of varying input displacement and velocity parameters of contusion and distraction injuries on primary rat cortical astrocyte responses *in vitro*.

This is to be achieved through the following objectives:

I. To assess the suitability of utilising the BOSE 5110 Electroforce BioDynamic as a rig capable of simulating controlled, repeatable loads representative of contusion and distraction injury scenarios.

II. To develop a protocol for the simulation of contusion and distraction injuries using three-dimensionally encapsulated astrocytes in collagen hydrogels.

III. To evaluate the biological responses of astrocytes to simulated contusion and distraction injury.

IV. To investigate the relationship between the primary mechanical input and responses of primary astrocytes cultured in isolation.

Chapter 2

General Materials and Methods

2.1 Equipment and Software

The equipment and software used, along with their suppliers, are listed in Appendix A, Table 6.1.

2.2 Consumables

The consumables used, along with their suppliers, are listed in Appendix A, Table 6.2.

2.3 Chemicals and Reagents

The chemicals and reagents used, along with their suppliers, are listed in Appendix A, Table 6.3.

2.4 Antibodies

The antibodies and nuclear stain used in this study are listed in Table 2.1. Astrocytes were immunolabelled using an anti-GFAP (glial fibrillary acidic protein) polyclonal antibody, which labels the cytoskeleton of the cell. GFAP is a widely used marker of astrocytes and is also a common marker of astrocyte activation, thus immunolabelling for this component is suitable for comparing injured and non-injured astrocytes in this study. Chondroitin sulfate proteoglycans (CSPG) were immunolabelled using a CS-56 monoclonal antibody, which is specific for the glycosaminoglycan (GAG) portion of CSPGs.

Table 2.1: List of Antibodies Used

Antigen	Clonality	Isotype	Host	Dilution	Supplier	Product Code
Primary Antibodies						
CSPG (CS-56)	Mono	IgM	Mouse	1:200	Sigma-Aldrich	C8035
GFAP	Poly	IgG	Rabbit	1:150	Dako	Z0334
Secondary Antibodies						
Alexa Fluor 488	Poly	IgG	Goat anti-rabbit	1:300	Thermo Fisher Scientific	A11070
Alexa Fluor 568	Poly	IgM	Goat anti-mouse	1:500	Thermo Fisher Scientific	A21043
Nuclear Stain						
DAPI	-	-	-	1:1000	Sigma-Aldrich	D9564

2.5 General Methods

2.5.1 Sterilisation

2.5.1.1 Disinfection of Surfaces

Surfaces, such as that of the Class II safety cabinet, were sterilised using 1% Trigene (v/v), followed by 70% (v/v) ethanol, then UV light. Prior to placing equipment and reagents into the hood, the surfaces were sprayed and cleaned with 1% (w/v) Virkon, followed by 70% (v/v) ethanol. The equipment was then sprayed with 70% (v/v) ethanol prior to placing into the hood. Solutions containing cells were disinfected in 1% (w/v) Virkon for 20 minutes before discarding.

2.5.1.2 Dry Heat Sterilisation

Equipment to be sterilised via dry heat were wrapped in aluminium foil and placed into an oven at 190 °C, for 4 hours. Delicate tools, such as dissection tools were sealed in a metal tin.

2.5.1.3 Moist Heat Sterilisation

Solutions and/or equipment were placed into autoclavable receptacles and labelled with autoclave tape. Lids on bottles were loosely screwed to enable steam to escape. The items were autoclaved at 121 °C, 15 psi, for 20 minutes.

2.5.1.4 Filter Sterilisation

Solutions which required filter sterilisation were done so using a syringe fitted with a 0.22 µm filter. The solution to be filter sterilised was drawn up into the syringe. The syringe was then inverted and any air bubbles expelled. The filter was then attached to the syringe and the solution filtered into a new sterile receptacle.

2.5.2 Measurement of pH

The pH meter was calibrated prior to use according to the manufacturer's instructions, using pH standard solutions at pH 4, 7, and 10. The pH of the solution being prepared was adjusted to its required pH, using 1 M sodium hydroxide or 1 M hydrochloric acid.

2.5.3 Preparation of General Solutions

2.5.3.1 Antibody Diluent

To prepare 60 mL of antibody diluent, 6 mL sodium azide (1% w/v) was mixed with 300 µL BSA solution (5% w/v), in 40 mL of 1x TBS. The pH of the solution was measured and adjusted to pH 7.6 where necessary, using 1 M hydrochloric acid or 1 M sodium hydroxide. The volume of the pH adjusted solution was then made up to 60 mL using 1x TBS. The solution was stored at 4 °C, for up to three months.

2.5.3.2 Bovine Serum Albumin

A 5% (w/v) solution of BSA was prepared by weighing out and dissolving 0.5 g BSA into 10 mL PBS.

2.5.3.3 DAPI (4',6-diamidino-2-phenylindole)

A stock solution of DAPI at 1 mg.mL^{-1} was prepared using distilled water. A working concentration of 1 µg.mL^{-1} was prepared for all experiments, by performing a 1:1000 dilution with the appropriate diluent.

2.5.3.4 Ethanol

A 70% (v/v) solution of ethanol was prepared by mixing together 7 L of 100% ethanol with 3 L of distilled water.

2.5.3.5 Hydrochloric Acid

A 1 M solution of hydrochloric acid (HCl) was prepared by adding 8.212 mL of HCl solution (37% w/w) to 25 mL deionised water, in a volumetric flask. The volume was then adjusted to 100 mL with deionized water.

2.5.3.6 LIVE/DEAD™Viability/Cytotoxicity Assay Solution

The viability status of mammalian cells can be distinguished by specific activities, which the LIVE/DEAD™assay exploits. Live cells can be characterised by their ubiquitous

intracellular esterase activity and the presence of an intact plasma membrane. A dual-stain, comprising calcein AM (CAM) and ethidium homodimer-1 (EthD-1) is applied to the cells, whereby CAM indicates intracellular esterase activity by green fluorescence (ex/em 495/515 nm), and EthD-1 indicates loss of plasma membrane integrity by red fluorescence (ex/em 495/635 nm). The individual reagents were stored at -20 °C protected from light. Once thawed at room temperature, a volume of 2 µL CAM and 3 µL EthD-1 was mixed with 3995 µL of the appropriate complete cell culture medium. The final concentration of CAM and EthD-1 was 2 and 1.5 µM, respectively. The solution was wrapped in foil to protect it from light, prepared fresh and used immediately.

2.5.3.7   Methanol

A 70% (v/v) solution of methanol was prepared by mixing 7 mL 100% methanol with 3 mL distilled water, and stored at room temperature for up to one month.

2.5.3.8   Phosphate Buffered Saline (PBS)

Into a clean glass Duran bottle, a solution of PBS was prepared by dissolving one PBS tablet per 100 mL distilled water. The solution was stirred using a magnetic stirrer until the tablet(s) completely dissolved. The solution was autoclaved using moist heat (Section 2.5.1.3).

2.5.3.9   Poly-D-Lysine

A 50 µg.mL^{-1} solution of PDL was prepared by dissolving 10 mg PDL powder in 200 mL sterile PBS. The solution was filter sterilised and aliquotted into 20 mL volumes. The solution was stored at -20 °C, for up to one year. The solution was reused up to three times before being discarded.

2.5.3.10   Sodium Chloride Solution

A 3 M solution of sodium chloride (NaCl) was prepared by dissolving 175.32 g sodium chloride in 1 L distilled water.

2.5.3.11   Sodium Hydroxide Solution

a 1 N solution was prepared by adding 4 g NaOH pellets to 100 mL distilled water and the solution stirred using a magnetic stirrer. The solution was stored at room temperature, for up to two years.

2.5.3.12   Tris Solution

A 2 M solution of Tris was prepared by dissolving 242.26 g Trizma base in 700 mL distilled water. The pH of the solution was adjusted to pH 7.6 with 6 M HCl before making the volume up to 1 L using distilled water.

2.5.3.13 Tris buffered Saline

Tris buffered saline (TBS; 20 mM Tris, 150 mM NaCl, pH 7.6) was prepared by mixing 25 mL Tris solution (2 M) and 50 mL NaCl (3 M) with 700 mL distilled water. The pH of the solution was adjusted to pH 7.6 with 6 M HCl before making the volume up to 1 L using distilled water. The solution was autoclaved by moist heat and stored at room temperature, for up to 3 months.

2.5.3.14 Triton X-100

Into a clean duran bottle, 100 µL 100% Triton X-100 and 99.9 mL sterile PBS were combined. The solution was stirred using a magnetic stirrer until the Triton X-100 completely dissolved. The solution was stored at room temperature, for up to 6 months.

2.5.3.15 Virkon

A 1% (w/v) solution of Virkon was prepared by dissolving 10 g Virkon powder per 1 L distilled water. The solution was stored at room temperature.

2.5.4 Primary Cell Culture

All procedures involving the use of animal tissue and/or cells were performed in accordance with the UK Animals (Scientific Procedures) Act, 1986. All procedures were performed under the project license number, 70/8085.

All centrifugation steps were performed at room temperature, and all incubation steps at 37 °C were performed in a humidified incubator at 8% CO_2:92% air, unless stated otherwise.

2.5.4.1 Poly-D-Lysine Coating

To facilitate adhesion of primary rat neural cells, tissue culture surfaces were coated with poly-D-lysine (PDL). Frozen aliquots of PDL were thawed at room temperature, then overlayed on the appropriate surface such as tissue culture flasks or glass coverslips. The flasks and/or coverslips were then incubated at 37 °C for at least one hour. The PDL solution was then aspirated and two PBS washes followed by one cell culture media wash performed. The media was aspirated and the surfaces dried at 37 °C. PDL-coated surfaces were stored at 4 °C for up to two weeks, sealed using parafilm.

2.5.4.2 Preparation of a Mixed Glial Culture

Primary cortical glial cells were sourced and isolated from female postnatal 2-3 day old Wistar rats, with the protocol used being based on that developed by McCarthy and De Vellis (1980). Rats younger than postnatal day 2 were not used as this ensures the absence of viable neurons in the cell suspension.

2.5.4.2.1 Mixed Glial Cell Culture Medium

Primary rat astrocyte cells were cultured and maintained in DMEM, containing 10% (v/v) FBS, 1% (v/v) L-Glutamine, and 1% (v/v) penicillin-streptomycin (100 Units.mL^{-1} and 100 µg.mL^{-1} streptomycin, respectively). This is referred to as DMEM complete. The medium solution was stored at 4 °C, for up to 2 weeks.

Table 2.2: Preparation of Solutions for Mixed Glial Cultures

Solution	Stock concentration	Working Concentration	Reconstitution Media
Deoxyribonuclease (DNase)	0.1 mg.mL^{-1}	0.05 mg.mL^{-1}	HBSS+
Poly-D-lysine (PDL)	50 µg.mL^{-1}	50 µg.mL^{-1}	dH$_2$O
Triturating Solution	10 mg.mL^{-1} BSA 500 µg.mL^{-1} trypsin inhibitor 20 µg.mL^{-1} DNase	2 mg.mL^{-1} BSA 100 µg.mL^{-1} trypsin inhibitor 4 µg.mL^{-1} DNase	HBSS-
Trypsin	1 mg.mL^{-1}	1 mg.mL^{-1}	PBS

HBSS+ denotes HBSS with magnesium and calcium. HBSS- denotes HBSS without magnesium and calcium. All stock solutions were filter sterilised and aliquots stored at -20 °C, for up to two years.

2.5.4.2.2 Dissection and Culture

Rats were euthanised using the Schedule 1 technique of cervical dislocation. Upon confirmation of complete dislocation, the heads were removed and sprayed with 70% (v/v) ethanol. Using sterile springbow scissors, an incision in the skin of the head was made along the midline, followed by the skull. Additional lateral cuts were made to the skull to enable better access to the brain. The brain was gently removed from the skull and placed in a petri dish filled with ice-cold HBSS. The two hemispheres were then separated, then under a dissection microscope the cortices were dissected out, and meninges and blood vessels removed using fine forceps. The cortices were pooled before mincing with a scalpel blade. The tissue suspension was transferred to a 15 mL falcon tube and centrifuged for 5 minutes at 150 g. The supernatant was discarded and the pellet resuspended in 1 mg.mL^{-1} trypsin (3000 - 20,000 U.mg^{-1}), then incubated for 20 minutes, at 37 °C, followed by the addition of 0.01 % (w/v) DNase (2000 U.mg^{-1}) and a further 5 minute incubation. The suspension was then centrifuged for 5 minutes at 150g. The supernatant was discarded and the pellet resuspended in a triturating solution, comprised of 10 mg.mL^{-1} BSA, 500 µg.mL^{-1} trypsin inhibitor, and 20 µg.mL^{-1} DNase in Ca^{2+} and Mg^{2+}-free HBSS. The suspension was dispensed into PDL-coated (50 µg.mL^{-1}) 75 cm^2 flasks at a density of two cortices per flask. An additional 10 mL complete DMEM was added to each flask, and incubated in a humidified incubator at 37 °C.

2.5.4.2.3 Preparation of an Enriched Astrocyte Culture

The cells were expanded in culture for 8 - 10 days, to allow confluency and stratification of the different cell types to be achieved. When required, the flasks were placed on an orbital shaker at 250 rpm for 4 hours (10 mm orbital diameter) to deplete the less adherent cells, namely microglia. Parafilm was used to seal the vents of the lids to prevent media spillage. Mechanical dissociation resulted in enriched cultures which were >95% astrocytes, as determined by immunoreactivity for GFAP and CD11b. After mechanical dissociation, the media (containing non-astrocyte cells) was discarded and the adherent astrocytes trypsinised for 10 minutes, followed by neutralisation with complete DMEM. The suspension was centrifuged for 10 minutes at 150 g. A Trypan blue exclusion assay was performed to assess cell viability and determine the number of cells required for the experiment.

2.5.4.3 Cell Maintenance and Passaging

Cell cultures were maintained in tissue culture flasks and confluency monitored. At 80% confluency, the media was discarded and two 10 mL DPBS(-) washes were performed to remove residual serum. A volume of 2.5 mL trypsin/EDTA was added to the cells and incubated for 7 minutes at 37 °C. The flask was then firmly tapped against a hard surface to aid cell detachment. The trypsin was neutralised with 10 mL cell culture medium and a cell scraper was used to aid cell detachment. The cell suspension was then transferred to a sterile universal and centrifuged at 150 g for 10 minutes. The supernatant was discarded and the pellet resuspended in 2 mL fresh cell culture medium. A cell count was performed (Section 2.5.4.4) and the desired number of cells was used for seeding into gels. Remaining cells were replated at a density of 1 x 10^6 cells per T75 flask. Additional cell culture medium was added to achieve a final volume of 10 mL in the flask and incubated at 37 °C. Primary astrocytes were not used beyond passage 2.

2.5.4.4 Cell Counting

Trypan blue is a dye which enables the visual distinction between viable and non-viable cells: viable cells possess intact cell membranes which are impermeable to the dye. Conversely, non-viable cells' damaged membranes are unable to exclude the dye thus the cell cytoplasm is visible as a blue colour. To perform this assay, the cell suspension was trypsinised and centrifuged as for passaging cells (Section 2.5.4.3). Once the pellet was resuspended in a volume of cell culture medium, 10 µL of cell suspension was mixed with 10 µL Trypan Blue dye. A haemocytometer was prepared by placing a moistened coverslip over the counting grid. The haemocytometer was loaded with 10 µL cell suspension-dye mix and cells visualised under an inverted light microscope. The total number of cells was counted within the four outer 4x4 grids (Figure 2.1). The following formula was then used to determine the total number of cells in the suspension and the concentration:

$$Concentration\ (cells.mL^{-1}) = \frac{\text{Total no. cells}}{4} \times 2 \times 10,000 \times V \qquad (2.1)$$

where V = volume of cell suspension.
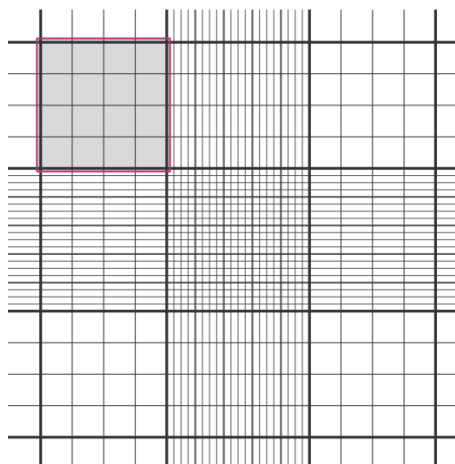
Figure 2.1: Counting grid of a haemocytometer. The red box indicates one of the four counting areas. Cells touching the line on the bottom and right hand side were excluded to prevent cells being double counted.

2.5.5   Preparation of Collagen Hydrogels

A commercially available rat tail type-I collagen (First Link UK Ltd.) was used throughout this project as it was easily available, less time consuming to acquire compared to in-house collagen production, and less batch-to batch variability. The hydrogel solution comprised the following reagents:

- Rat tail type-I collagen (80% v/v; >2 mg.ml^{-1} in 0.6% (v/v) acetic acid)
- 10X MEM (10% v/v)
- Neutralising Solution (5.8% v/v)
- Cell Suspension (4.2% v/v)

To minimise titration errors using in-house preparations of sodium hydroxide, a commercial neutralising solution was purchased from Lonza. Due to Lonza's proprietary rights, the only listed ingredient is sodium hydroxide. All hydrogel reagents and consumables (well plates and universals) were kept on ice to minimise premature gelation. Cell seeding density was calculated as the number of cells per mL gel solution. For example, a volume of 5 mL gel, seeded at a density of 5x10^5 cells.mL^{-1}, would contain 2.5x10^6 cells resuspended in 210 µL cell culture medium.

The required volumes of collagen and MEM were mixed in a sterile universal. To prevent the introduction of bubbles into the solution, a swirling motion was adopted to mix the reagents. The yellow colour of the solution indicated an acidic pH. The solution was then neutralised using the neutralising solution. Working swiftly, the cell suspension was resuspended in the gel solution and then immediately plated. The gels were then incubated for 10 minutes, at 37 °C, 8% CO$_2$:92% air to enable gelation to complete. The gels were then overlayed with complete cell culture medium.

2.5.6 ATPlite™Luminescence Assay System

Adenosine triphosphate (ATP) is a molecule which stores and provides energy to drive biological processes. It is a useful marker for metabolic activity and cell viability as it is present only in metabolically active cells. Its concentration declines when a cell undergoes necrosis or apoptosis. The ATPlite™Luminescence Assay is a system based on the production of light from the following chemical reaction:

$$\text{ATP} + \text{D}-\text{luciferin} + \text{O}_2 \xrightarrow[\text{Mg}^{2+}]{\text{Luciferase}} \text{Oxyluciferin} + \text{AMP} + \text{PP}_i + \text{CO}_2 + \text{Light} \quad (2.2)$$
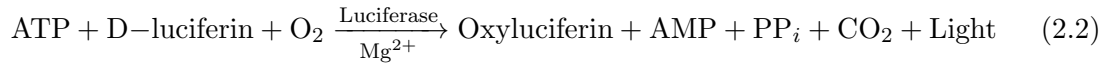
where AMP = adenosine monophosphate, and PP_i = pyrophosphate.

2.5.7 Immunofluorescence Staining

All steps were performed on an orbital shaker, at 110 rpm. Volumes of solutions used were twice that of the gel (600 µL for the contusion gels and 300 µL for the distraction gels). Antibodies were diluted in antibody diluent (Section 2.5.3.1). Following 3 x 5 minute PBS washes, gels were fixed with 4% (w/v) PFA for 4 hours, at 4 °C. Permeabilisation was performed with 0.1% (v/v) Triton X-100, for 45 minutes. Following 3 x 5 minute PBS washes, blocking of non-specific antibody binding sites was performed using powdered milk dissolved in PBS, for 45 minutes. After 3 x 5 min PBS washes, the gels were incubated in the primary antibody overnight, at 4 °C. Following 3 x 10 minute PBS washes, the gels were incubated in the secondary body containing DAPI (1:1000), at room temperature for 1.5 hours. Gels were washed with PBS (3 x 10 minutes) and then stored in PBS prior to confocal imaging. Antibodies and dilutions are detailed in Table 2.1.

2.5.8 Assembly of the BOSE 5110 Electroforce BioDynamic

The BOSE 5110 Electroforce BioDynamic Test Instrument is comprised of a main load frame, which houses the load cell and orthopaedic chamber (Figure 2.2). The system is controlled by the proprietary WinTest® Control System software on the attached computer.
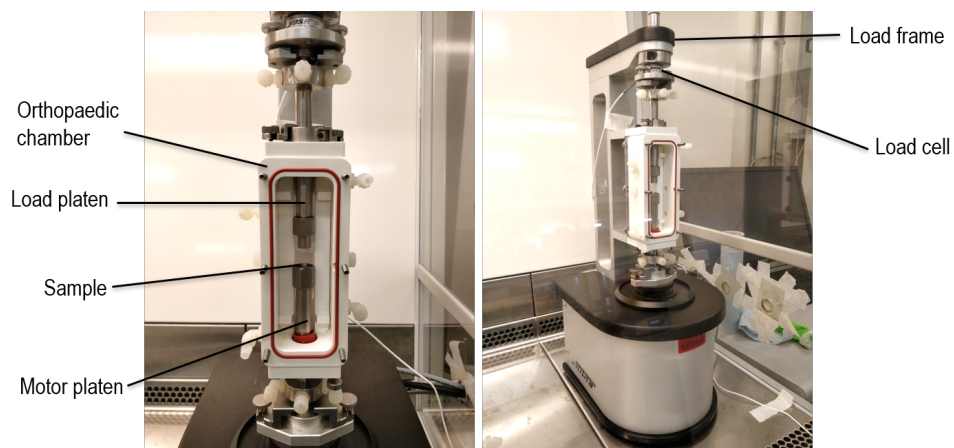
Figure 2.2: Setup of the BOSE 5110 Electroforce BioDynamic rig with compression platens.

The load frame provides mechanical stimulation to samples under sterile conditions, if desired. The chamber parts can be sterilised (Section 2.5.8.1), and the entire frame can be housed within a Class II Cabinet in order to operate the rig under sterile laminar air flow. The BioDynamic load frame specifications are detailed in Table 2.3 (BOSE, 2015).

Table 2.3: Specifications of the BOSE 5110 Electroforce BioDynamic

Model	5110
Loading	Axial
Chamber	Orthopaedic
Maximum Force	$\pm$200 N
Maximum Displacement	13 mm ($\pm$6.5 mm)
Minimum Displacement Increment	0.001 mm
Maximum Deformation Rate	740 mm.s^{-1}

2.5.8.1 Disinfection and Sterilisation of Components

All of the BioDynamic chamber components, including the manifold components, were sterilised using moist heat autoclaving. For efficiency the chamber was autoclaved pre-assembled, ensuring that the axial shaft locks and screw components were loosened to allow the pressurised steam to penetrate all areas. To maintain sterility, particularly inside the chamber and the platen fixtures which would come into direct contact with experimental samples, sterile gloves were used for assembly.

2.5.9 Microscopy

2.5.9.1 Brightfield Microscopy

An Olympus CK-40-SLP microscope was used under Köhler illumination to monitor cell cultures and perform cell counts.

2.5.9.2 Fluorescent Microscopy

A Zeiss Axio upright microscope was used for fluorescent imaging of two-dimensional cell cultures with the following filters: 49 DAPI (excitation 365, beam splitter 395, emission 450 nm), 38 GFP (excitation 470/40, beam splitter 495, emission 525/50 nm), and 20 Rhodamine (excitation 546/12, beam splitter 560, emission 575-640 nm).

2.5.9.3 Confocal Microscopy

All confocal images were acquired using a Zeiss LSM880 Axio Imager.Z2 upright microscope, equipped with an Axiocam camera, Zeiss Plan-Apochromat 20x 0.8 NA objective, and ZEN software. The lasers used were as follows: Diode: 405, Argon: 458, 488, 514, DPSS: 561, and HeNe: 633.

2.5.10   Statistical Analysis

2.5.10.1   Presentation of Data Variance

Numerical data was analysed using Microsoft Excel (version 1908), and presented as the mean (where n = $\geq$ 3) $\pm$ standard error of the mean (SEM). The SEM was calculated using the descriptive statistics package:

$$\text{Mean} = \frac{\sum x}{n} \tag{2.3}$$

$$\text{Standard Deviation (SD)} = \sqrt{\frac{\sum x^2}{n-1}} \tag{2.4}$$

$$\text{Standard Error of the Mean (SEM)} = \frac{SD}{\sqrt{n}} \tag{2.5}$$

where x = data value and n = sample number.

2.5.10.2   Comparison of Means

Group means were analysed using GraphPad Prism 8.0 (version 8.4.1.676). A student's t-test was used for the comparison of two means. A one-way or two-way analysis of variance (ANOVA) was used to compare the means of more than two groups. The individual differences between means were identified by calculating the minimum significant difference (MSD) at p = 0.05. For two-way ANOVA analyses a Tukey-Kramer post-hoc test was used to identify the location of significant differences, where every mean is compared with every other mean. Similarly, a Dunnett post-hoc test was used to compare group means to the mean of a control group.

Chapter 3

Development of Contusion and Distraction Traumatic Spinal Cord Injury Models *In Vitro*

3.1 Introduction

Traumatic spinal cord injury (TSCI) is clinically represented by a broad range of mechanisms and many experimental models exist. The dominance of the secondary response in the pathological process of SCI has meant that less focus has been placed on how the mechanisms of primary injury influences pathology. Relatively little research has been published which has attempted to perform direct comparisons of the effects of injury mechanism on histological and functional parameters *in vivo* (Chen *et al.,* 2016; Choo *et al.,* 2008, 2007, 2009). The results of these studies suggest that mechanism specific patterns of pathology exist due to differences in spinal cord deformation. Further, this was associated with differences in behavioural outcomes in rats observed up to 8 weeks following injury (Chen *et al.,* 2016). However, understanding of this heterogeneity is not yet refined enough to inform how treatments can be targeted towards mechanism-specific pathologies.

A current barrier to research investigating injury mechanics is the lack of apparatus available which are capable of experimentally simulating multiple mechanisms of injury, with the capability of independently controlling input biomechanical parameters, such as displacement and velocity. The experimental displacement and velocity values are also often unreported so there is no information on whether the values have been verified as accurate against the inputs. Since the objective of these studies is to utilise a standardised model to study a specific aspect of secondary injury and/or to test therapeutic interventions, the biomechanics of primary injury are less considered. The Infinite Horizons Impactor, for instance, is most commonly used to model contusion injuries *in vivo*. This force-controlled system does not allow for user control of input displacement or velocity. Smith (2016) used this apparatus to model contusion-type injuries *in vitro*, using primary astrocyte-seeded type-I collagen hydrogels. Due to the low elastic modulus of the gels, accurate impact force data could not be obtained as the force sensor was not sensitive enough to detect the presence of the gel. The lack of quality output kinetic data means associations could not be made between input mechanics and cellular behaviour, which is the aim of this project. The University of

British Columbia (UBC) multimechanism device is currently the only apparatus capable of experimentally simulating multiple injury mechanisms *in vivo*: contusion, dislocation, and distraction (Chen *et al.,* 2016; Choo *et al.,* 2008, 2007, 2009; Lam *et al.,* 2014).

The BOSE Electroforce BioDynamic 5110 (BOSE) is a commercially available bioreactor used to apply mechanical loads to single specimens to determine their mechanical properties. The user can independently control either force, or displacement and velocity. An experimental *in vitro* model of contusion injury was developed by Kirk (2018) using primary neural cell-seeded synthetic hydrogels, whereby an input velocity of 3000 mm.s^{-1} and a range of input displacement depths- from 50 – 100% gel height- was used to model a TSCI. Results demonstrated an increase in astrocyte and microglial metabolism with increasing contusion displacement depth, suggesting increased cellular reactivity. However, output biomechanical data, such as load, impact velocity and peak displacement were not reported. Therefore, it is unknown whether those input parameters were achieved experimentally. Additionally, characterisation of the apparatus was not performed, thus its capabilities remain unknown under conditions simulating a contusion injury.

With the availability of the BOSE and the potential to model at least two mechanisms of TSCI this apparatus was selected for this project. The BOSE is equipped for generating both uniaxial compressive and tensile loads. Contusion and distraction mechanisms were selected as these are clinically prevalent (Katsuura *et al.,* 2016; Wood *et al.,* 2014). Characterisation of the BOSE, over an input displacement range of 1 – 10 mm and input velocities of 100 and 1000 mm.s^{-1}, was performed in air in order to determine the capabilities of the apparatus for the aim of developing a contusion and distraction model *in vitro*. The system was then verified with the addition of hydrogels, to determine whether their presence affected output displacement and velocity measurements. It was hypothesised that the BOSE would be a suitable apparatus for generating accurate and reproducible compressive and tensile loads in air and with collagen hydrogels.

In vitro models present a potentially useful pre-animal model to further investigate and better inform *in vivo* studies, where outcomes can be highly variable, complex, and control of certain parameters is more difficult. *In vitro* systems are less complex and less variable than the native CNS, but the user can more precisely control the environment depending on the research question. Two-dimensional (2D) cultures are increasingly being rejected in favour of three-dimensional (3D) cultures due to their lack of physiological relevance and inability to faithfully replicate the cytoarchitecture of native tissue (Pampaloni *et al.,* 2007; Pedersen and Swartz, 2005). Regarding the central nervous system (CNS), a 2D environment has previously been shown to mimic a reactive environment, resulting in upregulation of astrocyte reactivity markers typically observed following a SCI (Du *et al.,* 2010; East *et al.,* 2009).

3D *in vitro* biomaterials have been used in neural tissue engineering due to their

improved abilities to support native cellular behaviour, allowing cell-cell and cell-matrix interactions to occur in all dimensions (Boni *et al.,* 2018). Type I collagen possesses many properties which make it suitable for use as a 3D biomaterial in this project: cytocompatible, contains intrinsic cell attachment motifs, easily accessible from a variety of sources, simple handling procedures, and fast preparation and gelation characteristics (Dinescu *et al.,* 2018). The modulus of collagen hydrogels (60 Pa, Smith (2016)) does not completely match that of CNS tissue, which values reported vary due to differences in specimen and testing method (Bartlett *et al.,* 2016b) and this may have implications for cellular responses *in vitro.* However, it was deemed a suitable choice of biomaterial herein due to its previously utilisation in neural tissue engineering to model the nervous system and associated pathologies (East *et al.,* 2009; Georgiou *et al.,* 2013; Kirk, 2018; O'Rourke *et al.,* 2017; Phillips, 2014b; Phillips *et al.,* 2005; Smith, 2016). These studies show that collagen is amenable to neural cell survival and mimics a non-reactive environment, particularly for glial cells.

In a more simplified environment of a 3D *in vitro* model, mechanical loads can be applied to different populations of neural cells in a highly controlled environment. The glial scar that forms after SCI is considered a major physical and physiological impediment to neuronal regeneration (Fawcett and Asher, 1999; Liu *et al.,* 2006; Yiu and He, 2006). It is composed largely of reactive, hypertrophic astrocytes, which up-regulate intermediate filaments including glial fibrillary acidic (GFAP) and vimentin, and deposit ECM molecules such as chondroitin sulfate proteoglycans (CSPGs). Since the lesion is composed largely of the dense reactive-astrocyte populated glial scar, and studies show mechanism-specific differences in lesion size, astrocytes were selected to be seeded into the collagen hydrogels.

Primary cortical astrocytes were isolated from early postnatal (P2 – 3) rats using a mixed glial preparation and mechanical shaking to enrich the astrocytes. The purity of the culture was assessed using immunocytochemical staining for glial fibrillary acidic protein (GFAP), a commonly used marker for astrocytes (Eng, 1985). Primary astrocytes were seeded into collagen hydrogels at various initial seeding densities, with cell metabolism and viability monitored to select an appropriate density for future experiments. It was hypothesised that cells would be viable and proliferate for up to 14 days in culture. This timeframe was chosen as this would be the end-point for subsequent experiments, and the glial scar has been shown to take approximately 14 days to form and begin maturing (Hackett and Lee, 2016). Further, due to lack of blood supply and other cells and molecules present, which likely contribute to cell survival, a timepoint of longer than 14 days would not have been relevant.

3.2   Aim and Objectives

3.2.1   Aim

The aim of this chapter was to assess the suitability of using the BOSE Electroforce BioDynamic 5110 apparatus to simulate clinically relevant contusion and distraction spinal cord injury mechanisms.

3.2.2   Objectives

The specific objectives were as follows:

   I. To characterise and verify the displacement and velocity parameters of the BOSE in air, under compressive and tensile waveforms.

  II. To determine the effects of collagen hydrogels on the output displacement and velocity values of the BOSE.

 III. To develop a protocol to enable accurate measurement of the initial dimensions of collagen hydrogels (contusion) and thus define the displacement parameters.

  IV. To define a set of velocity and displacement depth parameters to be simulated experimentally, in order to represent a range of injury severities *in vitro*.

   V. To select an appropriate primary astrocyte seeding density.

  VI. To define the shape and dimensions of a hydrogel to enable tensile loads to be applied, simulating distraction-type spinal cord injuries.

3.3   Specific Materials and Methods

3.3.1   Assembly of the BOSE Electroforce BioDynamic 5110 Rig

For the general set up and assembly of the BOSE chamber components, refer to Chapter 2 (Section 2.5.8).

3.3.1.1   Experimental Setup of Contusion Injury Simulation

The chamber was assembled and affixed to the load frame, according to the manufacturer's instructions. Due to manual differences in assembling the apparatus, and differences in the preparation of individual hydrogel samples, the height of each sample had to be calculated individually after being loaded onto the platen (Figure 3.1).
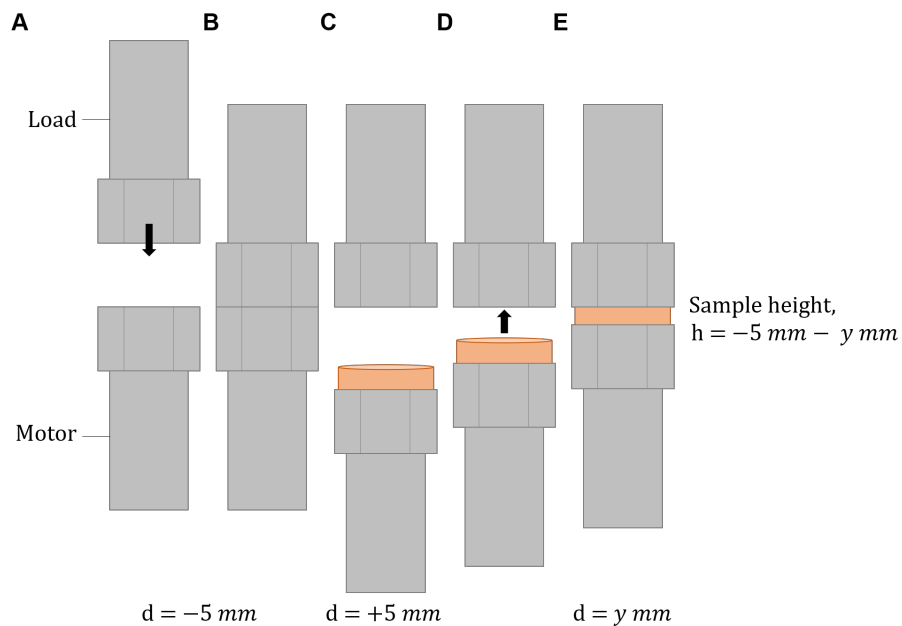
Figure 3.1: Calculation of the thickness of individual hydrogel samples using the BOSE. Movement of the lower motor platen was controlled using the WinTest software. The motor platen was moved upwards to an absolute displacement value of -5 mm (A). The load platen was then manually lowered until contact was registered with the motor platen, as indicated by a change in load of at least 0.1 N (B). This represents 100% compression. The motor platen was then moved downwards, to an absolute displacement value of +5 mm and the sample loaded onto the motor platen (C). The motor platen was moved upwards in increments, from 100 to 1 µm, as the sample approached the load platen (D). Contact with the top surface of the sample was registered when surface tension from the liquid caused the entire surface of the sample to be drawn to the load platen. The absolute displacement value at this point, y mm, was recorded (E). The height, h, of the gel was calculated by calculating the difference between y and the displacement value at which the two platens were in contact with each other i.e. -5 mm.

3.3.1.2   Experimental Setup of Distraction Injury Simulation

To facilitate the application of tensile strain on collagen type I hydrogels, the dimensions of the gel were modified from disc-shaped to I-shaped. A mould, originally designed by Phillips *et al.,* (2005), was used to cast the gels into the desired dimensions. The design

of the mould was modified to come as two separate components, held together with a pair of screws and dowels. For detailed designs of the distraction mould, refer to Appendix C (Figures 6.2 to 6.5) This enabled the gel to be loaded into the BOSE, with the ends of the moulds serving as attachment points with the tensile grips of the BOSE. Distraction moulds were disinfected and sterilised by soaking the individual components (mould pieces, parafilm, mesh bars) in 1% Trigene (v/v), followed by 70% (v/v) ethanol. The stainless steel dowels and screws were sterilised by dry heat (Chapter 2; Section 2.5.1.2). All components sterilised in solutions were allowed to air dry within a Class II safety cabinet. Once dry, the moulds were assembled in 6-well plates using sterile gloves and forceps. A volume of 150 µL neutralised gel solution was pipetted into each mould, taking care to ensure the solution was sufficiently integrated around and through the holes of the mesh. The gels were allowed to set by placing them in a humidified incubator at 37 °C, 8% CO_2:92% air. Once set, each gel was overlayed with 2 mL cell culture medium. After 24 hours incubation, the gels were ready to be experimented on.

To transfer the moulds from the well-plate and secure them into the tensile grips of the BOSE, a pair of sterile forceps was used to grasp onto a screw and transfer it to the lower grip. The end of the tensile grip was aligned with the end point of the scribe on the mould and secured by tightening the knurl screw. Under displacement control, the lower grip was moved upwards towards the upper grip until the mould entered the upper grip and the end point of the scribe aligned with the end of the upper tensile grip. The upper grip was then closed and tightened around the mould by tightening the knurl screw. The screws were then removed, followed by the dowels. Tensile loading forces were now able to be applied.

3.3.2 Waveform Setup and Data Acquisition

The waveform defined by the user was programmed into the Waveform Setup tab of the workspace (Figure 3.2).

A

	Block	Waveform	Control Channe	Waveform Definition	Conditional Statement	Move Type
Edit	1	Dwell	Disp	0.01 Sec	Double click to create.	Absolute
Delete	2	Ramp	Disp	1000 mm/Second to -4 mm	Double click to create.	Relative
Insert	3	Dwell	Disp	0.1 Sec	Double click to create.	Absolute
	4	Ramp	Disp	1000 mm/Second to 4 mm	Double click to create.	Relative
Acquisition	5	None				
	6	None				
Data Setup	7	None				

B

Figure 3.2: Building a waveform using the WinTest software. A view of the software interface where the user can input their desired waveform as a series of individual blocks (A). A visual representation of the input displacement profile of the waveform defined in A (B).

The waveform regime, defined to represent a contusion injury, was defined in the following steps:

1. **Dwell:** 10 ms

2. **Ramp:**

    (a) Velocity: 100, 1000, 3000 mm.s^{-1}.

    (b) Relative displacement: -1, -2, -4, -6, -8, -10 mm (characterisation in air); percentage of the total gel height (characterisation with collagen hydrogels). Note, displacement is negative as the lower motor platen moves upwards, towards the load platen.

3. **Dwell**: 100 ms

4. **Ramp:**

    (a) Velocity: 100, 1000, 3000 mm.s^{-1}.

    (b) Relative displacement: Return to starting displacement (air); 0% of gel height (hydrogels).

Data acquisition settings were defined in the Standard Timed Data tab of the workspace. The user is able to select which channels to acquire data on, and define the scan rate in the 'Scan Info' section. In this project, the scan information defined for each velocity used was the same:

- Scan time = 0.4096 s.

- Number of scan points = 2048.

- Number of scans = 1.

3.3.3 Proportional Integral Derivative Tuning

A proportional-integral-derivative (PID) controller is a control loop mechanism which continuously monitors the response of the specimen to a desired input, and then adjusts the system until the desired input is met (Åström and Hägglund, 1995). The PID system comprises three terms, which can be adjusted individually to achieve an optimal response. The proportional term (P term) calculates the difference between the input and output value and places a multiplier on the error. The integral term (I term) is a multiplier on the integral of the error, with respect to time. Integral tuning attempts to overcome the limitation of the P term by combining the error result from the proportional action and increasing the correction factor (although this can lead to an overshoot of the desired value). The derivative term (D term) is a multiplier on the differential of the error signal, with respect to time. Derivative tuning attempts to minimise overshoot by slowing the correction applied as the desired value approaches. The desired waveform was programmed and simulated, and the input (command) and output displacement and/or velocity profiles were visualised on the scope within the software. The PID parameters were then adjusted, according to the instructions in the manufacturer's reference manual (BOSE, 2015). These profiles were compared against the corresponding non-PID tuned simulations (waveforms simulated using the default proprietary TuneIQ®tuning system; TA Instruments, Newcastle, UK).

3.3.4 Verification of Output Measurements against the Input

Verification of both displacement and velocity was undertaken by comparing the output (recorded) peak displacement and velocity values against the input value. A percentage error was calculated using the following equation:

$$Error\ (\%) = \frac{experimental - theoretical}{theoretical} \text{ x } 100 \tag{3.1}$$

3.3.5 Preparation of Collagen Hydrogel Samples

For this study, a commercially available rat tail type-I collagen product was used (>2 mg.ml^{-1} in 0.6% (v/v) acetic acid). For details on the preparation of the collagen hydrogel solution, refer to Chapter 2 (Section 2.5.5). Samples for modelling contusion injury were prepared by pipetting 300 μL of the neutralised collagen solution into 48-well plates, which had a well diameter of 11 mm. Samples for modelling distraction injury were prepared by pipetting 150 μL of the neutralised collagen solution into the cavity of the distraction moulds set up as in Section . The gels were then incubated for 10 minutes, at 37 °C, 8% CO_2:92% air to enable gelation to complete. The gels were then overlayed with complete cell culture medium (300 μL per sample for contusion; 2 mL per sample for distraction).

3.4 Results

3.4.1 The BOSE Electroforce BioDynamic 5110 as an Apparatus for Inducing Contusion Injury

The BOSE has not been verified for use as an apparatus for generating high velocity compressive forces, on cell-seeded collagen hydrogels. As previously described, the limited studies utilising the BOSE system for simulating contusive spinal cord injuries *in vitro* did not compare input and output displacement and velocity parameters. This knowledge is essential in attempting to define how input mechanics may influence cell behaviour and whether thresholds exist. The work carried out in this section aimed to characterise and verify the feasibility of using the BOSE to simulate reproducible contusion injuries. This was achieved by, firstly, simulating defined contusion waveforms in air. The input and output velocity and displacement values were recorded and compared to their respective output values. The system was then tested with collagen hydrogels loaded onto the rig, using the same protocol.

3.4.1.1 Incorporation of a Dwell Step to Optimise the Displacement Parameter

The results in this section describe the outcomes of characterising the displacement parameter of the BOSE, in air, under a compression waveform to model the transient compressive forces imparted onto the spinal cord during contusion injury. The first waveform tested comprised a ramp to a displacement depth between 1 and 10 mm, immediately followed by a ramp back to the starting displacement (Section 3.3.2). This waveform was simulated at three velocities: 100, 1000, and 3000 mm.s^{-1}. The raw input (command) and output (experimental) displacement values were plotted against time and the resultant profiles compared (Figure 3.3).

The desired displacement was not achieved at any displacement depth. The error between the input and output displacement profiles increased as the input velocity was increased, at a given input displacement value (Appendix B Table 6.4). For instance, at an input displacement value of 1.000 mm the mean output peak displacement values were 0.642, 0.128, and 0.064 mm, at input velocities of 100, 1000, and 3000 mm.s^{-1}, respectively. Further, the error between the input and output displacement profiles decreased with increasing displacement, at a given input velocity. At 100 mm.s^{-1} the mean percentage error of the output peak displacement value decreased from 35.85% to 5.40%, as input displacement was increased from 1.000 mm to 10.000 mm. Similarly, the mean percentage error decreased from 87.20% to 22.37% and 93.65% to 61.11%, at input velocities of 1000 mm.s^{-1} and 3000 mm.s^{-1}, respectively.
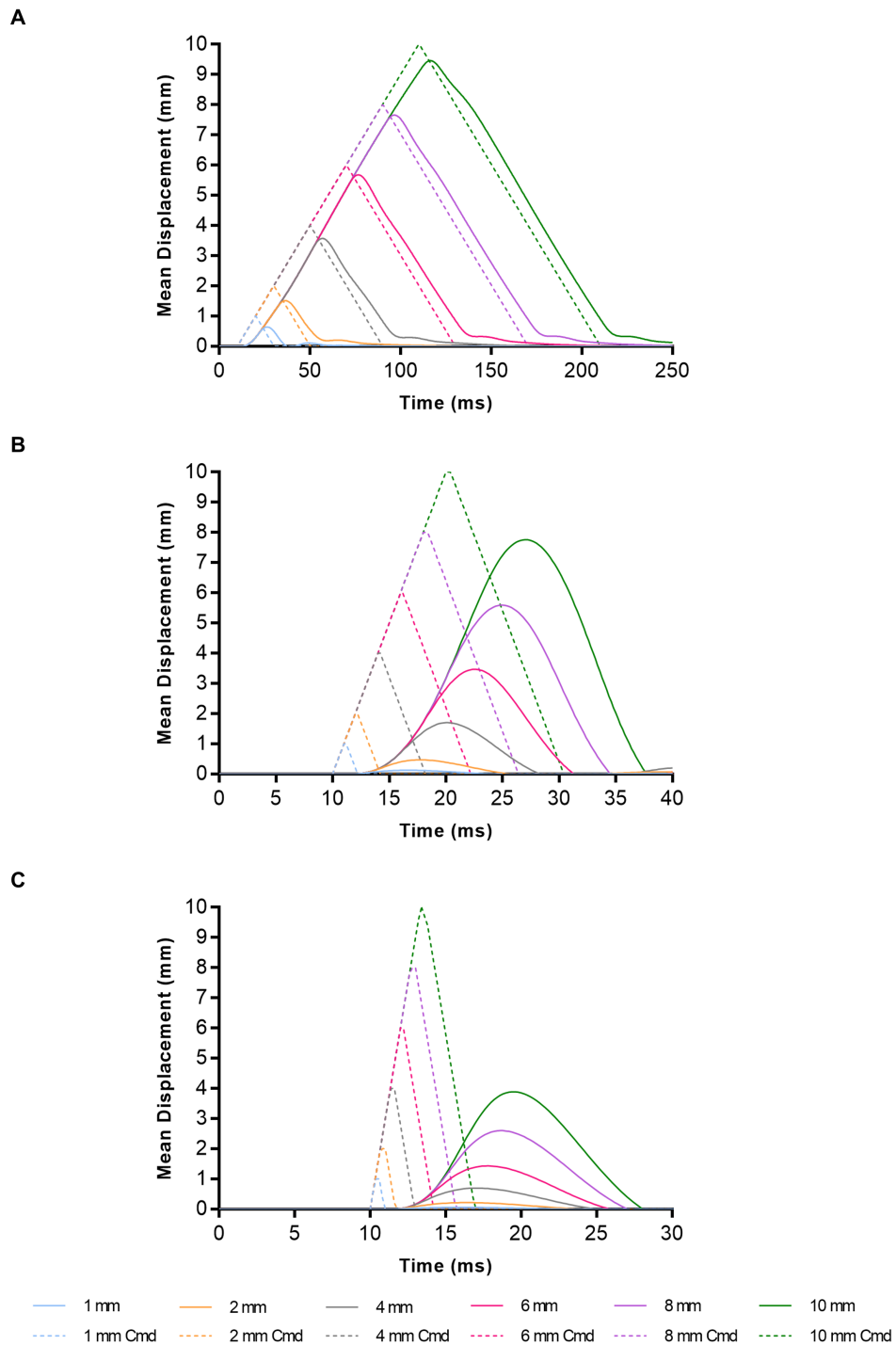
Figure 3.3: Comparison of input and output displacement profiles of a simulated contusion regime without the presence of a dwell period. Dashed lines represent the output profiles; solid lines represent the input command. The simulated waveform was programmed as follows: dwell (10 ms), ramp at 100 (A), 1000 (B), or 3000 mm.s^{-1} (C) to the defined displacement depth relative to 0 mm in compression, then ramp at 100, 1000, or 3000 mm.s^{-1} back to 0 mm. N = 4.

Each output displacement profile exhibited a lag period after displacement was defined to be initiated (at 10 ms), which was not observed in the input profiles. The mean time at which the first ramp initiated was 11.63 ± 0.05 ms, thus the mean lag time was calculated to be 1.63 ± 0.05 ms. The time at which peak displacement was achieved thus also shifted,

compared to the theoretical time at peak displacement (Table 3.1). For instance, at an input displacement and velocity of 1.000 mm and 100 mm.s^{-1}, respectively, the theoretical time at peak displacement was 20 ms. However, the mean experimental output time at peak displacement was 26.25 ± 0.05 ms, with a mean lag time of 6.25 ± 0.05 ms. The grouped mean lag time was 6.45 ± 0.05 ms at 100 mm.s^{-1}, 6.29 ± 0.1 ms at 1000 mm.s^{-1}, and 5.68 ± 0.04 ms at 3000 mm.s^{-1}.

Table 3.1: Mean lag time at peak displacement compared to the input command. Output displacement values were recorded, under waveforms of various combinations of input displacement and velocity parameters, with the time at which peak output displacement was achieved being selected and compared to the input time. Data is presented as the mean ± SEM. N=4.

Input Displacement (mm)	Mean Lag Time (ms)		
	100 (mm.s^{-1})	1000 (mm.s^{-1})	3000 (mm.s^{-1})
1.000	6.25 ± 0.05	5.50 ± 0.06	5.50 ± 0.10
2.000	6.40 ± 0.08	5.65 ± 0.05	5.40 ± 0.00
4.000	6.80 ± 0.08	6.00 ± 0.00	5.60 ± 0.00
6.000	6.60 ± 0.00	6.60 ± 0.00	5.80 ± 0.00
8.000	6.55 ± 0.05	7.00 ± 0.00	5.80 ± 0.00
10.000	6.10 ± 0.06	7.00 ± 0.00	6.00 ± 0.00

To this end, the initial waveform was modified to include an additional dwell period between the two ramp steps. A dwell time of 100 ms was selected as this was determined to be the shortest length of time possible to allow the desired displacement depth to be achieved, and without contributing potential confounding effects of prolonged compression of the sample. Further, this was to distinguish between compression models of injury, which comprises an initial contusion injury (milliseconds) followed by sustained compression over a period ranging from seconds to minutes (Cheriyan *et al.,* 2014). Again, the modified waveform was simulated, in air, and the input and output displacement profiles plotted and compared (Figure 3.4 and Appendix B Figure 6.1).

At each input displacement depth, there was a significant increase in peak displacement achieved with the incorporation of the dwell step, and this was observed at all input velocities. The dwell step also increased the accuracy of the peak displacement achieved as the percentage errors at each input displacement depth was reduced from approximately 95% to less than 1.00% (Appendix B Table 6.4). The greatest reduction in percentage error was observed with an input displacement of 1 mm and velocity of 3000 mm.s^{-1}: 93.65% to 0.10% (93.55% decrease). The improved capability of achieving the input displacement value was also observed visually, where the input and output displacement profiles aligned more closely.
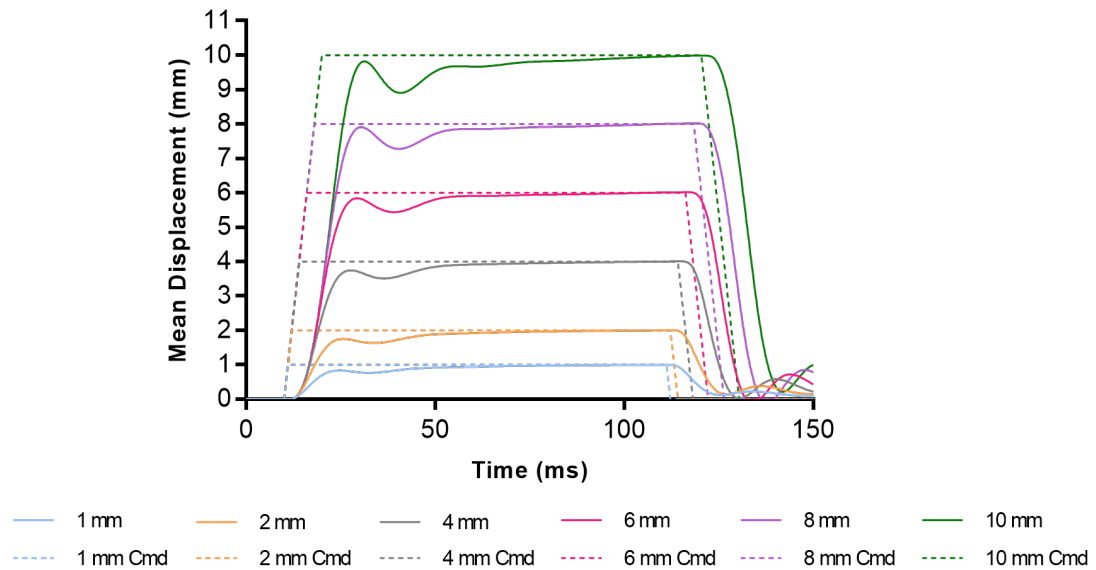
Figure 3.4: Comparison of input and output displacement profiles of a simulated contusion regime with the addition of a 100 ms dwell step at 100 mm.s^{-1}. Dashed lines represent the output profiles; solid lines represent the input command. The simulated waveform was programmed as follows: dwell (10 ms), ramp (1000 mm.s^{-1} to the defined displacement depth) in compression, dwell (100 ms), and ramp (1000 mm.s^{-1}) to 0.000 mm. Displacement profiles for all velocities can be seen in Appendix B (Figure 6.1).

Another observation of the displacement profiles showed a recoil event, which was not observed in the input command displacement profiles (Figure 3.4), nor the displacement profiles under the condition without the dwell step (Figure 3.3). This observation was more pronounced at velocities of 1000 and 3000 mm.s^{-1}. During the first ramp step to the desired input displacement value, displacement increased as expected. However, the system stopped short of the desired displacement value and decreased slightly, before increasing again to reach the input displacement value. The time at which the peak displacement was achieved was therefore shifted, compared to the input command profile, as described above.

Whilst the addition of the 100 ms dwell step to the waveform increased the accuracy of the desired output displacement values, the percentage errors calculated for peak velocity remained high compared to displacement error (Appendix B Table 6.5). At 100 mm.s^{-1}, there was no significant difference in peak velocity between conditions with and without the dwell step, at each input displacement depth. The mean percentage error of peak velocity ranged from 8.75 – 20.00% and 10.00 – 17.50%, without and with the dwell step, respectively. At both 1000 and 3000 mm.s^{-1}, there was a significant increase in the peak velocity achieved with the dwell step, at each displacement depth. The mean percentage errors were subsequently reduced; however, the condition which resulted in a peak velocity closest to the target value was with an input of 1000 mm.s^{-1} and 10.000 mm. This condition resulted in a mean peak velocity of 927.50 $\pm$ 1 mm.s^{-1}. This corresponds to an error of 7.25% which was much greater than the range of error values

calculated for peak displacement. Although the dwell step reduced the error in peak velocity achieved at 3000 mm.s^{-1}, the lowest error was still 60.69% (mean peak velocity of 1176.25 $\pm$ 1 mm.s^{-1}; 10.000 mm).

An exact output velocity of 100 mm.s^{-1} was not achieved: velocity was slightly undershooting at a mean of 80.00 and 91.25 $\pm$ 1 mm.s^{-1}, at input displacement values of 1.000 and 2.000 mm, respectively. Conversely, velocity was slightly overshooting the desired value between a mean of 110.00 and 113.75 $\pm$ 3 mm.s^{-1}, between input displacement values of 4.000 and 10.000 mm. An exact output velocity of 1000 mm.s^{-1} was not achieved, with the mean peak velocities of 918.75 $\pm$ 1 and 927.50 $\pm$ 1 without and with the dwell step, respectively, being the closest to the target (10.000 mm input displacement). An exact output velocity of 3000 mm.s^{-1} was not achieved: the mean peak velocities of 897.50 $\pm$ 1 and 1176.25 $\pm$ 3 mm.s^{-1} without and with the dwell step, respectively, were closest to the target velocity (10.000 mm input displacement). At input velocities of 1000 and 3000 mm.s^{-1} the mean output peak velocity increased with increasing input displacement.

The results here demonstrate that an output velocity of 3000 mm.s^{-1} could not be feasibly achieved. With an input velocity of 3000 mm.s^{-1}, increasing the working displacement distance to 10 mm, and incorporating a 100 ms dwell step to the waveform only resulted in a mean peak output velocity of 1176.25 $\pm$ 3 mm.s^{-1} (mean percentage error of 60.79%). Therefore, this velocity was omitted from the subsequent experiments. Further characterisation and optimisation of the BOSE parameters was undertaken with input velocities of 100 and 1000 mm.s^{-1}, and with the addition of the 100 ms dwell step.

3.4.1.2 Manual Proportional Integrative Derivative Tuning

By incorporating the 100 ms dwell step into the contusion waveform, an output velocity of 100 mm.s^{-1} was achieved with a minimum percentage error of 10% (input displacement of 2.00 and 4.00 mm). Similarly, an output velocity of 1000 mm.s^{-1} was achieved with a minimum percentage error of 7.25 $\pm$ 0.1% (input displacement of 10.00 mm). Proportional Integrative Derivative (PID) tuning was undertaken to evaluate whether the accuracy of the BOSE system could be further optimised. The default tuning system developed by the manufacturer is called TuneIQ®, with all the data presented thus far using this method of control optimisation. The following data compared output peak velocity values between TuneIQ®and manual PID tuning. For details of the individual PID values for each input displacement and velocity combination, refer to Appendix B (Table 6.6).

The addition of PID tuning imparted minor differences to the output displacement profiles (Figure 3.5). By plotting the displacement profiles of the non-tuned and PID tuned experiments onto a graph, it was observed that output displacement profiles of the tuned experiments aligned closer to the corresponding command profiles. At both input velocities, PID tuning shifted the profiles to the left thus the time to reach the first peak decreased (examples highlighted in Figure 3.5 A – C). However, at 1000 mm.s^{-1} and

10.000 mm, an overshoot in displacement was observed with PID tuning at the first peak in the displacement profile, at 29.8 ms (mean 10.236 mm). This corresponded to the peak output displacement depth. This contrasts to the other input displacement depths, where the first peak was less than the actual peak displacement and the actual peak displacement was achieved at approximately 108 ms.
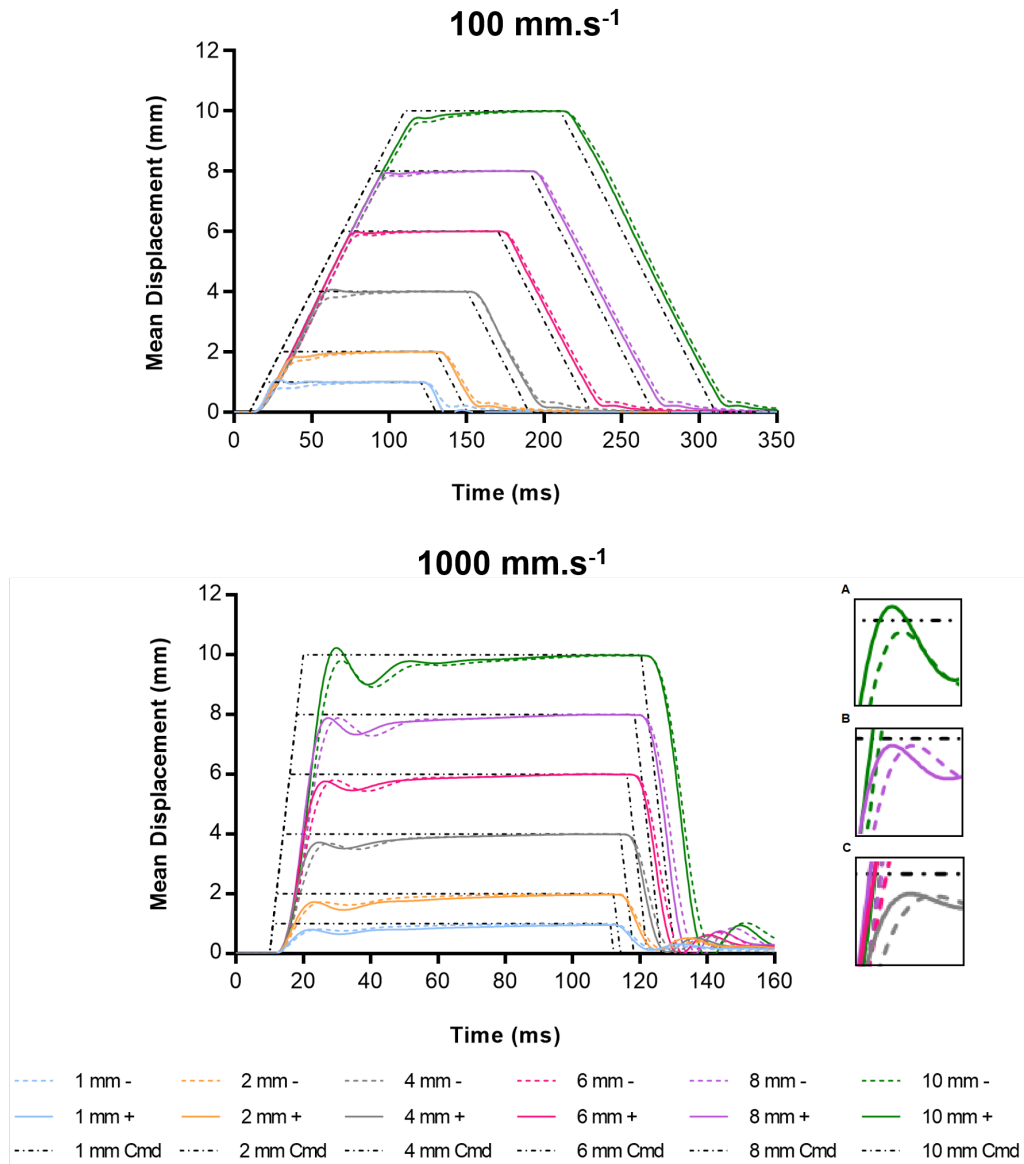
Figure 3.5: Comparison of input and output displacement profiles of a simulated contusion regime at 100 and 1000 mm.s^{-1} with and without PID tuning. Coloured dashed lines represent non-PID tuned profiles (TuneIQ); corresponding coloured solid lines represent PID tuned profiles; dashed black lines represent the input command profiles. Higher magnification images of profiles at 10.000 (A), 8.000 (B), and 6.000 mm (C) displacement. N = 4.

At 100 mm.s^{-1}, there was a significant difference in the mean peak displacement between the non-tuned and PID tuned conditions at 1, 4, and 10.000 mm (Figure 3.6). At 1000 mm.s^{-1}, there was a significant difference in the mean peak displacement between the non-tuned and PID tuned conditions at all displacement depths. PID

tuning generally reduced the percentage error of peak displacement, but actually increased the error under the following conditions: 100 mm.s^{-1} at 1 and 4.000 mm, and 1000 mm.s^{-1} at 1, 2, and 10.000 mm.

At an input velocity of 100 mm.s^{-1}, PID tuning resulted in a significant increase in the mean peak velocity achieved, between 1 – 4.000 mm, compared to the non-tuned values. At 1.000 mm, PID tuning resulted in a change from an undershoot (82.50 mm.s^{-1}) to an overshoot (117.00 mm.s^{-1}) in peak velocity achieved, although the mean percentage errors remained similar (mean 17.50% vs. 17.00% for non-tuned vs. tuned, respectively). PID tuning reduced the extent of undershoot in velocity at 2.000 mm which was closer to 100 mm.s^{-1}, and the error was reduced from 10 to 6.00%. However, tuning further increased the extent of overshoot at 4.000 mm and thus increased the mean error from 10 to 18.00%.

Conversely, PID tuning decreased the mean peak velocity achieved between 6 – 10.000 mm, although this was only significant at 8.000 mm. At this displacement range, PID tuning reduced the extent of the overshoot that was observed without tuning, thus the errors also decreased as the values were closer to 1000 mm.s^{-1}. At an input velocity of 1000 mm.s^{-1}, PID tuning resulted in a significant increase in the mean peak velocity achieved compared to the non-tuned values, at each displacement depth. This resulted in peak velocity values which were closer to the desired 1000 mm.s^{-1}. PID tuning resulted in a peak velocity closest to 1000 mm.s^{-1}, using an input displacement of 10.000 mm (mean 1031.00 mm.s^{-1}; 3.10% error).
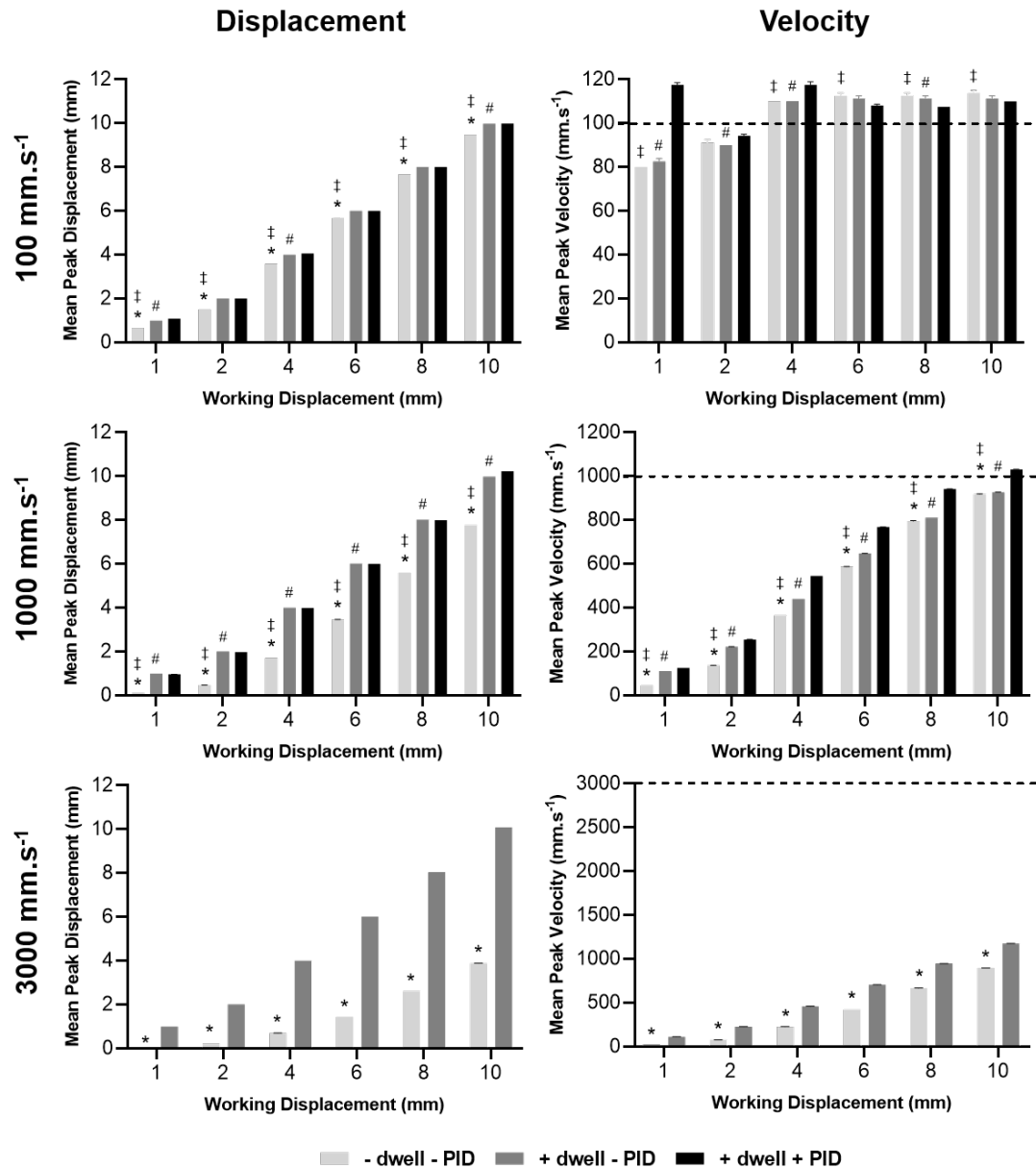
Figure 3.6: Summary of the effects of a 100 ms dwell step and PID tuning on output peak displacement and velocity measurements of the BOSE. Black dashed line represents the target velocity. Data presented as the mean $\pm$ SEM. Two-way ANOVA with Tukey's post-hoc test performed for each displacement group. Statistical significance levels * $p<0.05$ ($-$ dwell $-$ PID vs. $+$ dwell $-$ PID); # $p<0.05$ ($+$ dwell $-$ PID vs. $+$ dwell $+$ PID); ‡ $p<0.05$ ($-$ dwell $-$ PID vs. $+$ dwell $+$ PID). N = 4. Note: PID tuning experiments were not undertaken at an input velocity of 3000 mm.s^{-1} as results from the preceding experiments showed this velocity could not be feasibly achieved.

Overall, the input displacement value which resulted in the most accurate output measurements at both 100 and 1000 mm.s^{-1} was 8.000 mm since this was a large enough distance for the system to accelerate to the desired velocity (Table 3.2). This was in addition to modifications to the contusion protocol, including incorporating the 100 ms dwell step and performing PID tuning. Therefore, for subsequent characterisation experiments utilising hydrogel specimens, the initial distance between the sample and the upper load platen was set to 8.000 mm (working displacement).

Table 3.2: Summary of the output peak displacement and velocity measurements representing the most accurate contusion protocol. Input displacement 8.000 mm. Data is presented as the mean (% error). N=4.

	100 mm.s^{-1}	1000 mm.s^{-1}
Peak displacement (%)	8.003 (0.04%)	7.997 (0.04%)
Peak velocity (mm.s^{-1})	107.50 (7.50%)	943.00 (5.70%)

3.4.1.3 Characterisation of the BOSE under Compression with Collagen Hydrogels

Further characterisation of the displacement and velocity parameters of the BOSE was undertaken with the presence of acellular rat tail type-I collagen hydrogels. The objective was to determine whether the presence of the gels significantly affected the ability of the system to achieve the input displacement and velocity defined and whether this differed from tests in air (control). Gels were prepared to a volume of 300 µL in 48 well-plates (11 mm diameter discs), according to the methods described in Section3.3.5. The gels were transferred to the BOSE apparatus and the height of each individual gel was calculated, according to the methods described in Section 3.3.1.1. The working distance- the distance between the surface of the gel and the upper load platen- was set to 8.000 mm based on the preceding results suggesting this as the displacement for achieving optimum desired output displacement and velocity (Section 3.4.1). Given the height of the gel, the desired displacement depth was calculated as a percentage of the total height (25, 50, 75%). After experimental contusion was performed on each gel, the same waveform was simulated in air to serve as the control.

Comparison of the recorded peak displacement and velocity values showed that there was no significant difference between the gel and air, thus the PID settings were suitable for use with the hydrogels (p> 0.05; Figure 3.7). All input displacement depths were achieved with high precision and accuracy, as demonstrated by the low percentage errors and small error bars (Appendix B Table 6.7). A mean peak velocity of 115 mm.s^{-1} was achieved under all input displacement and velocity conditions. This resulted in a higher percentage error (15%) than previously reported in air. Greater variation was observed with the output velocity data, compared to displacement. At an input velocity of 1000 mm.s^{-1} resulted in a mean peak velocity ranging from 900.00 – 967.50 mm.s^{-1}. Output peak velocity appeared to increase with increasing displacement, although this was not statistically significant (p>0.05).
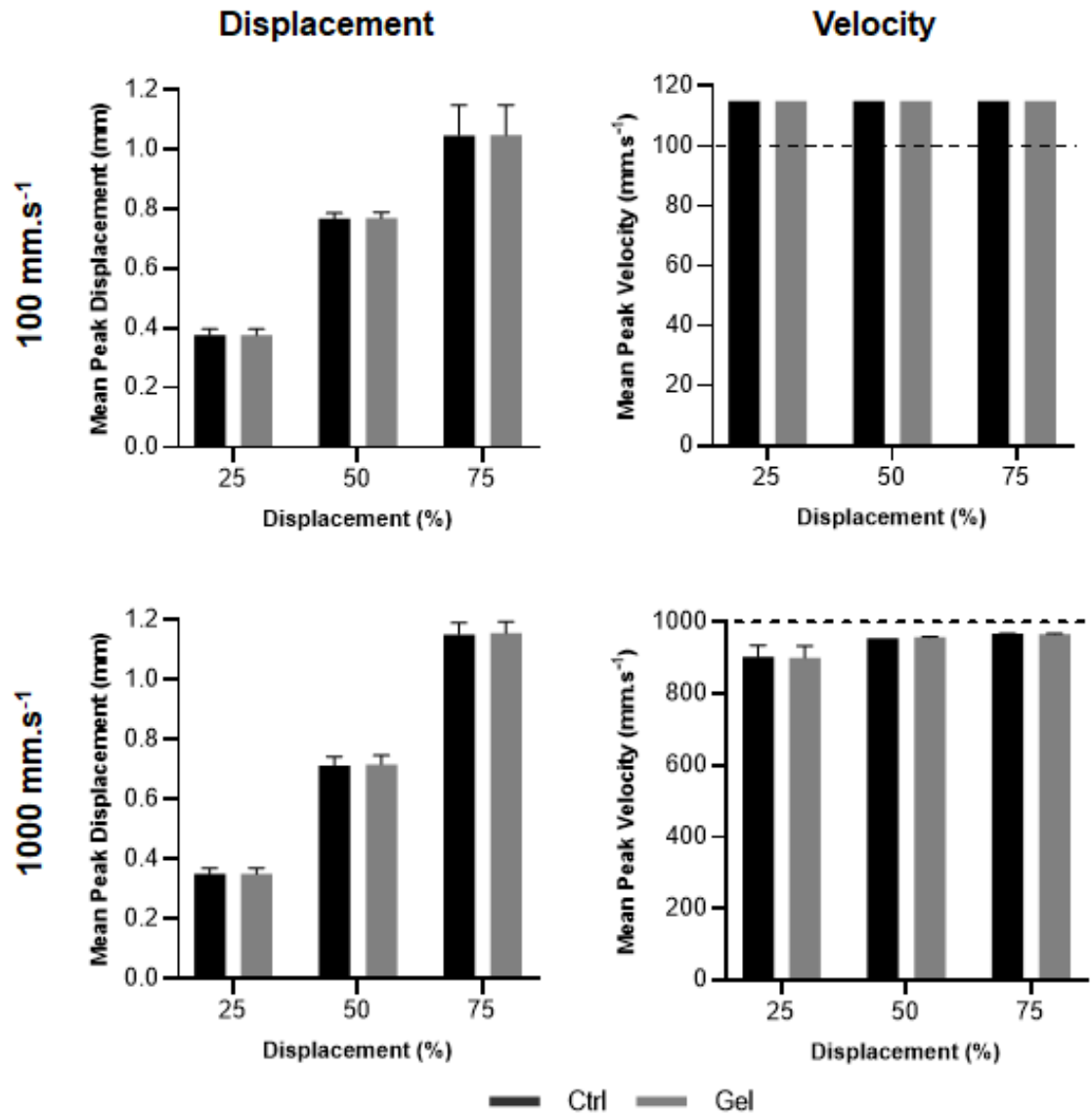
Figure 3.7: Output peak displacement and velocity parameters of the BOSE with and without collagen hydrogels. Rat tail type-I collagen (2 mg.mL^{-1}) was used to prepare 300 µL, 11 mm disc-shaped hydrogels in 48-well plates. Contusion waveforms were simulated, using velocities of 100 and 1000 mm.s^{-1}, and displacement depths calculated as 25, 50, and 75% of the total gel height. The peak displacement and velocity values were recorded. Under control conditions, the same waveform was performed as above, but without the gel. Dashed black lines represent the target velocities. Data presented as the mean $\pm$ SEM. One-way ANOVA with Tukey's post-hoc test performed. N = 3.

Comparison of the output displacement and velocity profiles also demonstrates that there was little disparity between the presence of the gel, and air (Figure 3.8). At an input velocity of 100 mm.s^{-1} the target displacement was achieved and was maintained for the duration of the 100 ms dwell step. A recoil event was observed in the displacement profiles with an input velocity of 1000 mm.s^{-1}, which was not observed at 100 mm.s^{-1}. The recoil was observed in profiles for both experimental and control experiments but shows that the target displacement was achieved. Recoil was also observed in the velocity profiles at an input velocity of 100 mm.s^{-1}, but not 1000 mm.s^{-1}. Some noise was recorded as the target

velocity was achieved, illustrated by the oscillations in velocity during the dwell step and there was an overshoot in velocity. However, this velocity was generally maintained in a stable manner and was observed both with gels and in air.
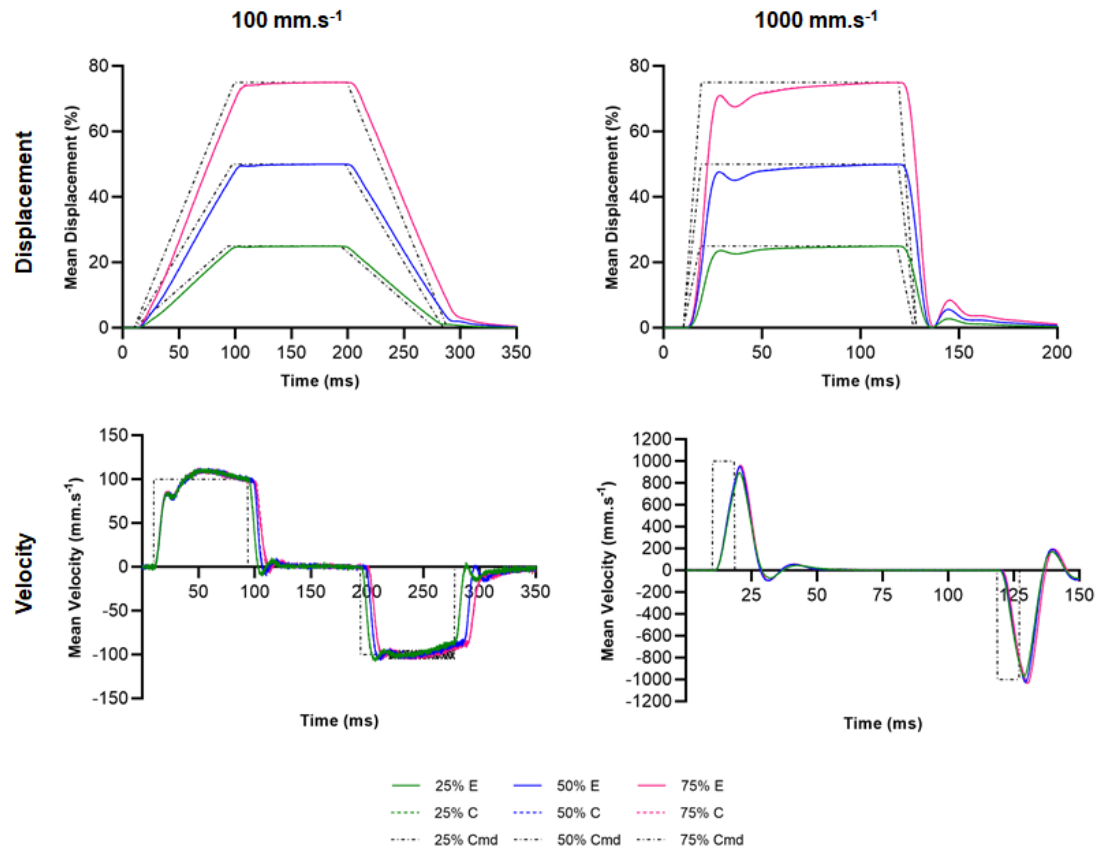
Figure 3.8: Output displacement and velocity profiles with and without collagen hydrogels. Contusion waveforms were simulated, using various combinations of input displacements (% gel height) and velocities, with displacement and velocity data recorded. Solid coloured lines represent experiments with the presence of a gel. Corresponding dashed coloured lines represent experiments in air (control). Black dashed lines represent the input command profiles. N = 3.

To summarise, a reproducible contusion protocol was developed, although certain modifications to the waveform and sample set up were required. Increasing the initial distance between the two platens (working displacement), and the addition of the 100 ms dwell step enabled the system to reach the target velocity and displacement depth and reduced the error. Manual PID tuning reduced the error in the peak velocity and enabled the displacement profiles to better match their command profiles. Applying this waveform to the hydrogels showed that there were no significant differences in the recorded displacement and velocity parameters between air and in the presence of the hydrogel. Thus, no further modifications to the protocol were required.

3.4.2 Modelling Contusion Injury Using the BOSE – Compression Platen Fixture Design

The original compression platen fixtures supplied by the manufacturer consisted of a flat surface on which the sample could sit, but with an angled raised circumference (Figure 3.9A). This was screwed onto a ported shaft, which was then attached to the motor shaft

(i.e. movement of this platen was controlled by being connected to the motor).The diameter of the cavity was measured to be 12 mm; thus the diameter of the hydrogels selected for experiments was 11 mm (48-well plate). A volume of gel of 300 µL was selected as it was the smallest volume of gel which enabled its transferral to and from the plate and the BOSE rig without damaging it. The diameter of the upper load platen fixture (connected to the load cell) was 10 mm, and was selected as this resulted in the majority of the gel being in contact with the load platen during compression (global compression as opposed to a focal one). With the edges of the gel being cultured in a hard plastic well-plate and manipulated by the spatula during transferral to and from the well-plate and the BOSE, these areas would be excluded from subsequent cell behaviour analysis.
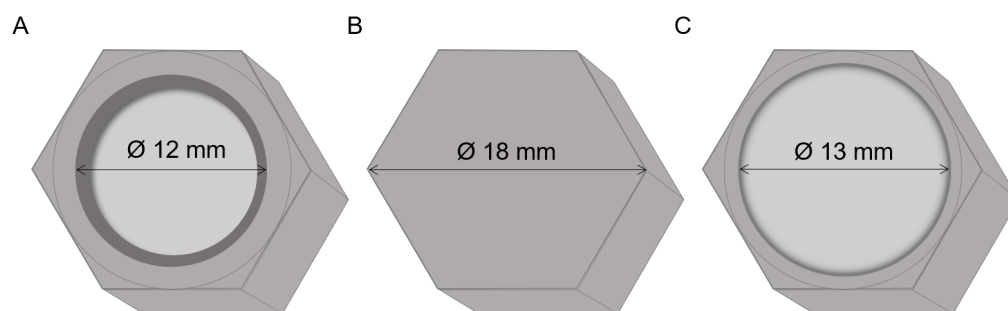
Figure 3.9: Diagram of the different platen fixtures tested for compressing collagen hydrogels. The original compression platen fixture supplied by the manufacturer exhibited a circular central cavity with a slanted circumference (A). First design iteration of the compression platen, modified to exhibit a flat surface on which the sample could sit (B). Second design iteration and working prototype of the compression platen, modified with a larger cavity and vertical sides (C).

The highly hydrated nature of hydrogels meant the structure collapsed slightly when removed from the well plate. Consequently, the gels would have been compressed to a greater extent towards the edges compared to the inner region. A new platen was manufactured which featured an entirely flat surface ($\varnothing$ 18 mm) on which the hydrogel could sit (Figure 3.9B). This enabled the gel to be compressed in an unconfined system, removing confinement as a potential confounding factor in how cells react to the application of compressive forces in subsequent experiments. Unfortunately, during a simulated contusion the gels did not remain on the platen and became displaced (Figure 3.10). As such, it was difficult to determine whether complete compression of the gel took place. Recovery of the sample was also difficult as it was often ejected outside the chamber, thus compromising sample integrity and sterility.

A design modification was thus made to the original manufacturer's compression platen design, by increasing the diameter of the internal cavity from 12 mm to 13 mm (Figure 3.9C). The enlarged cavity was designed to allow better handling of the hydrogel sample (11 mm) to and from the platen minimising damage to the edges with a spatula. Additionally, the additional space enables uniform compression across the gel surface and. Testing an acellular hydrogel under a contusion waveform using this modified compression platen resulted in the gel successfully remaining within the cavity of the platen for the entire duration of the experiment. Consequently, this platen was used for the remaining experiments.
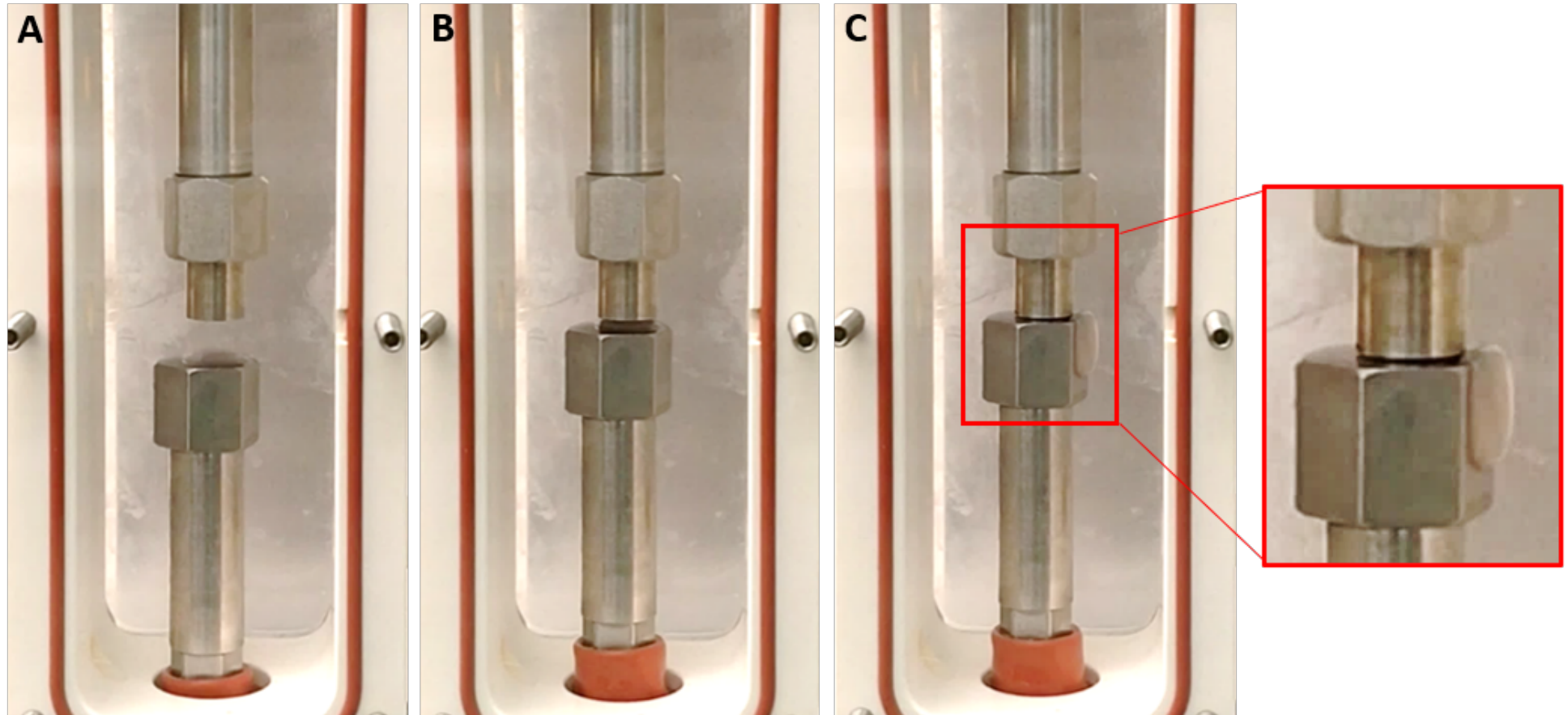
Figure 3.10: Gels did not remain on the platen with a flat surface following compression. The original platen design comprised a completely flat surface. The gels were placed on the lower motor platen, which travels towards the upper load platen, once the waveform is initiated (A). As the surface of the gel makes contact with the load platen (B) and is compressed, it was observed that the gel would slip off the platen (C).

3.4.3   Evaluation of the BOSE Electroforce BioDynamic 5110 with Collagen Hydrogels – Measurement of Gel Height

In order to control and accurately apply contusion injury to the hydrogels a quick, accurate and non-destructive method to measure the gel height was required which also minimised the total volume of starting reagents. Acellular collagen hydrogels were prepared according to the protocol in Chapter 2 (Section 2.5.5) and cast in a 48 well-plate as these produced uniform sized hydrogels of a diameter suitable for loading into the BOSE. Preliminary experiments indicated that a minimum gel volume of 300 µL resulted in hydrogels which were easy to handle. The height of the gels were measured in the BOSE according to the method described in Section 3.3.1.1. To assess the reproducibility of this method and of the preparation of gels at 300 µL, this was performed across multiple independent experiments (Figure 3.11).
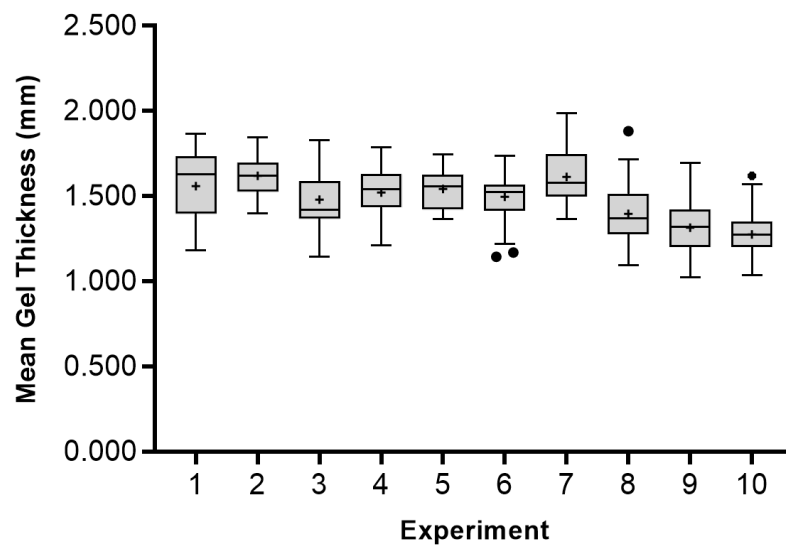
Figure 3.11: Height of collagen hydrogels measured across independent experiments. Rat tail type-I collagen hydrogels were seeded with primary rat cortical astrocytes at a density of 5 x 10^5 cells.mL^{-1} gel (300 µL) and their heights measured using the BOSE. Box represents the interquartile range (IQR). Line across the box represents the median. Whiskers represent the non-outlier minimum and peak values. Mean is denoted as '+'. Individual data values plotted show those which are less than the lower quartile - 1.5 IQR, or greater than the upper quartile + 1.5 IQR (circles). N ranged from 12 – 72 for each experiment.

Between experiments, the mean height of the gels ranged from 1.276 ± 0.1 mm in Experiment 10, to 1.619 ± 0.1 mm in Experiment 2. The mean height of gels in Experiments 9 and 10 were significantly lower than Experiments 1 – 7 (p<0.05, one-way ANOVA with post-hoc Tukey test), but all experiments displayed a similar spread, with a mean range of 0.603 mm. The mean interquartile range across all experiments was 0.213 mm. Although the absolute displacement imparted onto the gels may influence subsequent cellular behaviour, the gel preparation and height measurement protocols resulted in heights with a similar spread, thus was deemed a reproducible method. In the context of this contusion model, a threshold for the range of thickness values considered acceptable was not considered, since the displacement parameters were calculated based on the individual samples themselves.

3.4.4   Development of an *In Vitro* Model of Distraction Injury

Distraction is another mechanism of TSCI, which remains infrequently modelled *in vivo* compared to contusion SCI. Tensile grips were provided with the BOSE, which enables the user to perform tensile tests. The grips are of a clamp design with a knurled screw for securing the sample between a serrated grip surface (Figure 3.12). Development of a protocol to model distraction injury using collagen hydrogels required characterisation and verification of the BOSE system under tensile loads. As with characterisation and verification of the BOSE under contusion loads, various combinations of input distraction lengths and velocities were tested and the respective output values compared. Additionally, gel shape and dimensions were investigated to determine the optimum method of gel preparation and handling with the BOSE apparatus.
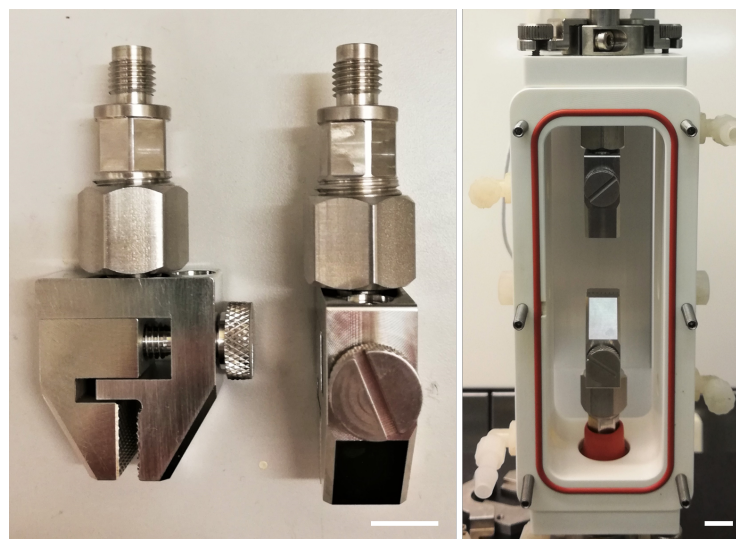
Figure 3.12: Tensile Grips of the BOSE. Photo of the tensile grips provided by the manufacturer for the BOSE Electroforce BioDynamic 5110 (left) and configuration of the grips on the BOSE apparatus (right). Scale bar represents 10 mm.

3.4.4.1   The BOSE Electroforce BioDynamic 5110 as an Apparatus for Inducing Distraction Injury

Characterisation of the BOSE was performed under a distraction waveform to determine whether accurate and reproducible tensile loads could be modelled in air and with the presence of the distraction mould, using the BOSE. The waveform was similar to that of contusion, except this time the displacement ramps were distracted as opposed to moving towards each other. Input velocities of 100 and 1000 mm.s^{-1} were tested, at input distraction lengths of 2, 4 and 6.000 mm. Characterisation results for contusion suggested the use of PID tuning could increase the accuracy of the output parameters achieved (Section 3.4.1.2). Therefore, comparison of distraction waveforms was performed with and without PID tuning. The use of PID tuning generated displacement profiles which better aligned with the command profiles, compared to the non-PID tuned profiles (Figure 3.13). This was more evident at 6 mm distraction, where a larger disparity was observed between the non-tuned and PID tuned profiles during the first ramp step.
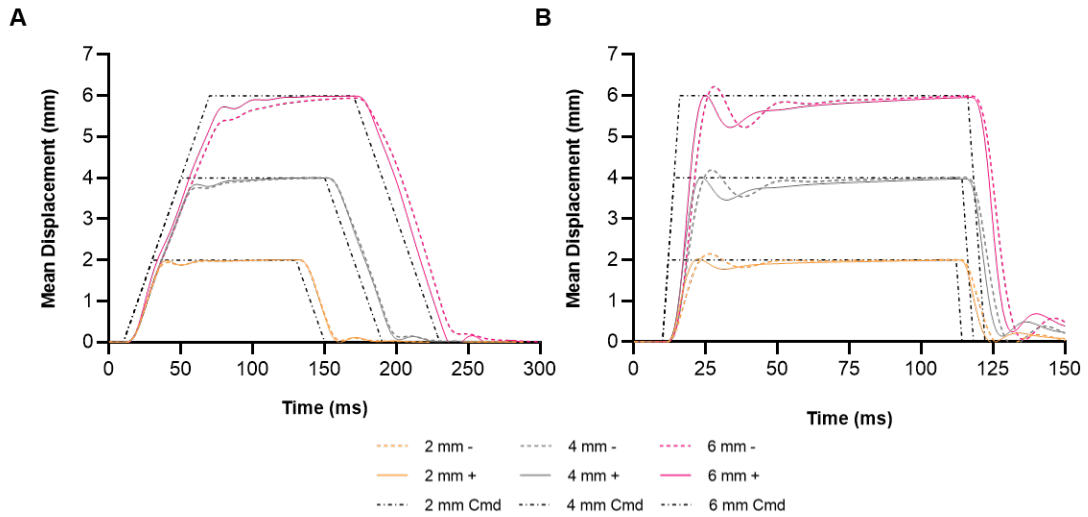
Figure 3.13: Comparison of input and output displacement profiles of a simulated distraction regime with and without PID tuning in air. Distraction waveforms were simulated, using various combinations of input displacements and velocities, with displacement data recorded. Coloured dashed lines represent non-PID tuned profiles (TuneIQ); corresponding coloured solid lines represent PID tuned profiles; dashed black lines represent the input command profiles. N=3.

At an input velocity of 1000 mm.s^{-1}, PID tuning reduced the extent of displacement overshoot which was observed during the first ramp step in the non-tuned displacement profiles (Figure 3.13B). At all input distraction lengths, displacement at this first peak (at approximately 25 ms) also corresponded to the actual peak displacement under both non-tuned and PID tuned conditions. Conversely, at an input velocity of 100 mm.s^{-1} the first peak did not correspond to the actual peak displacement, which was not achieved until towards the latter stages of the dwell step (at approximately 143 ms). At an input velocity of 100 mm.s^{-1}, both non-tuned and PID tuning conditions resulted in the desired input displacements being achieved accurately and precisely, with no significant difference in the mean peak displacement achieved (Figure 3.14). The percentage error in peak displacement was slightly higher with an input velocity of 1000 mm.s^{-1} due to the overshoot in displacement in the non-tuned conditions. PID tuning significantly reduced the mean peak displacement achieved at all depths, resulting in values closer to the target displacement and thus reducing the error (Appendix B Table 6.8).

A velocity of 100 mm.s $^{-1}$ was achieved at all distraction lengths, although slightly overshooting, with a mean peak velocity of 111.11 mm.s^{-1} across all lengths (Figure 3.14A). PID tuning did not have a significant effect on the mean peak velocity achieved, compared to the non-tuned values (p>0.05). At an input velocity of 1000 mm.s^{-1}, increasing the distraction length also resulted in an increase in the peak velocity. PID tuning resulted in a significant increase in the peak velocity achieved at each distraction length. However, the target velocity could not be achieved at any distraction length under both non-tuned and PID tuned conditions. The maximum velocity achievable was 856.67 mm.s^{-1}, using a 6 mm input distraction length and PID tuning, which resulted in a mean error of 14.33% (Appendix B Table 6.8).
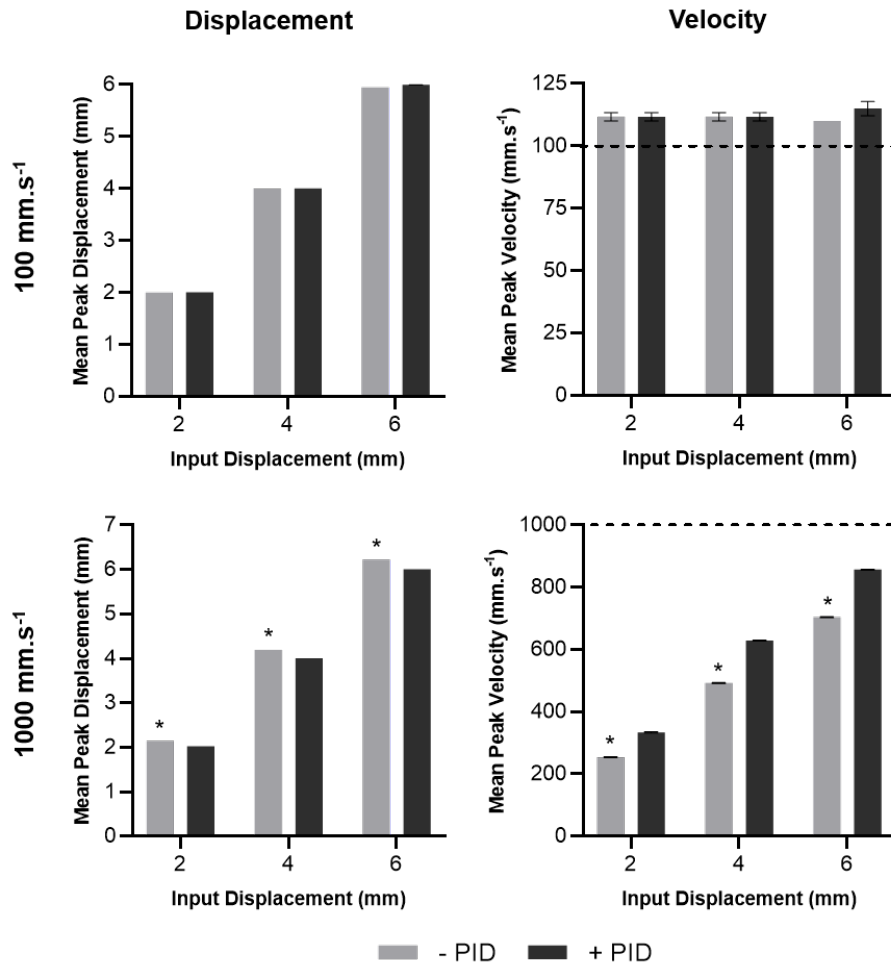
Figure 3.14: Peak output displacement and velocity of a simulated distraction regime with and without PID tuning in air. Distraction waveforms were simulated, using various combinations of input displacements and velocities, with peak displacement and velocity values calculated. Dashed black lines represent the target input velocity. Data presented as the mean ± SEM. Two-way ANOVA with Tukey's post-hoc test performed. Statistical significance * $p < 0.05$ untuned vs. PID tuned at each distraction length. N=3.

Due to the setup of the BOSE, the tensile grips would be in a fixed starting displacement length, securing the samples and maintaining them at 0% distraction. Therefore, working displacement could not be modified to allow the system a greater distance to accelerate to the higher velocity as was performed in the contusion experiments. This meant that with an input velocity of 1000 mm.s−1, the maximum velocity achievable was 333.33 and 628.33 mm.s^{-1}, at 2 and 4.000 mm, respectively. The significant differences in the peak velocity achievable at different distraction lengths meant that this input velocity could not be used.

3.4.4.2 Design of a Mould for Modelling Distraction Injury

The BOSE instrument is designed for the evaluation of biologically oriented samples, including biomaterials and soft tissue constructs. In typical tensile testing experiments, a specimen is loaded between two grips, which secures the specimen and allows tensile forces to be applied to it. However, the low elastic modulus and hydrated properties of the collagen hydrogels used in this study presented challenges regarding loading and

securing them to the tensile grips. Therefore, an alternative method was sought which would not require the sample to be in direct contact with the tensile grips. Engineered anisotropic tissue constructs with aligned cell and ECM structures has resulted in 3D hydrogel models which better mimic the spatial organisation of cells in the native spinal cord (Silva *et al.,* 2014). A mould, developed by Phillips *et al.,* (2005), was originally developed to generate self-aligned hydrogels, using Schwann cells and fibroblasts, without the application of an external stimulus (Figure 3.15). Cell-seeded collagen hydrogels prepared in these moulds have previously been used to model contusion injury, along with the Infinite Horizons Impactor to apply the mechanical load (Smith, 2016).
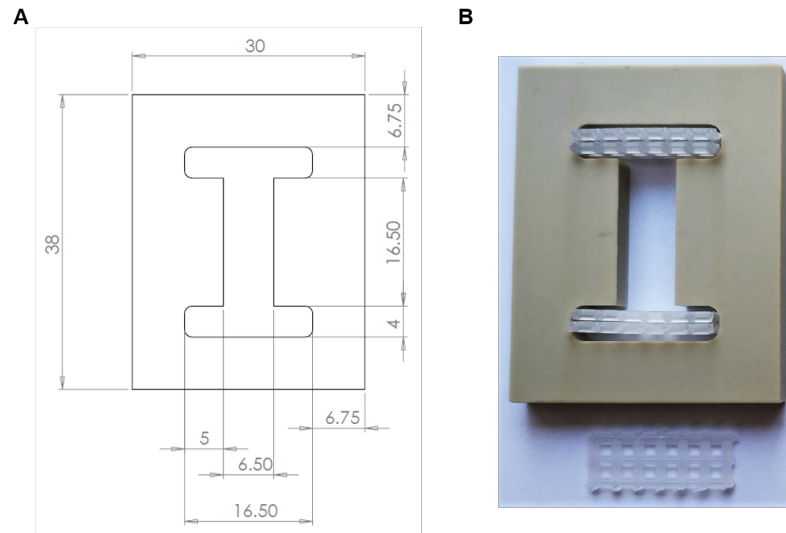
Figure 3.15: Tethered hydrogel mould. CAD drawing of a hydrogel mould originally designed to prepare matrix and cell-aligned gels (A). Photo of the mould manufactured out of polyether ether ketone (PEEK), with the placement of plastic mesh bars at each end (B). Two mesh bars were required at each end and a volume of 1 mL of gel solution was required to fill each mould. Measurements are in millimetres (mm).

As the moulds have already been used to model one mechanism of TSCI, it was hypothesised that it could be adapted for use as a distraction model as well. Because the ends of the gel were cast around plastic mesh bars, it was hypothesised that these could be used to secure the gel within the tensile grips of the BOSE instead of the gel itself. Acellular gels were prepared in this mould to investigate this hypothesis. The size of the original mould required 1 mL of hydrogel solution to fill the I-shaped cavity. Additionally, the size of the mould meant it could not fit in standard sized well-plates and had to be cultured in individual petri dishes, which required greater volumes of cell culture medium. The mould was therefore initially scaled down by half to reduce the starting material and cell culture reagents required (Figure 3.16). The smaller moulds required a volume of 150 µL hydrogel solution and could be housed in wells of a 6 well-plate, overlayed with 2 mL of cell culture medium.
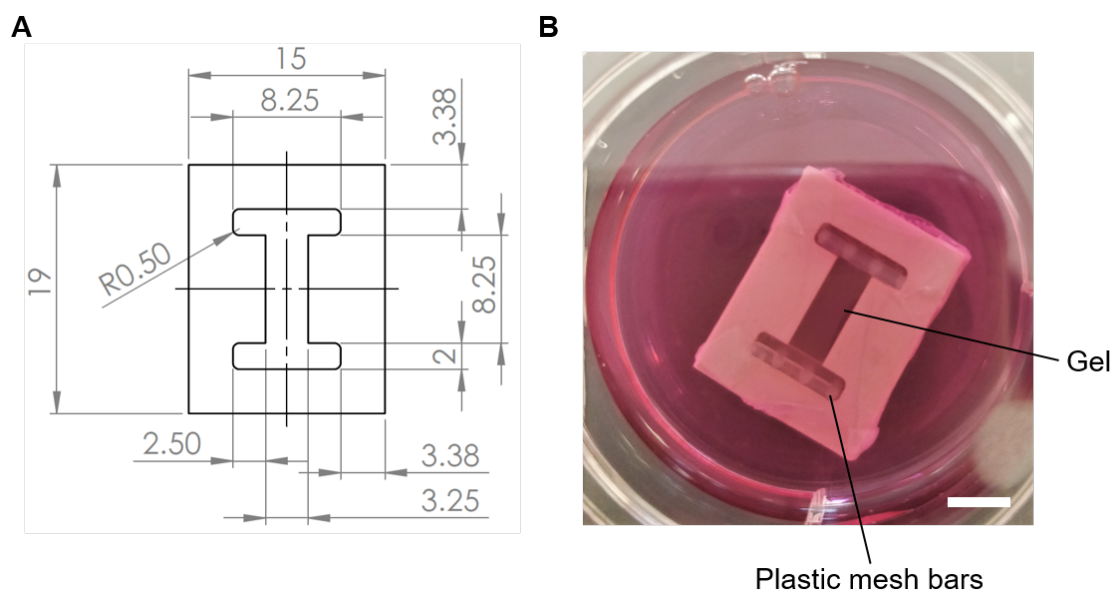
Figure 3.16: 0.5X scaled tethered hydrogel mould. CAD drawing of the 0.5 X scaled mould (A). Measurements are in millimetres (mm). Photo of a mould with an acellular rat tail type-I collagen hydrogel cast within it (B). One mesh bar was required at each end of the mould. Scale bar represents 5 mm.

To remove the gels from the mould, a 23 G needle was used to separate the gel from the edges of the mould. A pair of tweezers was then used to grip onto the tethered mesh bars at the ends of the gels to remove the construct. However, it was difficult to maintain the dimensions of the gel once it was removed from the mould, and often became stretched during transfer from the mould to the tensile grips of the BOSE. Additionally, the small contact surface area between the mesh bars and the tensile grips meant securing the sample without it slipping was unsuccessful. Therefore, instead of the need to remove the gel from the mould and securing it directly into the tensile grips, a design modification was made which would remove this requirement and a method to secure the mould to the tensile grips was explored. A mould with two separate pieces, which could then be connected and secured as one piece was designed (Figure 3.17). For detailed CAD drawings with full measurement specifications refer to Appendix C.
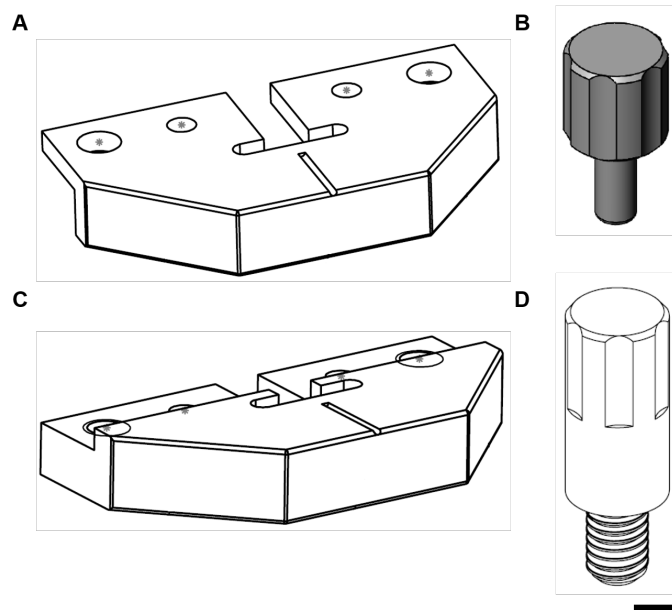
Figure 3.17: CAD drawing of the components of the tethered mould. CAD drawings of four main components of the distraction mould: top piece (A), bottom piece (B), dowel (C), and screw (D). Scale bar represents 2 mm.

The mould components were manufactured out of PEEK, with the two pieces held together with pairs of 316 stainless steel dowels and screws. The moulds were tested in the BOSE system and set up according to the methods in Section 3.3.5. Handling of the mould was easy and sterility was maintained as demonstrated by the absence of visual contamination when the acellular gels were tested on and then cultured for a period of 14 days. Testing was less high-throughput compared to the gels used to model contusion injury due to the addition of several more time-consuming components: assembly and set up of the mould, removal of the parafilm used to cast the gel to allow separation of the mould pieces once in the BOSE, alignment and securing of the mould into the tensile grips, removal and installment of the screws and dowels before and after testing.

However, successful distraction of the mould pieces was achieved, so the system was then tested with gels. With a gauge length of 8.25 mm, distraction lengths of 25, 50, and 75% of the total length was tested. It was hypothesised that these values would represent a range of injury severities and represented the same range used in the contusion experiments. However, results showed that at distraction lengths of 50 and 75%, failure of the gels was observed. Failure always occurred at the ends of the gel, where the gel interfaced with the plastic mesh bars, and at the bottom end of the gel, which was connected to the moving motor shaft (Figure 3.18B). This could potentially be due to increased stress concentration in this region, where there is a change in geometry, or incomplete integration of the gel and the mesh bars.
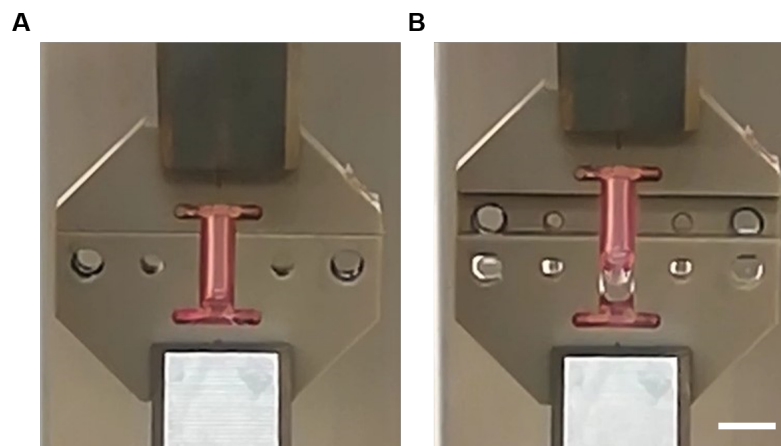
Figure 3.18: Application of tensile load to gels prepared in the distraction mould. Video stills from the simulation of a distraction type injury on gels prepared in the distraction mould. At 0% displacement (A) and 50% distraction (B), where failure of the gel was observed. Scale bar represents 5 mm.

Failure was determined to not be due to insufficient integration of the gel with the tethered bars, as the gel could be successfully removed from the mould with the gel and tethered bars still intact. The original design purpose for the tethered bars was to create anchor points for cells to generate tension and contract the gel and self-align at a certain seeding density. As this was not necessary for this study, the tethered bars were removed. However, failure of the gels was still observed under tensile loads above 50% displacement, and at the same end regions of the gel as with the presence of the tethered bars. Therefore, an experiment was performed to determine the maximum displacement achievable without gel failure. The maximum displacement achieved without resulting in failure of the gel was 35%, which corresponds to a distraction length of 2.888 mm. For subsequent experiments using cell-seeded gels in this system, distraction lengths of 10, 20, and 30% would be used.

3.4.4.3 The effects of the distraction mould on output parameters of the BOSE

Verification of the input and output displacement and velocity parameters of the BOSE was undertaken with the presence of collagen hydrogels prepared in the distraction moulds. The objective was to determine whether the presence of the mould and/or gel significantly affected the ability of the system to achieve the input displacement and velocity defined. Previous results showed that 35% was the maximum achievable distraction length without causing failure of the gel. Additionally, a velocity of 1000 mm.s^{-1} could not be achieved at any distraction length. Therefore, testing of the BOSE system with the distraction mould was performed using an input velocity of 100 mm.s^{-1} and three different distraction lengths: 10, 20, and 30% of the gel gauge length (8.25 mm). This corresponds to absolute distraction lengths of 0.825, 1.650, and 2.475 mm, respectively.

There was a good concordance between the displacement profiles of the gels subjected to tensile forces (experimental) and control (air) simulations, indicating that

the presence of the gel did not adversely affect the ability of the system to achieve the desired displacements. Similarly both of these profiles aligned well with the command profiles (Figure 3.19). Recoil was observed at all distraction lengths during the first ramp step towards the desired length. However, the target distraction lengths were achieved during the dwell step and remained stable.
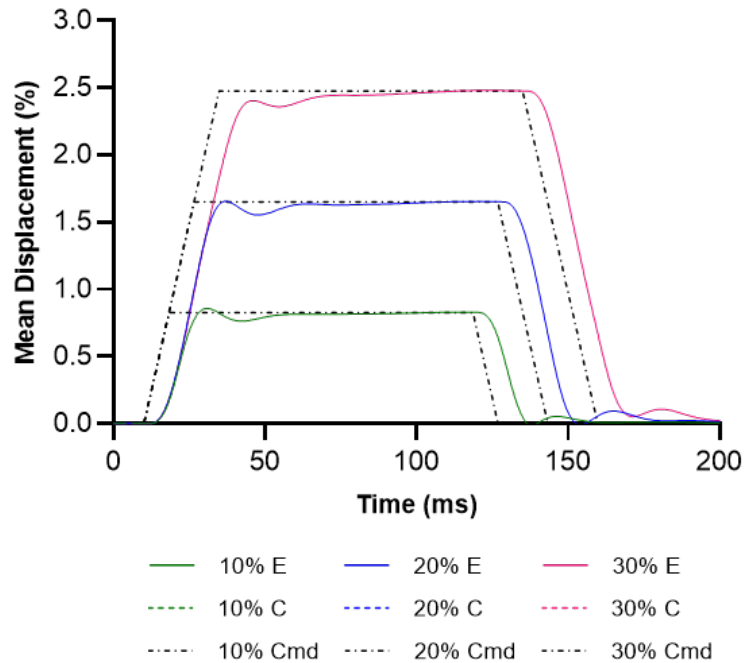
Figure 3.19: Output displacement profiles after applying distraction loads to gels matched those in air. Solid coloured lines represent the experimental profiles (with gel); corresponding coloured dashed lines represent the control profiles (air); black dashed lines represent the input command profiles. N = 3.

Statistical analysis showed that there was no significant difference in the peak displacement achieved, between air (control) and the gels at each distraction length (Figure 3.20A). The target lengths were achieved with precision as demonstrated by the small error bars (Appendix B Table 6.9). Slightly more variation was observed in the peak velocity data. The peak velocity achieved in air was significantly higher than with the gel, at 10% distraction, which was undershooting at 90.00 $mm.s^{-1}$ (Figure 3.20B). There was no significant difference between air and the gel at 20 and 30% distraction. The input velocity of 100 $mm.s^{-1}$ was achieved, although there was an overshoot in velocity in all conditions at 115.00 $mm.s^{-1}$.
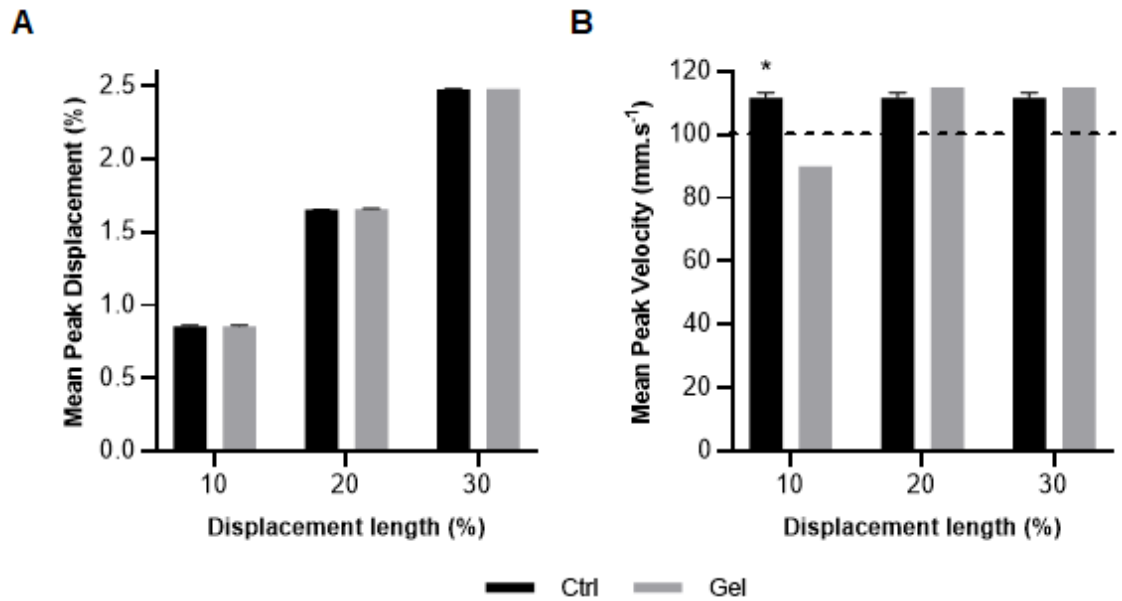
Figure 3.20: Peak output displacement and velocity values are applying distraction loads to gels prepared in the distraction mould. Black dashed line represents the target velocity. Two-way ANOVA with Tukey's post-hoc test performed. Significance levels * $p < 0.05$ control (air) vs. gel. N = 3.

3.4.5 A Biologically Relevant In Vitro Model of the Spinal Cord

With a protocol developed for applying mechanical forces in a reproducible and accurate manner, the aim of this study was to develop a three-dimensional biological model of the spinal cord which would be capable of being subjected to mechanical forces, using the BOSE.

3.4.5.1 Analysis of Purification of Astrocytes from a Mixed Glial Culture

Primary rat astrocytes were selected in this project to evaluate the effects of varying severities of contusion and distraction loads on cellular outcomes, such as viability and reactivity. The method used to isolate these cells involved generating a culture of mixed glial cells in the first instance. After a period of 7 – 10 days, astrocytes were enriched by mechanically separating them from the rest of the cell types (Section 2.5.4.2). To characterise potential contamination of other neural cells which may exert confounding influences on astrocyte behaviour and viability, the purity of the enriched astrocytes was analysed. Immunocytochemical staining for glial fibrillary acidic protein (GFAP) was performed (Figure 3.21). The population of cells was predominantly GFAP-positive, demonstrated by nuclei associated with GFAP staining (green). In comparison, there were few GFAP-negative cells which were demonstrated by nuclei which were not also GFAP-positive. Quantification of the percentage purity of enriched astrocytes was performed across three independent preparations and the mean astrocyte purity was calculated to be more than 90% (data not shown).
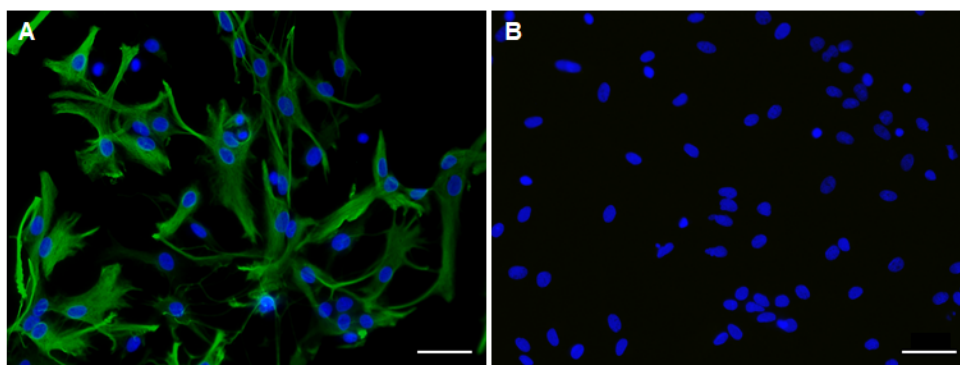
Figure 3.21: Immunocytochemical staining of enriched astrocytes using GFAP.
Astrocytes were seeded onto PDL-coated glass coverslips at 5 x 10^4 cells and cultured for
24 hours before fixing and immunostaining for astrocytes (A). Primary antibody control
(B). Astrocytes (GFAP; green), nuclei (DAPI; blue). Scale bar represents 50 µm.

3.4.5.2   Selection of an optimal primary astrocyte initial seeding density

The selection of three different input displacement depths and two different input
velocities (one velocity for distraction) to apply to 3D seeded astrocytes (300 µL gels)
and evaluate responses over a 14 day time period presented the issue of selecting a
seeding density that would result in the preparation of enough samples for a single
experiment. Further, subsequent studies using cell-seeded hydrogels would be cultured
for up to 14 days. Therefore, an initial seeding density which, by Day 14, would result in
a density which was still easy to perform image analysis was ideal. To obtain an
appropriate number of cells and account for variation across different animals, primary
astrocytes were isolated and pooled from six pre-weaner female Wistar rats. All gels for
one experiment were prepared at the same time to minimise cross-experiment
confounding factors, such as differences in the preparation of the cells and hydrogels.

A preliminary experiment was set up with 100 µL hydrogels seeded at a range of
different densities, from 5 x 10^4 to 4 x 10^6 primary astrocytes per mL of hydrogel. The
hydrogels were cultured in an equal volume of cell culture media, with media changes
undertaken 24 hours after plating, and every two to three days thereafter. On Days 1, 7,
and 14 the metabolic activity of the cells was measured, using the ATPlite™Luminescence
Assay System (Figure 3.22). With an initial seeding density of 5 x 10^5 and 1 x 10^6
cells.mL^{-1} gel, there was no significant change in metabolic activity across the 14-day
time period. Both conditions resulted in a slight decrease in metabolic activity at Day 7,
but this was not significant and had recovered by Day 14. At an initial seeding density of
2 x 10^6 cells.mL^{-1} gel, a significant decrease in metabolic activity was observed between
Days 1 and 7 and Days 7 and 14, suggesting a suboptimal environment leading to decreased
viability. There was no significant difference in metabolic activity between Days 1 and
14. At an initial seeding density of 4 x 10^6 cells.mL^{-1} gel, metabolic activity significantly
decreased between Days 1 and 7, before significantly increasing again by Day 14. However,
metabolic activity remained significantly lower compared to Day 1. Live/dead cytotoxicity
staining was also performed to compare with the ATPlite data and supported the selection
of an initial seeding density of 5 x 10^5 primary astrocytes per millilitre of gel, with no
significant difference in percentage viability over the 14 day culture period (mean 86.4%

viability).
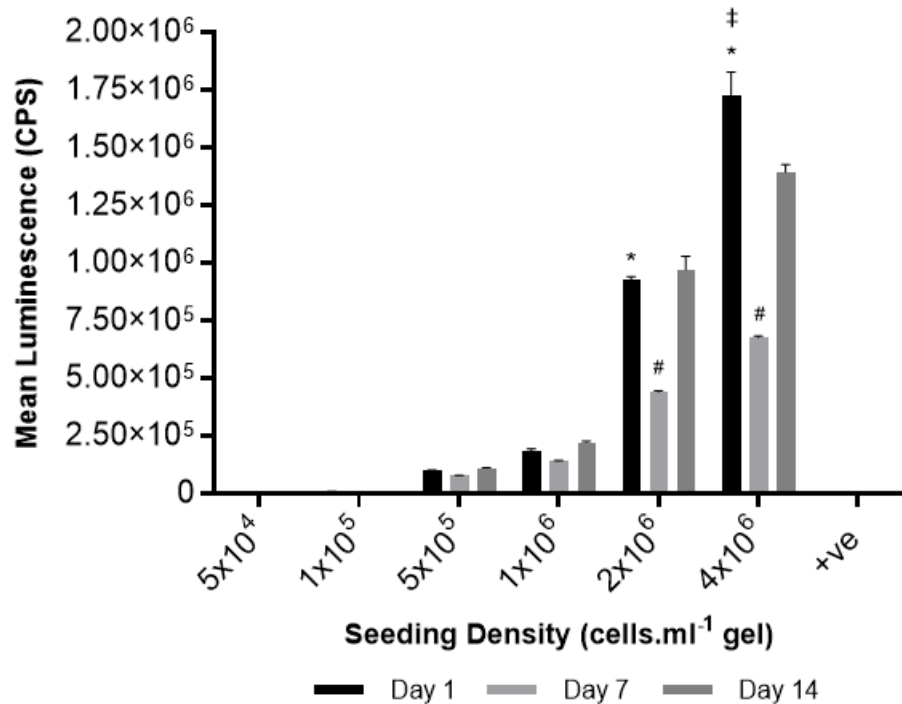
Figure 3.22: Metabolic activity of primary astrocytes seeded into hydrogels at various initial densities. Rat tail type-I collagen hydrogels were seeded with primary rat cortical astrocytes at various initial seeding densities, ranging from 5 x 10^4 to 4 x 10^6 cells p.ml^{-1} gel. At Days 1, 7, and 14 metabolic activity of the cells was evaluated using the ATPlite assay. The positive control represents 70% methanol treatment for one hour. Error bars represent the mean $\pm$ SEM. Two-way ANOVA with post-hoc Tukey test. Significance levels * p<0.05 (Day 1 vs. Day 7); # p<0.05 (Day 7 vs. Day 14); ‡ p<0.05 (Day 1 vs. Day 14). N = 3.

Immunohistochemical staining of primary astrocytes for GFAP was also performed to evaluate the distribution of cells at a seeding density of 5 x 10^{-5} over a period of 14 days. However, there were few GFAP-positive cells, thus using GFAP as a marker to evaluate the morphology of non-reactive astrocytes in 3D could not be achieved. Those cells which were GFAP-positive were small and round in morphology. This contrasts to primary astrocytes seeded at an initial density of 4 x 10^{-1} cells.mL^{-1}, where after 24 hours in culture there were more GFAP-positive cells and they exhibited a reactive morphology with ramification of processes and hypertrophy (Figure 3.23). Overall, an initial seeding density of 5x10^5 cells.mL^{-1} demonstrated stable metabolic activity and viability over a period of 14 days whilst maintaining a non-reactive morphology. This also meant that enough samples and replicates could be prepared for one experiment in a suitable timeframe. Therefore, this seeding density would be used in subsequent experiments in the proceeding chapters.
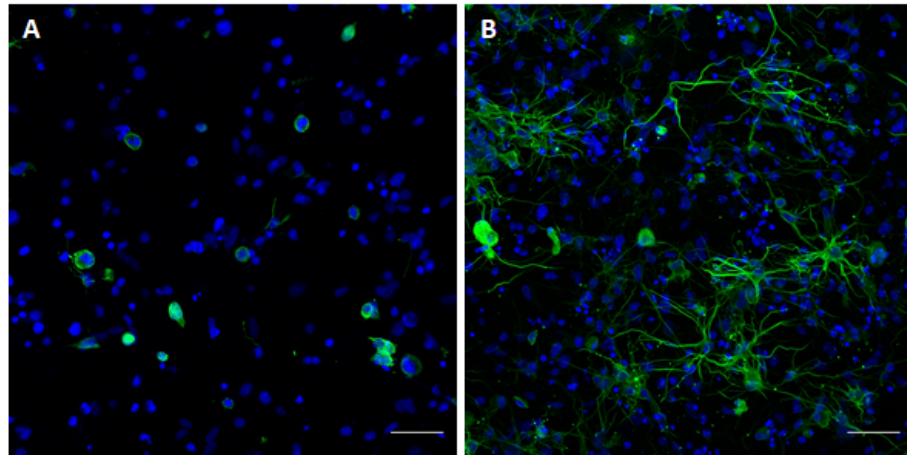
Figure 3.23: Higher seeding densities resulted in a more reactive astrocyte morphology in 3D. Astrocytes were seeded into collagen hydrogels at 5 x 10^5 (A) and 4 x 10^6 (B) cells.mL^{-1} gel and cultured for 24 hours before fixing and immunostaining for astrocytes. Astrocytes (GFAP; green), nuclei (DAPI; blue). Confocal maximum intensity projection, 36 µm z-stack. Scale bar represents 50 µm.

3.5 Discussion

The aim of this chapter was to verify the capabilities of the BOSE Electroforce BioDynamic 5110 apparatus and determine whether clinically relevant TSCI mechanisms (contusion and distraction) could be simulated in a controlled and reproducible manner *in vitro*, using cell-seeded collagen hydrogels as a 3D model of the environment of the spinal cord. The study successfully enabled precise and accurate compressive and tensile loads to be applied to hydrogels. Protocols were defined with a range of input displacement and velocity parameters to represent contusion and distraction injury with ranging severities in subsequent chapters. Additionally, an appropriate method was defined for the preparation and seeding of collagen hydrogels with primary astrocytes, including the optimal gel volume and dimensions, and initial cell seeding density.

3.5.1 Contusion

Modification of the initial compression waveform tested in this study, by increasing the initial working distance between the platens and incorporating a dwell step, reduced the error between the input and output peak displacement value to less than 0.5%. Kirk (2018) also reported work on modelling contusion injury *in vitro* using the same BOSE apparatus. However, characterisation and verification of the parameters was not undertaken in air. In that study, the distance between the two platens was set to 4.000 mm, representing 100% displacement in the presence of the hydrogel. The height of the gels was not reported so the actual working distance is unknown. Verification of displacement in this study, using an input of 4.000 mm and 3000 mm.s^{-1} (the parameters of Kirk (2018)), resulted in peak displacement values of 0.699 ± 9 x 10^{-4} and 4.007 ± 5 x 10^{-4} without and with a 100 ms dwell step, respectively. A dwell step of 10 ms was used by Kirk (2018) and the actual input and output displacement values were not reported so it is difficult to verify how accurate the displacement parameter was in that study. However, by comparing the input and output displacement profiles using the

same input displacement and velocity parameters as in that study, it is suggested that the desired input displacement depths were unlikely to have been achieved.

It was clear that a velocity of 3000 mm.s^{-1} could not be achieved in this study, despite this being the maximum value that was allowed to be inputted into the waveform. The velocity of 3000 mm.s^{-1} stated by Kirk (2018) was therefore not achieved. As mentioned previously, the distance between the two platens was set up to be 4 mm in that study. Characterisation of the BOSE in air in this study showed that at an input velocity of 3000 mm.s^{-1}, displacement of 4 mm, and 100 ms dwell step (without PID tuning) the resultant mean peak output velocity was only 458.75 $\pm$ 1 mm.s^{-1}.

The results in this study showed the presence of recoil in the system, which occasionally led to an overshoot in velocity and displacement. This was observed both in air and with hydrogels, suggesting this is instability within the BOSE itself. Kirk (2018) also observed recoil with the BOSE and hypothesised that this was due to the elastic properties of the hydrogels, but did not perform the same experiment in air to compare. The contusion protocol in that study was modified to account for the recoil by setting the first ramp step to move at 3000 mm.s^{-1} to a displacement depth that was 0.1 mm less than the desired displacement depth. An additional ramp step was then incorporated to move the motor platen the remaining 0.1 mm, but at a lower velocity of 3 mm.s^{-1}.

However, the displacement profiles presented in that study showed a recoil of up to 0.5 mm remained present. The peak displacement values were not reported, but visually comparing this point of the displacement profile to the command profile suggests the peak displacement remained below that of the desired displacement. The shape of this recoil was similar to that observed in this study, but given the longer dwell step of 100 ms, the target displacement was then achieved here. Impact velocity and the velocity at peak displacement was not likely to have been 3000 mm.s^{-1} due to the input velocity being reduced to 3 mm.s^{-1}. This makes it difficult to know what the precise output velocity measurements were to discuss and compare the relationship between velocity and cellular response in this subsequent work. However, the original aim of that study was to evaluate the effects of only displacement on cellular response.

An overshoot in displacement was also reported *in vivo* by Kim *et al.,* (2009), using the UBC multimechanism electromagnetic device to inflict contusion SCI on mouse spinal cord. An overshoot in displacement of ~0.02 mm was reported, both in air and with mouse spinal cord. This was deemed insignificant compared to the desired input displacement values. Once optimisation steps were undertaken in this study (increasing working distance; 100 ms dwell step; PID tuning) an overshoot in displacement of less than 0.089 and 0.236 mm was observed at 100 and 1000 mm.s^{-1}, respectively. Where an undershoot in displacement was observed this was calculated to be 0.007 and less than 0.039 mm with an input velocity of 100 and 1000 mm.s^{-1}, respectively. These values are within a similar range to that observed by Kim *et al.,* (2009).

Overshoot was also observed by Brody *et al.,* (2007), who designed a custom electromagnetic device to model controlled cortical impact (CCI). The apparatus generated overshoots in displacement of 0.28 – 0.31 mm. These values are an order of magnitude greater than those measured by Kim *et al.,* (2009) and in this study, although higher velocities were used in that study (3.6 and 5.2 m.s^{-1}). The overshoot was found to be caused by deformation of the apparatus support structures during the impact stroke and not the dynamic response of the tissues. Compared to a commercially available pneumatic device, these electromagnetic devices are more accurate, with Brody *et al.,* (2007) measuring an overshoot in displacement of up to 0.61 mm with the pneumatic device under the same conditions. These studies demonstrate that overshoot is a common effect observed with multiple apparatus designed to model high velocity contusion-type injuries; however, as the scale of overshoot is relatively small compared to the desired displacement, correction was not undertaken. Similarly, correction for overshoot or undershoot was not performed in subsequent experiments.

PID tuning did not significantly improve the accuracy of the displacement parameter, and actually decreased its accuracy under some conditions. This could potentially be attributed to the nature of PID tuning itself as higher values may result in a more aggressive response to reach the desired values, increasing instability. As it was also performed manually, sub-optimal modifications to the tuning parameters by the user could have increased instability in the system. There are numerous other methods of PID tuning available, including heuristic and automated methods, which may provide a more accurate and methodical approach to tuning which should be considered in future (Bucz and Kozáková, 2018; Ziegler and Nichols, 1942).

However, the PID tuning undertaken in this study did improve the accuracy of the peak velocity measured, with errors reduced to less than 10% at 8.000 and 10.000 mm displacement at both velocities tested. The errors were still greater for velocity compared to those for displacement, which was observed in other contusion studies too (Chen *et al.,* 2016; Choo *et al.,* 2007; Lam *et al.,* 2014). For instance, percentage errors of 1 – 3% and 3 – 10% were calculated for displacement and velocity, respectively, given the mean values reported by Lam *et al.,* (2014). Tuning was either not applied to other TSCI apparatus or was not reported, thus the characterisation and verification processes of other *in vivo* studies using mechanical injury apparatus is not known.

The most common method for registering the surface of the spinal cord *in vivo* is to gradually lower the impacting tip towards the cord until a change in load is registered. An additional 'pre-load' is commonly applied to maintain standardisation across subjects. However, this method could not be employed in this study due to the lack of sensitivity. The low elastic modulus of the hydrogel meant that a change in load was not registered, even when the upper load platen was clearly in contact with the surface of the gel. Busby *et al.,* (2013) was able to use a change in load (0.01 N) to register the surface of rat-tail type I collagen hydrogels (0.2, 0.3, 0.4% w/v) used in their study using the

BOSE (3200 model). However, this was not possible in this study as the apparatus was housed in a Class II cabinet to maintain sample sterility. The fan used in the cabinet caused oscillations in load which made it difficult to distinguish between baseline noise, and contact with the sample surface. The environment surrounding the BOSE apparatus in the Busby *et al.,* (2013) was not reported.

Therefore, the height of the gel was measured by moving the motor platen containing the sample towards the load platen until contact was achieved with the surface of the gel. Despite a limitation being that determining when the surface of the gel was in contact with the load platen was manual, being able to control displacement to a resolution down to 0.001 mm increased the reliability of this method. This protocol was used by Koivisto *et al.,* (2017) to set the starting point of the compression experiment as opposed to specifically measuring its height. Instead, calipers were used to measure the dimensions of their gels, which were considerably thicker at approximately 6.5 mm. It was not clear whether the caliper measurements were performed before or after loading the sample into the BOSE (5100 model), and which method was used to calculate the subsequent displacement value to be used for compression testing.

Most studies reporting use of the BOSE Electroforce BioDynamic system performed mechanical testing experiments and, as such, output biomechanics were generally not characterised or reported (Bartlett *et al.,* 2016a; Busby *et al.,* 2013; Koivisto *et al.,* 2017; Sparrey and Keaveny, 2011). The strain rates used here were greater than those used for mechanical testing, but characterisation data showed the BOSE was capable of modelling different mechanisms of TSCI *in vitro*. The input displacement and velocity range of the BOSE is comparable to other apparatus used to model SCI *in vivo*. Although it was hypothesised that a velocity of 3000 mm.s^{-1} could be achieved based on indications by the software and work by Kirk (2018), the results herein show that this was not the case. However, input velocities of 100 and 1000 mm.s^{-1} could be achieved. These are within the range of previous contusion studies *in vivo* (Chapter 1; Table 1.5). The output displacement measurements were precise and had minimal percentage errors within a similar range to the UBC multimechanism device, as described above.

The BOSE possesses more controllable parameters compared to some other contusion apparatus used *in vivo* and offers high quality real-time data acquisition capabilities. The IH impactor, for instance, offers only force control. Displacement was controlled to an extent by Smith (2016) via manually adjusting the starting height of the impactor tip, but this is not a standardised or validated method. The TestBench™system, also manufactured by TA Instruments, was adapted for modelling contusion injury in non-human primates (NHP) *in vivo* (Salegio *et al.,* 2016). The system offers the same controllable parameters as the BOSE Electroforce BioDynamic series and the study reported various impact mechanical data, including input and output displacement and velocity, time to maximum displacement, force at peak displacement, and peak force. The output velocity ranged from 270 – 580 mm.s^{-1} which was lower than the input velocity of 1000 mm.s^{-1}. Output displacement ranged from 1.71 – 1.91 mm, 2.66 – 2.78

mm, and 3.46 – 3.72 mm for inputs of 2.0, 3.0. and 4.3 mm, respectively showing an undershoot of at least 0.09 mm which is greater than that in this study.

This demonstrates that the BOSE used in this study is more accurate compared to the TestBench™system. Standard deviation was not reported so repeatability cannot be discussed. The UBC multimechanism device is the only apparatus which is designed to model contusion, distraction and dislocation mechanisms of SCI in rats *in vivo* (Chen *et al.,* 2016; Choo *et al.,* 2008, 2007, 2009; Lam *et al.,* 2014). Again, input displacement and velocity can be defined by the user and output injury mechanics include impact depth, impact velocity, force, and energy applied Lam *et al.,* (2014). Similar to the BOSE, variability was greater for velocity compared to displacement. Optimisation of the apparatus and reduction in variability has been achieved through improvements in vertebral clamp design to prevent slippage, for instance.

3.5.2 Distraction

Verification of the BOSE with the gels revealed higher errors in the peak displacement achieved, compared to in air. The PID values used were based on input distraction lengths of 2, 4, and 6.000 mm, thus the PID values may not have been entirely appropriate for the gels since the distraction lengths used for the gels ranged from 0.857 (10%) – 2.480 (30%). These values were selected based on results showing 35% being the maximum distraction length without causing gel failure. Consequently, a limitation of this study is that the low mechanical strength of collagen hydrogels precluded longer distraction lengths being used. However, there was no significant difference in the peak displacement achieved between control and gel. Additionally, each distraction length was significantly different from one another so the error is unlikely to affect subsequent cellular outcomes. The distraction lengths used in this study are slightly lower than the range of values used *in vivo* in rodents, where distraction lengths ranged from 2.5 – 7 mm (Chapter 1 Table 1.5).

An input velocity of 100 mm.s^{-1} was achieved in air and with the gels, with a similar magnitude of error (mean 109.17 mm.s^{-1} across all conditions). However, a significant difference in the peak velocity was calculated between control and gel at 10% distraction length (Figure 3.20). It is not clear why the presence of the gels resulted in a significantly lower peak velocity at 10% distraction, whilst there were no significant differences between air and the gel at 20 and 30% distraction. A peak velocity of 90 mm.s^{-1} was achieved for all three replicates at 10%, so it was unlikely due to differences in the gel itself. The command data showed the correct velocity and displacement values were inputted into the system. For future studies, the peak velocity would be evaluated after the test and repeated and/or re-tuned if necessary.

An input velocity of 1000 mm.s^{-1} could not be achieved accurately in air over the distraction range (Figure 3.14). For contusion injury, increasing the working distance was hypothesised to enable a greater peak velocity to be achieved, which was shown to be true. However, the setup of the BOSE for tensile studies meant that the mould was secured

into the grips in a fixed position of 0% distraction. As there was a positive correlation between the distraction length and peak velocity, an inaccurate peak velocity was achieved regardless of the input velocity. Therefore, 1000 mm.s^{-1} was excluded from subsequent experiments modelling distraction injury. The *in vivo* distraction studies which utilised the UBC multimechanism device used an input velocity of 1000 mm.s^{-1}; Dabney *et al.,* (2004) used input velocities of 1, 5, and 10 mm.s^{-1}, whilst the remaining studies used manual distraction methods where velocity was not controlled (Table 1.5). An input velocity of 100 mm.s^{-1} is thus within the range of velocities used *in vivo*. However, it would be difficult to discuss future results in the context of these studies as the input distraction length and velocity varies.

3.5.3   3D Model of the Spinal Cord Environment

Primary astrocyte-seeded collagen hydrogels were selected to model contusion and distraction type SCI *in vitro*. In order to develop a model which was suitable for use with the BOSE, a protocol was needed which specified the gel volume, dimension, initial seeding density and an accurate method for measuring gel dimensions. Mechanical enrichment of primary astrocytes has been used successfully in other studies, where populations of 95% (East *et al.,* 2009) and 85 – 90% (Kerstetter and Miller, 2012) astrocytes were considered acceptable for subsequent experimentation. The mean astrocyte purity achieved in this study was 92.87%, which is within the range of that reported by other studies.

The hydrogels prepared in this study were cast in 48-well plates, using a volume of 300 µL gel solution per sample. This resulted in gels with a diameter of 11 mm (as defined by the diameter of the well). Smaller diameter gels were considered but for ease and time reasons, standard well-plates were used. A gel volume of 300 µL was the smallest volume which enabled ease of handling in and out of the BOSE, without damaging the gel or causing folding. For contusion model development, measurement of the gel heights using the BOSE was selected over methods such as taking a photo or calipers which required additional tools and increased the time spent outside the cell culture medium. Using the platens of the BOSE in displacement control reduced the amount of handling required as the gel was then already in position to be experimented on.

The mean height of gels across 10 independent experiments was 1.276 ± 0.1 mm. McMurtrey (2016) calculated a viable tissue thickness range of 0.4 – 2 mm, given the oxygen consumption and diffusion coefficient values of human neurons. This thickness limit for cell viability was similarly observed in hydrogels seeded with 4 x 10^5 differentiated SH-SY5Y neurons (McMurtrey, 2014). The limit of diffusion can also dependent on many factors, such as cell type, seeding density, cellular activity, and matrix concentration (Cheema *et al.,* 2012; Griffith *et al.,* 2005). Although the hydrogels used in this study lack a complex microvascular system to facilitate mass transfer, the height of gels used should support adequate oxygen and nutrient diffusion throughout the gel.

The initial seeding density was evaluated in order to determine the density which would enable a high number of samples and replicates to be prepared in a single session. The ATPlite™Luminescence Assay was used to monitor metabolic activity over a period of 14 days. Results showed that both densities of 5 x 10^5 and 1 x 10^6 cells.mL^{-1} exhibited stable metabolic activity over 14 days. The decrease in astrocyte metabolic activity at 2 and 4 x 10^6 cells.mL^{-1} gel could have been due to insufficient nutrients available from the volume of cell culture medium used. Figueiredo *et al.,* (2018) observed a significant reduction in glucose and oxygen concentration after 6 hours, with an almost complete depletion of oxygen concentration at 72 hours, using human adipose derived stem cell-seeded hydrogels at 4 x 10^6 cells.mL^{-1} (cellulose-derived hydrogel; 1 cm thick 24 well-plate). Due to the number of samples which were calculated to be required in this project, an initial density of 5 x 10^5 cells.mL^{-1} was selected.

Immunostaining for glial fibrillary acidic protein (GFAP) was performed to analyse the morphology of the astrocytes at 5 x 10^5 cells.mL^{-1} gel and to determine whether there was an appropriate distribution of astrocytes. However, the lack of GFAP positive cells meant that this could not be achieved. This effect has previously been reported by East *et al.,* (2007) and Smith (2016) *in vitro*, whereby cells seeded in 3D hydrogels expressed low levels of GFAP, and were small and rounded in morphology. East *et al.,* (2007) also demonstrated that astrocytes cultured in 3D had lower levels of mRNA for GFAP, compared to 2D cultured astrocytes. This was attributed to the less reactive phenotype of the astrocytes. The presence of a predominantly astrocyte population was confirmed when cells from the same suspension were seeded into gels and onto PDL-coated coverslips at the same time, with the majority of cells on coverslips being GFAP-positive. As the live/dead cytotoxicity staining and metabolic activity (ATPlite) results suggested that the majority of the cells were viable, so the lack of GFAP-positive astrocytes did not suggest they were non-viable.

When developing the distraction model, one difficulty encountered was what the gel shape and dimensions should be. Application of tensile loads for mechanical testing of hydrogels, for instance, is generally performed on rectangular strips or rings of sample (Ahearne *et al.,* 2008). Due to the low stiffness of the collagen hydrogels used in this study, a literature search was performed to investigate whether there were existing protocols on how to prepare similar hydrogels for modelling tensile loads, or for mechanical tensile testing. Many *in vitro* models of CNS injury utilise tissue (such as organotypic brain slices) or cells attached to a substrate which strain can then be applied to, as reviewed by LaPlaca *et al.,* (2007). Although distraction injuries likely involve shear deformation, this does not fully represent the tensile loads also being applied to the tissue. Additionally, studies where cells were cultured directly onto deformable membranes are 2D in nature so the 3D microenvironment is lacking.

Although not necessarily evaluating cellular responses to mechanical loads, mechanical testing of hydrogel biomaterials and constructs have been performed. Studies

which involved mechanical testing of collagen hydrogels using tensile methods were looked at to determine the sample setup, their dimensions, and how samples were secured to tensile clamps. Brown *et al.,* (2005) used uniaxial tensile testing to determine the Young's modulus of plastically compressed spiral constructs made of rat tail type-I collagen (2 mg.mL^{-1}). These spiral constructs- 13 mm long and 1.75 mm in diameter- were clamped into the tensile testing grips of a DMA-7e rig using strips of cyanoacrylate-reinforced steel mesh. Hadjipanayi *et al.,* (2009) performed dynamic mechanical analysis (DMA) of rat tail type-I collagen (2.2 mg.mL^{-1}) in tension, using plastically compressed strips of collagen (1 mm wide; 0.1 mm thick) although no details of how the sample was affixed to the rig were reported. These studies used a similar starting collagen material as used in this study (2 mg.mL^{-1} in 0.6% v/v acetic acid; First Link, UK Ltd.). However, due to the materials' low stiffness, plastic compression was used in both studies to generate denser, mechanically stronger hydrogels which were amenable to manipulation such as tensile testing and forming layered constructs.

Plastic compression (PC) utilises the application of a weight to remove interstitial fluid, thus stabilising the specimen and increasing protein density but also irreversibly modifying its structure. PC has been widely used to modulate the mechanical properties of various collagen hydrogel constructs for tissue engineering applications (Bitar *et al.,* 2007; Brown *et al.,* 2005; Neel *et al.,* 2006), including in the nervous system (Georgiou *et al.,* 2013; Kayal *et al.,* 2020; Phillips, 2014a). One issue with PC is whether this has an effect on cell viability or behaviour. Bitar *et al.,* (2007) found no differences in cell viability and responses between non-compressed and compressed matrices, seeded with a human osteosarcoma cell line. Brown *et al.,* (2005) and Hadjipanayi *et al.,* (2009) used adult human dermal fibroblasts and found PC supported cell viability and proliferation for up to 5 weeks in culture. These cell types are generally associated with tissues (bone and skin) which are stiffer than neural tissue (Barnes *et al.,* 2017). Therefore, PC of these gels likely does not increase the stiffness of the matrix enough to significantly affect cell behaviour.

Astrocytes have been shown to be responsive to stiffness (Georges *et al.,* 2006). For example, East *et al.,* (2009) observed increased reactivity of astrocytes at the edges of the 3D cultures, which were in closer proximity to the tissue culture plastic. Smith (2016) reported that astrocytes cultured in plastically compressed collagen hydrogels were more hypertrophied and ramified in morphology, compared to the smaller rounded astrocytes in the fully hydrated gels. Further, they expressed significantly more GFAP compared to astrocytes in fully hydrated gels. In order to evaluate the effects of injury mechanics on astrocyte responses, the astrocytes need to have a low baseline reactivity phenotype. Therefore, PC was not used in this study. Instead, a mould previously designed to generate neural cell-aligned constructs (engineered neural tissue, EngNT) was used to prepare gels with an I-shape suitable for applying tensile loads (Section 3.4.4.2). As the mechanical properties of the hydrogels were not modified, the mould was adapted to consist of two pieces held together with screws and dowels, with the gel cast in the I-shaped cavity in the centre (Figure 3.18A). These were secured into the tensile grips instead of having to

remove the gel and secure it directly into the grips, which could not be achieved without stretching or damaging the gel.

3.6 Conclusions

The displacement and velocity parameters of the BOSE 5110 Electroforce BioDynamic were verified against the input values and determined to be accurate and precise, with protocols for modelling both contusion and distraction injury being developed using collagen hydrogels as the substrate. This apparatus was easy to use and set up, providing an extra tool for researchers to investigate traumatic spinal cord injury biomechanics *in vitro* which is comparable to those used *in vivo*. This chapter addressed the main objectives of the project, which were to assess the suitability of utilising the BOSE as a rig capable of simulating controlled, repeatable loads representative of contusion and distraction injury scenarios, and to develop a protocol for the simulation of contusion and distraction injuries using three-dimensionally encapsulated astrocytes in collagen hydrogels (Chapter 1).

The specific objectives set out in this chapter were met with the following observations:

 I. *Characterise, verify and optimise the displacement and velocity parameters of the BOSE in air, under compressive and tensile waveforms:*

- Addition of a 100 ms dwell step, increasing working distance between the sample and load platen (contusion) and PID tuning increased the accuracy of the output peak displacement and velocities achieved.

- The most accurate peak velocity achieved was 943.00 mm.s^{-1} under the following conditions: compression; input displacement 8.000 mm; input velocity 1000 mm.s^{-1}; + 100 ms dwell step; + PID tuning.

 II. *Determine the effects of collagen hydrogels on the output displacement and velocity values of the BOSE:*

- Modelling of contusion and distraction waveforms with hydrogels did not significantly affect the displacement and velocity profiles, nor their peak values compared to air.

 III. *Develop a protocol to enable accurate measurement of the initial dimensions of collagen hydrogels (contusion) and thus define the displacement parameters:*

- Measurement of the height of gels for contusion studies was successfully achieved using the BOSE, by determining the distance between the surface of the gel and the upper load platen.

 IV. *Define a set of velocity and displacement parameters to be simulated experimentally, in order to represent a range of injury severities in vitro:*

- A range of velocity and displacement depth/distraction length parameters have been defined, which will represent a range of injury severities *in vitro* in subsequent studies (Table 3.3).

V. *Select an appropriate primary astrocyte seeding density:*

- An initial astrocyte seeding density of 5 x 10^5 cells.mL^{-1} gel was determined as the optimal density for preparing a large number of samples, with stable metabolic activity and low reactive phenotype across 14 days.

VI. *To define the shape and dimensions of a hydrogel to enable tensile loads to be applied, simulating distraction-type spinal cord injuries:*

- A mould was adapted to prepare I-shaped collagen hydrogel samples (150 µL), from which the mould could be affixed into the tensile grips of the BOSE and distracted.

The input biomechanical parameters for contusion and distraction injury to be used in Chapters 4 and 5 are described in Table 3.3.

Table 3.3: Input biomechanical parameters for modelling of contusion and distraction injury. The working displacement is applicable for contusion injuries and defines the distance between the surface of the gel and the upper load platen. Since in distraction injury the distraction mould is fixed into both tensile grips, the working displacement cannot be modified so is not applicable.

	Contusion	Distraction
Input displacement (%)	25, 50, 75% gel height	10, 20, 30% gel length
Input velocity (mm.s^{-1})	100, 1000	100
Working Displacement (mm)	8.000	NA
PID Values	*100 mm.s^{-1}:* P(0.658296) I(0.009272) D(-2.81748) *1000 mm.s^{-1}:* P(0.658296) I(0.007746) D(-2.81748)	P(0.383529) I(0.006831) D(-2.023999)

NA = Not Applicable.

Chapter 4

The Effects of Varying Displacement Depth and Velocity on Astrocyte Responses in an *In Vitro* Model of Contusion Spinal Cord Injury

4.1 Introduction

Contusion spinal cord injury (SCI) most commonly arises as the result of failure of the vertebral column, caused by a burst fracture. It is one of the most prevalent mechanisms of TSCI in humans (Sekhon and Fehlings, 2001). The contusion mechanism also remains the most widely modelled injury mechanism *in vivo* (Sharif-Alhoseini *et al.,* 2017). Increasing attention is being paid towards evaluating the relative importance of mechanical parameters in determining injury severity, although this idea has been investigated as early as the 1980s by Kearney *et al.,* (1988), who described the spinal cord as rate sensitive: displacement acted as the dominant determinant of injury severity at low impact velocities; however, with increasing velocities (up to 6 m.s^{-1}) injury severity becomes a function of the viscous response.

Mechanical thresholds for astrocyte damage, including viability and reactivity, are not fully defined. Establishing such tolerances may be beneficial in understanding the pathophysiology of trauma as a function of biomechanical parameters, and may lead to more directed therapeutic targets as well as improved preventative measures. In this study, combinations of velocity and displacement were modelled on primary rat astrocyte-seeded collagen hydrogels. There is a lack of consensus on which biomechanical parameter(s) is/are dominant in determining the severity of contusion injury *in vivo*. Velocity has been shown to primarily influence injury severity at a fixed displacement (1 mm) in a rat model (Sparrey *et al.,* 2008); Kim *et al.,* (2009) demonstrated that velocity did not influence injury severity at a fixed displacement (0.8 mm) in a mouse model. Ghasemlou *et al.,* (2005) concluded that displacement and force were important in determining injury severity, although displacement and velocity will have been inherently coupled with the IH impactor used. Other studies have shown that both velocity and displacement can be used to predict injury severity and an interaction between the two exists due to the viscoelastic properties of the spinal cord (Kearney *et al.,* 1988; Lam *et al.,* 2014). Differences in animal model, injury model (including whether displacement and velocity were decoupled), biomechanical parameters, and outcome measures used

have contributed to the difficulties in comparing studies and defining thresholds.

Input contusion displacement depth values reported in *in vivo* studies are often reported as an absolute value. Additionally, injury is commonly categorised as either mild, moderate, or severe based on a range of outcome functional and histological measures. For instance, Anderson *et al.,* (2009) classed injuries which resulted in forelimb motor deficits as mild, and injuries which resulted in complete loss of forelimb motor function as moderate. Therefore, the severity of the outcome has typically been used to inform the input mechanical parameters. The anteroposterior diameter of a rat spinal cord has been reported to be approximately 2.4 mm (Watson *et al.,* 2009). Given the values of input displacement reported in rat contusion studies, this represents an approximate percentage cord displacement range between 33% (Pearse *et al.,* 2005) and 83% (Bresnahan *et al.,* 1987). Studies by Wilcox *et al.,* (2003, 2002) used an *ex vivo* bovine model to dynamically investigate canal occlusion at velocities of $3.7 - 5.2$ m.s^{-1}. Maximum canal occlusion was found to be upwards of 80%, although the spinal cord does not occupy the entire canal volume. Due to variations in the injury location, impact tip dimensions, and animal model between studies the displacement values selected in this project were calculated as a percentage of the sample thickness. A range of displacement (25, 50, 75% gel height) and velocity (100 and 1000 mm.s^{-1}) values were selected to investigate primary astrocyte responses over a range of injury severities.

TSCI can be broadly described by the initial injury, which encompasses the mechanical injury and events that occur immediately after. This is followed by the secondary injury, a cascade of biological and biochemical reactions which attempt to remediate further damage and repair the injury (Sekhon and Fehlings, 2001). This phase can last from weeks to years in humans. A key feature is the formation of a cystic cavity and glial scar around the injury site. The glial scar is composed mainly of reactive cells, including astrocytes, microglia, fibroblasts and oligodendrocyte precursor cells (OPCs), and extracellular matrix components (Silver and Miller, 2004). Reactive astrocytes form a dense physical and chemical barrier which inhibits axonal outgrowth. Markers of astrogliosis are varied and numerous: upregulation of GFAP expression, proliferation, migration to the lesion core, alterations to astrocyte morphology including hypertrophy and ramification, and expression of neuroinhibitory molecules, such as inflammatory cytokines and CSPGs (Sofroniew, 2009; Sofroniew and Vinters, 2010). Aside from its neuroinhibitory effects, astrogliosis has been shown to be beneficial by limiting further extension of the lesion and facilitating regenerative activities, such as the secretion of neurotrophic factors. Further, genetic ablation of astrocytes or prevention of glial scar formation has been shown to impede regeneration and lead to worsened functional outcomes *in vivo* (Rolls *et al.,* 2009).

To summarise, although research is beginning to appreciate and consider injury mechanisms and biomechanics in their models, it is still unclear precisely how parameters, such as displacement, velocity and force determine injury outcomes. With the complexity of *in vivo* systems presenting varying results, it may be beneficial to

utilise a more simplified *in vitro* model to investigate how the biomechanics of injury affects individual cell populations, without confounding influences from other cell types. As a key cellular component of the lesion, primary rat cortical astrocytes were utilised in an isolated *in vitro* culture. This may provide information on the precise contributions of astrocytes to the primary and secondary pathophysiology of TSCI. As a positive astrogliosis control, transforming growth factor β-1 (TGF-β1) was selected. TGF-β1 plays a role in regulating the induction of glial scar formation (Silver and Miller, 2004; Wang *et al.,* 2018), and has been shown to induce astrogliosis *in vivo* (Logan *et al.,* 1994) and *in vitro* (Cullen *et al.,* 2007; East *et al.,* 2009; Kirk, 2018; Smith, 2016).

4.2   Aim and Objectives

The aim of this chapter was to evaluate the responses of primary astrocytes to contusion injury, using a range of displacement and velocity parameters representing different injury severities.

The specific objectives were as follows:

I. Verify the accuracy and precision of the BOSE 5110 Electroforce BioDynamic (BOSE) at simulating contusion injury at velocities of 100 and 1000 mm.s^{-1} and displacement depths of 25, 50, and 75% using primary astrocyte-seeded hydrogels.

II. Calculate the kinetic outputs following simulated injury using the BOSE apparatus, including the impact velocity, peak displacement, peak load, and energy applied.

III. Measure the responses of primary astrocytes to contusion injury through GFAP immunostaining, CSPG expression, metabolic activity and viability analyses.

IV. Compare the biological responses of primary astrocytes to contusion injury against a known chemical inducer of astrogliosis, TGF-β1.

V. Evaluate the effects of contusion injury mechanics on astrocyte responses.

The null hypotheses postulated for the study were as follows:

I. There is no statistical difference between the reactivity of astrocytes in response to contusion injury compared to no injury (control).

II. There is no statistically significant relationship between injury velocity and astrocyte reactivity.

III. There is no statistically significant relationship between injury displacement depth and astrocyte reactivity.

IV. There is no statistically significant relationship between astrocyte reactivity and time.

4.3 Specific Materials and Methods

4.3.1 BOSE Waveform Setup and Data Acquisition

For details on the assembly and set up of the BOSE apparatus, refer to Chapter 2 (Section 2.5.8). The parameters for contusion injury, including the input displacements, velocities, and PID values were developed in Chapter 3, and defined in Table 3.3. The waveform regime, defined to represent a contusion injury, was set up using the parameters in the following steps:

1. **Dwell:** 10 ms

2. **Ramp:**

   (a) Velocity: 100 or 1000 mm.s^{-1}.

   (b) Displacement: 25, 50, or 75% of gel height.

3. **Dwell**: 100 ms

4. **Ramp:**

   (a) Velocity: 100 or 1000 mm.s^{-1}.

   (b) Displacement: Return to 0% of gel height.

Following this, the following data was exported into Excel: time (s), experimental displacement (mm), axial command (input displacement, mm), load (N).

The data acquisition settings were as follows:

- Scan time = 0.4096 s.

- Number of scan points = 2048.

- Number of scans = 1.

4.3.2 Calculation of Energy Applied

The energy applied, or work done, is a measure of energy transfer: when an external force moves an object through a distance, energy is transferred from one store to another. For work done by a constant force, this is defined as:

$$Work\ done\ (J) = F \times d \tag{4.1}$$

where F = force (N) and d = distance (m).

In this study, a variable force was observed during the contusion event. Therefore, the energy applied was calculated by performing a trapezoidal integration of the area underneath the load-displacement curve for each sample, using the following equation:

$$Work\ done\ (mJ) = \frac{1}{2} \sum_{t_I}^{t_i} (x_{i+1} - x_i)(y_{i+1} + y_i) \tag{4.2}$$

where x = displacement and y = load. The experimental displacement and load values plugged into the equation were derived from the moment of impact (t_I), until the end of the dwell step (t_i).

4.3.3   Preparation of astrocyte-seeded hydrogels

Hydrogels seeded with 5 x 10^5 primary rat astrocytes per mL of gel were prepared, as described in Chapter 2 (Section 2.5.5). Gels were incubated at 37 °C, 8% CO_2:92% air for 24 hours prior to experimentation. TGF-β1 treatment was used as a positive astrogliosis control. For these gels, complete cell culture medium supplemented with TGF-β1 (10 ng.mL^{-1}) and pipetted on top of the gels, refreshing every two days.

4.3.4   Immunohistochemical Staining

Astrocyte-seeded hydrogels were processed for immunofluorescent staining using the methods described in Chapter 2 (Section 2.5.7). Primary antibodies specific for glial fibrillary acidic protein (GFAP) and chondroitin sulfate proteoglycan (CS-56) were used to label astrocytes and CSPGs, respectively, and DAPI was used as a nuclear counterstain. Details of the antibodies used, including their dilutions are described in Table 2.1 (Chapter 2 Section 2.4). Hydrogels were incubated with isotype control antibodies, and omission of the primary antibodies was routinely used as the negative control.

4.3.5   Confocal Image Acquisition

Confocal z-stack images were acquired using a Zeiss LSM880 Axio Imager.Z2 upright microscope (Chapter 2 Section 2.5.9.3). A total of five fields of view were acquired for each gel (Figure 4.1).
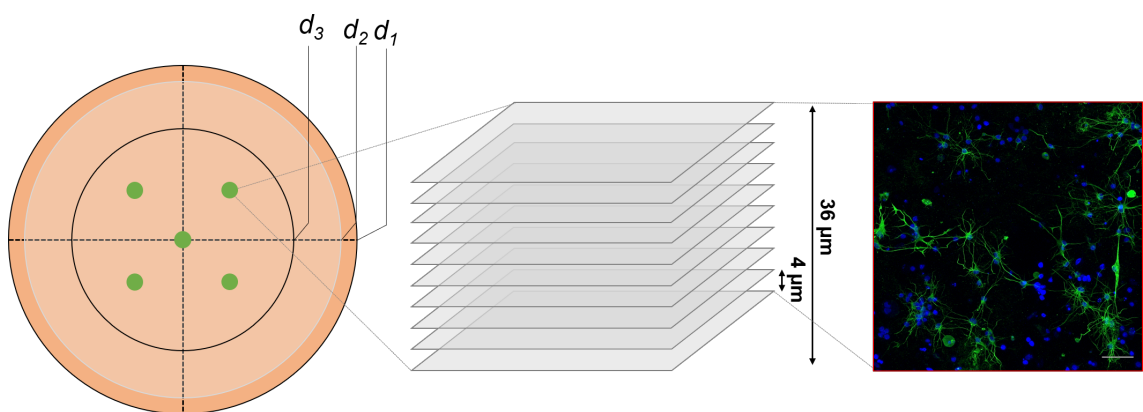
Figure 4.1: Image acquisition locations of a hydrogel following experimental contusion injury. Five fields of view were imaged per gel, with images acquired from the same five positions, as denoted by the green dots. d_1 = diameter of the gel, 11 mm; d_2 = diameter of the impact area, 10 mm; d_3 = outer edge of the imaging region, with diameter 7 mm. At each imaging position, a 36 µm z-stack was acquired, composed of 10 z-slices at 4 µm intervals. Confocal images presented in this report are maximum intensity projections.

The surface of the gel was located, as defined by the z-position in which the cells first became visible. Each z-stack was 36 µm in depth, with 10 slices acquired at 4 µm intervals. To ensure consistency in image acquisition, the laser settings were configured for the sample with the greatest GFAP expression. Confocal images of cell-seeded hydrogels presented in this study are maximum intensity projections generated from their respective stacks.

4.3.6   Image Analysis

4.3.6.1   Volume of GFAP Expressed Per Cell

For three-dimensional analysis of astrocyte GFAP volume the .czi files were loaded into the Volocity 3D Image Analysis Software (Volocity). The objects (cells) were located in the GFAP channel and an automatic threshold was used. A minimum object size limit was set to 100 μm^3, which excluded objects below this volume threshold. The objects were pseudo-coloured as a rainbow to visualise the individual objects. The volume measurement was selected to calculate the total volume of GFAP expressed per cell, from which the mean volume of GFAP per cell was calculated.

4.3.6.2   Shape Factor – Sphericity of Astrocytes

The shape factor of the astrocytes with and without injury were measured using Volocity, following the same protocol as in 4.3.6.1 to locate the objects. The shape factor measurement was selected to be measured. Shape factor is a dimensionless numerical indication of the shape of an object and, in this study, describes how similar a 3D object is to a sphere (sphericity). A value of 1 describes a perfect sphere, with decreasing values indicating more irregular shapes. Sphericity is defined as the ratio of the surface area of a sphere- with the same volume as the given object- to the surface area of the object, first described by Wadell (1935):

$$Sphericity, \ \Psi = \frac{\pi^{\frac{1}{3}}(6V_0)^{\frac{2}{3}}}{A_0} \tag{4.3}$$

where A_0 = object area and V_0 = object volume.

4.3.6.3   Chondroitin Sulfate Proteoglycan Expression

The total area of CSPG expression was measured using the Fiji Is Just ImageJ (FIJI) image analysis software, together with a macro to run automatic analysis. Each fluorescent multi-channel confocal image file (.czi) was exported as TIFFs into their separate fluorophore channels: GFAP (green channel), CS-56 (red channel), and DAPI (blue channel). The CSPG image files were then imported into FIJI and converted into 8-bit images. The Phansalkar Auto Local Threshold method was used to binarise the images and distinguish cells from the background. The total area of CSPG expression was then measured.

4.3.7 Analysis of Astrocyte Viability

Viability of the astrocytes following simulated contusion injury was assessed using the LIVE/DEAD™Viability/Cytotoxicity Assay Kit. The live/dead solution was prepared according to Chapter 2 (Section 2.5.3.6) and handled under dark working conditions. The positive cell death control consisted of cell-seeded gels treated with 70% (v/v) methanol for one hour. After aspirating the cell culture medium, the gels were washed twice with 600 µL PBS to remove residual esterase activity from the complete cell culture medium (methanol from positive control samples). A volume of live/dead solution twice that of the gel (i.e. 600 µL) was pipetted on top of each gel. The plate was then covered with foil and incubated for 1 hour on an orbital shaker (90 rpm), at 37 °C, 8% CO_2:92% air. The live/dead solution was then discarded and 3x 5 minute PBS washes were performed at 37 °C, on an orbital shaker (90 rpm). The cells were imaged using confocal microscopy, and percentage viability was calculated using the following formula:

$$Viability\ (\%) = \frac{\#\ \text{viable cells}}{\#\ \text{viable cells} + \#\ \text{dead cells}} \times 100 \tag{4.4}$$

4.3.8 Quantification of Astrocyte Metabolic Activity

Metabolic activity of astrocytes following simulated contusion injury was performed using the ATPlite™Luminescence Assay System, with the methods described in Chapter 2 (Section 2.5.6). The cell culture medium was aspirated from each gel and replaced with mammalian cell lysis solution at a volume twice that of the gel (600 µL). The gels were incubated at room temperature for 30 minutes, with agitation at 700 rpm to lyse the cells and release the ATP. Working under dark conditions, a volume of 50 µL from each sample was transferred to an individual well of a 96-well Optiplate™. An equal volume of substrate solution was then added to each well. The plate was sealed, covered with foil, and incubated at room temperature for 15 minutes with agitation at 700 rpm. The plate was then placed into the plate reader spectrophotometer and dark adapted for 10 minutes. Luminescence was measured at 570 nm, with the data being exported into Excel for analysis. The positive cell death control consisted of cell-seeded gels treated with 70% (v/v) methanol for one hour.

4.3.9 Collagenase Treatment of Astrocyte-Seeded Hydrogels

Astrocyte-seeded hydrogels were treated with collagenase in order to digest the collagen and recover the cells for analysis of GFAP expression in 2D. A stock solution of collagenase, at 0.2% (w/v), was prepared by reconstituting 20 mg collagenase powder into 10 mL DMEM. The solution was filter sterilised and aliquoted into 2 mL volumes. The solution was stored at -20 °C, for up to one year. The cell culture medium was aspirated and replaced with 0.2% (w/v) collagenase solution, at a volume twice that of the gel (600 µL). The gels were incubated for 15 minutes, at 37 °C 8% CO_2:92% air. Following this, the cell solution was gently triturated to evenly suspend the cells and plated onto PDL-coated glass coverslips. The coverslips were incubated for 30 minutes, at 37 °C to enable cell attachment, before overlaying with complete DMEM cell culture medium.

4.3.10 Digestion of CSPGs with Chondroitinase ABC

Chondroitinase ABC (ChABC) is an enzyme derived from the bacterium *Proteus vulgaris*, and has been shown to create a more permissive environment for neuroregeneration by degrading CSPGs deposited by reactive astrocytes following SCI (Bradbury *et al.*, 2002). ChABC catalyses the degradation of chondroitin sulfate and dermatan sulfate chains of proteoglycan molecules (chondroitin-4-sulfate, chondroitin-6-sulfate, dermatan sulfate), with some hyaluronidase activity (Prabhakar *et al.*, 2005). A stock solution of ChABC (10 U.mL^{-1}) was prepared by reconstituting 5 µg ChABC powder in 500 µL PBS. Aliquots of 50 µL were prepared and stored at -20 °C, for up to 3 years. A working concentration used in this study was 200 mU and was prepared by diluting the required volume of stock ChABC solution in complete cell culture medium (DMEM).

Astrocyte-seeded hydrogels (5 x 10^5 cells.mL^{-1}) subjected to contusion injury at 100 mm.s^{-1} were incubated for 14 days. Following this, the cell culture medium was aspirated and replaced with complete cell culture medium supplemented with ChABC, at a volume twice that of the gel (600 µL). The gels were incubated for 4 hours at 37 °C, 8% CO$_2$:92% air. After 4 hours, the media was aspirated and 3x 5 minute PBS washes were performed at 37 °C. Complete cell culture medium was pipetted on top of the gels and incubated for a further 48 hours before fixing for immunohistochemical analysis using antibodies against GFAP and CS-56 (Section 5.3.3).

4.3.11 Evaluation of Cytokine Expression using an Enzyme-Linked Immunosorbent Assay

One of the objectives of the study was to evaluate the expression of several pro- and anti-inflammatory cytokines known to be released by reactive astrocytes following SCI, including IL-6, IL-10, TNF-α, and IL-1β. The first cytokine to be evaluated was IL-6, using an enzyme-linked immunosorbent assay (ELISA). The reagents were prepared according to the manufacturer's instruction (Table 4.1).

Table 4.1: Preparation of reagents for the Rat IL-6 DuoSet ELISA assay.

Reagent	Working Concentration	Diluent
Capture Ab	4.00 ug.mL^{-1}	PBS
Detection Ab	100 ng.mL^{-1}	Reagent Diluent with 2% (v/v) NGS
IL-6 Standard	125 - 8000 pg.ml^{-1}	Reagent Diluent
Streptavidin-HRP	1:200	Reagent Diluent
Substrate Solution	1:1	Colour Reagent A: Colour Reagent B

Reagent diluent = 1% BSA in PBS; NGS = normal goat serum; Colour Reagent A = H$_2$O$_2$; Colour Reagent B = tetramethylbenzidine

All incubation steps were performed at room temperature. A 96-well plate was coated with 100 µL of the Capture Antibody, sealed, then incubated overnight. The solution was

then aspirated and washed three times with 400 uL wash buffer (0.05% v/v Tween 20 in PBS) per well. The plate was blotted onto a paper towel to remove residual solution. Blocking was performed by adding 300 uL of Reagent Diluent to each well and incubating the plate for 1 hour. The solution was then aspirated and three wash steps performed as before. A volume of 100 uL of sample or standard was then added to each well, the plate sealed, then incubated for two hours. The aspiration/wash step was then performed. A volume of 100 uL of Detection Antibody was added to each well, sealed, then incubated for two hours. The aspiration/wash step was then performed and 100 uL of Streptavidin-HRP added to each well. The plate was covered and incubated for 20 minutes, followed by the aspiration/wash step. A volume of 100 uL of Substrate Solution was then added to each well then incubated for 20 minutes. A volume of 50 uL of Stop Solution (2 N H_2SO_4) was then added to each well and the plate gently tapped against a surface to ensure proper mixing. The optical density of each well was determined at 450 nm using a plate reader.

4.4   Results

Contusion SCI was modelled *in vitro* using input velocities of 100 and 1000 mm.s^{-1}, and displacement depths of 25, 50, and 75% of the height of the gel. Time (s), experimental displacement (mm), axial command (input displacement, mm), and load (N) data was recorded by the BOSE and exported to Excel for data processing. At Days 1, 7, and 14 after injury, the gels were processed in order to investigate a number of astrocyte responses: cell viability by live/dead staining, metabolic activity using the ATPlite assay, astrocyte reactivity by immunostaining for GFAP, and expression of CSPGs by immunolabelling with a CS-56 antibody. Attempts were made at quantifying the concentrations of known pro- and anti-inflammatory cytokines in the cell culture medium: IL-6, IL-10, and IL-1β, using an ELISA assay. However, the concentration of analyte was not sufficient to be detectable by the assay at the timepoints used in this study.

4.4.1   Kinetic Outputs

Using the data recorded by the BOSE, additional kinetic outputs were calculated: the peak experimental displacement (mm), impact velocity (mm.s^{-1}), peak velocity (mm.s^{-1}), peak load (N), and energy applied (mJ) (Appendix D; Table 6.10). Impact velocity was determined as the velocity at which the upper load platen first came into contact with the surface of the gel, and the peak velocity was the greatest velocity value that was recorded.

There was little variation in the peak experimental displacement achieved at all displacement depths as demonstrated by the small errors (Figure 4.2). The error was also similar at both input velocities. The peak displacement achieved was expected to be the same at each input displacement depth, regardless of input velocity. There was slight variation in the peak displacement achieved when comparing the same displacement depth across both velocities. For instance, the mean peak displacement achieved at 50% was 0.770 ± 0.01 and 0.737 ± 0.02 mm at 100 and 1000 mm.s^{-1}, respectively. However, statistical analysis showed there was no significant differences at all displacement depths

(p>0.05).   Thus, displacement depth was achieved consistently across both input velocities.
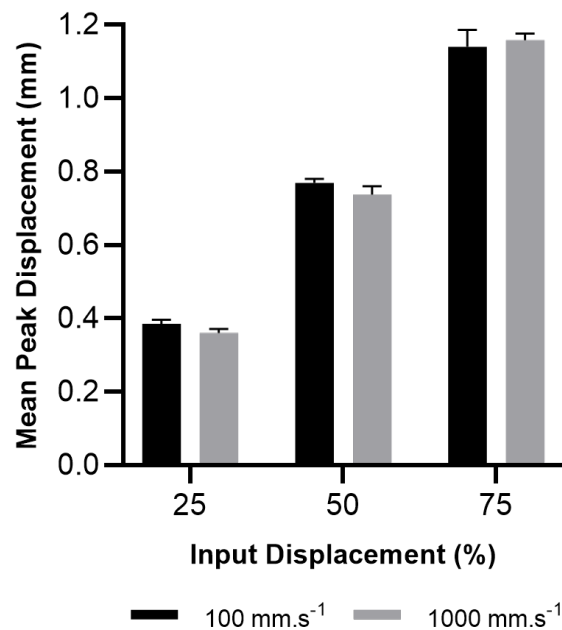
Figure 4.2: Peak experimental displacement achieved at input velocities of 100 and 1000 mm.s^{-1}. Astrocyte-seeded hydrogels were subjected to contusion injury at varying input velocities and displacement depths (calculated as a percentage of the total height of the gel), with the peak displacement calculated. Data presented as the mean ± SEM and analysed by two-way ANOVA with Tukey's post-hoc test. Significance levels * p<0.05. N = 12 per condition.

Greater variation was observed in the impact velocity measurements compared to peak displacement, with larger errors. At both 100 and 1000 mm.s^{-1}, there was an undershoot in velocity at the point of impact (Figure 4.3). Further, the peak velocity was achieved prior to the peak displacement being achieved. The extent of undershoot was greater at an input velocity of 1000 mm.s^{-1}, where a mean impact velocity of 669.31 mm.s^{-1} was achieved across all displacement depths (Figure 4.4). The mean impact velocity achieved across all displacement depths, with an input of 100 mm.s^{-1}, was 97.64 mm.s^{-1}.
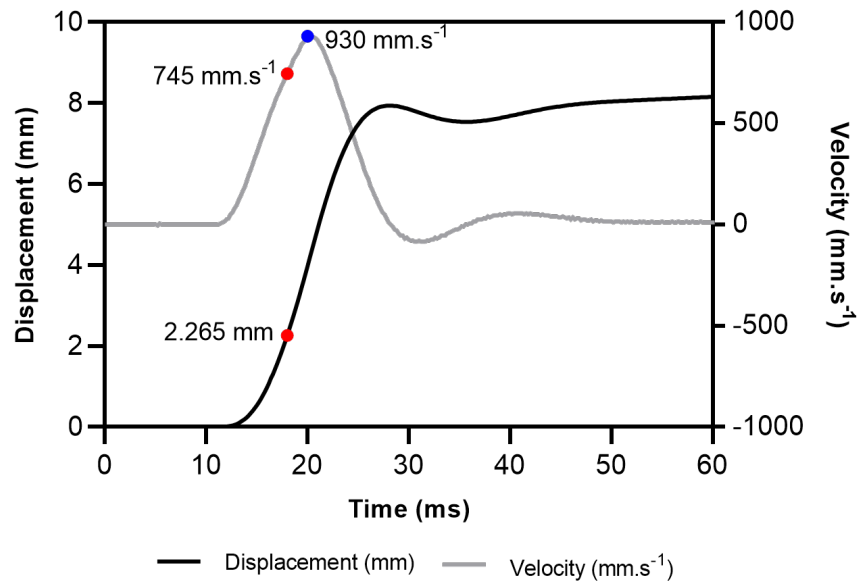
Figure 4.3: The impact velocity is lower than the peak velocity in an example of experimental contusion injury at 1000 mm.s^{-1} to 25% displacement. Example profile of a contusion experiment with the impact velocity and corresponding displacement (red circles) and peak velocity (blue circle) depicted.

A

B
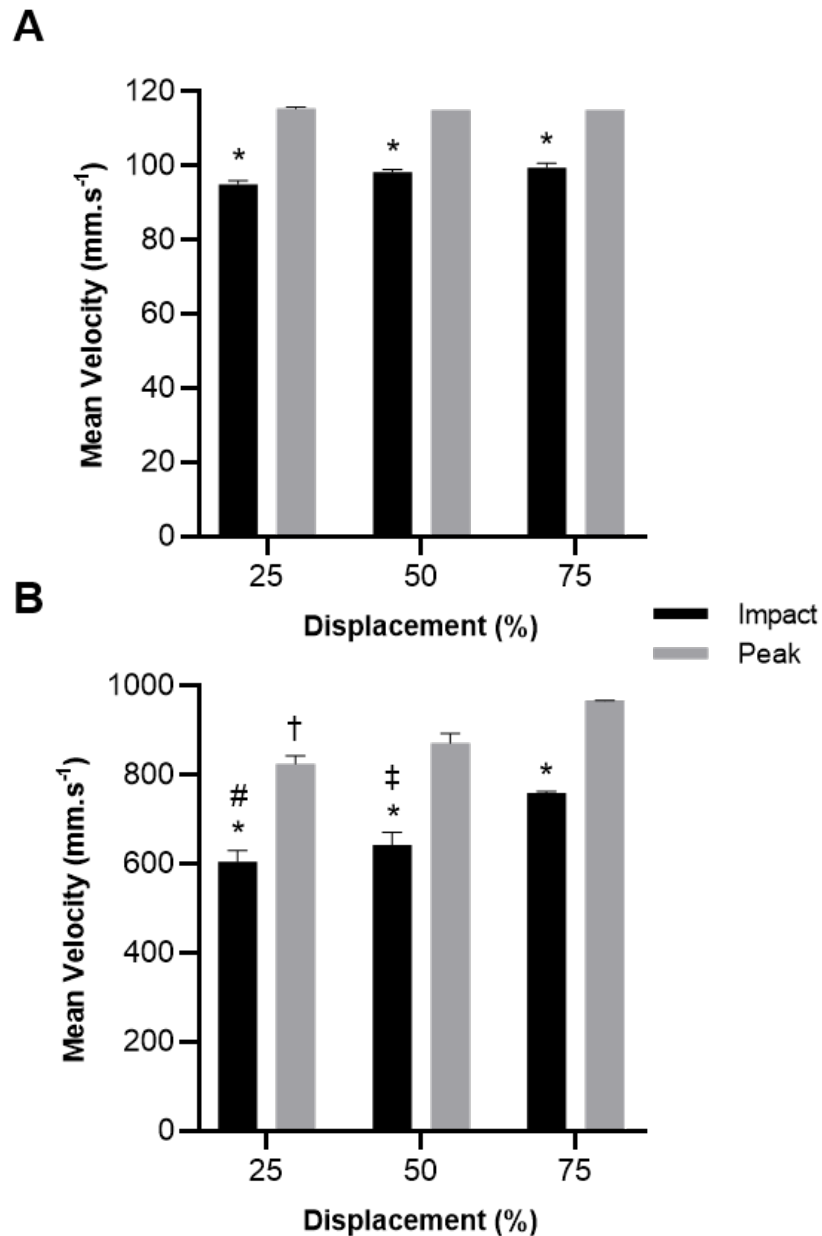
Figure 4.4: Impact vs. peak velocity following simulated contusion injury. 100 mm.s^{-1} (A) and 1000 mm.s^{-1} (B). Data presented as the mean $\pm$ SEM and analysed by two-way ANOVA with Tukey post-hoc test. Significance levels * $p<0.05$ (impact vs peak at each displacement depth); # $p<0.05$ (25 vs 75% impact velocity); ‡ $p<0.05$ (50 vs 75% impact velocity); † $p<0.05$ (25 vs 75% peak velocity). N = 12 per condition.

At an input velocity of 100 mm.s^{-1}, there was no significant difference in the impact or peak velocity achieved across the displacement depths (Figure 4.4A). However, at an input velocity of 1000 mm.s^{-1}, there was a significant difference in impact velocity between 25 and 75% and 50 and 75% displacement depths (Figure 4.4B). Further, the peak velocity at 25% displacement was significantly lower than the peak velocity at 75% displacement. Therefore, inconsistent impact and peak velocities were achieved at 1000 mm.s^{-1}. The peak velocities achieved were significantly greater than the impact velocities achieved, under all conditions. The mean peak velocity across all displacement depths was 115.14 and 887.92 mm.s^{-1} at input velocities of 100 and 1000 mm.s^{-1}, respectively.

An increase in displacement resulted in an increase in the peak load measured, and increasing the input velocity to 1000 mm.s^{-1} resulted in a further increase in the peak loads measured across all displacement depths (Appendix D; Table 6.10). As such, the calculated energy applied followed the same trend (Figure 4.5).
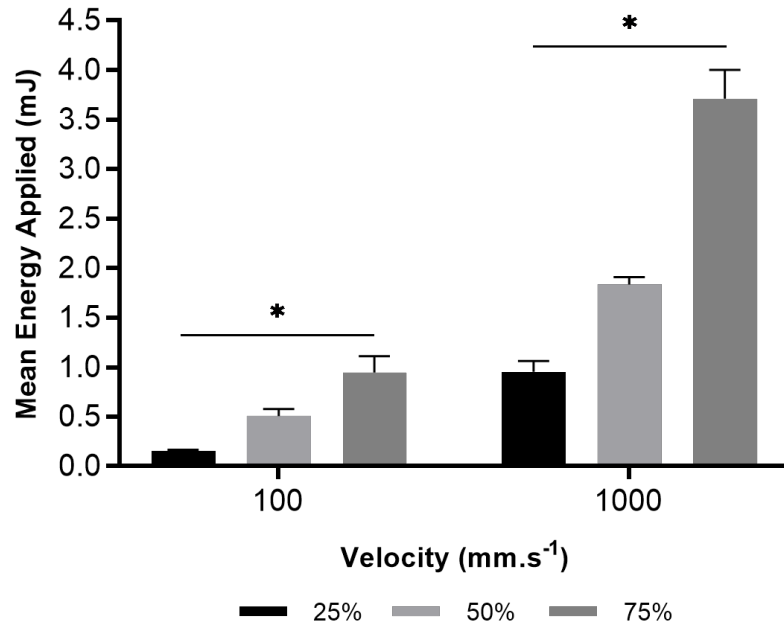
Figure 4.5: Mean energy applied scales with velocity and displacement depth. Rat tail type-I collagen hydrogels (2 mg.mL^{-1}; 300 µL; 11 mm) were seeded with primary rat cortical astrocytes at 5 x 10^5 cells.ml^{-1} gel and subjected to contusion injury. Energy applied was calculated by performing a trapezoidal integration of the area under the curve of the load-displacement curves. Data presented as the mean ± SEM and analysed by two-way ANOVA with Tukey's post-hoc test. Significance levels * $p < 0.05$. N = 12 per condition.

At each input velocity group, there was a significant increase in the mean energy applied with increasing displacement depth. The mean energy applied increased from 0.150 ± 0.008 to 0.945 ± 0.08 mJ at 100 mm.s^{-1}, and from 0.954 ± 0.05 to 3.709 ± 0.1 mJ at 1000 mm.s^{-1}. At each displacement depth, the mean energy applied was significantly greater at an input velocity of 1000 mm.s^{-1}, compared to 100 mm.s^{-1}. Comparison of the energy applied across both input velocities and displacement depths showed that there was no significant difference between the following conditions: 100 mm.s^{-1} – 75% displacement, and 1000 mm.s^{-1} – 25% displacement ($p > 0.05$), with mean energy applied values of 0.945 ± 0.08 and 0.954 ± 0.05 mJ, respectively.

4.4.2 Primary Astrocyte Behaviour Following a Contusion Injury

Astrocytes respond to mechanical trauma through a vast number of morphological, biochemical, transcriptional, physiological, and functional changes across a spectrum of severity and time, in a process called astrogliosis. Hypertrophy and ramification of processes are common morphological features of reactive astrocytes, which was evaluated by immunostaining for glial fibrillary acidic protein (GFAP), a cytoskeletal protein also

known to be upregulated following injury.

4.4.2.1   GFAP Expression and Gross Morphology

Figure 4.6 illustrates representative images of GFAP stained astrocytes in hydrogels following simulated contusion at 100 mm.s^{-1}, over a 14 day time period. Quantification of the mean volume of GFAP expressed per cell was also performed (Figure 4.7). For details of the individual values, refer to Appendix D (Table 6.11). Under control conditions (no injury), few astrocytes were GFAP-positive, as shown by the majority of nuclei not being co-stained with GFAP. Morphologically, the GFAP-positive cells were small and rounded with fewer processes. Astrocytes in the control group represented the group with the lowest mean volume of of GFAP expressed per cell, across the 14 day time period: 427.67 $\pm$ 40 µm^3 (Day 1), 873.93 $\pm$ 30 µm^3 (Day 7), and 867.08 $\pm$ 50 µm^3 (Day 14). However, GFAP volume did significantly increase between Day 1 and 7, but not between Day 7 and 14.

Upon application of mechanical contusion injury, a progressive change in morphology was observed, which also resulted in differences in the mean GFAP volume per cell. At 25% displacement, the mean volume of GFAP expressed per cell was significantly greater than the control on Day 1 post-injury (mean 758.73 $\pm$ 40 µm^3), but not on Days 7 and 14. Over 14 days, GFAP volume at 25% was only significantly different between Days 1 and 14, with the greatest GFAP volume expressed on Day 14 (1064.99 $\pm$ 80 µm^3). The morphology of the GFAP-positive astrocytes at 25% displacement were similar to those in the control group, with some astrocytes beginning to possess processes.

At 50% displacement, the mean volume of GFAP expressed per cell was significantly greater than the control at all timepoints. GFAP volume significantly increased between Days 1 and 7, but not between Days 7 and 14, with the greatest GFAP volume expressed on Day 7 (1452.23 $\pm$ 80 µm^3). Morphologically, the GFAP-positive astrocytes appeared less rounded in shape compared to the control astrocytes, and ramification was observed on Day 1 and increasing with time. On Day 14 post-injury, interdigitation of the processes was observed.

At 75% displacement, the mean volume of GFAP expressed per cell was significantly greater than the control at all timepoints. There was a significant increase in GFAP volume per cell between Days 1 and 7, and Days 7 and 14 post-injury, with the greatest GFAP volume expressed on Day 14 (1834.90 $\pm$ 100 µm^3). Morphologically, evidence of reactive gliosis was observed from Day 1 post-injury, with the cells appearing larger, with many processes developing at Day 7 and 14. An increase in the density of the overlapping domains was observed (Figure 4.6; inset at Day 7 – 75% displacement).

TGF-β1 treatment did result in an astrogliosis response, as expected. The mean GFAP volume of cells in these gels were significantly greater than the respective control groups at each time point. On Day 1 post-injury, TGF-β1 treatment was not significantly different

from the experimental contusion injury groups. On Day 7 post-injury, TGF-β1 treatment resulted in a significantly higher mean GFAP volume compared to 25% but not 50 and 75%. On Day 14 post-injury, TGF-β1 treatment resulted in significantly higher GFAP volume than 25 and 50%, but not 75% contusion displacement. Within the TGF-β1 treatment group, there was a significant step-wise increase in GFAP volume as time progressed.
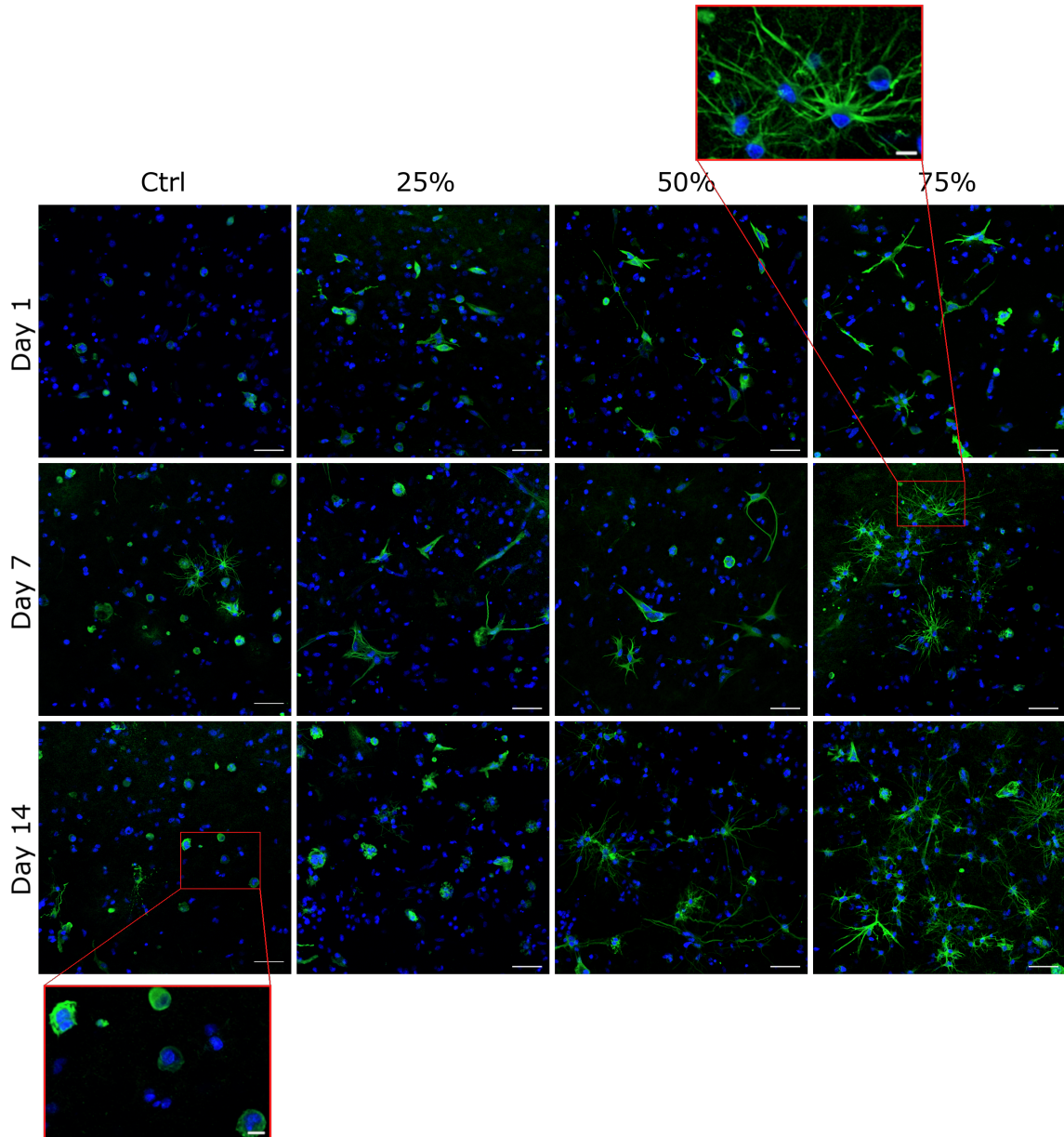
Figure 4.6: Mechanical contusion injury at 100 mm.s^{-1} induces astrogliosis which progresses over 14 days. Representative immunofluorescent maximum intensity projection images of primary rat cortical astrocyte-seeded hydrogels (5 x 10^5 cells.mL^{-1}) and subjected to contusion injury. Cells were labelled with a polyclonal antibody against GFAP (astrocytes, green) and counterstained with DAPI (nuclei, blue). 36 µm depth. Scale bar represents 50 µm. Scale bar of inset images represents 10 µm.

Only on Day 14 post-injury was there a step-wise significant increase in GFAP volume per cell with a corresponding increase in displacement depth. On Day 1 post-injury, there was no significant difference in GFAP volume per cell between any of the displacement depths. On Day 7, there was a significant increase in GFAP volume per cell from 25 and 50% and 25 and 75%, with no significant difference between 50 and 75%. A contusion

displacement depth of 75% resulted in the greatest volume of GFAP being expressed per cell at each timepoint. Overall, the condition which resulted in the greatest GFAP volume expression per cell was 75% on Day 14 post-injury, with a mean of 1834.90 $\pm$ 100 μm^3.
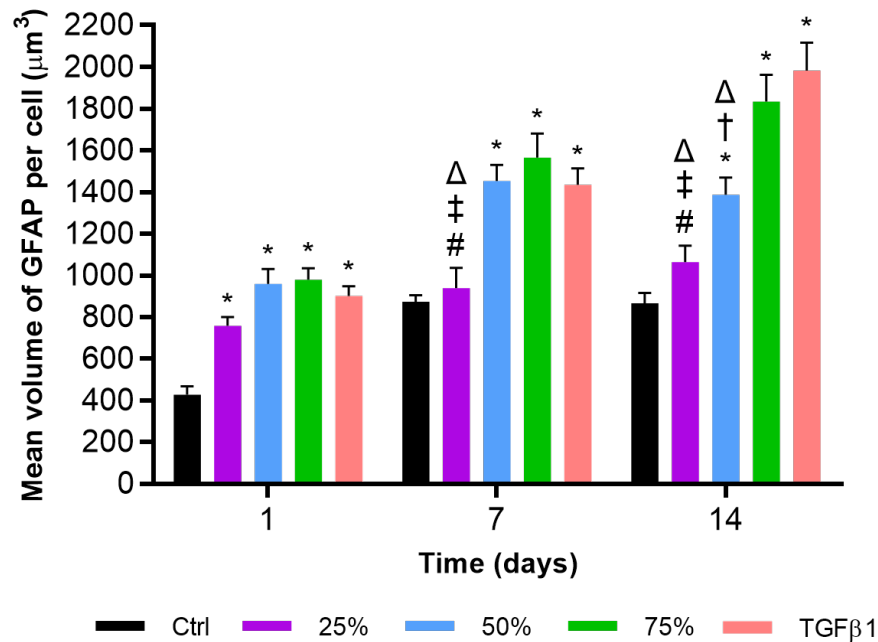
Figure 4.7: Volume of GFAP measured over 14 days following simulated contusion at 100 mm.s^{-1}. Rat tail type-I collagen hydrogels (2 mg.mL^{-1}; 300 µL; 11 mm) were seeded with primary rat cortical astrocytes at 5 x 10^5 cells.ml^{-1} gel and subjected to contusion injury. The 3D volume of GFAP expression per cell was measured using Volocity. Data presented as the mean $\pm$ SEM and analysed by two-way ANOVA. Significance levels * p<0.05 (vs. control, Dunnett's post-hoc); # p<0.05 (25% vs. 50%, Tukey's post-hoc); † p<0.05 (50% vs. 75%, Tukey's post-hoc); ‡ p<0.05 (25% vs. 75%, Tukey's post-hoc); Δ p<0.05 (vs. TGF-β1, Tukey's post-hoc). N=3.

Contusion injury was also modelled at an input velocity of 1000 mm.s^{-1}. Figure 4.8 illustrates representative images of GFAP stained astrocytes in hydrogels following simulated contusion at 1000 mm.s^{-1}, over a 14 day time period. Quantification of the mean volume of GFAP expressed per cell was also performed (Figure 4.9). For details of the individual values, refer to Appendix D (Table 6.11). In agreement with the immunohistochemical analysis of astrocytes following contusion injury at 100 mm.s^{-1}, mechanical injury at 1000 mm.s^{-1} also induced an astrogliosis response, compared to the control. However, a more prominent response was observed at an earlier time point, and at a lower displacement depth.

The morphology of astrocytes in the control group remained similar over the 14 day period: most of the GFAP-positive astrocytes were small and rounded in shape, with little observation of ramification. This contrasts with the morphology of astrocytes from the experimental groups. Hypertrophy and ramification was observed in all conditions, and from as early as Day 1 post-injury. A contrasting morphological observation was made between the two injury velocities at 25% displacement on Day 1 post-injury. At 100 mm.s^{-1}, the GFAP-positive astrocytes were hypertrophied but did not exhibit many

processes, with a mean GFAP volume per cell of 758.73 ± 40 µm^3. At 1000 mm.s^{-1}, both hypertrophy and ramification was observed, with a mean GFAP volume per cell of 2455.26 $\pm$ 200 µm^3.
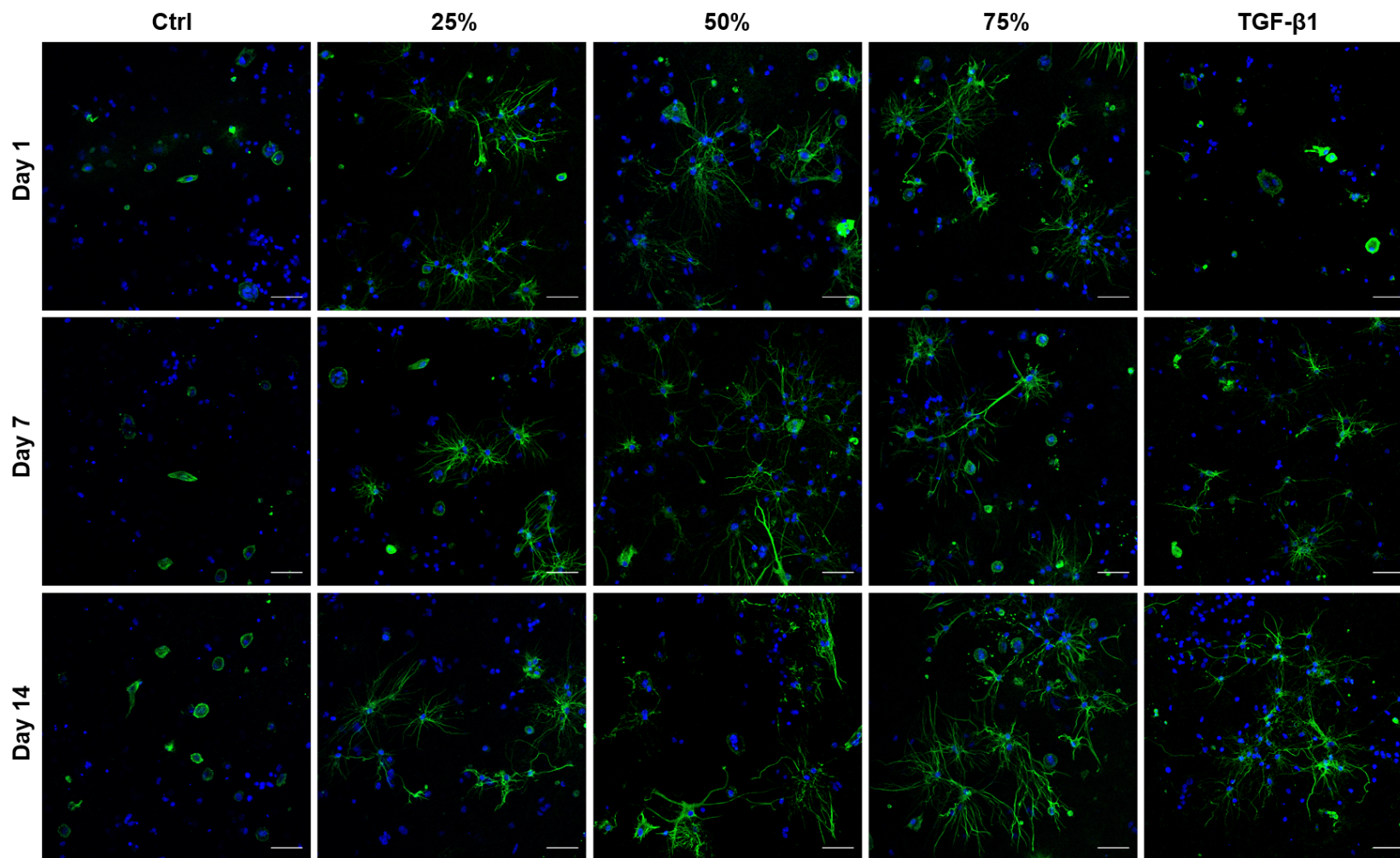
Figure 4.8: Mechanical contusion injury at 1000 mm.s^{-1} induces an astrogliosis response from as early as Day 1 post-injury. Representative immunofluorescent maximum intensity projection images of primary rat cortical astrocyte-seeded hydrogels (5 x 10^5 cells.mL^{-1}) and subjected to contusion injury. TGF-β1 (10 ng.mL^{-1}) was used as a positive astrogliosis control. Cells were labelled with a polyclonal antibody against GFAP (astrocytes, green) and counterstained with DAPI (nuclei, blue). 36 µm depth. Scale bar represents 50 µm.
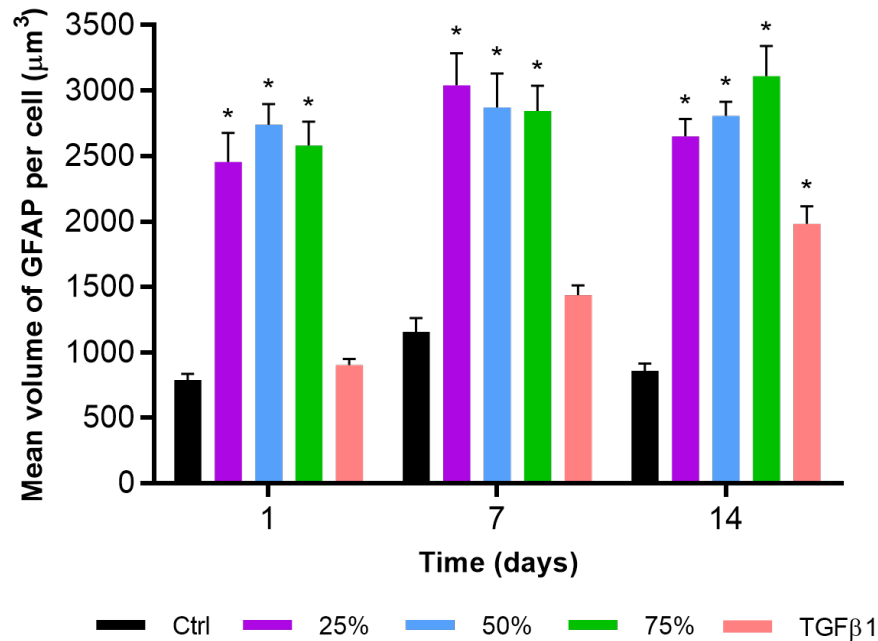
Figure 4.9: Astrocytes appear to respond in a binary manner to contusion injury at 1000 mm.s^{-1}. Rat tail type-I collagen hydrogels (2 mg.mL^{-1}; 300 µL; 11 mm) were seeded with primary rat cortical astrocytes at 5 x 10^5 cells.ml^{-1} gel and subjected to contusion injury. The 3D volume of GFAP expression per cell was measured using Volocity. Data presented as the mean $\pm$ SEM and analysed by two-way ANOVA. All experimental contusion groups were significantly greater than the TGF-β1 group (Tukey's post-hoc, p<0.05). Significance levels * p<0.05 (vs. control, Dunnett's post hoc). N=3.

Astrocytes in the experimental groups expressed significantly greater volumes of GFAP per cell than those in the control group, at all displacement depths and across all timepoints. The mean GFAP volume expressed per cell for the control group was 930.13 µm^3, across the 14 day time period. At a fixed time point, there was no significant difference in the volume of GFAP expressed per cell between the three displacement depths (p>0.05), with means of 2591.21 $\pm$ 100, 2919.12 $\pm$ 100, and 2857.40 $\pm$ 100 µm^3 at Days 1, 7, and 14 post-injury, respectively. Further, at a fixed displacement depth, there was no significant difference in the mean GFAP volume expressed per cell across the 14 day time period. TGF-β1 treatment was significantly greater than the control group on Day 14, but was significantly lower than the experimental contusion injury groups, at all timepoints.

Comparison of the volume of GFAP expression per cell for both input velocities showed that increasing the input velocity to 1000 mm.s^{-1} resulted in a more severe reactive astrogliosis response, as measured morphologically. The mean volume of GFAP expressed per cell was significantly higher at 1000 mm.s^{-1} compared to 100 mm.s^{-1}, at all displacement depths and timepoints. At each timepoint, there was no significant difference between the control groups at both input velocities. On Day 1 post-injury, there was an approximate 2.8-fold increase in the mean GFAP volume across all displacement depths, as input velocity was increased from 100 to 1000 mm.s^{-1}. Similarly, an increase in velocity to 1000 mm.s^{-1} resulted in a 2.2-fold and 2.0-fold

increase at Day 7 and 14, respectively.

4.4.2.2 Sphericity

Sphericity was another morphological feature which was analysed in astrocytes, since the progression of non-injured astrocytes to activated astrocytes is characterised by an increase in ramification of processes. An increase in ramification is associated with a decrease in sphericity, thus this measure was used as another indication of astrogliosis. Figure 4.10 illustrates the sphericity of astrocytes, following simulated contusion at 100 and 1000 mm.s^{-1}, over a 14 day time period.

At 100 mm.s, there was no significant difference in mean sphericity between the experimental and control groups on Day 1 post-injury (Figure 4.10A). On Day 7, the mean sphericity of the 50 and 75% displacement and TGF-β1 groups was significantly lower than the control, with means of 0.27 ± 0.01 AU, 0.30 ± 0.01 AU and 0.25 ± 0.01 AU, respectively. Similarly, the mean sphericity of these same three groups was significantly lower than the control on Day 14 post-injury, with means of 0.27 ± 0.01 AU and 0.27 ± 0.01 AU and 0.28 ± 0.01 AU, respectively. Evaluating the change in sphericity at a fixed displacement depth over time, there was a significant decrease in sphericity between Days 1 and 14 in the control group suggesting a potential increase in the reactivity of astrocytes in this group. In all test groups, there was a significant decrease in sphericity between Days 1 and 7, and Days 1 and 14 post-injury.

At 1000 mm.s^{-1}, the mean sphericity of all displacement groups was significantly lower than the control, at each timepoint (Figure 4.10B). On Day 1 post-injury, increasing displacement depth did not significantly affect the sphericity of astrocytes. The mean sphericity across the displacement depths was 0.26 ± 0.01 AU, compared to a mean of 0.39 ± 0.02 AU in the control group. Similarly, increasing displacement depth did not significantly affect the sphericity of astrocytes on Day 7 and 14, with means of 0.23 ± 0.008 AU and 0.21 ± 0.007 AU (grouped displacement). Over time, the sphericity of astrocytes in the control group significantly decreased between Days 1 and 14 (from a mean of 0.39 to 0.32 AU), although remained significantly higher than the experimental groups. There was no significant change in sphericity over time, at 25% displacement. At 50%, there was a significant reduction in sphericity between Days 1 and 7, followed by no further significant change between Days 7 and 14. At 75%, there was a trend of decreasing sphericity over time, but was only significant between Days 1 and 14.
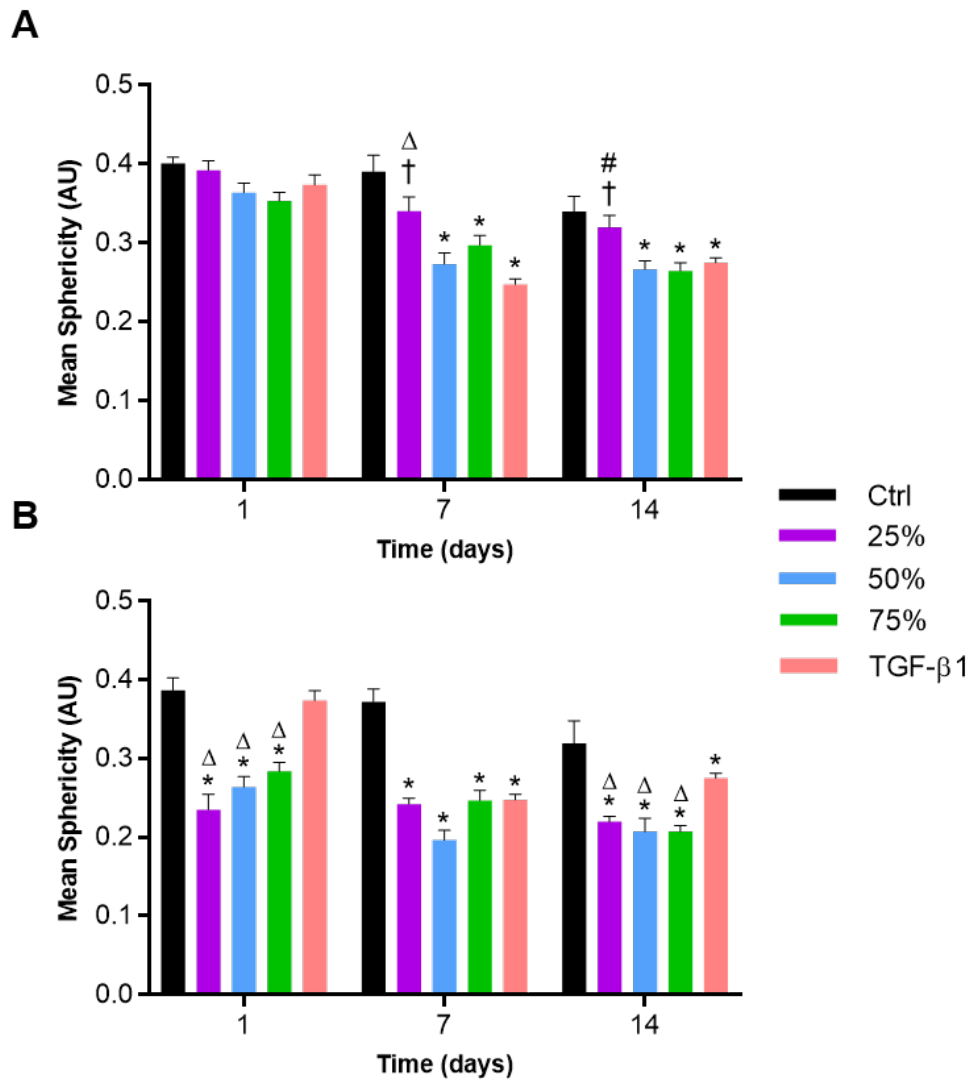
Figure 4.10: Sphericity of astrocytes following simulated contusion at 100 and 1000 mm.s^{-1}. Primary astrocyte-seeded hydrogels (5 x 10^5 cells.mL^{-1}) were subjected to contusion injury at 100 mm.s^{-1} (A) and 1000 mm.s^{-1} (B). Sphericity was measured using Volocity. Data presented as the mean $\pm$ SEM and analysed by two-way ANOVA. Significance levels * p<0.05 (vs. control, Dunnett's post-hoc) † p<0.05 (25% vs 50%, Tukey's post-hoc). # p<0.05 (25% vs 75%, Tukey's post-hoc); Δ p<0.05 (vs. TGF-β, Tukey's post-hoc). N=3.

4.4.3 Astrocyte Viability Following Contusion Injury

Together with morphological changes following injury, astrocyte viability was evaluated over 14 days using the LIVE/DEAD™Viability/Cytotoxicity Assay in order to determine whether mechanical insult is particularly cytotoxic to astrocytes. Viability was calculated as the percentage of live cells out of the total number of live and dead cells counted (Figure 4.11). TGF-β1 treatment had no effect on astrocyte viability over the 14 day time period.

At 100 mm.s^{-1}, the viability of astrocytes in the control group remained stable over the 14 day time period, with a mean viability of 79.86 $\pm$ 4% (Figure 4.11A). On Day 1 post-injury, there was a trend of decreasing viability with increasing displacement depth.

However, viability was only significantly lower than the control at 50 and 75% displacement. Viability was reduced to its lowest at 75% displacement, with a mean viability of 56.87 ± 2%. Further, viability at 75% was significantly lower than viability at 25% displacement. On Days 7 and 14, there was similar trend of decreasing viability with increasing displacement depth, similar to that observed on Day 1. However, viability on Day 7 was only significantly reduced at 75% displacement (mean 71.01 ± 2%), compared to the control group. There was no significant difference between viability in the experimental and control groups at Day 14.

At 1000 mm.s^{-1}, viability in the control group remained stable over the 14 day time period, with a mean viability of 86.45 ± 1% (Figure 4.11B). On Day 1 post-injury, a widespread decrease in viability was observed at all displacement depths, which was significantly lower than the viability of the control group. There was no significant difference in the mean viability between the experimental groups, with a mean viability of 58.19 ± 1%, over all three displacement depths. On Days 7 and 14, there was no significant difference in viability between the experimental and control groups.
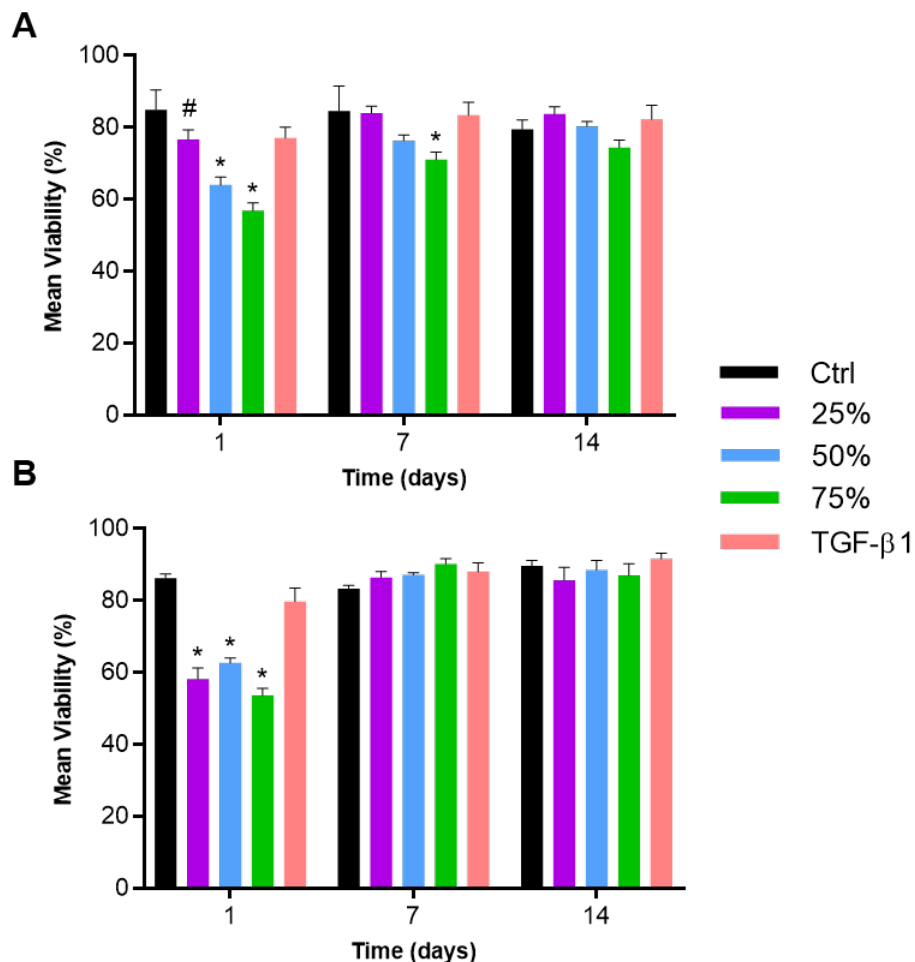
Figure 4.11: Astrocyte viability following simulated contusion at 100 and 1000 mm.s^{-1}. Astrocyte-seeded hydrogels were subjected to contusion injury at 100 mm.s^{-1} (A) and 1000 mm.s^{-1} (B), with cell viability measured over 14 days, using the live/dead assay and Equation 4.4. Data presented as the mean ± SEM and analysed by two-way ANOVA. Significance levels * $p<0.05$ (vs. control, Dunnett's post-hoc), # $p<0.05$ (25% vs 75%, Tukey's post-hoc). N=3.

To investigate the relative contributions of the number of viable and dead cells to the total population- particularly from Day 7 onwards where percentage viability was not significantly different than the control the number of live and dead cells were evaluated, with data presented at 100 mm.s^{-1} (Figure 4.12). A similar observation of trends in the viable and dead cell populations was made at 1000 mm.s^{-1} (data not shown). There was no significant difference in the mean number of live cells between the experimental and control groups, on Day 1 suggesting there was no injury-induced proliferation. Between Days 1 and 7, there was a decrease in the number of live cells, although this was not significant (p>0.05).

There was an increase in number of live cells between Days 7 and 14, which was only significant at 50 and 75% displacement. Overall, there was no significant change in the mean number of live cells between Days 1 and 14. It is difficult to determine whether the increase in the number of live cells between Days 7 and 14 was due to proliferation as a result of mechanical trauma, or the general process of cell growth and division. However, the percentage increase was greater in the experimental groups, compared to the control. The mean percentage increase in the number of live cells was 15.2% for the control group. The mean percentage increase was 24.0, 45.3, and 30.9% at 25, 50, and 75% displacement, respectively.

Analysis of the mean number of dead cells showed that cell death was greatest on Day 1, with cell death at 50 and 75% displacement significantly higher than the control. Given there was no difference in the number of live cells on Day 1, this increase in cell death contributed to the reduction in percentage viability (Figure 4.11A). A significant reduction in the number of dead cells was then observed in all groups, on Day 7 (Figure 4.12B). There was no significant reduction in the number of live cells between Days 1 and 7, thus percentage viability was no different compared to the control, except at 25% displacement. There was then no further significant change in the number of dead cells observed between Days 7 and 14, suggesting cell death primarily occurred as an acute response to mechanical injury.
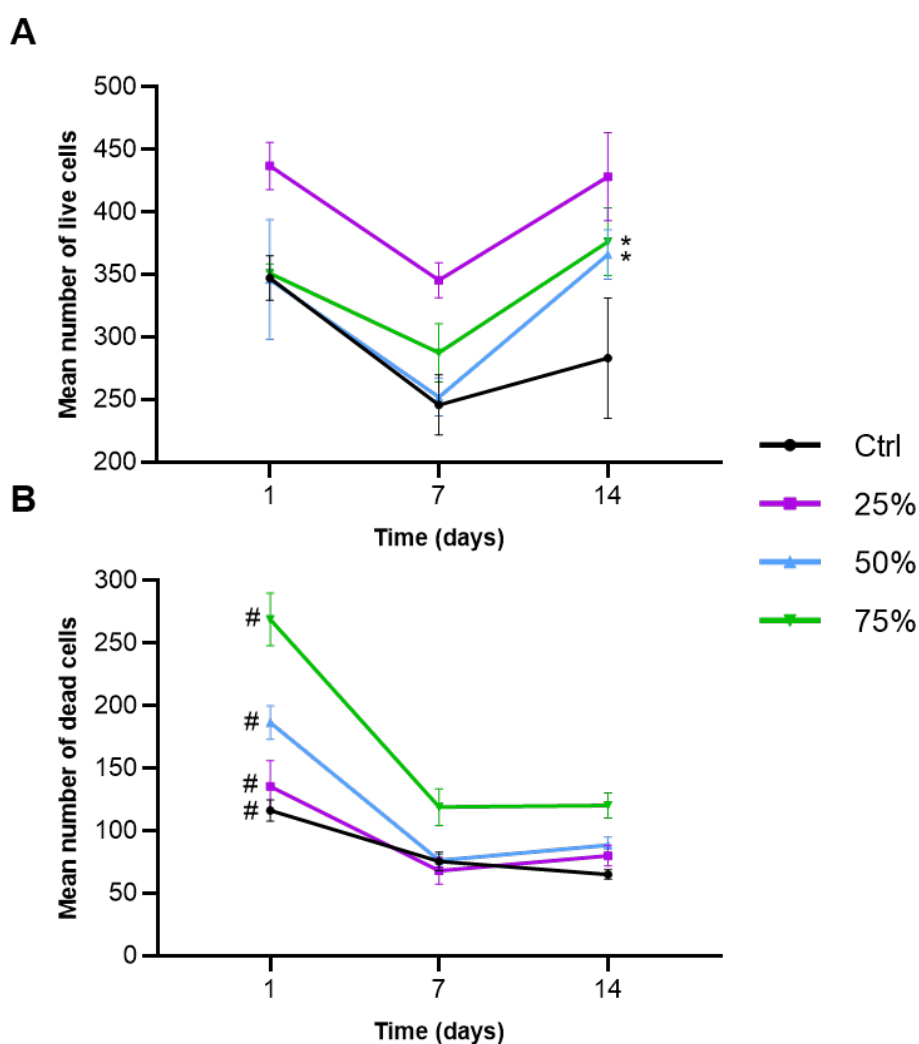
Figure 4.12: Quantification of the number of live and dead cells following contusion injury at 100 mm.s^{-1}. Astrocyte-seeded hydrogels were subjected to contusion injury at 100 mm.s^{-1} and a live/dead assay performed to quantify the number of live (A) and dead cells (B) per field of view, over 14 days. Data presented as the mean ± SEM and analysed by two-way ANOVA with Tukey's post-hoc test. Significance levels * p$<$0.05 (Day 7 vs Day 14), # p$<$0.05 (Day 1 vs Day 7). N=3.

4.4.4   Astrocyte Metabolic Activity Following Contusion Injury

The adenosine triphosphate (ATP) content of astrocytes per sample was measured following contusion injury using the ATPlite™Luminescence Assay System, as described in Section 4.3.8. Metabolic activity of astrocytes in the control groups (no injury) remained stable across the 14 day time period, with no significant differences in metabolic activity between the timepoints at both 100 and 1000 mm.s^{-1} (Figure 4.13). Treatment of the cells with 70% (v/v) methanol (positive cell death control) successfully resulted in a significant reduction in ATP content compared to the control. Acellular gels were included as a control to show that the gels did not contribute significant artefacts which may have affected the measurements.

Contusion injury inflicted at 100 mm.s^{-1} did induce changes in astrocyte metabolic activity (Figure 4.13A). On Day 1, contusion injury resulted in increased metabolic

activity, which was significantly greater than the control at 50 and 75% displacement. However, there was no significant difference in metabolic activity between any of the displacement depth groups. Chemical treatment with TGF-β1 did not significantly affect astrocyte metabolic activity. On Day 7, metabolic activity of the experimental injury groups was greater than the control, but this was only significant at 25% displacement. TGF-β1 treatment did not significantly affect astrocyte metabolic activity. Contusion injury to 25 and 75% displacement depth resulted in a significantly higher metabolic activity compared to the TGF-β1 group. On Day 14, all test groups showed significantly increased metabolic activity compared to the control.   Contusion injury to 75% displacement depth resulted in the greatest metabolic activity (mean 7.01 x 10^5 $\pm$ 1 x 10^5 CPS). Metabolic activity at 75% was also significantly greater than that at 25 and 50% displacement, and the TGF-β1 group.   Evaluating each test group over time revealed that between Days 1 and 7, there was no significant change in metabolic activity of any of the groups. However, a significant increase in metabolic activity was observed in all test groups between Days 7 and 14 (and thus Days 1 and 14).

Contusion injury inflicted at 1000 mm.s^{-1} did not result in any significant changes to the metabolic activity of the astrocytes on Day 1, nor were there any differences between the test groups (Figure 4.13B). On Day 7, only contusion to 75% displacement depth results in a significant increase in metabolic activity compared to the control group. However, this was not significantly different from any of the other test groups. On Day 14, all test groups showed significantly increased metabolic activity compared to the control. Contusion injury to 75% displacement depth resulted in the greatest metabolic activity (mean 8.50 x 10^5 $\pm$ 1 x 10^5 CPS), which was also significantly higher than all other test groups. At 75% displacement, metabolic activity significantly increased with time. However, similar to 100 mm.s^{-1}, metabolic activity for the other test groups did not significantly change until Day 14.
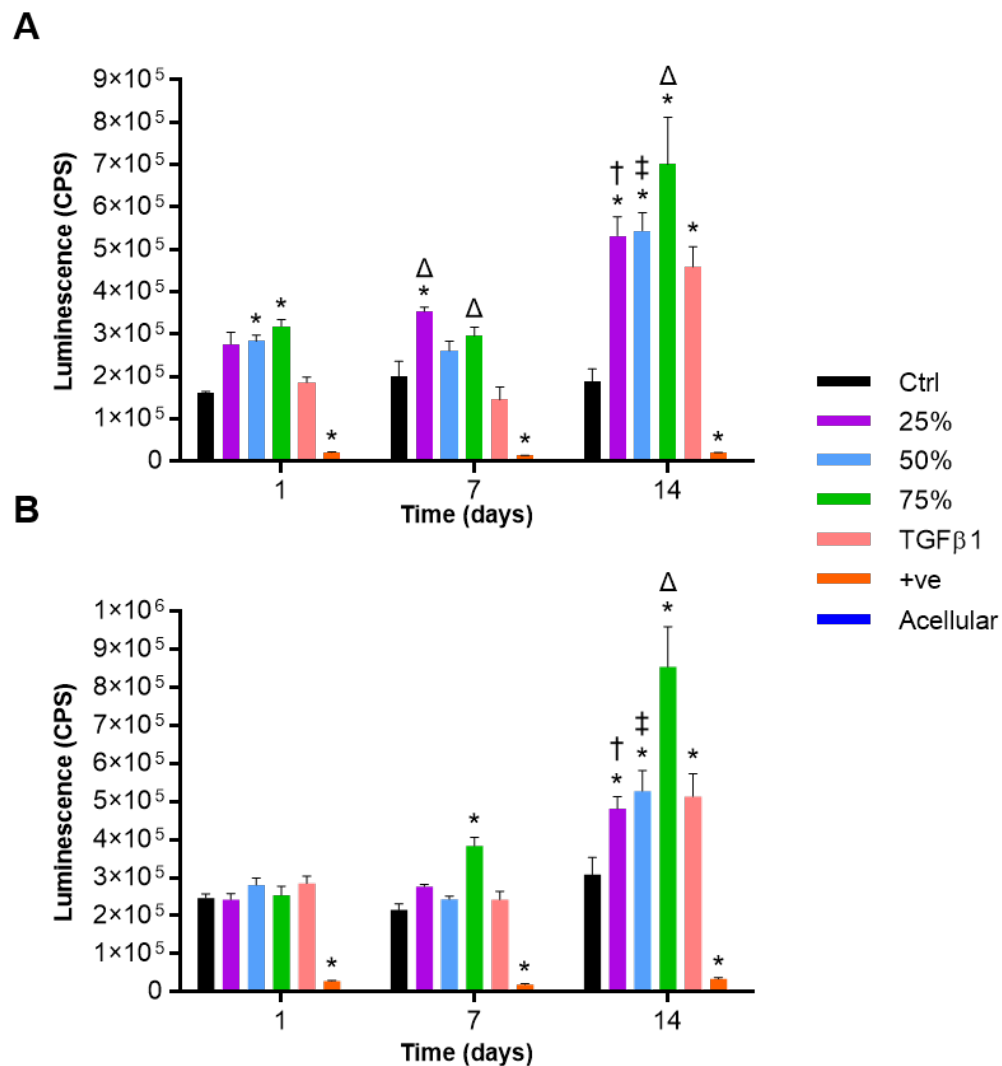
Figure 4.13: Astrocyte metabolic activity following simulated contusion at 100 and 1000 mm.s^{-1}. Astrocyte-seeded hydrogels (5 x 10^5 cells.mL^{-1}) were subjected to contusion injury at 100 mm.s^{-1} (A) and 1000 mm.s^{-1} (B) and ATP content was measured over 14 days. Data presented as the mean counts per second (CPS) $\pm$ SEM. Data analysed by two-way ANOVA. Significance levels * $p < 0.05$ (vs. ctrl, Dunnett's post-hoc); † $p < 0.05$ (25% vs. 75%, Tukey's post-hoc); ‡ $p < 0.05$ (50% vs. 75%, Tukey's post-hoc); Δ $p < 0.05$ (vs. TGF-β1, Tukey's post-hoc). TGF-β1 (positive astrogliosis control) and +ve (positive cell death control; 1 hour 70% v/v methanol treatment). N=4.

4.4.5 Chondroitin Sulfate Proteoglycan Expression

Astrocytes are known to secrete several molecules which are inhibitory to neuroregeneration. A group of such molecules, chondroitin sulfate proteoglycans (CSPGs), are expressed by astrocytes following injury. The monoclonal antibody, CS-56, was used to label the glycosaminoglycan portion of CSPGs following contusion injury. Figure 4.14 shows representative images of CS-56 labelling in astrocyte-seeded hydrogels 14 days following contusion injury, at 100 mm.s^{-1}. Differences were observed in the area of CSPG expressed, particularly in the control group where little CSPG expression was observed. Contusion injury and TGF-β1 treatment appeared to induce astrocytes to express and release more CSPG into the surrounding microenvironment. Quantification was undertaken by calculating the total area of CSPG expression using FIJI (Figure

4.15).
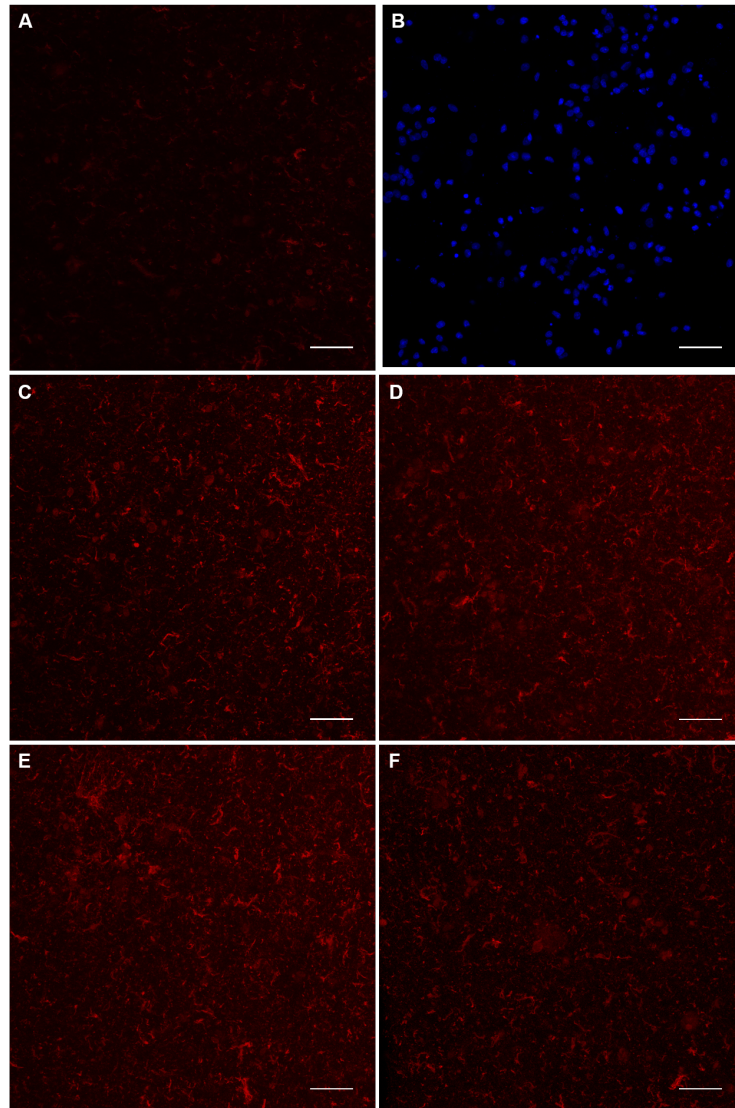
Figure 4.14: Immunofluorescent labelling of CS-56 in astrocyte-seeded hydrogels 14 days post-contusion injury at 100 mm.s^{-1}. Representative maximum intensity projection images (36 µm depth) of astrocyte-seeded gels subjected to no injury (A), isotype control (B), contusion to 25% (C), 50% (D), and 75% (E) displacement, and TGF-β1 treatment (F) and incubated for 14 days before labelling with a monoclonal antibody against CS-56 (CSPG, red). Nuclei were counterstained with DAPI in B (blue). Scale bar represents 50 µm.

Contusion injury at 100 mm.s^{-1} to varying displacement depths did have an effect on CSPG expression (Figure 4.15A). On Day 1, increasing displacement depth resulted in a trend for increased CSPG expression; however, this was only significantly higher than the control at 75% displacement. On Day 7, significantly greater CSPG expression was observed at 50 and 75% displacement. TGF-β1 treatment also resulted in significantly higher CSPG expression compared to the control. On Day 14, all test groups showed greater CSPG expression compared to the control. Astrocytes in the 75% displacement group expressed more significantly more CSPG compared to those in the 25% and TGF-β1 group. Within each test group, there was no significant increase in the mean CSPG area between Days 1 and 7, except for the TGF-β1 group. However, significant increases were observed between Day 7 and 14 in all test groups. In the control group, CSPG area

significantly increased between Days 7 and 14.
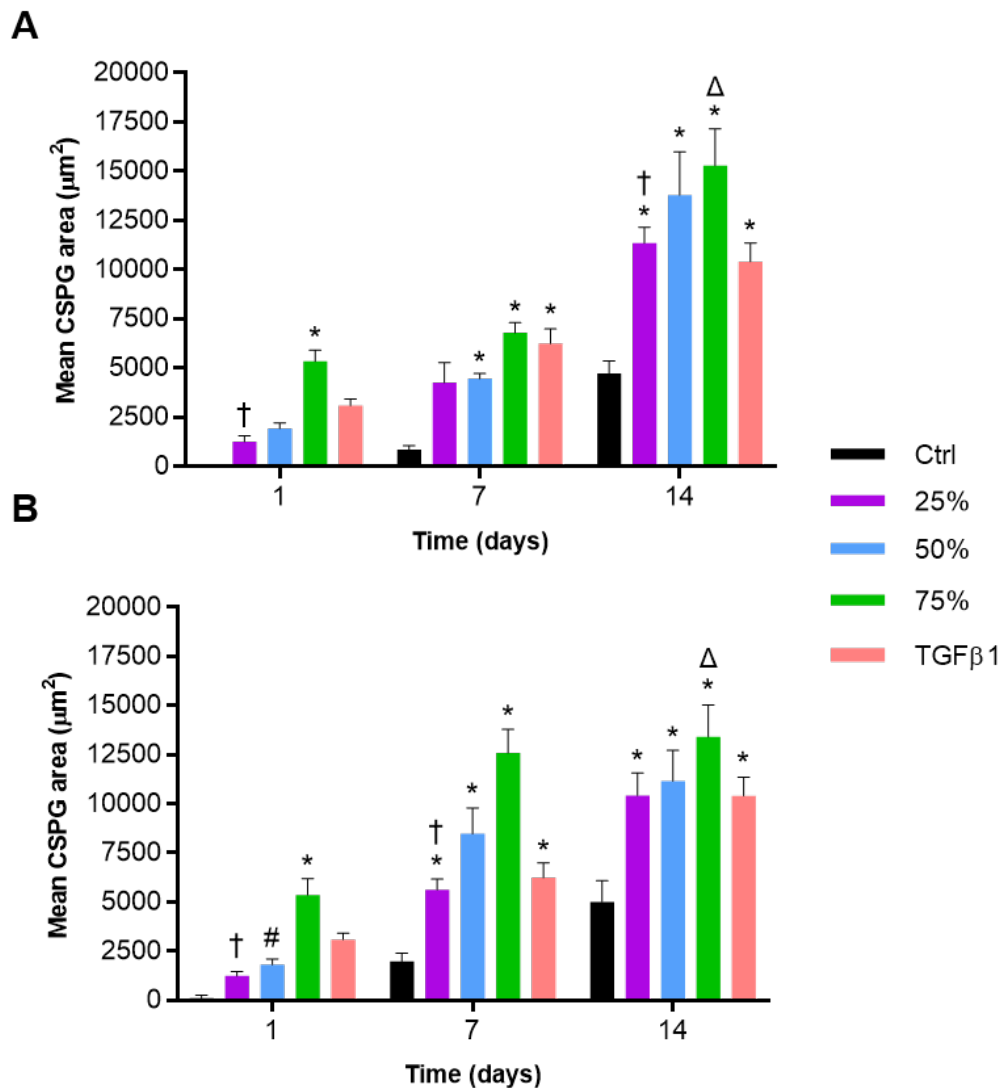
Figure 4.15: Expression of CSPGs following simulated contusion at 100 and 1000 mm.s^{-1}. 100 mm.s^{-1} (A) and 1000 mm.s^{-1} (B). Data presented as the mean ± SEM. Data analysed by two-way ANOVA. Significance levels * $p<0.05$ (vs. control, Dunnett's post-hoc); † $p<0.05$ (25% vs. 75%, Tukey's post-hoc); # $p<0.05$ (50% vs. 75%, Tukey's post-hoc); Δ $p<0.05$ (vs. TGF-β1, Tukey's post-hoc). N=4.

Contusion injury at 1000 mm.s^{-1} to varying displacement depths also had an effect on CSPG expression (Figure 4.15B). At Day 1 post-injury, astrocytes in the 75% displacement group expressed significantly more CSPG than all other groups, although there was no difference between 25 and 50%. On Day 7 post-injury, all test groups expressed significantly more CSPG compared to the control. As displacement increased, the mean CSPG area also increased, although this was not statistically significant ($p>0.05$). Astrocytes in the 75% displacement group expressed significantly more CSPG than those in the 25% and TGF-β1 groups. On Day 14, all test groups expressed significantly more CSPG compared to the control group. There were no differences in the mean CSPG area between any of the test groups. Over time, astrocytes in the 25% displacement group saw a step-wise significant increase in CSPG area. At 50 and 75% displacement, the mean CSPG area significantly increased between Days 1 and 7, but

not between Days 7 and 14.

4.4.5.1   Summary of Primary Astrocyte Outcomes Following Contusion Injury

Overall, mechanical trauma simulating contusion injury induced changes in astrocyte behaviour which differed to that of non-injured astrocytes.   Astrocyte morphology progressively changed from small and rounded, to larger and more ramified with many interdigitating processes. Significant changes in GFAP volume were observed from Day 1 at 100 mm.s^{-1}, although without a corresponding decrease in sphericity suggesting hypertrophy of astrocytes initiated earlier (Figure 4.10).   At 1000 mm.s^{-1}, a similar reduction in sphericity was observed across all displacement depths and timepoints, which corresponded to the increase in GFAP volume, suggesting hypertrophy and ramification was induced at the same time.

The viability and metabolic activity data did not fully corroborate each other, with maximum cell death occurring at Day 1 post-injury but with no difference in ATP content compared to control.   Further, a significant increase in metabolic activity was observed between Days 7 and 14, but there was no significant change in GFAP volume per cell or sphericity.   It was suggested that cell death was offset by increased proliferation; however, the number of live cells was not significantly greater than the control group. However, the rate of increase in the number of live cells between Days 7 and 14 was greater in the experimental groups compared to the control, suggesting more proliferation as a result of injury and thus increased metabolic activity.   Temporal differences in CSPG expression were also observed following injury, with velocity having little effect on the level of expression.   There was more variation in quantification of CSPG area as demonstrated by the large error bars so although displacement appeared to influence the level of CSPG expressed, this was largely not significant.

There was evidence of astrocytes in the control group beginning to deviate from the baseline non-reactive state by the end of the 14 day time period. Increased GFAP volume and CSPG expression, and decreasing sphericity of astrocytes in the control group suggests that although they were not as adversely affected as the injured groups, some stresses may have been experienced by the cells. TGF-β1 treatment did induce astrogliotic changes; however, the response was not as immediate as with mechanical trauma and less severe.

4.4.6   Effect of Enzymatic Digestion of CSPGs on Astrocyte Reactivity

Enzymatic digestion of CSPGs by chondroitinase ABC (ChABC) has previously been utilised *in vivo* to digest and remove the neuroinhibitory molecules and create a permissive microenvironment for axon outgrowth (Bradbury *et al.,* 2002). In this study, the effects of CSPG digestion on astrocyte reactivity was briefly explored. Astrocyte-seeded hydrogels subjected to contusion injury at 100 mm.s^{-1} to displacement depths of 25, 50, and 75% were cultured for 14 days. The gels were then treated with cell culture medium supplemented with 200 mU ChABC, for 4 hours, before removing the treatment and incubating the gels for a further 48 hours. Immunostaining for CS-56 and GFAP was then performed to evaluate astrocyte morphology (Figure 4.16).
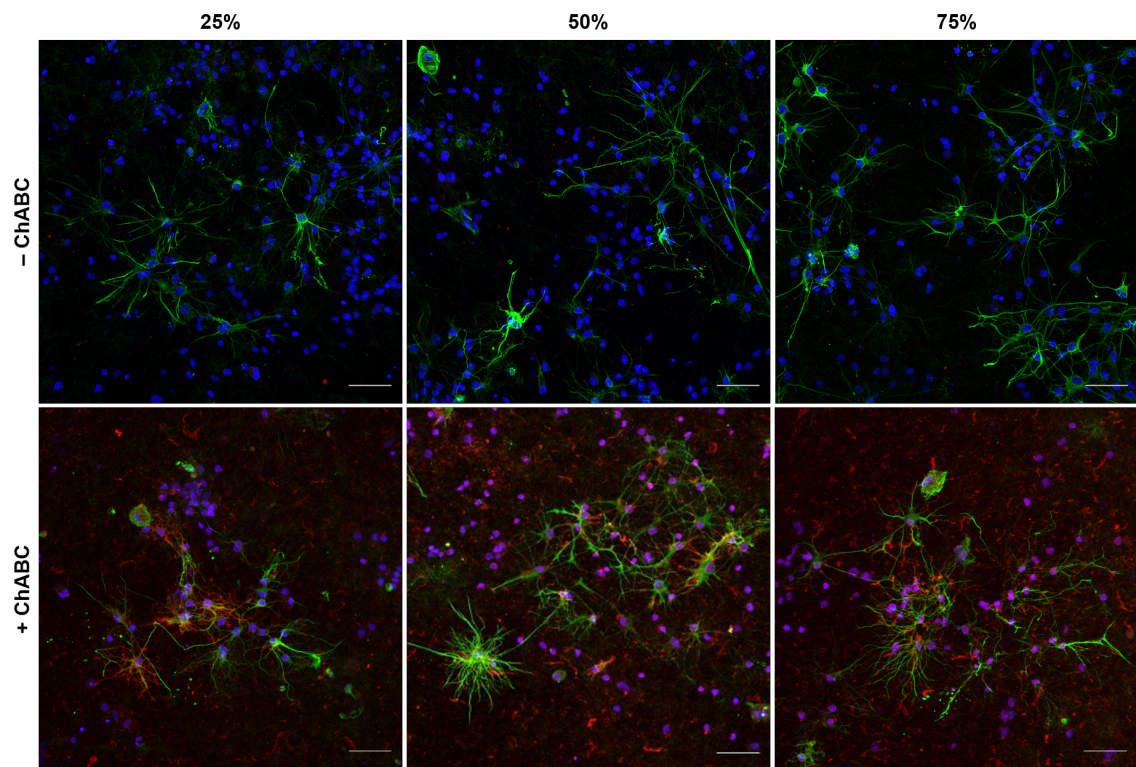
Figure 4.16: Astrocyte morphology following chondroitinase ABC digestion of CSPGs at 14 days post-injury. Primary rat cortical astrocyte-seeded hydrogels (5×10^5 cells.mL^{-1}) were subjected to contusion injury at 100 mm.s^{-1} and incubated for 14 days before treating with ChABC (200 mU; 4 hours). After 48 hours, the cells were fixed and immunostained for CS-56 (CSPG, red) and GFAP (astrocytes, green), and counterstained with DAPI (nuclei, blue). Representative maximum intensity projection images of astrocytes following ChABC treatment. 36 μm depth. Scale bar represents 50 μm.

Four hours treatment with ChABC resulted in successful digestion of CSPGs as shown by the lack of CS-56 staining, and successful digestion was achieved across all displacement depths. GFAP staining of astrocytes showed that 48 hours post-treatment, the astrocytes maintained their reactive morphology, with ramification and interdigitation of their processes with neighbouring astrocytes. This could suggest that the injury was severe enough to induce a permanent non-reversible astrogliosis state, in which removal of CSPGs does not reverse this, or that CSPG expression and release does not feed back into the astrogliosis pathway. However, a longer incubation period post-CSPG digestion is required to further investigate the possibility of astrogliosis being reversible and/or able to be attenuated under these conditions.

4.4.7 An Enriched Population of Astrocytes Persists Following Removal of Cells from Gels

Immunohistochemical staining of astrocytes using an anti-GFAP antibody revealed that, although mechanical injury resulted in the induction of an astrogliotic response, a large proportion of the astrocytes remained GFAP-negative. This was despite the confirmation of an enriched population of astrocytes, which was achieved by staining cells for GFAP seeded onto glass coverslips, prior to seeding hydrogels for subsequent experimentation.

Therefore, an experiment was performed whereby astrocyte-seeded hydrogels subjected to contusion injury were digested with collagenase, with the cells reseeded onto glass coverslips and immunostained with GFAP (Figure 4.17).
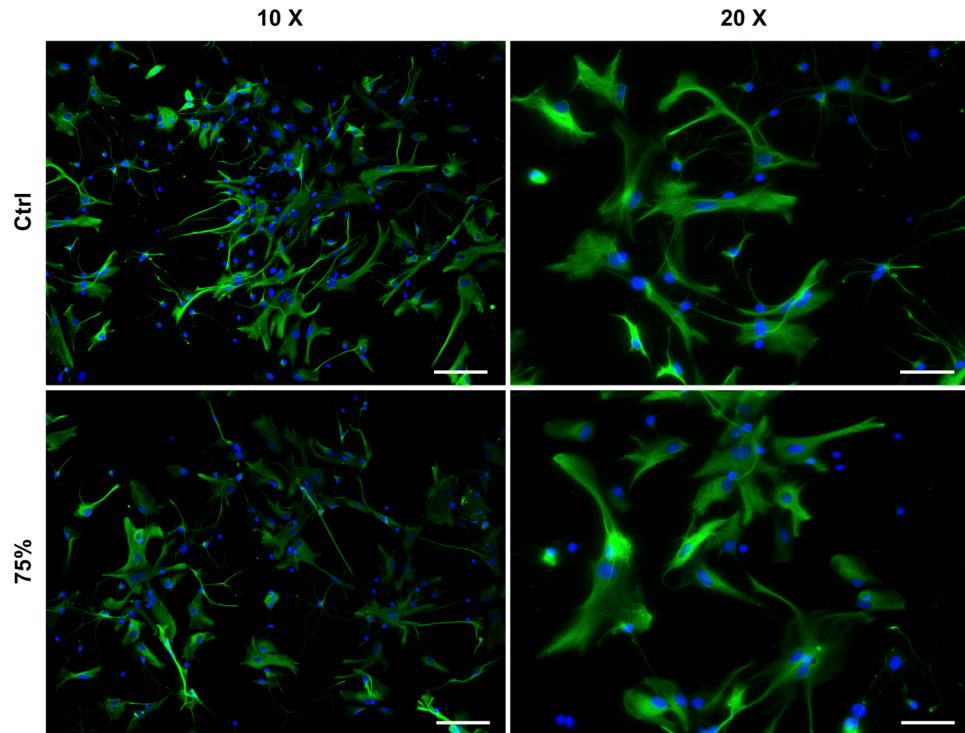
Figure 4.17: GFAP immunoreactivity of primary astrocytes isolated from experimental hydrogels. Representative immunofluorescent images of primary astrocyte-seeded hydrogels subjected to simulated contusion injury, at 1000 mm.s^{-1} to 75% displacement, and incubated for 14 days. The cells were isolated using collagenase treatment (0.125% w/v) for 15 minutes and seeded onto PDL-coated glass coverslips for subsequent immunolabelling with a polyclonal antibody against GFAP (astrocytes, green) and counterstained with DAPI (nuclei, blue). Control astrocytes were cultured in tissue culture flasks and seeded onto PDL-coated coverslips. Scale bar represents 100 µm (10 X) and 50 µm (20 X).

Figure 4.17 shows representative images of cells recovered from collagenase-digested hydrogels, which had been subjected to contusion injury at 1000 mm.s^{-1} to 75% displacement. Astrocytes in the control panels contained astrocytes which had undergone culture and enrichment in tissue culture flasks before seeding straight onto PDL-coated coverslips. The majority of the cells derived from the digested hydrogels stained positive for GFAP, with very few GFAP-negative nuclei. The cells in the control group were also primarily GFAP-positive, similar GFAP expression and morphology to cells derived from the hydrogels. This confirms that the population of cells were indeed astrocytes, despite the lack of GFAP staining.

4.5 Discussion

The aims of this chapter were to apply the contusion injury protocol developed in Chapter 3 to primary astrocyte-seeded hydrogels and evaluate responses of the astrocytes to a range of input velocity and displacement values *in vitro*. Over 14 days, astrocyte responses were

evaluated through a range of assays to evaluate astrocyte morphology, viability, metabolic activity, and secretion of chondroitin sulfate proteoglycans (CSPG).

4.5.1 Biomechanics of Contusion Injury *In Vitro*

The contusion protocol used in this chapter was developed based on characterisation of the BOSE 5110 Electroforce BioDynamic (Chapter 3), which showed that a maximum input velocity of 1000 mm.s^{-1} was achievable, with up to 10% error. This velocity is within the range of velocities used in *in vivo* studies, particularly in smaller animals such as rodents (Chapter 1 Table 1.5). As it is impossible to measure the precise velocity of a clinical injury, cadaveric models have been useful tools for measuring deformation rates. Impact velocities between $0.08 - 10$ m.s^{-1} have been measured in human and bovine cadaveric burst fracture models (Panjabi *et al.,* 1994; Saari *et al.,* 2011; Wilcox *et al.,* 2004), thus the velocities reported in this study could be considered relevant too.

The input displacement was consistently achieved with the gels, as shown by the small error bars and there was no significant difference between the peak displacement achieved between both input velocities. There was more variation in the velocities achieved, which is consistent with the verification work performed in Chapter 3 and with studies *in vivo* (Chen *et al.,* 2016; Choo *et al.,* 2007; Lam *et al.,* 2014). Here, an unexpected increase in mean velocity with an increase in displacement was observed. This was not observed with gels in Chapter 3 (Figure 3.7) so the reason for this change is unknown and will likely affect the interpretation of the results as velocity was not consistent and thus the energy applied will be affected. The *in vivo* contusion models summarised in Chapter 1 (Table 1.5) mostly report either the impact or peak velocity, so it is difficult to determine whether those values were significantly different to their peak velocities.

Lam *et al.,* (2014) reported detailed kinetic information following contusion SCI in a rat model, using the University of British Columbia (UBC) multimechanism device. A range of input displacement and velocity values were used: 0.9 and 1.5 mm displacement, and 8, 80, and 800 mm.s^{-1}. From low displacement and low velocity to high displacement and high velocity, incremental increases in force and energy applied were measured ($0.250 - 1.775$ mJ). The displacement depths and velocities used in this study are of similar magnitude, and the mean energy applied ranged from $0.150 - 3.709$ mJ, which is similar to the values observed by Lam *et al.,* (2014). The differences may be attributed to the differing mechanical properties between collagen hydrogels and rat spinal cord tissue and the presence of supporting tissue structures, including dura and ligaments in the *in vivo* model.

In this study, the impact velocity was determined as the velocity at which the platen first came into contact with the surface of the gel. A limitation of this method is that it was potentially not an accurate way to verify whether the initial calculation of the height of the gel remained the same at the point of impact. Additionally, it was difficult to assess by eye the precise point at which the load platen first came into contact with the gel and

compare this with the theoretical impact position. Other studies which report impact velocity, such as Lam *et al.,* (2014) and Choo *et al.,* (2007) do not detail how impact velocity was determined but it is assumed that the value is derived from the displacement position where the initial surface of the cord was registered (force value of 0.03 N). In future, further preliminary experiments could be undertaken to verify the precise impact position, such as measuring the gel height multiple times over a given period of time to determine whether this changes. Alternatively, a high speed video camera could be set up to film the injury process, such as one used by Wilcox *et al.,* (2002) to measure the dynamics of canal occlusion in an *ex vivo* model of thoracolumbar burst fracture. Analysis of the still frames could be used to determine the impact position and the time at which this occurs. The time at impact could be used with the output biomechanical data to then determine the actual impact velocity.

4.5.2 Effects of Contusion Impact Depth and Velocity on Astrocyte Responses

The advantage of using the BOSE to model mechanical injury is that velocity and displacement can be decoupled. An additional input velocity of 100 mm.s^{-1} was selected, alongside three displacement depths (25, 50, 75% gel height) in order to generate a range of injury conditions.   The aim was to evaluate the relative importance of each biomechanical parameter in determining astrocyte responses and its severity. In this study, it was hypothesised that an increase in velocity and displacement would result in an increase in the severity of the astrogliosis response, due to the increased energy applied to the cells.

However, an input contusion velocity of 1000 mm.s^{-1} resulted in an increase in astrogliosis severity, whereby displacement depth had little effect on astrocyte volume and sphericity across 14 days, and little effect on viability and metabolic activity at the earlier timepoints. This suggests the potential for a threshold for astrogliosis which may have been surpassed at 1000 mm.s^{-1}. Tissue-level strain thresholds have been reported for axonal injury through measuring morphological and functional changes following tensile stretching of optic nerve axons (Bain and Meaney, 2000), but less is known about astrocyte tolerances to mechanical injury. Cullen *et al.,* (2007) found that astrocytes were less susceptible to cell death compared to neurons, 48 hours following shear deformation.

Lam *et al.,* (2014) reported no significant differences in the energy applied between velocities at a fixed displacement depth except between 80 and 800 mm.s^{-1}, at 1.5 mm displacement. However, differences were observed in behavioural deficit measurements at 0.9 mm – 800 mm.s^{-1} and 1.5 mm – 8 mm.s^{-1}, for instance, despite no significant difference in their energy applied (0.506 and 0.711 mJ, respectively). This was thought to be due to the increased strain experienced by the nerve fibres at 1.5 mm, which resulted in demyelination and thus affecting cell behaviour. In this study, a similar energy applied was calculated for the following conditions: 100 mm.s^{-1}–75% and 1000 mm.s^{-1}–25% (0.945 and 0.954 mJ, respectively). Comparison of the outcome measures for these two injury

groups was performed (Table 4.2).

Table 4.2: Comparison of outcome measures for injury groups with similar energy applied. The following injury groups had energy applied values which were not significantly different from one another: 100 mm.s^{-1}–75% and 1000 mm.s^{-1}–25%. Comparison of the outcome measures for these two groups were made by two-way ANOVA with a Tukey's post-hoc test. Significance levels * $p < 0.05$. n.s = not significant.

	Day 1	Day 7	Day 14
Volume GFAP.cell^{-1} μm^3)	*	*	*
Sphericity (AU)	*	n.s	n.s
Viability (%)	n.s	*	n.s
Metabolic activity (CPS)	n.s	n.s	*
CSPG expression area (μm^2)	n.s	n.s	*

Despite energy applied being similar for those two conditions, there were some differences in astrocyte responses over time, although there was no clear pattern. For example, there were differences in astrocyte morphology between the two injury groups, but not for viability, metabolic activity, or CSPG expression one day post-injury. The volume of GFAP per cell was the only outcome measure which significantly differed between the two groups at all timepoints, whereby the values at 1000 mm.s^{-1}–25% were significantly greater than those at 100 mm.s^{-1}–75%. This could be due to the viscoelastic behaviour of cells: the elastic component dominates at the higher strain rate causing the cells to behave in a more rigid manner. Conversely, at the lower strain rate, the viscous component dominates and the cells may be able to accommodate deformation better. It may be expected then that all the outcome measures would exhibit differences. However, the activation mechanisms and pathways of these activities may be differentially affected by mechanical trauma.

Several *in vivo* studies have reported on the existence of dominant biomechanical parameters in determining injury severity: Kim *et al.,* (2009) observed no significant decrease in functional outcomes of mice at a fixed displacement depth (0.8 mm), with increasing impact velocity (100, 200, and 400 mm.s^{-1}). Pearse *et al.,* (2005) observed an increase in axon demyelination and decrease in motor function with increasing impact depth (0.80, 0.95, and 1.1 mm), at a fixed velocity (100 mm.s^{-1}). Sparrey *et al.,* (2008) reported that contusion velocity affected the magnitude of white matter and neuronal damage in the rat spinal cord at a displacement depth of 1 mm. Basso *et al.,* (1996) reported a reduction in locomotor outcomes following increasing drop height (6.25, 12.5, 25, and 50 mm), thus impact velocity and depth using the NYU impactor. However, it is difficult to compare these studies with one another as each used different experimental procedures, including the injury apparatus, animal model, and input biomechanical parameters (where some studies varied both displacement and velocity; others only one). Further, impact velocity and depth are inherently coupled in the Basso *et al.,* (1996) study, thus an increase in one parameter results in an increase in the other. This makes it difficult to evaluate the relative importance, if any, of each parameter in determining injury severity.

4.5.2.1 Experimental Model and Setup

The diameter of the impactor tip used in this study was 10 mm with a flat surface, which generated a global injury on the gels which were 11 mm in diameter. This contrasts to the smaller impactor tips used in *in vivo* studies, which range from 0.6 – 2.0 mm in rodents (Chapter 1, Table 1.5), and are typically rounded in geometry. Larger animal model studies, such as porcine and non-human primates (NHP) employed larger impactor tips up to 15 mm, due to the increase in size of the spinal cord compared to rodents. A similar *in vitro* contusion study using the BOSE apparatus used a 3.34 mm diameter impactor tip to inflict a focal injury to cell-seeded hydrogels (Kirk, 2018). These studies contrast to this study as a focal injury was modelled, which resulted in the generation of a defined lesion. The aim of this study was to evaluate the effects of varying contusive impacts on astrocyte responses as an overall population, thus a focal injury was not modelled. However, this prevented the formation of a lesion which would have facilitated more in depth analysis of the lesion epicentre, lesion border, and the uninjured local and distal microenvironment. Also, employment of a smaller impaction tip means force is distributed over a smaller area, thus the astrocytes may respond differently.

There are some similarities between this study and other *in vitro* studies, including those by Smith (2016) and Kirk (2018). Smith (2016) used the same cell type and collagen hydrogels to model contusion SCI using the Infinite Horizons impactor. The hydrogels used by Kirk (2018) were reported to be a volume of 100 µL prepared in 96 well-plates (1 x 10^6 cells.mL^{-1}). The thickness of these gels were not reported and contusion displacement depths used were 50, 80, and 100%. Therefore, it is difficult to compare the absolute displacement values with those in this study; however, both studies showed a response by the astrocytes to injury.

Separate gels were prepared for each assay: immunostaining, viability, metabolic activity. Viability and metabolic activity both exploit characteristics of cells which are distinct between viable and dead cells, thus have been used interchangeably to evaluate viability. However, the characteristics of astrogliosis, including hypertrophy, ramification, and proliferation may affect metabolic activity in such a way that makes distinguishing the contribution of these activities against cell death difficult. This may necessitate further validation with additional assays but proliferation specific markers such as BrdU could be utilised, for instance.

Whilst the BOSE 5110 Electroforce BioDynamic apparatus was shown to be capable of modelling precise and accurate displacement of gels, simulating contusion injury, a number of practical limitations exist. Firstly, the system is low-throughput and relatively time consuming. The platens only had a capacity for testing one gel at any one time. Manufacturing or acquiring a platen with the capacity for more than one sample would be beneficial and could increase the precision of the injury simulated across samples. TA Instruments advertises a four chamber model (model 5270) but this may be cost prohibiting due to the increased number of components and a load cell required for

each chamber.

Another practical limitation of the apparatus in this study was that manual alignment of platens was required during assembly of the chamber, and manual adjustment was often required once the chamber was loaded to the apparatus frame and stabilising collars were removed. This limitation did not impede the simulation of contusion injury with the gels as the impacting tip could easily be centred over each specimen. However, proper alignment of tensile grips for the distraction study (Chapter 5) may be more difficult as the specimen is secured to both grips and erroneous load readings and/or distribution of strain may occur with unaligned grips. Additionally, the requirement of sterility meant the apparatus was housed in a Class II cabinet. These cabinets do not have solid surfaces to enable appropriate circulation of laminar air flow. As such, some noise was present in the load readings caused by vibrations from movement of the platens, and the air flow. The effects of these were reduced by placing a rubber sheet underneath the apparatus with the aim of absorbing some of the vibrations. Also, the safety cabinet screen was closed and power of the laminar air flow was reduced for the short duration of the experiment itself, which did not affect the sterility of the samples.

4.5.3 Astrocyte Responses to Contusion Injury *In Vitro*

Astrocytes respond to insult by undergoing numerous cellular, molecular, and functional changes, all of which contribute to the overall process of astrogliosis. GFAP is widely used as a marker for reactive astrocytes as its upregulation is associated with injury (Sofroniew, 2009). In this study, mechanical trauma resulted in morphological alterations consistent with astrogliosis, including hypertrophy, ramification, overlapping of parenchymal domains, and an increase in the volume of GFAP expressed per cell (Anderson *et al.,* 2014; Pekny and Nilsson, 2005; Sofroniew, 2009).

Evidence of a gradated response to injury was observed at 100 mm.s^{-1}, where an increase in displacement depth was associated with an increase in astrocyte reactivity. This is consistent with the general consensus that astrocyte responses vary with injury severity, along a spectrum (Sofroniew and Vinters, 2010). However, at 1000 mm.s^{-1}, the astrocytes were observed to be morphologically reactive at all displacement depths, with similar GFAP volume expression and ramification. This suggests some threshold for robust morphological alterations exists, although there were still differences in CSPG expression, metabolic activity. Overlapping of astrocyte processes was observed, particularly at the higher displacement depths and at later timepoints. Non-reactive astrocytes have been shown to occupy distinct anatomical domains from one another, with minimal overlap of processes (Bushong *et al.,* 2002). Process overlapping is associated with scar-forming astrocytes and as a more robust response to moderate to severe injury (Sofroniew, 2009). These reactive astrocytes contribute to the glial scar, a physical and chemical barrier against neuroregeneration.

Astrocytes under control conditions contrasted morphologically to those under injury conditions, whereby they were smaller and more rounded in shape with a lower level of

GFAP volume expressed per cell. This observation is also consistent with studies which have demonstrated the mechanosensitive nature of astrocytes: astrocytes are small and round in soft hydrogels while highly spread in stiffer gels (Georges *et al.*, 2006; Pogoda and Janmey, 2018). Many of the nuclei stained notably did not also stain positive for GFAP. Numerous reports have discussed the heterogeneity of astrocytes, including the differential expression of GFAP in astrocytes from different tissue regions, and under physiological and pathological states (Anderson *et al.*, 2014), and is discussed in more detail in the General Discussion (Chapter 6).

4.5.3.1   Astrocyte Viability and Metabolic Activity

Temporal changes in astrocyte cell death and metabolism has not been the primary focus of many *in vivo* and *in vitro* studies of contusion SCI, although research has reported sustained neuronal, oligodendrocyte and microglial cytotoxicity following SCI (Beattie *et al.*, 2002; Gaudet and Fonken, 2018; Shuman *et al.*, 1997; Yong *et al.*, 1998). This may suggest that astrocyte cell death is not a dominant pathophysiological feature of SCI. In this study, cell death was maximal 24 hours post-injury, and viability was mostly insignificant compared to the control group from Day 7 post-injury.

In a similar *in vitro* model using the same BOSE apparatus, Kirk (2018) observed a significant increase in ATP content 24 hours post-injury, at focal contusion displacement depths of 80% and 100% gel height (input velocity of 3000 mm.s^{-1}). The study used the ATPlite assay as a measure of cell metabolic activity, viability and astrocyte reactivity, and inferred that the increase in ATP content was due to the processes involved in astrogliosis. If this is true, potential cell death could have been masked and metabolic activity and live/dead data here suggests so.   Viability was not assessed at later timepoints. Smith (2016) generated a contusion model using primary astrocyte-seeded collagen hydrogels and modelled the injury using the IH impactor.   Contrastingly, cell death was insignificant compared to the control group at Days 1 and 5 post-injury, and significantly greater than the control on Day 10 post-injury, as measured using the live/dead assay. Both Kirk (2018) and Smith (2016) modelled focal contusion injuries, thus there are differences in methods used to calculate viability/cell death compared with each other and this study. Kirk (2018) used the ATPlite assay which measures the ATP content of the bulk sample and does not specifically quantify cell death; whereas Smith (2016) measured cell death at eight different regions around the sample, including around the impact area, and reported the mean value. Therefore, artefacts from imaging location choice may have affected the calculation.

In other *in vitro* studies, Cullen *et al.*, (2007) applied shear strain to neuron-astrocyte hydrogels at different strain rates and observed significant cell death of neurons at moderate (10 s^{-1}) and high (30 s^{-1}) strain rates two days post-injury. Astrocyte viability was not significantly affected, suggesting neurons were more susceptible to high rate shear strains. Total cell density was significantly increased at the low (1 s^{-1}) and moderate strain rates suggesting a proliferative response. In this study, significant cell death observed one day post-injury was consistent with a significant

reduction in the percentage of viable cells (Figure 4.11 and 4.12B). Cullen *et al.,* (2007) did not evaluate cell death at time points later than two days so comparisons cannot be made regarding longer term cell death. Together with the analysis of astrogliotic changes (morphology and CSPG expression), Cullen *et al.,* (2007) showed that low strain rates (1 s^1) resulted in astrogliotic changes but did not produce significant cell death. This suggests that local cell death is not necessary for initiating an astrogliosis response. In this study, viability was not significantly different from the control group from Day 7 onwards, whereas expression of GFAP volume was significantly increased at these timepoints. This also suggests cell death may not be required to sustain astrogliosis.

The live/dead assay used here is an end point assay, meaning that a repeated measure of viability from the same sample could not be performed. Continuous monitoring of viability would have been preferred, thus cumulative viability could be measured whilst also reducing the need to prepare independent samples for the same injury conditions for the three timepoints. Results in this study showed that the number of dead cells was maximal Day 1 post-injury, but subsequently decreased with time. This suggests that the immediate impact of mechanical damage causes some cell death, but with the onset of secondary injury minutes later astrogliosis is initiated in injured but viable astrocytes (Beattie *et al.,* 2002; Sofroniew and Vinters, 2010). Additional extracellular signals, such as damage and release of cytokines from other cell types, and hypoxia are not as faithfully modelled in this system which may influence the viability and behaviour of astrocytes long term.

Astrocyte proliferation is a known characteristic of astrogliosis and has been shown to be prominent around the lesion area, enabling the formation of a compact scar (Sofroniew, 2009). The lack of a focal lesion in this model could have meant there was no signal for defined migration and proliferation of astrocytes around a lesion. Some aspects of astrogliosis, such as proliferation, may not have been faithfully modelled in this study due to the presence of astrocytes cultured in isolation. Neuronal injury has been shown to induce astrogliosis so significant proliferation in an isolated astrocyte culture may not have been detectable without additional extracellular signals (Zhang *et al.,* 2010a). Cullen *et al.,* (2007) observed an increase in total cell density, suggesting a proliferative response to shear deformation in their neuron-astrocyte co-culture model. Clear evidence for astrocyte proliferation was not observed in this study, and the live/dead cytotoxicity assay does not specifically probe for newly synthesised DNA of replicating cells. Instead, the number of viable cells was quantified, which revealed that the number of live cells significantly increased between Days 7 and 14 post-injury, at 50 and 75% displacement, and at a greater rate than the control group. Therefore, assays specifically probing cell proliferation, such as BrdU incorporation, would provide a clearer picture of whether astrocytes proliferate following mechanical injury in this particular model.

The ATPlite assay is also said to evaluate cell viability, through measuring the ATP content of the sample, but can also indicate proliferation and potentially astrocyte reactivity too. Activities associated with astrogliosis- hypertrophy, increased synthesis

and expression of GFAP and CSPGs, proliferation- are ATP dependent activities, thus these activities increase the cells' metabolic demands. Increases in GFAP volume expression were observed as early as Day 1 post-injury and the magnitude of expression was greater at 1000 mm.s^{-1}. However, this was not reflected in the metabolic assay results, particularly on Day 1 at 1000 mm.s^{-1}. More significant changes in ATP content were observed at Day 7 and Day 14 at both velocities. Further, significant cell death was observed Day 1 post-injury but this was not reflected in terms of ATP content. With astrogliosis encompassing a wide array of cellular and molecular changes, this assay may not be sensitive enough to describe astrocyte behaviour.

4.5.3.2 CSPG Expression

Many neural cells express different members of the CSPG family in an organised spatiotemporal pattern, as reviewed by Siebert *et al.,* (2014), and increased CSPG expression has been associated with SCI (Lemons *et al.,* 1999; Moon *et al.,* 2002). In this study, CSPGs released from astrocytes following injury were visualised and quantified through immunolabeling with a CS-56 antibody. Results showed that mechanical injury resulted in increased CSPG expression in the microenvironment, compared to the control group. Expression was maximal at 14 days post-injury, and was significantly greater than at Day 7 at 100 mm.s^{-1}.

CSPG expression has been shown to peak mostly two weeks after injury, in a transection SCI model (Jones *et al.,* 2003). It would be interesting to monitor CSPG expression beyond 14 days to determine whether 14 days also corresponded to peak expression in this study. Reactive astrocytes have been shown to synthesise brevican, neurocan, and phosphacan (Jones *et al.,* 2003; McKeon *et al.,* 1999; Siebert *et al.,* 2014; Wanner *et al.,* 2008) in response to injury and this study supports the notion that reactive astrocytes are a source of CSPGs *in vitro*. However, the antibody used in this study, CS-56, does not distinguish between specific core proteins thus it was not possible to determine the precise identities of the CSPGs synthesised.

Increased CSPG expression is known to be inhibitory to neuronal regeneration, generating a potent physical and chemical barrier against axon regeneration (Ohtake and Li, 2015). Thus, modulation of the inhibitory microenvironment is an attractive target. In particular, enzymatic degradation of CSPGs has been investigated *in vivo* with some successes, including improved axonal sprouting and growth, and recovery of motor function (Bradbury *et al.,* 2002; Silver and Miller, 2004). Subsequently, ChABC-mediated removal of these CSPGs was briefly explored in this *in vitro* study. Results showed that successful removal of CSPGs was achieved with 4 hours treatment with ChABC.

Due to time constraints, only the short term effects of CSPG removal on astrocyte reactivity could be studied. Preliminary results showed that astrocyte reactivity was not affected by CSPG removal, after 48 hours. This could be due to the fact that the injuries modelled were severe thus the astrogliosis response was irreversible. Further, removal of

CSPGs alone may not be enough to reverse or attenuate the process. However, a longer timepoint would need to be explored. One limitation with a long-term study using ChABC is that the enzyme is thermally unstable, with activity shown to be reduced by 50% after 1 hour of incubation, at 37 °C (Tester *et al.,* 2007). This would therefore require repeated treatment with fresh enzyme, which may be cost-inhibiting in the current setup. Due to its neuroinhibitory effects, removal of CSPGs in a more complex astrocyte-neuron co-culture model could also be utilised to evaluate neuronal behaviour following mechanical injury *in vitro*.

Little is known about the effects of CSPG removal on reactive astrocyte behaviour and whether the glial scar can be modulated in this way, since more focus has been placed on the enhancement of axonal regeneration. A study by Milbreta *et al.,* (2014) utilised a rat hemitransection SCI model, with ChABC-mediated digestion of CSPGs immediately following injury. Peak CSPG immunoreactivity and a well-established glial scar was observed at 14 days post-injury. However, digestion of CSPGs resulted in altered astrocyte dynamics: reduced GFAP expression, reduced density of astrocytes surrounding the lesion, reduced interdigitation of processes, and an increased propensity for astrocyte processes to be oriented towards the lesion site. These observations were made from one to ten weeks post-injury. As ChABC was administered before the glial scar matured, its effects on astrocyte behaviour are still not known once the glial scar has already formed. In this study ChABC was administered at 14 days-post injury, but a time point of 48 hours was insufficient to fully evaluate the responses of the astrocytes to CSPG removal. Future research should be directed towards this and 3D models, such as the one used in this study, may be particularly beneficial as more clinically relevant injury mechanisms can be modelled. This may enable a better understanding of the relationship between CSPGs and reactive astrocytes in glial scar dynamics.

4.5.3.3 Analyses of Cytokine and RNA Expression

Cytokines are signalling proteins which play an important role in regulating the immune response to SCI. Astrocytes have been shown to release numerous pro- and anti-inflammatory cytokines in response to injury (Mukhamedshina *et al.,* 2017; Stammers *et al.,* 2012). An ELISA assay was attempted to measure the levels of IL-6, IL-10 and IL-1β cytokines in the media surrounding the gels following injury. However, the ELISA assay used here was not sensitive enough to detect the low concentration of cytokines present in the samples. Lyophilisation of the media and reconstituting it into a smaller volume in order to concentrate the cytokines was unsuccessful.

Kirk (2018) reported the successful use of the ELISA assay to quantify cytokine expression following simulated contusion injury using the BOSE. The study used the same ELISA assay kit as in this study (Rat IL-6 DuoSet ELISA, Bio-Techne) and reported cytokine levels of IL-6 and TNF-α of greater than 300 and 200 pg.mL^{-1}, respectively. This was despite using smaller hydrogels with a lower density of astrocytes: 5 x 10^4 cells in 100 µL gels. The input velocity used was 3000 mm.s^{-1}, although results in this project showed that the maximum velocity achieved was only 1176.25 $\pm$ 3 mm.s^{-1}

(Chapter 3). Further, displacement depths of 50, 80, and 100% gel height were used which is within the upper range of those used in this study. The differences observed could be due to the fact that Kirk (2018) modelled a focal contusion injury, with a smaller impaction tip (3.34 mm rounded) meaning force was distributed over a smaller area, thus the astrocytes may have responded differently.

Extraction of RNA for RT-PCR analysis was also attempted but could not be explored in detail due to time constraints. The advantages of using this type of analysis is that little starting material is required and multiple targets can be probed. Genomic analysis of mouse astrocytes in response to ischaemic and lipopolysaccharide (LPS) endotoxin treatment was performed by Zamanian *et al.,* (2012), using Affymetrix GeneChip Arrays. An interesting observation made was that at least 50% of the altered genes measured were specific to a given injury mechanism. Therefore, it would be interesting to use the same assay to compare gene expression of astrocytes in response to different mechanical injuries. In future, using multiplex ELISA assays and gene profiling would provide a better profile of astrocytes following injury, as more targets of interest can be targeted quantitatively.

4.6   Conclusions

Mechanical trauma simulating contusion injury *in vitro*, using the BOSE 5110 Electroforce BioDynamic apparatus, resulted in morphological changes in astrocytes which were characteristic of astrogliosis observed elsewhere *in vitro* and *in vivo*. Multiple aspects of astrogliosis were modelled *in vitro*, despite comprising an isolated population of astrocytes. This model provides researchers with a simple but effective tool for probing TSCI and cellular pathologies, with the capability of performing a wide range of assays beyond those used in this study. This chapter addressed the main objectives of the project, which were to evaluate the biological responses of astrocytes to simulated contusion and distraction injury, and to investigate the relationship between the primary mechanical input and responses of primary astrocytes cultured in isolation (Chapter 1).

The specific objectives set out in this chapter were met with the following observations:

I. *Verify the accuracy and precision of the BOSE 5110 Electroforce BioDynamic (BOSE):*

   - The input displacement and velocity parameters were achieved with high precision and accuracy and matched the data from Chapter 3.

II. *Calculate the kinetic outputs following simulated:*

   - Energy applied was calculated using the load displacement graphs, which showed a significant step-wise increase in energy applied with increasing displacement depth and velocity, except between 100 mm.s^{-1}–75% and 1000 mm.s^{-1}–25%.

III. *Measure the responses of primary astrocytes to contusion injury:*

- Astrocytes responded to mechanical injury in a variety of ways which were characteristic of astrogliosis, and differed from the control. Morphologically, astrocytes became hypertrophied, ramified, and overlapping of domains was observed.

- Reactive astrocytes in experimental groups expressed CSPGs at a greater level compared to the control group. Further, significant cell death was observed at Day 1 post-injury and ATP content was significantly increased at Day 14 post-injury.

IV. *Compare the biological responses of primary astrocytes to contusion injury against a known chemical inducer of astrogliosis, TGF-β1:*

- Astrocytes subjected to mechanical contusion injury were observed to be more reactive than astrocytes treated with TGF-β1 (positive astrogliosis control).

V. *Evaluate the effects of contusion injury mechanics on astrocyte responses:*

- Both displacement and velocity were correlated with astrocyte reactivity, with a stronger correlation between velocity and GFAP volume.

Several hypotheses were also postulated at the beginning of the study:

I. *There is no statistical difference between the reactivity of astrocytes in response to contusion injury compared to no injury (control).*

- Mechanical simulation of contusion injury induced astrocyte changes which were consistent with astrogliosis and which was not observed in the control groups.

II. *There is no statistically significant relationship between injury velocity and astrocyte reactivity.*

- An increase in injury velocity resulted in an increase in astrogliosis severity, in terms of GFAP volume, sphericity, and CSPG expression.

III. *There is no statistically significant relationship between injury displacement depth and astrocyte reactivity.*

- An increase in displacement depth resulted in a corresponding increase in astrocyte reactivity at 100 mm.s^{-1}, but not at 1000 mm.s^{-1}, specifically in terms of morphology.

IV. *There is no statistically significant relationship between astrocyte reactivity and time.*

- The astrogliosis response progressed over time, in terms of metabolic activity and CSPG expression. At 1000 mm.s^{-1}, astrocyte morphology did not change significantly over time.

Chapter 5

The Effects of Varying Displacement Depth and Velocity on Astrocyte Responses in an *In Vitro* Model of Distraction Spinal Cord Injury

5.1 Introduction

Traumatic distraction spinal cord injury is another common mechanism of TSCI, in which the vertebrae and spinal cord are subjected to axial tensile forces, and can arise from hyperextension or flexion-distraction events (Dumont *et al.,* 2001). Whilst there are a myriad of contusion models available, distraction injury remains less frequently modelled *in vivo* and *in vitro*. The tools available to model distraction injury lag behind in terms of reproducibility and validation, and the main limitation of distraction models is the high variability observed in outcome measures, even within injury grades (Chen *et al.,* 2016; Cheriyan *et al.,* 2014). Further, relatively low distraction velocities have been modelled which are less clinically relevant ($1 - 10$ mm.s^{-1}; Chapter 1 Table 1.5). The development of the University of British Columbia (UBC) multimechanism device has seen an improvement in this, with a distraction velocity of up to 1000 mm.s^{-1} modelled in rats (Chen *et al.,* 2016; Choo *et al.,* 2008, 2007, 2009).

It has become increasingly apparent that mechanism-specific characteristics of injury exist, and that these differences could be exploited to enhance treatment paradigms. A number of *in vivo* studies have directly compared two or more TSCI mechanisms within the same study and distraction injury has been shown to be morphologically distinct from contusion in rodents (Bhatnagar *et al.,* 2016; Chen *et al.,* 2016; Choo *et al.,* 2008, 2007; Guo *et al.,* 2019). For instance, contusion is typically a focal injury that causes localised membrane compromise and the lesion cavity is confined to the epicentre. Contrastingly, distraction injuries are more diffuse and result in widespread membrane compromise and an extended lesion cavity (Choo *et al.,* 2007; Wang *et al.,* 2019). These morphological differences have also extended to temporal behavioural differences (Chen *et al.,* 2016; Guo *et al.,* 2019). As such, it is of benefit to patients, healthcare providers, and researchers to understand the effects of different injury mechanisms on physiological and behavioural outcomes.

So called stretch injury models have been developed *in vitro* to investigate the effects

of rapid mechanical stretch on glial and neuronal physiology (Ahmed *et al.,* 2000; Cullen and LaPlaca, 2006; Cullen *et al.,* 2007; Ellis *et al.,* 1995; Geddes-Klein *et al.,* 2006; Miller *et al.,* 2009). Altered astrocyte cellular dynamics have been observed following injury: increased GFAP expression (Miller *et al.,* 2009), increased cell density (Cullen *et al.,* 2007), membrane damage and altered ATP content (Ahmed *et al.,* 2000). However, it should be noted that whilst these have been called 'stretch models' shear deformation was typically applied to cell-seeded flexible membranes, thus strain was transferred from the substrate to the cells. Distraction injuries likely involve shear forces, but pure uniaxial tensile force was modelled in this study in a 3D model.

In vivo distraction models using defined distraction lengths have demonstrated that injury severity is proportional to displacement (Dabney *et al.,* 2004; Seifert *et al.,* 2011; Wu *et al.,* 2016). Dabney *et al.,* (2004) modelled mild (3 mm), moderate (5 mm), and severe (7 mm) distraction injury in a rat model and concluded that distraction length was the primary determinant of injury, regardless of velocity (1, 5 or 10 mm.s^{-1}). Like the other studies, relatively low velocities were used, so it is difficult to determine whether these observations are reflected at higher, more clinically relevant velocities. Chen *et al.,* (2016) and Choo *et al.,* (2008, 2007) characterised the histopathological and functional outcomes of high velocity (up to 1000 mm.s^{-1}) spinal distraction injuries in rats. However, velocity nor displacement was varied as the aim was to compare the damage patterns of different injury mechanisms.

Displacement parameters varied between studies depending on specimen dimensions, injury location, animal type, and the optional incorporation of flexion into the injury model. Wu *et al.,* (2016) used a custom-designed distractor to apply caudal distraction to L1 − L3 segments of male rabbits. Displacement was calculated as a percentage of the distance between the L1 and L3 vertebral segments: control (0%), 10%, 20%. and 30%. Other studies selected discrete displacement values: 5.6 mm in adult male Sprague-Dawley (SD) rats (Chen *et al.,* 2016), 5.1 − 6.1 mm in adult male SD-rats (Choo *et al.,* 2009), 4.1 mm in adult male SD-rats (Choo *et al.,* 2008, 2007), and 3 mm (mild), 5 mm (moderate), and 7 mm (severe) in adult female Long-Evans rats (Dabney *et al.,* 2004). Yang *et al.,* (2013) used transcranial electrical stimulation-motor evoked potential (TES-MEP) signals to increase displacement in 1 mm increments until a SCI was achieved in pigs (as defined by a reduction in >80% TES-MEP signal). Results from Chapter 3 demonstrated that failure of the hydrogel was observed when distraction displacement values of 40% gel length and above were used (Section 3.4.4.2). Therefore, three distraction lengths were selected: 10, 20, and 30% of the gel gauge length.

In summary, there is growing evidence for mechanism-specific differences in rodent pathophysiology and behaviour. This highlights the importance of modelling the variety of injury mechanisms observed in humans in order to better capture the heterogeneity of TSCI, and improve preventative and interventional treatment regimes. However, whilst multiple TSCI mechanisms have been modelled *in vivo* to evaluate physiological and behavioural outcomes, these strains have not been modelled and directly compared *in*

vitro, particularly for single cell populations.   Therefore, primary astrocyte-seeded hydrogels were subjected to uniaxial tensile forces, modelling the biomechanics of a distraction injury at a velocity of 100 mm.s^{-1}.

5.2   Aim and Objectives

The aim of this chapter was to evaluate the responses of primary astrocytes to tensile forces experienced during distraction spinal cord injury, using a range of displacement and velocity parameters representing different injury severities.

The specific objectives were as follows:

I. Verify the accuracy and precision of the BOSE 5110 Electroforce BioDynamic (BOSE) at simulating distraction injury at a velocity of 100 mm.s^{-1} and distraction lengths of 10, 20, and 30%, using primary astrocyte-seeded collagen hydrogels.

II. Calculate the kinetic outputs following distraction injury using the BOSE apparatus, including the impact velocity, peak displacement, peak load, and energy applied.

III. Measure the responses of primary astrocytes to distraction injury through GFAP immunostaining, CSPG expression, metabolic activity and viability analyses.

IV. Compare the biological responses of primary astrocytes to mechanical distraction to a known chemical inducer of astrogliosis, TGF-β1.

V. Compare the behaviour of astrocytes in response to contusion and distraction injury.

The null hypotheses postulated were as follows:

I. There is no statistical difference between the reactivity of astrocytes in response to distraction injury compared to no injury (control).

II. There is no statistically significant relationship between distraction length and astrocyte reactivity.

III. There is no statistically significant relationship between astrocyte reactivity and time following distraction injury.

5.3   Specific Materials and Methods

5.3.1   Preparation of astrocyte-seeded hydrogels

Distraction tethered moulds were disinfected and sterilised by soaking the individual components (mould pieces, parafilm, mesh bars) in 1% Trigene (v/v), followed by 70% (v/v) ethanol. The stainless steel dowels and screws were sterilised by dry heat (Chapter 2; Section 2.5.1.2). All components sterilised in solutions were allowed to air dry within a Class II safety cabinet. Once dry, the moulds were assembled in 6-well plates using sterile gloves and forceps.

Hydrogels seeded with 5×10^5 primary rat astrocytes per mL of gel were prepared, as described in Chapter 2 (Section 2.5.5). A gel volume of 150 µL per mould was used. The gels were allowed to set by placing them in a humidified incubator at 37 °C, 8% CO_2:92% air. Once set, each gel was overlayed with 2 mL cell culture medium. After 24 hours incubation, the parafilm was removed and discarded using sterile forceps. TGF-$\beta 1$ treatment was used as a positive astrogliosis control. For these gels, complete cell culture medium supplemented with TGF-$\beta 1$ (10 ng.mL^{-1}) and pipetted on top of the gels, refreshing every two days.

5.3.1.1   Sample Setup in the BOSE

To transfer the moulds from the well-plate and secure them into the tensile grips of the BOSE, a pair of sterile forceps was used to grasp onto a screw and transfer it to the lower grip. The end of the tensile grip was aligned with the end point of the scribe on the mould and secured by tightening the knurl screw. Under displacement control, the lower grip was moved upwards towards the upper grip until the mould entered the upper grip and the end point of the scribe aligned with the end of the upper tensile grip. The upper grip was then closed and tightened around the mould by tightening the knurl screw. The screws were then removed, followed by the dowels. Tensile loading forces were now able to be applied.

5.3.2   BOSE Waveform Setup and Data Acquisition

For general assembly and set up of the BOSE Electroforce BioDynamic 5110, refer to Chapter 2 (Section 2.5.8). The parameters for distraction injury, including the input displacements, velocities, and PID values were developed in Chapter 3, and defined in Table 3.3. The waveform regime, defined to represent a distraction injury, was defined in the following steps:

1. **Dwell:** 10 ms

2. **Ramp:**

    (a) Velocity: 100 mm.s^{-1}

    (b) Relative displacement: 10, 20, and 30% of the gel gauge length (8.25 mm). This represented displacement lengths of +0.825, +1.650, and +2.475 mm,

respectively. Note, displacement is positive as the lower motor platen moves downwards, away from the load platen.

3. **Dwell**: 100 ms

4. **Ramp:**

    (a) Velocity: 100 mm.s^{-1}

    (b) Relative displacement: Return to 0% distraction

Following this, the following data was exported into Excel: time (s), experimental displacement (mm), axial command (input displacement, mm), load (N).

The data acquisition settings were as follows:

- Scan time = 0.4096 s

- Number of scan points = 2048

- Number of scans = 1

From the acquired raw data the following was calculated: peak experimental displacement, peak experimental velocity, and energy applied. Energy applied was calculated by performing a trapezoidal integration of the area underneath the load-displacement curve for each sample, using Equation 4.2.

5.3.3   Immunohistochemical Staining

Astrocyte-seeded hydrogels were processed for immunofluorescent staining using the methods described in Chapter 2 (Section 2.5.7). A 23 G needle was used to detach the gel from the mould. The gels were transferred to a 48-well plate to reduce the volume of reagents required for IHC processing. Primary antibodies specific for glial fibrillary acidic protein (GFAP) and chondroitin sulfate proteoglycan (CS-56) were used to label astrocytes and CSPGs, respectively, and DAPI was used as a nuclear counterstain. Details of the antibodies used, including their dilutions are described in Table 2.1 (Chapter 2 Section 2.4). Hydrogels were incubated with isotype control antibodies, and omission of the primary antibodies was routinely used as the negative controls.

5.3.4   Confocal Image Acquisition

Confocal z-stack images were acquired using a Zeiss LSM880 Axio Imager.Z2 upright microscope (Chapter 2 Section 2.5.9.3). A total of five fields of view were acquired for each gel (Figure 5.1).
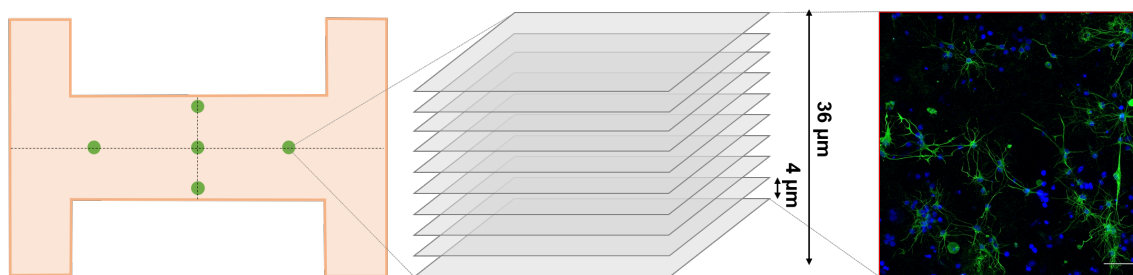
Figure 5.1: Image acquisition positions of a hydrogel following experimental distraction injury. Five fields of view were imaged per gel, with images acquired from the same five positions, as denoted by the green dots. At each field of view, a 36 µm z-stack was acquired, composed of 10 z-slices at 4 µm intervals. Confocal images presented in this report are maximum intensity projections.

The surface of the gel was located, as defined by the z-position in which the cells first became visible. Each z-stack was 36 µm in depth, with 10 slices acquired at 4 µm intervals. To ensure consistency in image acquisition, the laser settings were configured for the sample with the greatest GFAP expression. Confocal images of cell-seeded hydrogels presented in this study are maximum intensity projections generated from their respective stacks.

5.3.5   Image Analysis

Evaluation of astrocyte morphology and behaviour, including GFAP volume, sphericity and CSPG expression was undertaken using the same image analysis protocols detailed in Chapter 4 (Section 4.3.6).

5.3.6   Analysis of Astrocyte Viability

Viability of the astrocytes following simulated distraction injury was assessed using the LIVE/DEAD™Viability/Cytotoxicity Assay Kit (Chapter 2; Section 2.5.3.6). The hydrogels were detached and removed from the distraction mould using a 23 G needle, then transferred to a 48-well plate to reduce the volume of live/dead reagents required per sample. The positive cell death control consisted of cell-seeded gels treated with 70% (v/v) methanol for one hour. After aspirating the cell culture medium, the gels were washed twice with 500 µL PBS to remove residual esterase activity (methanol for positive control samples). A volume of live/dead solution twice that of the gel (i.e. 300 µL) was pipetted on top of each gel. The plate was then covered with foil and incubated for 1 hour on an orbital shaker (90 rpm), at 37 °C, 8% CO_2:92% air. The live/dead solution was then discarded and 3x 5 minute PBS washes were performed at 37 °C, on an orbital shaker (90 rpm). The cells were imaged using confocal microscopy, and percentage viability was calculated using Equation 4.4.

5.3.7   Quantification of Astrocyte Metabolic Activity

Metabolic activity of astrocytes following simulated distraction injury was performed using the ATPlite™Luminescence Assay System (Chapter 2; Section 2.5.6). The hydrogels were detached and removed from the distraction mould using a 23 G needle, then transferred to

a 48-well plate to reduce the volume of assay reagents required per sample. The cell culture medium was aspirated from each gel and replaced with mammalian cell lysis solution at a volume twice that of the gel (300 µL). The gels were incubated at room temperature for 30 minutes, with agitation at 700 rpm to lyse the cells and release the ATP. Working under dark conditions, a volume of 50 µL from each sample was transferred to an individual well of a 96-well Optiplate™. An equal volume of substrate solution was then added to each well. The plate was sealed, covered with foil, and incubated at room temperature for 15 minutes with agitation at 700 rpm. The plate was then placed into the plate reader spectrophotometer and dark adapted for 10 minutes. Luminescence was measured at 570 nm, with the data being exported into Excel for analysis. The positive cell death control consisted of cell-seeded gels treated with 70% (v/v) methanol for one hour.

5.4   Results

Distraction SCI was modelled *in vitro* using an input velocity of 100 mm.s^{-1}, and distraction lengths of 10, 20, and 30% of the gauge length of the gel. Time (s), experimental displacement (mm), axial command (input displacement, mm), and load (N) data was recorded by the BOSE and exported to Excel for processing. At Days 1, 7, and 14 after injury, the gels were processed in order to evaluate a number of astrocyte responses: cell viability by live/dead staining, metabolic activity using the ATPlite assay, astrocyte reactivity by immunostaining for GFAP, and expression of CSPGs by immunolabelling with a CS-56 antibody.

5.4.1   Kinetic Outputs

Following distraction injury, the following kinetic outputs were calculated: the peak experimental displacement (mm), peak velocity (mm.s^{-1}), peak load (N), and energy applied (mJ) (Appendix E; Table 6.12). The peak displacement and velocity was calculated in order to verify the characterisation results in Chapter 3 and ensure that the correct output values were being achieved with the experimental samples. Because the hydrogels were cast into pre-manufactured moulds the sample dimensions, including gauge length, were identical ($\pm$ 0.01 mm). Therefore, there was no requirement to calculate the length of each sample before simulating the injury and the input displacement lengths were the same for each distraction group (Section 5.3.2).

There was little variation in the peak experimental displacement achieved at all distraction lengths, as demonstrated by the small standard errors (Figure 5.2). The percentage error was calculated using the input and output displacement value as the theoretical and experimental values, respectively. The mean percentage error at 10, 20, and 30% distraction was 3.2, 0.40, and 0.30%, respectively.
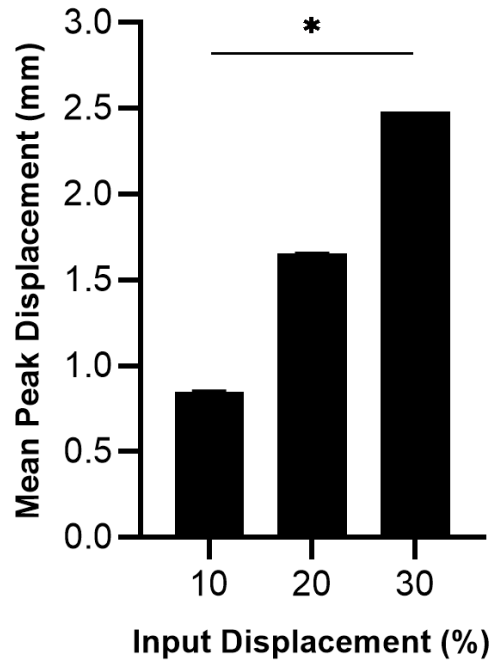
Figure 5.2: Peak experimental displacement achieved at various distraction lengths. Astrocyte-seeded hydrogels were subjected to distraction injury at 100 mm.s^{-1} to displacement lengths of 10, 20, and 30%. Data presented as the mean $\pm$ SEM and analysed by one-way ANOVA with Tukey's post-hoc test. Significance levels * p$<$0.05. N=9.

The error in distraction length was greater at 10%, whereas a similar error was calculated at 20 and 30%. This was attributed to the larger overshoot which was observed at 10% displacement during the distraction phase (Figure 5.3). However, each distraction group was significantly different from each other.
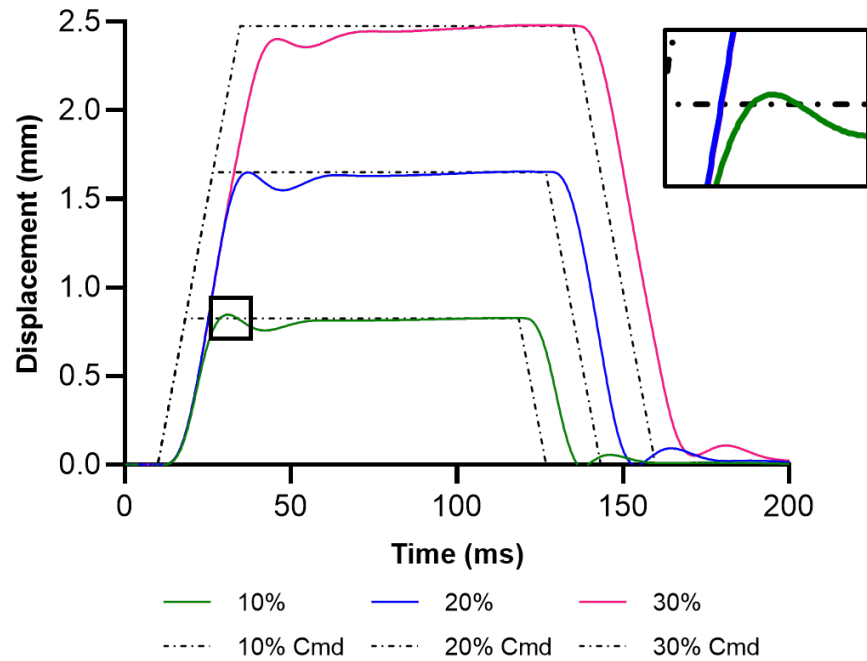
Figure 5.3: Displacement profiles after applying distraction loads at 100 mm.s^{-1} show a displacement overshoot at 10% distraction during the distraction phase. Astrocyte-seeded hydrogels were subjected to distraction injury at 100 mm.s^{-1} to displacement lengths of 10, 20, and 30%. In the first 50 ms of the experiment where the distraction was applied to the sample, a displacement overshoot was observed at 10% displacement and this represented the peak displacement. At 20 and 30% distraction, the peak displacement was not achieved until later during the dwell phase. Solid coloured lines represent the experimental profiles; dashed lines represent the input (command) profile. N=9.

As discussed in Chapter 3, a velocity of 1000 mm.s^{-1} could not be achieved under tensile forces, thus a velocity of 100 mm.s^{-1} was used with three different distraction lengths. Unlike contusion injury, where the impact and peak velocity was calculated, there was no impact with the distraction injury and so only the peak velocity was calculated. The input velocity of 100 mm.s^{-1} was achieved at all distraction lengths (Figure 5.4). However, an overshoot in velocity was observed in all groups: 107.22 $\pm$ 2 mm.s^{-1} at 10%, and 115.56 $\pm$ 1 mm.s^{-1} at both 20 and 30%. The error in velocity was 8.33% at 10% distraction, and 15.56% at 20 and 30% distraction. This was within the range of errors calculated in the characterisation study in Chapter 3 (Section 3.4.4.1).
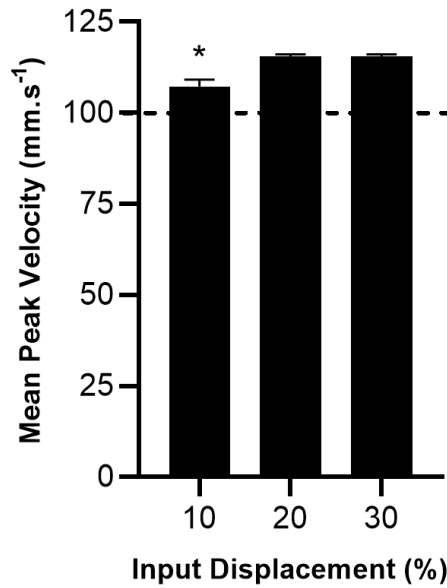
Figure 5.4: Peak experimental velocity achieved at various distraction lengths. Astrocyte-seeded hydrogels were subjected to distraction injury at 100 mm.s^{-1} to displacement lengths of 10, 20, and 30%. Data presented as the mean $\pm$ SEM and analysed by one-way ANOVA with Tukey's post-hoc test. Significance levels * $p < 0.05$. N=9.

The output load and displacement data was also used to calculate the energy applied following distraction injury (Figure 5.5). The mean energy applied increased as distraction length also increased. Further, with each increase in distraction length, there was a significant increase in energy applied. The mean energy applied increased from 0.057 ± 0.003 at 10% distraction to 0.143 ± 0.01 mJ at 30% distraction. Between 10 and 20% distraction there was a near doubling in energy applied, although the relationship was not directly proportional.
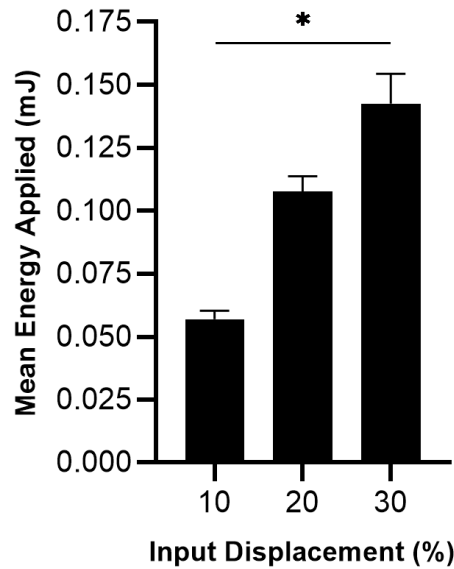
Figure 5.5: Mean energy applied scales with the distraction length. Astrocyte-seeded hydrogels were subjected to distraction injury at 100 mm.s^{-1} to displacement lengths of 10, 20, and 30%. Energy applied was calculated by performing a trapezoidal integration of the area under the curve of the load-displacement curves. Data presented as the mean $\pm$ SEM and analysed by one-way ANOVA with Tukey's post-hoc test. Significance levels * p<0.05. N=9.

5.4.2 Primary Astrocyte Behaviour Following a Distraction Injury

Changes in astrocyte morphology in response to mechanical trauma have previously been shown, both in this project (Chapter 3) and other *in vitro* studies. However, there has been no direct comparison of astrocyte behaviour between different injury mechanisms in those studies. Therefore, a distraction injury was modelled in this study and primary astrocyte behaviour was evaluated using the same outcome measures as for the contusion study, including GFAP expression to evaluate morphology, viability, metabolic activity, and chondroitin sulfate proteoglycan (CSPG) expression. Initial grouping of data by imaging position was performed in order to determine whether there were any differences in the outcome measures evaluated based on the location of the gel that was imaged. However, there were no significant differences and so all the values were analysed together regardless of location.

5.4.2.1 GFAP Expression and Gross Morphology

The morphology of primary astrocytes was evaluated following distraction injury, using an input velocity of 100 mm.s^{-1}, and distraction lengths of 10, 20, and 30% of the gel gauge length. This was achieved through immunolabelling astrocytes with an anti-GFAP antibody. As a cytoskeletal marker, this enabled visualisation of gross cell morphology (Figure 5.6).
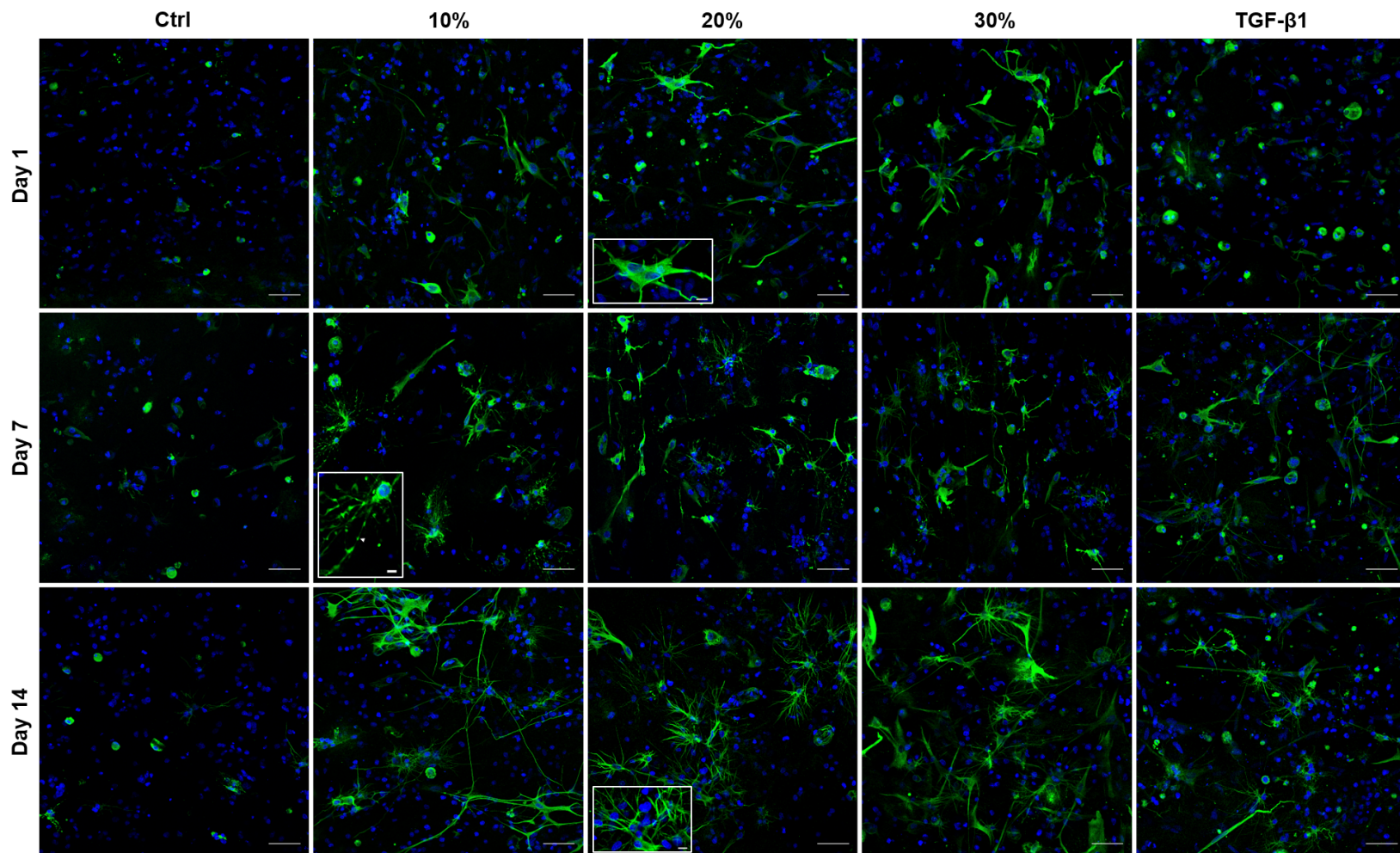
Figure 5.6: Progression of astrogliosis over 14 days following simulated distraction injury at 100 mm.s^{-1}. Representative maximum intensity projection images (36 µm depth) of astrocyte-seeded hydrogels subjected to distraction injury. Inset image at 10% Day 7 and 20% Day 1 demonstrates the presence of process beading and swollen cell bodies, respectively. Astrogliosis appeared more severe with increasing distraction length and time, with astrocytes progressing from less ramified, with distinct domains, to hypertrophied and ramified with domain overlapping (inset Day 14 20%). Cells were labelled with a polyclonal antibody against GFAP (astrocytes, green) and counterstained with DAPI (nuclei, blue). Scale bar represents 50 µm and 10 µm (inset).

Under control conditions the majority of the cells were GFAP-negative, with few cells labelling positive with GFAP. These GFAP-positive cells were small and rounded in morphology, which was maintained over the 14-day period suggesting little reactivity. Chemical treatment of astrocytes with TGF-β1 resulted in an astrogliosis response as expected. At Day 1, the majority of GFAP-positive cells remained rounded in morphology, but were more hypertrophied compared to the astrocytes in the control group. Evidence of ramification was also observed but not as frequently as astrocytes in the experimental distraction injury groups on Day 1. With time, the astrocytes became increasingly more reactive, as shown by the increased ramification of processes, hypertrophy, and overlapping of domains. GFAP reactivity was calculated by calculating the percentage of GFAP-positive cells out of the total number of nuclei. Astrocytes in the experimental groups (injury and TGF-β1) were significantly more GFAP reactive compared to the control (mean 8 $\pm$ 1% GFAP-positive), with a maximum of 21% GFAP-positive astrocytes (data not shown). There was no significant difference in GFAP reactivity between the experimental groups.

Upon application of mechanical distraction injury a change in morphology was observed. From as early as Day 1 post-injury, hypertrophy and ramification was observed but with little overlapping of domains. Differences in reactivity were observed between the distraction groups at this time point. For instance, at 10% distraction, alongside non-reactive cells which were small and rounded there were astrocytes which were hypertrophied and extended a number of processes. At 30% distraction astrocytes were observed to be more hypertrophied compared to those at 10% distraction, with more processes.

As time progressed, the extent of ramification increased and the majority of GFAP-positive cells appeared morphologically reactive. There was also evidence of astrocyte process beading and fragmentation (Figure 5.6 inset). At Day 14 post-injury, astrocytes were observed to possess a higher density of processes (although not quantified), which were finer and in some cases extended over longer distances compared to astrocyte processes on Day 1. Further, increased domain overlapping was observed on Day 14 which contrasts to astrocytes at the earlier timepoints where, although they were hypertrophied and ramified, there were fewer finer processes and less interdigitation.

Three-dimensional image analysis was performed to measure the volume of GFAP expressed per cell (Figure 5.7). The mean volume of GFAP expressed per cell for astrocytes in the control group remained stable throughout the 14-day time period, with no significant changes (mean volume 587.76 $\pm$ 30 μm^3 across all time points).
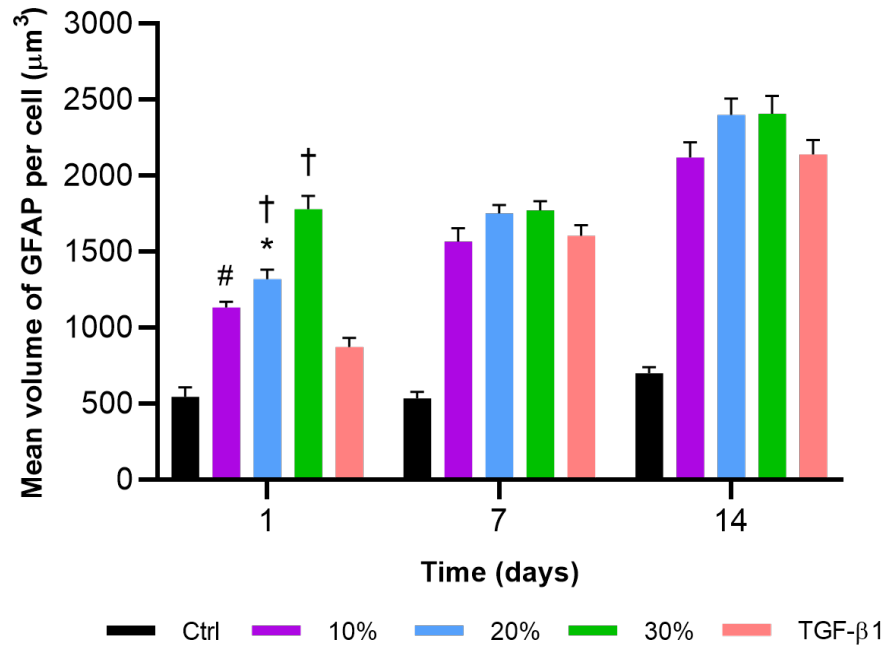
Figure 5.7: Volume of GFAP expression in astrocytes following simulated distraction injury at 100 mm.s^{-1}. Data presented as the mean $\pm$ SEM and analysed by two-way ANOVA. All experimental groups were significantly greater than the control group at each time point (Dunnett's post-hoc, $p<0.05$). Significance levels * $p<0.05$ (20% vs. 30%, Tukey's post-hoc); # $p<0.05$ (10% vs. 30%, Tukey's post-hoc); † $p<0.05$ (vs. TGF-β1, Tukey's post-hoc). N=3.

At Day 1 post-injury, the GFAP volume of astrocytes in all distraction injury groups was significantly greater than the control. The mean volume of GFAP expressed per cell increased significantly from 1134.42 ± 30 at 10% to 1781.22 ± 90 µm^3 at 30% distraction. The GFAP volume of astrocytes in the TGF-β treated group was significantly higher compared to the control, but significantly lower than the 20 and 30% distraction groups. At Day 7 post-injury, the volume of GFAP expressed per cell was significantly higher than the control in all of the experimental groups. Further, there was no significant difference between any of the experimental groups, with a mean volume of 1671.22 ± 40 µm^3 across all groups. A similar trend was observed at Day 14 post-injury as at Day 7: GFAP volume was significantly higher than the control in all of the experimental groups. GFAP volume was slightly higher in the 20 and 30% distraction groups but there was no statistically significant difference between any of the experimental groups.

Considering each displacement group individually, over time, GFAP volume of astrocytes in the 10 and 20% distraction, and TGF-β1 treated groups increased significantly at each time point. At 30% distraction, there was no significant change in GFAP volume between Days 1 and 7 (1781.22 ± 90 µm^3 vs. 1773.31 ± 60 µm^3, $p>0.05$), but there was a significant increase between Days 7 and 14. Astrocyte GFAP volume was greatest on Day 14 for all experimental groups, with an overall mean volume of 2279.16 ± 60 µm^3 across all experimental groups.

5.4.2.2 Sphericity

The sphericity of the astrocytes, how closely the shape of each cell resembled a perfect sphere, was another morphological measurement used to describe the reactivity of the cells in response to distraction injury (see Chapter 4 Section 4.3.6.2 and Equation 4.3). Figure 5.8 illustrates the sphericity of astrocytes, following simulated distraction injury at 100 mm.s^{-1} and distraction lengths of 10, 20, and 30%, over a 14-day time period. Sphericity of astrocytes in the control group significantly decreased between Days 7 and 14 (from 0.45 $\pm$ 0.02 to 0.37 $\pm$ 0.02 AU), although remained significantly higher than the experimental groups.
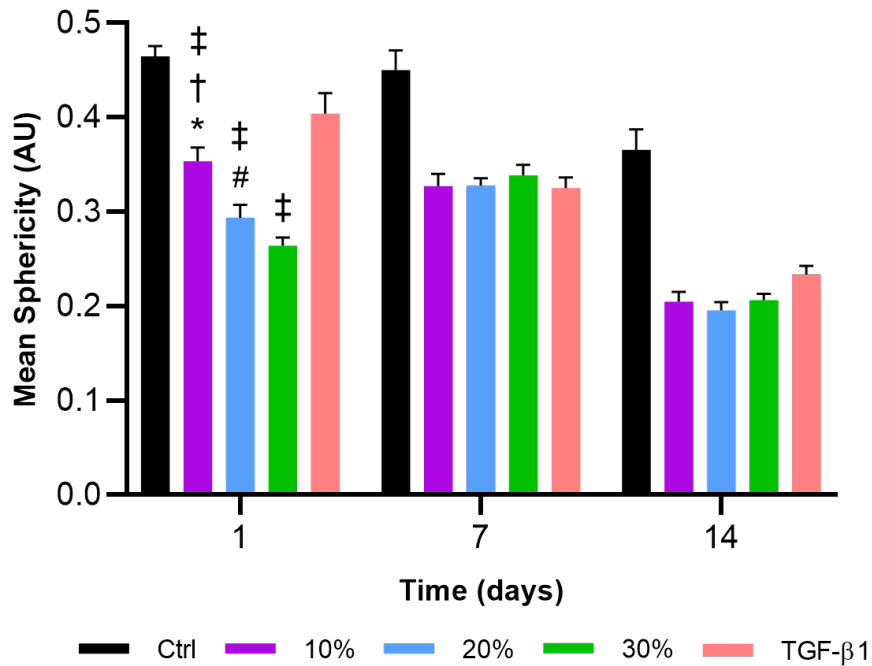
Figure 5.8: Astrocyte sphericity following simulated distraction injury at 100 mm.s^{-1}. Data presented as the mean $\pm$ SEM and analysed by two-way ANOVA. All experimental groups were significantly lower than the control group at each time point (Dunnett's post-hoc, $p<0.05$). Significance levels * $p<0.05$ (10% vs. 20%, Tukey's post-hoc); # $p<0.05$ (20% vs. 30%, Tukey's post-hoc); † $p<0.05$ (10% vs. 30%, Tukey's post-hoc); ‡ $p<0.05$ (vs. TGF-β1, Tukey's post-hoc). N=3.

At Day 1 post-injury, the sphericity of astrocytes in all experimental groups was significantly lower than those in the control group. As the distraction length was increased, there was also a significant step wise reduction in sphericity, from 0.35 $\pm$ 0.02 AU at 10% distraction to 0.26 $\pm$ 0.01 AU at 30% distraction. Although sphericity of astrocytes in the TGF-β1 treated group was significantly lower compared to the control group, it remained significantly greater compared to the experimental distraction injury groups (mean 0.40 $\pm$ 0.02 AU).

At Day 7 post-injury, the sphericity of astrocytes was significantly reduced to a similar level, compared to the control group and there were no significant differences in sphericity between any of the experimental groups. The overall mean sphericity was 0.33 $\pm$ 0.01 AU across all of the experimental groups. Similarly, sphericity of astrocytes was

reduced to a similar level in all experimental groups at Day 14 post-injury, with a mean of 0.24 ± 0.01 AU across all experimental groups.

Considering each experimental group over time, it was observed that the sphericity of astrocytes in the TGF-β1 treated group significantly decreased at each time point, from 0.40 ± 0.02 on Day 1 to 0.23 ± 0.01 on Day 14. Conversely, there was no change in sphericity between Days 1 and 7 at 10 and 20% distraction, and sphericity actually increased significantly at 30%. Between Days 7 and 14, astrocyte sphericity significantly decreased in all experimental groups. Further, sphericity was at its lowest on Day 14, suggesting reactivity was maximal at this time point.

5.4.3 Primary Astrocyte Viability Following Simulated Distraction Injury

Astrocyte viability was evaluated over 14 days using the LIVE/DEAD™Viability/Cytotoxicity Assay in order to determine whether tensile forces resulted in alterations to cell viability. Viability was calculated as the percentage of live cells out of the total number of live and dead cells counted (Figure 5.9).

Astrocytes in the control group remained viable and viability was stable across the 14-day time period, with an overall mean viability of $82.67 \pm 1\%$. TGF-β1 treatment had no effect on astrocyte viability over the 14-day time period, with viability being non-significant compared to the control. The mean viability of astrocytes in this group was $81.67 \pm 1\%$, across the 14-day time period. Treatment of astrocytes with 70% (v/v) methanol (positive cell death control) successfully resulted in a significant reduction in viability compared to the control.
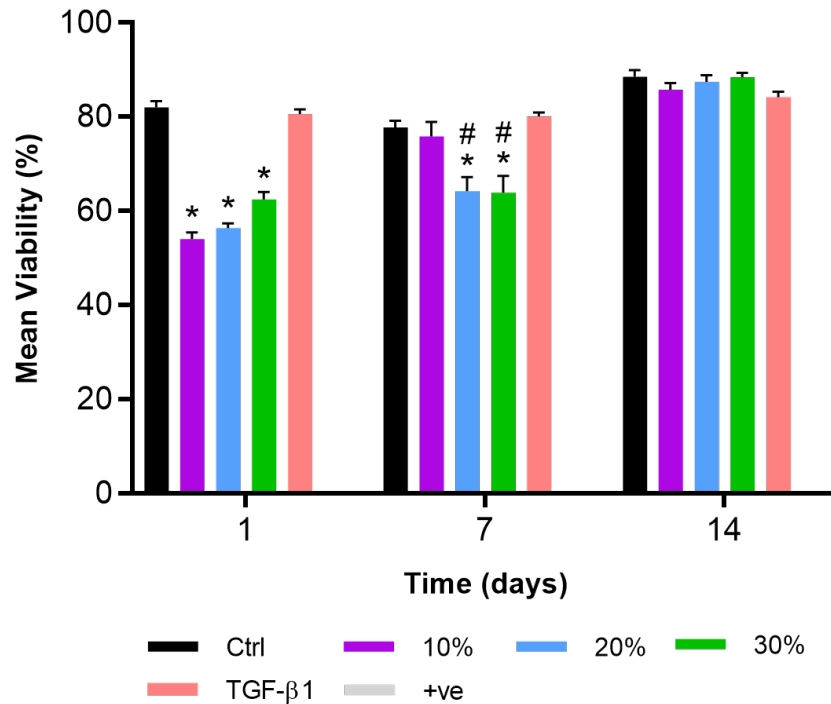
Figure 5.9: Astrocyte viability following simulated distraction injury at 100 mm.s^{-1}. Data presented as the mean $\pm$ SEM and analysed by two-way ANOVA. Significance levels * p<0.05 (vs. ctrl, Dunnett's post-hoc); # p<0.05 (vs. 10%, Tukey's post-hoc). N=3.

At Day 1 post-injury, viability was significantly reduced in all distraction injury groups compared to the control. Viability was lowest in the 10% distraction length group (54.03 $\pm$ 1%); however, there was no significant difference in viability between the different distraction lengths. At Day 7 post-injury, viability remained significantly lower than the control at 20 and 30% distraction, but not at 10%. No significant difference was observed in viability between 20 and 30%, with mean viabilities of 64.17 $\pm$ 3% and 63.85 $\pm$ 4%, respectively. At Day 14 post-injury, the viability of astrocytes in all of the experimental distraction injury groups were not significantly different compared to the control. There were also no significant differences in viability between the distraction groups.

The viability of astrocytes at each distraction length, over time, was also evaluated. At Day 1 post-injury, viability in the 10% distraction group decreased significantly but subsequently recovered to a value which was not significantly different to the control at Day 7 (75.85 $\pm$ 3%). Viability increased significantly by Day 14 (85.76 $\pm$ 1%, p<0.05) but was at a similar level to the control (p>0.05). At 20 and 30% distraction lengths, viability remained significantly less than the control at both Days 1 and 7 post-injury. Further, there was no significant change in viability in those groups between Days 1 and 7. At Day 14 post-injury, viability in all distraction injury groups had recovered to values within the range of the control group.

5.4.3.1 Primary Astrocyte Metabolic Activity Following Distraction Injury

The ATP content of astrocytes was measured following distraction injury using the ATPlite™Luminescence Assay System, as described in Section 5.3.7. Metabolic activity of astrocytes in the control group was observed to increase over time, with activity significantly increased between Days 1 and 7, but not between Days 7 and 14 (Figure 5.10). Treatment of the cells with 70% (v/v) methanol (positive cell death control) successfully resulted in a significant reduction in ATP content compared to the control.
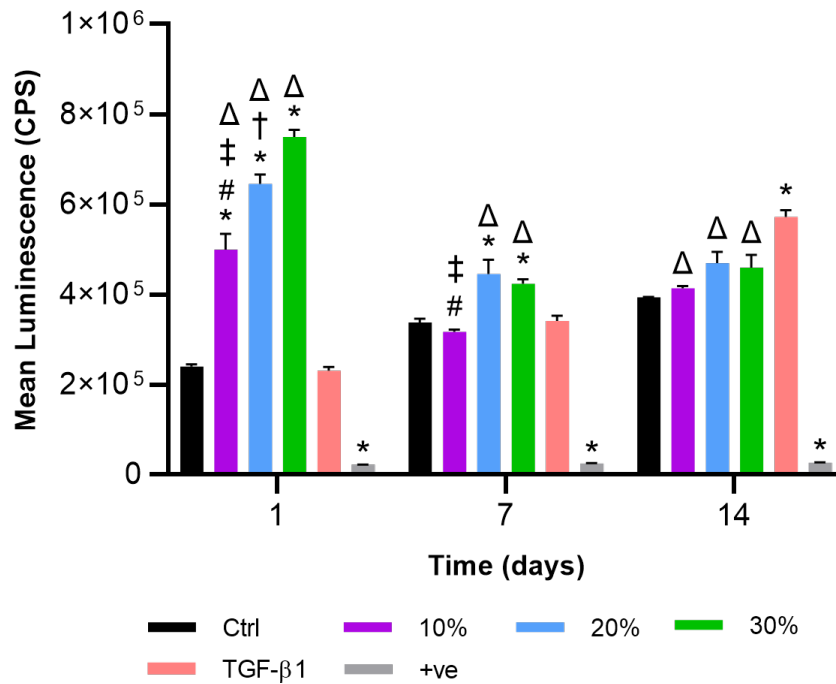
Figure 5.10: Astrocyte metabolic activity following simulated distraction injury at 100 mm.s^{-1}. Data presented as the mean $\pm$ SEM and analysed by two-way ANOVA. Significance levels *p<0.05 (vs. ctrl, Dunnett's post-hoc); # p<0.05 (10% vs. 20%, Tukey's post-hoc); † p<0.05 (20% vs. 30%, Tukey's post-hoc); ‡ p<0.05 (10% vs. 30%, Tukey's post-hoc); Δ p<0.05 (vs. TGF-β1, Tukey's post-hoc). TGF-β1 (positive astrogliosis control) and +ve (positive cell death control; 1 hour 70% v/v methanol treatment). N=3.

At Day 1 post-injury, the ATP content of astrocytes in all of the experimental distraction injury groups was significantly greater compared to the control. Additionally, there was a significant step-wise increase in ATP content as the distraction length was increased. There was no significant difference in ATP content between the control and TGF-β1 treated groups. At Day 7 post-injury, metabolic activity of astrocytes was significantly increased at distraction lengths of 20 and 30%, but not 10%. There was no significant difference in metabolic activity between 20 and 30%, and both groups were significantly greater than 10% distraction and the TGF-β1 treated groups. At Day 14 post-injury, there was no significant difference in metabolic activity between any of the distraction groups compared to the control. Astrocytes in TGF-β1 treated gels exhibited greater metabolic activity than the control and distraction injury groups.

Over time, astrocyte metabolic activity significantly increased in the TGF-β1 treated group, from 2.30 x 10^5 $\pm$ 8 x 10^4 to 5.72 x 10^5 $\pm$ 2 x 10^4 CPS. On the other hand, metabolic activity of astrocytes in all distraction injury groups significantly decreased between Days 1 and 7. Activity then plateaued between Days 7 and 14, with no significant change when comparing each distraction group against time. Metabolic activity of astrocytes in the distraction injury groups was greatest on Day 1, with the 30% distraction group exhibiting the greatest activity overall (mean 7.5 x 10^5 $\pm$ 2 x 10^4 CPS).

5.4.3.2 Chondroitin Sulfate Proteoglycan Expression

Whilst astrocyte morphology has been extensively investigated *in vitro* in response to mechanical trauma, CSPG expression has been less frequently evaluated, particularly when comparing between injury mechanisms. In this study, CSPG expression was evaluated following distraction injury at 100 mm.s^{-1} to various distraction lengths. Figure 5.11 illustrates representative images of CS-56 labelling in astrocyte-seeded hydrogels 14 days following distraction injury at 100 mm.s^{-1}. Quantification of the area of CS-56 labelling was also undertaken (Figure 5.12).
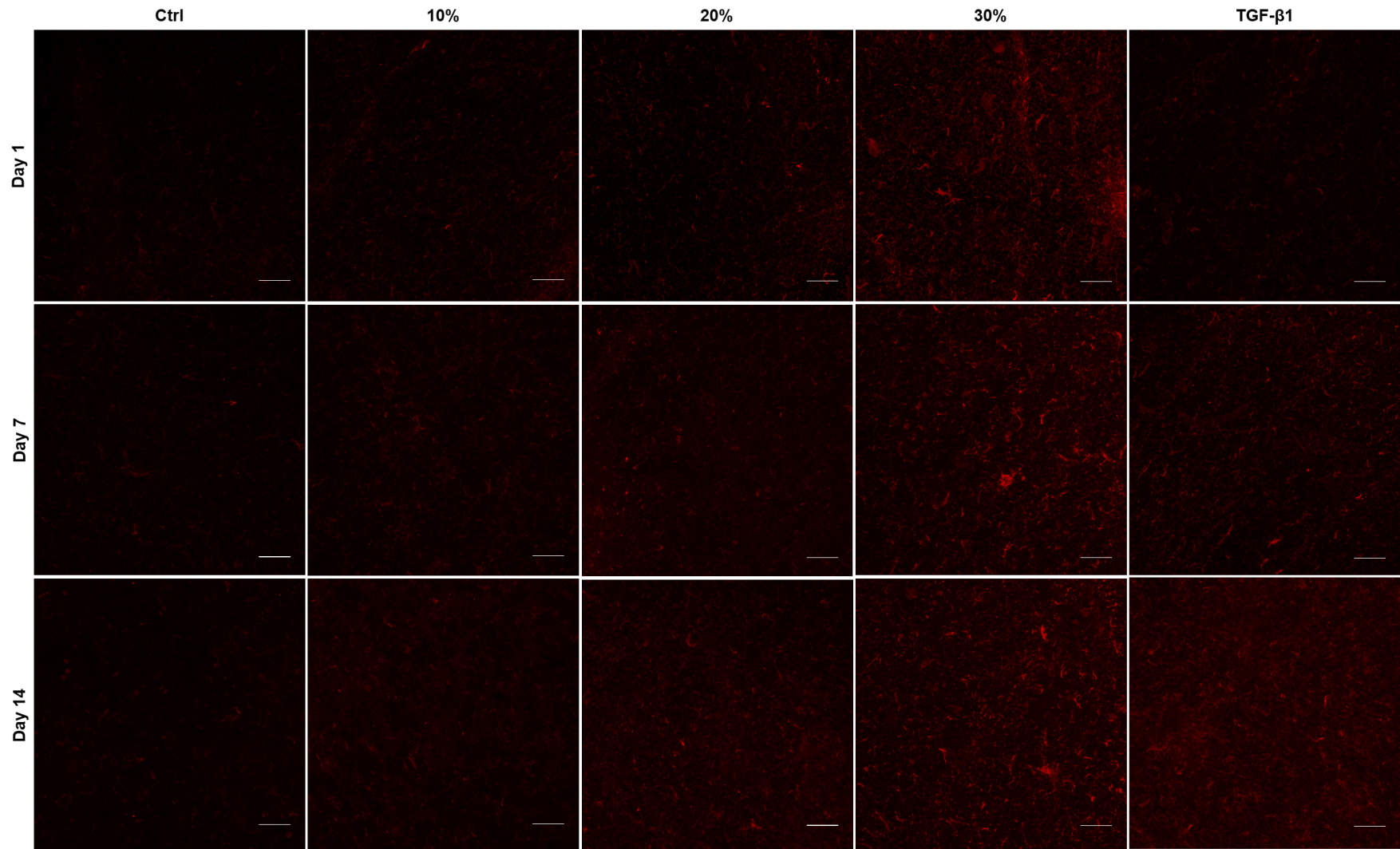
Figure 5.11: CSPG deposition increases with increasing distraction length but not time at 100 mm.s^{-1}. Representative maximum intensity projection images (36 µm depth) of primary rat cortical astrocyte-seeded collagen gels (5 x 10^5 cells.ml^{-1}) subjected to distraction injury at 100 mm.s $^{-1}$ and distraction lengths of 0, 10, 20, and 30% of the gauge length, and incubated for 14 days before labelling with a monoclonal antibody against CS-56 (CSPGs, red). Nuclei were counterstained with DAPI in B (blue). Scale bar represents 50 µm.

CSPG expression by astrocytes in the control group remained stable across the 14-day time period and was significantly lower than all the experimental groups. Further, there was no significant change in CSPG expression in the control group over time (mean 1131.18 ± 100 µm^2). Astrocytes treated with TGF-β1 responded by expressing CSPG, which was significantly greater than the control at all time points. As time progressed, CSPG expression also increased significantly, and expression was maximal on Day 14 (mean 8954.9 ± 600 µm^2).
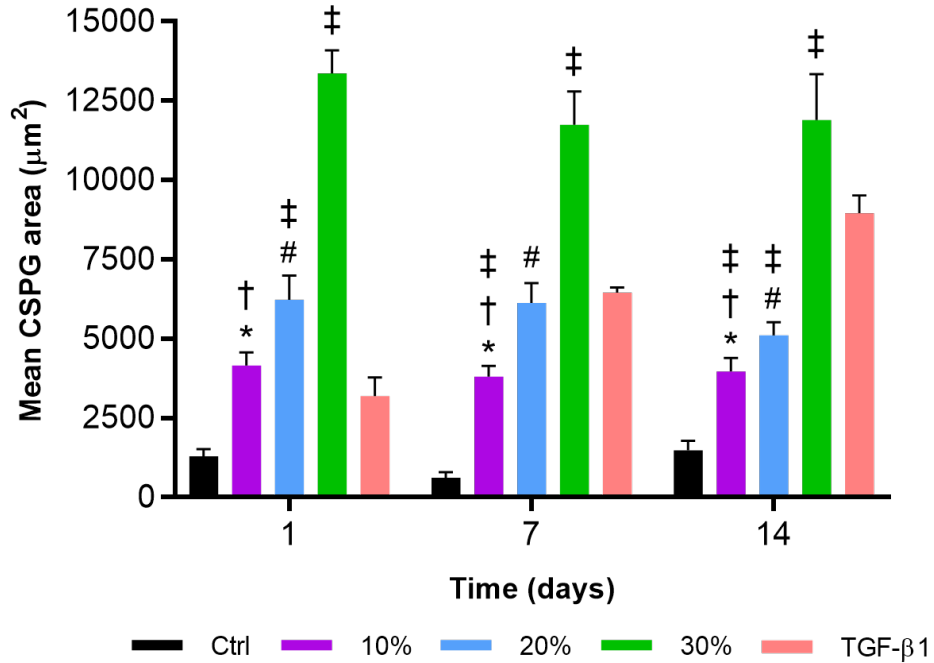
Figure 5.12: CSPG expression by primary astrocytes following simulated distraction injury at 100 mm.s^{-1}. Primary rat cortical astrocyte-seeded hydrogels (5×10^5 cells.ml^{-1}) were subjected to distraction injury at 100 mm.s^{-1} and 10, 20, or 30% displacement, with immunolabelling for CSPGs performed using a CS-56 antibody. Data presented as the mean $\pm$ SEM and analysed by two-way ANOVA. All experimental groups were significantly different from the control (Dunnett's post-hoc, $p<0.05$). Significance levels * $p<0.05$ (10% vs 20%, Tukey's post-hoc); # $p<0.05$ (20% vs 30%, Tukey's post-hoc); † $p<0.05$ (10% vs 30%, Tukey's post-hoc); ‡ $p<0.05$ (vs. TGF-β1, Tukey's post-hoc). TGF-β1 (positive astrogliosis control). N=3.

At Day 1 post-injury, astrocytes in all experimental distraction injury groups expressed significantly more CSPG compared to the control. As displacement increased, CSPG expression also increased significantly, from 4156.61 ± 400 µm^2 at 10% distraction to 13367.70 ± 700 µm^2 at 30% distraction. CSPG expression in the TGF-β1 treated group was significantly higher than the control group, but significantly lower than the 20 and 30% distraction groups.

A similar trend in CSPG expression in the distraction injury groups was observed at Day 7 post-injury: as distraction length increased the mean CSPG area also increased significantly, from 3808.83 ± 300 µm^2 to 11745.02 ± 1000 µm^2. The mean CSPG area of the TGF-β1 treated group was similar to that at 20% distraction (6453.76 ± 200 µm^2 vs. 6136.87 ± 600 µm^2, respectively; $p> 0.05$).

Again, at Day 14 post-injury, the mean CSPG area increased as distraction length was increased from 10 to 30%, although the increase from 10 to 20% distraction was not statistically significant (p> 0.05). The mean CSPG area expressed in the TGF-β1 treated group was significantly higher than the 10 and 20% distraction injury groups, but was significantly lower than the 30% distraction injury group.

Interestingly, there was no significant change in CSPG area with time, when evaluating each experimental distraction group over time (p>0.05). This contrasts with the TGF-β1 treated group where CSPG area increased over time. Expression was consistently highest in the 30% distraction group, with an overall mean CSPG area of 12357.40 $\pm$ 600 μm^2, over the 14-day time period.

5.4.3.3 Summary of Primary Astrocyte Outcomes Following Distraction Injury

Overall, mechanical trauma simulating distraction spinal cord injury induced changes in astrocytes which differed to that of non-injured astrocytes (control). Distraction injury at 100 mm.s^{-1} resulted in astrocytes which changed from small and rounded to hypertrophied and more ramified, with some loss of individual domains. Distraction length was observed to influence astrocyte reactivity mainly at Day 1 post-injury: as distraction length increased, GFAP volume increased and sphericity decreased. However, at the later time points, distraction length had little effect on these outcomes (Figure 5.7).

Similarly, astrocyte viability and metabolic activity was significantly altered in response to distraction injury, with a significant reduction in viability and significant increase in metabolic activity occurring at Day 1 post-injury. Distraction length had little effect on the severity of cell death (Figure 5.9), but did scale with metabolic activity at Day 1 post-injury (Figure 5.10).

A significant increase in CSPG expression was observed by astrocytes in response to distraction injury and CSPG area scaled with distraction length at all time points (Figure 5.12). However, there was no change in expression area over time when considering each distraction group individually. This suggests that although astrocytes in each distraction group became morphologically more reactive over time (as measured by GFAP volume and sphericity), this did not affect CSPG expression.

5.4.4 Comparison of Primary Astrocyte Outcomes Following Contusion and Distraction Injury *In Vitro*

One of the aims of this research was to evaluate astrocyte behaviour in response to not only differing biomechanical inputs, but also different mechanisms of TSCI *in vitro*. As previous *in vivo* models of contusion and distraction TSCI have highlighted distinct patterns of histopathology and behaviour, this research was proposed to determine

whether mechanism specific differences could be observed at an individual cell population level in an *in vitro* model. This could have positive implications for developing biomechanically faithful models to improve screening of therapeutic interventions, or to better inform *in vivo* studies.

Results from Chapter 4 showed that as contusion displacement increased- from 25% to 75%- the calculated energy applied also increased. An increase in velocity from 100 to 1000 mm.s^{-1} also resulted in an increase in the energy applied. Similarly, results here show that as distraction length was increased from 10% to 30%, the mean energy applied increased from 0.057 to 0.143 mJ (Figure 5.5). It is difficult to compare like for like the energy applied values between the two injury mechanisms. Limitations in the mechanical strength of the hydrogel and capabilities of the BOSE meant that the input velocity and distraction length (displacement) parameters were lowered to values which did not result in failure of the gel. The distraction lengths used (10, 20, 30%), however, represented absolute displacement values which were within the upper range of those used in the contusion study (Table 5.1). Despite this, the calculated energy applied values for distraction were significantly lower than those for contusion injury.

Table 5.1: Comparison of kinetic outputs between contusion and distraction injury. The displacement and load data were used to calculate the peak displacement and energy applied values. Data presented as the mean $\pm$ SEM. N=12 (contusion); N=9 (distraction).

			Peak Displacement (mm)	Energy Applied (mJ)
Contusion	*100 mm.s^{-1}*	*25%*	0.386 $\pm$ 0.01	0.150 $\pm$ 0.008
		50%	0.770 $\pm$ 0.01	0.506 $\pm$ 0.03
		75%	1.140 $\pm$ 0.05	0.945 $\pm$ 0.08
	1000 mm.s^{-1}	*25%*	0.361 $\pm$ 0.01	0.954 $\pm$ 0.05
		50%	0.737 $\pm$ 0.02	1.836 $\pm$ 0.03
		75%	1.159 $\pm$ 0.02	3.709 $\pm$ 0.1
Distraction	*100 mm.s^{-1}*	*10%*	0.852 $\pm$ 0.005	0.057 $\pm$ 0.003
		20%	1.656 $\pm$ 0.001	0.108 $\pm$ 0.006
		30%	2.482 $\pm$ 0.0003	0.143 $\pm$ 0.01

Differences in the gel geometry, dimensions and injury setup will likely have affected the mechanical strength of the resulting samples due to collagen's viscoelastic and anisotropic properties. For instance, gels prepared for contusion injury were comprised of 300 µL gel solution, which resulted in discs which had a mean thickness of 1.276 $\pm$ 0.1 mm. For distraction experiments, a lower volume of gel solution was used to prepare individual samples for distraction experiments (150 µL). This generated samples which were much thinner (thickness could not be measured accurately) and significantly harder to handle due to its softness.

It was previously hypothesised that astrocyte reactivity would increase as energy applied also increased. However, as described in Chapter 4, the scaled increase in energy

applied with increasing input velocity and displacement did not result in a proportionate increase in astrocyte reactivity. Here, a similar observation was made in response to distraction injury. GFAP volume increased and sphericity decreased with increasing distraction length, at Day 1 post-injury. However, there were no significant differences in GFAP volume or sphericity between the distraction lengths at Day 7 and 14. GFAP volume increased with time, reaching a maximum mean of 2279.16 ± 60 µm^3 on Day 14 (across all distraction groups). Correspondingly, sphericity decreased with time, reflecting the increased ramification of the astrocytes. On the other hand, at Day 1 post-contusion injury, GFAP volume significantly increased but there were no significant differences between the groups, at both 100 and 1000 mm.s^{-1}. At 100 mm.s^{-1}, GFAP volume scaled with displacement depth as time progressed.

A comparison between the mean energy applied and astrocyte reactivity (as measured by GFAP volume per cell) for both contusion and distraction injury was made. This showed that although less energy was applied to astrocytes which had been subjected to distraction injury, a greater volume of GFAP was expressed per cell compared to contusion injury at 100 mm.s^{-1} (Figure 5.13), although this could be due to the slightly higher displacement values used for distraction injury. Contusion injury at 1000 mm.s^{-1} resulted in greater energy being applied to the astrocytes compared to contusion and distraction injury at 100 mm.s^{-1}, which also translated into greater astrocyte reactivity.
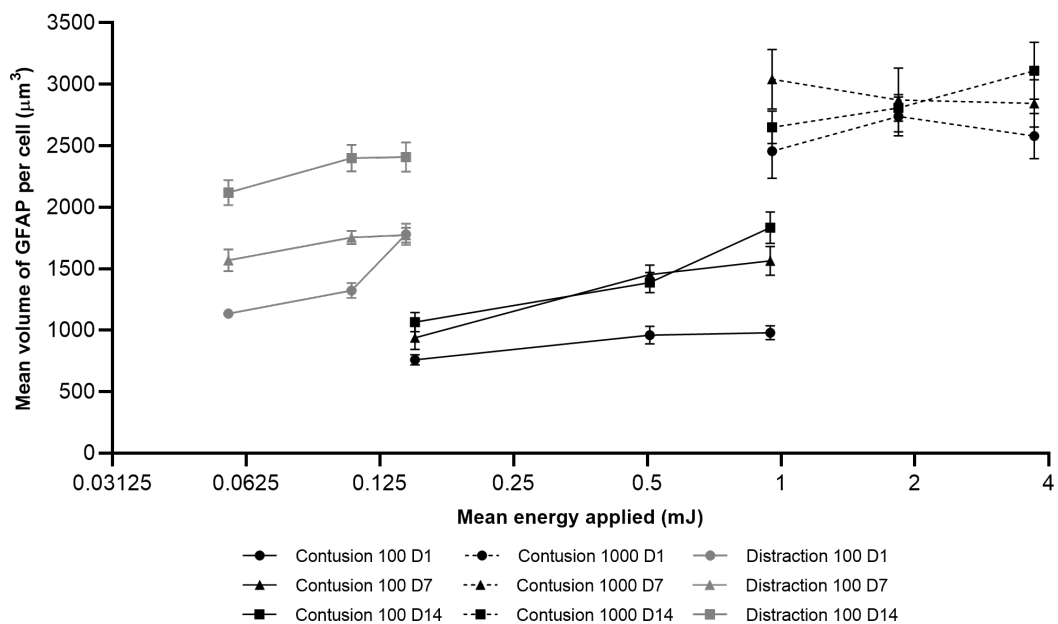
Figure 5.13: The mean volume of GFAP expressed per cell does not scale with energy applied. The displacement and load data were used to calculate the peak displacement and energy applied values. Data presented as the mean $\pm$ SEM on a log 2 scale. N=12 (contusion); N=9 (distraction).

In response to both contusion and distraction, alterations in morphology were observed which were indicative of astrogliosis. One observation was that increased process branching was associated with increased injury severity and progression of astrogliosis. In response to both contusion and distraction injury at 100 mm.s^{-1}, there was a gradual progression

of astrocytes from being small and rounded to increasingly hypertrophied and ramified. Further, cells occupied distinct domains with little overlapping of processes at earlier timepoints (Figure 5.14A and B). At later timepoints, however, the extension of a greater number of and finer processes occurred which then began interdigitating (Figure 5.14D). Contrastingly, in response to contusion injury at 1000 mm.s^{-1}, astrocytes subjected to distraction injury exhibited extensive ramification of processes with fine branches and domain overlapping even at the lower displacement depths and from as early as Day 1 post-injury (Figure 5.14C).
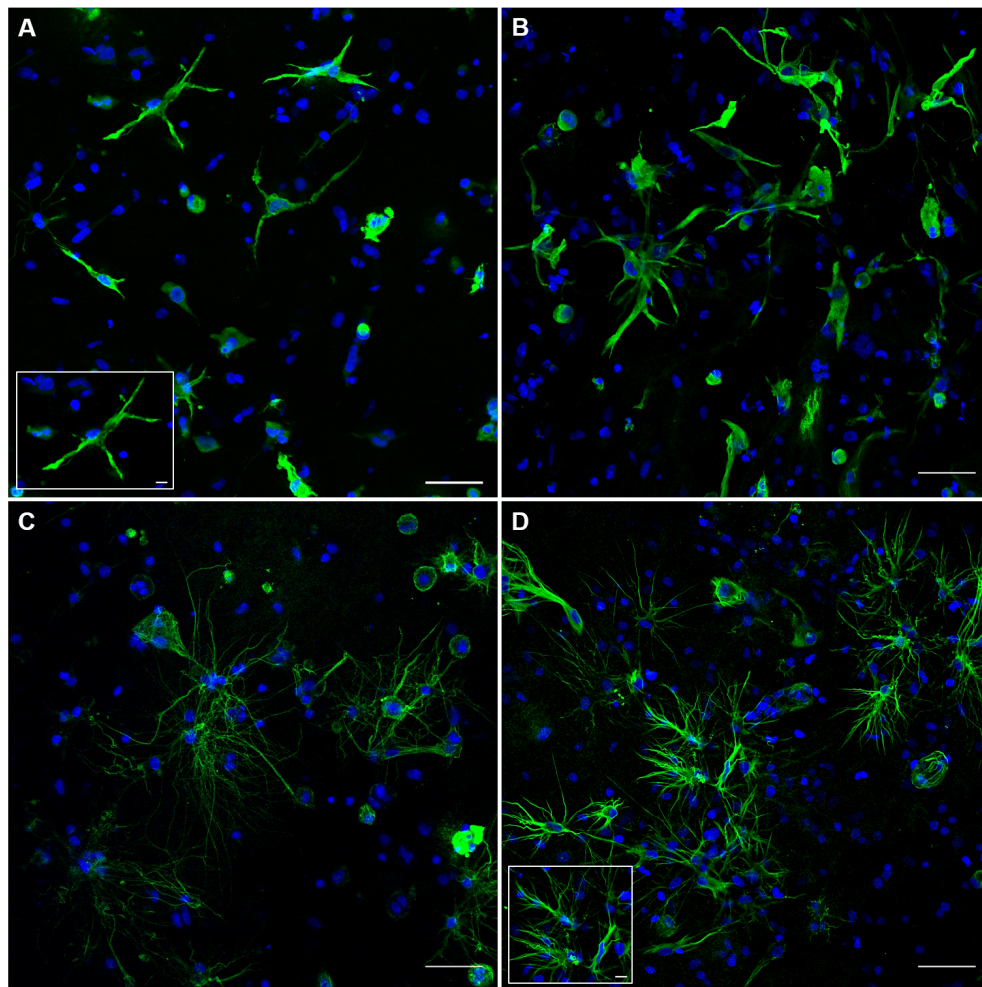
Figure 5.14: Extensive astrocyte process branching develops in response to increased injury severity. Representative immunofluorescent maximum intensity projection images of astrocytes in response to contusion injury at 100 mm.s^{-1}-75% Day 1 post-injury (A), distraction injury at 100 mm.s^{-1}-30% Day 1 post-injury (B), contusion injury at 1000 mm.s^{-1}-50% Day 1 post-injury (C), and distraction injury at 100 mm.s^{-1}-20% Day 14 post-injury (D). Cells were labelled with a polyclonal antibody against GFAP (astrocytes, green) and counterstained with DAPI (nuclei, blue). 36 µm depth. Scale bar represents 50 µm and 10 µm (inset).

Astrocyte susceptibility to cell death was observed to be similar for both contusion and distraction injury. Both contusion and distraction injury induced significant cell death at Day 1 post-injury, whereby viability was reduced to overall grouped means of 65.88% (contusion, 100 mm.s^{-1}), 58.19% (contusion, 1000 mm.s^{-1}), and 57.62% (distraction, 100 mm.s^{-1}). Further, viability had recovered to a level similar to the

control group for both injury mechanisms by Day 14. Contusion displacement and distraction length did not have an effect on the extent of cell death.

Both contusion and distraction injury resulted in an increase in ATP content of gels, suggesting increased metabolic activity. However, there were differences in the amount of ATP measured over time. In response to contusion injury, in general there was little change in the metabolic activity of astrocytes for the first 7 days (Figure 4.13). Significant increases in ATP content were measured at Day 14, at both 100 and 1000 mm.s^{-1}. Displacement depth had little effect on ATP content following contusion injury. Contrastingly, in response to distraction injury, a significant increase in ATP content was observed at Day 1 post-injury and this scaled with the distraction length. Subsequently, metabolic activity decreased and by Day 14 was similar to the control.

Astrocytes expressed and released significantly higher amounts of CSPG in response to both contusion and distraction injury. However, some differences in expression were observed between the two injury mechanisms.   In response to distraction injury, astrocytes expressed CSPGs which increased significantly as the distraction length also increased (Figure 5.12). However, there were no temporal differences in CSPG area. In response to contusion injury, there was a trend for increased CSPG area with increasing displacement depth, although this was generally not significant due to the high amount of variation observed. In contrast to distraction injury, CSPG expression increased with time (Figure 4.15).

Overall, both contusion and distraction injury induced an astrogliosis response in primary astrocytes in this *in vitro* model of TSCI, and there were some similarities in astrocyte responses. For instance, both injury mechanisms elicited significant cell death at earlier timepoints (Day 1).   However, there were also differences in astrocyte behaviour which were mainly temporal. Displacement appeared to influence astrocyte responses at earlier time points for distraction injury; whereas displacement had less of a clear influence on astrocyte reactivity in response to contusion injury.

5.5   Discussion

The aims of this chapter were to apply the distraction injury protocol, developed in Chapter 3, to primary astrocyte-seeded hydrogels and evaluate responses of the astrocytes to a range of input displacement values *in vitro*. Over 14 days, astrocyte responses were evaluated through a range of assays to evaluate astrocyte morphology, viability, metabolic activity, and secretion of chondroitin sulfate proteoglycans (CSPG).

5.5.1   Biomechanics of Distraction Injury *In Vitro*

The input velocity and distraction lengths used in this study were successfully achieved with accuracy and repeatability similar to that demonstrated in previous results (Chapter 3). In this study, distraction of experimental samples at 10% resulted in a mean peak velocity of 107.22 ± 2 mm.s^{-1}. In Chapter 3, an undershoot in velocity was

observed at 10% distraction with the gel (90.00 mm.s^{-1}). This was significantly lower than the velocity measured at 20 and 30% distraction, and lower than the velocity measured in this study. One reason for this could be that misalignment of the distraction mould pieces in the previous study may have introduced friction which could have prevented the input velocity from being achieved experimentally. However, an overshoot in velocity was achieved in this study. A higher error in displacement was also calculated at 10% distraction compared to the other groups, which could be attributed to the larger overshoot observed (Figure 5.3). Improved tuning may reduce the amount of error in displacement.

The simple design of the hydrogel and mould meant it was suitable for distraction studies using the BOSE and no issues were experienced with securing the mould into the grips or maintaining security and alignment of the pieces during the experiment. However, distraction injuries modelled *in vivo* are significantly more complex due to the spinal cord being enclosed within a rigid spinal column. High variability has been observed in animal outcomes following distraction injury *in vivo*. This is predominantly due to the experimental setup, where clamps are used to hold the transverse processes, and the distraction injury is applied indirectly to the cord (Chen *et al.,* 2016; Choo *et al.,* 2007). Maintaining clamp-vertebrae integrity was shown to be difficult, with slippage occurring on occasion.

The loads measured in *in vivo* distraction models were significantly higher than those measured in this study, and were greater than loads measured for other injury mechanisms such as contusion and dislocation. Choo *et al.,* (2007) modelled contusion, fracture-dislocation and flexion-distraction at 100 mm.s^{-1}, in rats, and measured mean loads of 2.0, 20.7, and 38.6 N, respectively. The displacement parameters varied between each mechanism, all of which were aimed at producing a moderate injury. Chen *et al.,* (2016) also modelled these three mechanisms in rats using an input velocity of 1000 mm.s^{-1} and observed the same pattern of load, whereby distraction injury resulted in the greatest load measured out of the three mechanisms (mean 52.2 N). Notably in these studies, load was applied to the vertebral column for dislocation and flexion-distraction mechanisms, thus the loads measured were greater than the loads measured in this study. There were no measurements of load or energy applied directly from the cord, so it is difficult to compare to this study.

The energy applied parameter calculated in this study revealed that distraction injury resulted in lower energies compared to contusion injury. Collagen hydrogels exhibit viscoelastic and anisotropic properties which explains the differing responses of the material under compression and tension. Strain stiffening occurs whereby the matrix becomes stiffer under higher strain rates (Nam *et al.,* 2016). As mechanosensitive cells, astrocytes may have responded to this by altering their behaviour and becoming more reactive.

One objective with this study was to use the same input parameters used in the

contusion study for the distraction study here. This would have enabled a direct comparison of the load and energy applied measurements and subsequently astrocyte responses between the two injury mechanisms. However, results from Chapter 3 showed that the gel was too weak to withstand tensile displacement of more than 35%. Further, the BOSE was incapable of reaching a velocity of 1000 mm.s^{-1} so only a velocity of 100 mm.s^{-1} was used. The range of distraction lengths used in this study did, however, represent absolute lengths which were within the range of displacement depths used in the contusion study.

5.5.1.1 Astrocyte Behaviour

There is little research where the effects of pure tensile forces have been evaluated in the CNS *in vitro*. Instead, stretch models have been extensively used, particularly in modelling traumatic brain injuries (TBI). Stretch models involve the application of shear strain to a specimen and has been applied to astrocytes in multiple studies *in vitro* (Ahmed *et al.,* 2000; Cullen *et al.,* 2007; Floyd *et al.,* 2001; McKinney *et al.,* 1996). Astrogliosis has been modelled extensively *in vitro* using various mechanical and chemical means, but not using tensile loading. Results in this study show that distraction of astrocyte-seeded gels resulted in significant alterations to astrocyte morphology. These alterations were also observed in the same model in response to contusion injury (Chapter 4), and is consistent with astrogliotic responses observed in other research (Cullen *et al.,* 2007; East *et al.,* 2009; Kirk, 2018; Smith, 2016; Yu *et al.,* 2012).

Cullen *et al.,* (2007) applied different shear strain rates (10, 20, 30 s^{-1}) to 3D co-cultures of primary neurons and astrocytes at 0.50 strain and assessed reactivity, viability and CSPG expression 48 hours following injury. Increased GFAP expression, hypertrophy, and ramification was observed. However, process density was only significantly higher than the control in the 10 s^{-1} and the TGF-β1 treated group as there was high variation in the data. Other reasons could be the short timescale of the analysis (48 hours) and relatively low strain rates which may not have induced a significant change at earlier time points. Higher strain rates were used in this study which resulted in an immediate (24 hours) increase in GFAP volume. The authors did state that a significant increase in process density was observed at 5 days post-injury, but data was not shown. Further, they reasoned that a high severity injury may have necessitated a recovery period, after which process density increased significantly. The results of this study do not support this argument, since significant increases in GFAP volume were observed at all distraction lengths from Day 1 post-injury. Although process density was not measured here, ramification was observed at Day 1 post-injury which corresponded with a decrease in sphericity.

Fragmentation and beading of astrocyte processes was observed in some cells following distraction injury, although this was not widespread (Figure 5.6). These observations could be associated with clasmatodendrosis, which also include cytoplasmic swelling and vacuolation (Duchen, 1992). The term has mainly been discussed in studies regarding pathologies in the brain, such as Alzheimer's and dementia (Sahlas *et al.,* 2002;

Tomimoto *et al.,* 1997), and trauma (Sakai *et al.,* 2013). Process beading and fragmentation has also been observed in human astrocytes *in vitro* in response to stretch-induced injury using a pressure pulse (Halford *et al.,* 2017). Further, a lumbar crush injury was performed to model compression injury in mice and histology results showed evidence of disintegrating and beaded astrocyte processes in both the white and grey matter, 3 days post-injury (Levine *et al.,* 2016). As process damage was not observed in all samples in this study, it may not be a prominent feature of astrogliosis in response to distraction injury.

Cullen *et al.,* (2007) also measured viability using the live/dead assay, and found that viability was reduced to approximately 65% 48 hours following the highest shear strain deformation (30 s^{-1}). However, further analysis showed that astrocyte viability was not significantly affected, suggesting the majority of cell death was not occurring in the astrocyte population. In this study, viability of astrocytes was significantly reduced at 24 hours post-injury (mean 54.03 – 62.47%) and subsequently recovered by Day 7 onwards. Different strain rates were used compared to this study, which may have affected the susceptibility of astrocytes to deformation. Further, as viability was measured at 48 hours by Cullen *et al.,* (2007), it is unknown whether alterations in astrocyte viability occur at a much more acute timeframe, and/or whether the presence of neurons contributes to astrocyte cell survival.

In this study, ATP content significantly increased one day following distraction injury, and subsequently decreased at the later timepoints. There was no significant change in cell density suggesting proliferation was not significant, although it was expected as a process which is part of astrogliosis. The increase in ATP content at Day 1 post-injury was thus not associated with proliferation. Ahmed *et al.,* (2000) used an *in vitro* model of stretch injury with astrocytes cultured on deformable silastic membranes and observed a significant decline in ATP content 15 minutes following injury. However, this had recovered by 24 hours. In an *in vitro* model of traumatic brain injury, Geddes *et al.,* (2003) cultured primary rat neurons on silicone substrate which were then subjected to stretch injury (10 s^{-1}, 0.30 strain). Intracellular ATP was quantified using a luciferin/luciferase assay which revealed a reduction of ATP of up to 40% 60 minutes post-injury- however, ATP levels had recovered by 24 hours. Although a different neural cell type was used in the Geddes *et al.,* (2003) study, both of these studies suggest that ATP dynamics may occur at much more acute timescales (< 24 hours).

There is a complexity associated with metabolic activity in astrocytes following induction of astrogliosis, and the ATPlite assay may be confounded by the variety of astrogliotic responses, including increased protein expression (e.g. GFAP), cell damage, death, proliferation, and inflammation that also occur over a range of timescales (Burda and Sofroniew, 2014). This necessitates the use of assays which are more targeted. For instance, analysis of proliferation could be achieved using a bromodeoxyuridine (BrdU) cell proliferation assay, utilising a thymidine analog which is incorporated into newly synthesised of actively proliferating cells. Additionally, markers of astrocyte damage

could be evaluated, such as cell permeability and proteins released into the medium.

The results of this study showed that distraction injury induced an astrogliosis response in an isolated culture of primary astrocytes *in vitro*. However, there is a need for more quantitative measures of astrogliosis, such as gene expression, which would provide a more detailed picture of the profile of astrogliosis. Other features of astrogliosis, including inflammatory responses could be evaluated by measuring cytokine expression in the cell culture medium. Cytokine expression by ELISA was not used in this study due to its limited sensitivity for detecting measurable levels of cytokines in response to contusion injury. Further, smaller gels were used and the size of the moulds necessitated the use of larger well-plates, thus more cell culture medium was required to overlay the gels. Therefore, the cytokines would have been further diluted.

5.5.1.2   Contusion vs. Distraction Injury

Limited data is available regarding the behaviour of astrocytes in a direct comparison of contusion and distraction injury mechanisms. Cullen *et al.,* (2011) compared astrocyte viability 48 hours following bulk shear or compression at various strain rates *in vitro* (0.50 shear/compressive strain; 1, 10, 30 s^{-1}). Shear loading significantly reduced the percentage of viable cells at 30 s^{-1}, although there was no significant difference between shear or compression. However, shear deformation induced significantly higher cell death compared to compression at 10 and 30 s^{-1} strain rate. In this study, there was no difference in astrocyte viability between contusion and distraction, with a similar reduction in viability observed at Day 1 post-injury, which then subsequently recovered by Day 14. Higher strain rates were used in this study which could have exceeded the threshold(s) of cell death for both mechanisms.

Additionally, Cullen *et al.,* (2011) observed that the extent of membrane damage was not significantly different between shear and compression, but there were differences in calcein uptake: more calcein was present in the cellular processes following shear deformation compared to compression, suggesting that the processes could be more susceptible to, and loading thresholds lower, for shear. Membrane damage was not evaluated in this project and different displacements were used for each mechanism, but there were differences in the volume of GFAP expressed between both mechanisms at 100 mm.s^{-1}. For instance, displacement affected GFAP volume at Day 1 post-injury for distraction but not for contusion injury. Conversely, displacement affected GFAP volume at Days 7 and 14 for contusion but not distraction injury.

In this study, distraction injury induced increased CSPG release, which also increased with increasing distraction length. However, there were no temporal differences in CSPG area. Contrastingly, CSPG expression generally increased with displacement (although not always significant) in response to contusion, which also increased with time. Further, a higher contusion velocity (1000 mm.s^{-1}) did not result in greater CSPG expression compared to lower velocity (100 mm.s^{-1}). This suggests that there are potentially additional aspects of astrogliosis, which were not evaluated,

influencing CSPG dynamics. Molecular and genetic analysis of astrocytes and their products may provide more information on how astrocytes control CSPG expression. Cullen *et al.,* (2007) showed that CSPG expression was not significantly different from the control, 48 hours following shear deformation. It was suggested that the injury was too severe to induce astrogliosis mediated CSPG expression which does not agree with the results of this study. CSPG expression has not been extensively evaluated *in vivo*, with more focus on gross tissue damage and the analysis of neuronal pathologies as they are common targets of therapeutic interventions.

There are also few studies showing the direct comparison of different SCI mechanisms *in vivo*. Chen *et al.,* (2016) used the UBC rig to model cervical contusion, distraction, and dislocation in rats and results showed the lesion extent was greater following distraction compared to contusion and dislocation injury. Another observation made was that tissue damage was more diffuse at earlier time points in the study following distraction injury: significant haemorrhage and plasma membrane compromise was apparent as early as 5 minutes and 3 hours post-injury, whereas it was not as apparent following contusion and dislocation injury. The injury mechanism was also shown to affect different cell populations in different ways: contusion injury resulted in the greatest loss of myelinated axons in the dorsal white matter, whereas distraction injury spared the most myelinated axons. It would be interesting to investigate the effects of different injury mechanisms on multiple cell types *in vitro* in the model used in this study. The more diffuse injury caused by distraction injury could contribute to the reason why astrocyte volume increased and sphericity decreased to a greater extent at Day 1 post-injury, compared to contusion injury at the same velocity (100 mm.s^{-1}), in this study.

It is difficult to discuss the results in this study in the context of *in vivo* research as different outcome measures were used and acute astrogliosis is not frequently evaluated. However, the results here show that, in isolation, astrocytes do not respond in the same way to different mechanisms of deformation. Taking into consideration the biomechanics of injury in the design of a SCI model is important for understanding the heterogeneity of pathophysiological mechanisms underlying SCI. As astrocytes are known to be key for the survival and proper functioning of other cells, including neurons, cell-cell interactions and downstream responses are likely to be influenced by these acute changes in astrocyte behaviour and knowledge of this may aid predictions about the nature of the injury microenvironment.

5.5.1.3 Experimental Model and Setup

The original design of the gel cavity of the distraction mould for this study was developed previously in order to generate self-aligned Schwann cell-fibroblast, and astrocyte-neuron seeded collagen type-I hydrogels (Phillips and Brown, 2011). Treatment of astrocyte-seeded gels in this tethered mould with TGFβ1 was shown to induce astrocytes to contract the matrix and elongate, arranging themselves along the longitudinal axis of the gel. Alignment was not introduced into the model in this study

as a baseline non-reactive state was required in order to measure the expression of GFAP in response to mechanical injury. The addition of TGF-β1 to induce alignment would have generated cultures which were reactive prior to application of a mechanical injury. However, replicating the spatial organisation of cells in the CNS, including the organised tracts of the spinal cord, would provide a model that is more representative of native spinal cord. Further, Cullen and LaPlaca (2006) showed that bulk deformation of 3D matrices resulted in localised cellular strain that was a function of cell orientation.

Distraction injuries observed in humans are typically biaxial; however, the apparatus used in this study was limited to applying tensile forces uniaxially. Geddes-Klein *et al.,* (2006) applied uni and biaxial stretch to embryonic rat cortical neurons cultured on an elastic substrate and demonstrated increased membrane permeability and cytoplasmic calcium levels were significantly higher (indicating neuronal dysfunction) in biaxially stretched neurons compared to uniaxial. This highlights the sensitivity of cellular responses to the type of injury modelled and that this can be demonstrated *in vitro*.

5.6   Conclusions

Mechanical trauma simulating distraction injury *in vitro*, using the BOSE 5110 Electroforce BioDynamic apparatus, resulted in morphological changes in astrocytes which were characteristic of astrogliosis observed elsewhere *in vitro* and *in vivo*. Multiple aspects of astrogliosis were modelled *in vitro*, with an isolated population of astrocytes in a 3D hydrogel. Further, use of this model to simulate two different TSCI mechanisms, contusion and distraction, revealed differences in astrocyte pathology which warrant further investigation to probe the mechanisms behind this. This chapter addressed the main objectives of the project, which were to evaluate the biological responses of astrocytes to simulated contusion and distraction injury, and to investigate the relationship between the primary mechanical input and responses of primary astrocytes cultured in isolation (Chapter 1).

The specific objectives set out in this chapter were met with the following observations:

I. *Verify the accuracy and precision of the BOSE 5110 Electroforce BioDynamic (BOSE) under distraction forces:*

- The input displacement and velocity parameters were achieved with high precision and accuracy and matched the data from Chapter 3.

II. *Calculate the kinetic outputs following distraction injury:*

- Energy applied was calculated using the load displacement graphs, which showed a significant step-wise increase in energy applied with increasing distraction length.

III. *Evaluate the responses of primary astrocytes to distraction injury:*

- Astrocytes responded to mechanical injury in a variety of ways which were characteristic of astrogliosis. Morphologically, astrocytes became hypertrophied, ramified, and overlapping of domains was observed, suggesting a more severe reactive response.

- Reactive astrocytes in experimental groups expressed CSPGs at a greater level compared to the control group.

- Significant cell death was observed at Day 1 post-injury and ATP content was significantly increased at Day 1 post-injury.

IV. *Compare the responses of primary astrocytes to distraction against TGF-β1:*

- Astrogliotic related alterations in morphology occurred earlier in response to distraction injury compared to astrocytes treated with TGF-β1 (positive astrogliosis control).

V. *Compare the behaviour of astrocytes in response to contusion and distraction injury:*

- Temporal differences in the progression of astrogliosis was observed between contusion and distraction injury.

Several null hypotheses were also postulated at the beginning of the study:

I. *There is no statistical difference between the reactivity of astrocytes in response to distraction injury compared to no injury (control):*

- Mechanical simulation of distraction injury induced astrocyte changes which were consistent with astrogliosis and which was not observed in the control groups.

II. *There is no statistically significant relationship between distraction length and astrocyte reactivity:*

- An increase in distraction length resulted in a corresponding increase in astrocyte reactivity at Day 1 post-injury. At later timepoints, distraction length did not affect the severity of astrogliosis.

III. *There is no statistically significant relationship between astrocyte reactivity and time following distraction injury:*

- The astrogliosis response progressed over time, in terms of GFAP volume and metabolic activity. At each distraction length, CSPG expression did not significantly change with time.

Chapter 6

General Discussion

Traumatic spinal cord injury (TSCI) remains a highly complex injury to manage and treat effectively. Where a greater understanding of the epidemiology of TSCI has led to improved implementation of injury prevention strategies, it is unlikely that the TSCI itself can be completely eliminated. The unexpected and devastating nature of this high energy event means time is of the essence when it comes to treating the cord injury, whilst also managing the patient's comorbidities, including maintaining the airway and stabilising the vertebral column. Effective treatment(s) for TSCI with improved neurological outcomes remains elusive despite the promising number of preclinical studies (Tator, 2006; Varma *et al.,* 2013). One important reason for this is the complex and heterogeneous nature of human TSCI, which is under-represented in TSCI models, and even a clinically relevant animal model reflects only a small proportion of TSCI cases in humans.

Greater effort is being put into implementing a more coordinated approach to understanding and treating TSCI, including a better understanding of the relationship between injury mechanics and secondary pathophysiology (Mattucci *et al.,* 2019). Since the biomechanics of human TSCI cannot be measured at the point of injury, experimental models were developed to replicate the clinical injury scenario *in vivo* and *in vitro* (Sharif-Alhoseini *et al.,* 2017; Slovinska *et al.,* 2016). These models are predominantly used to model specific aspects of the secondary pathophysiological cascade, thus the input biomechanical parameters are tailored based on that. Less emphasis has been placed upon how injury biomechanics itself contribute to the secondary response, particularly for evaluating thresholds in different cell populations.

For instance, transection models were primarily developed to evaluate axon regeneration and test therapeutic interventions (Spillmann *et al.,* 1997). However, transection injuries, particularly complete transection, are not commonly observed in humans thus lacks clinical relevance. Further, as animal models are continually being refined, more consideration is being placed upon using more accurate biomechanical models as evidence emerges of mechanically distinct damage patterns and pathologies (Bhatnagar *et al.,* 2016; Chen *et al.,* 2016; Choo *et al.,* 2008, 2007). Decoupling of biomechanical parameters, including velocity, displacement, and force has been a challenge for those designing the tools to simulate trauma.

The rationale for this research was that different mechanisms of TSCI result in different biological responses, and it was hypothesised that this would be reflected at an individual cell population level *in vitro*. Primary rat cortical astrocytes were selected as astrocytes play a major role in the formation of the glial scar, which has been a therapeutic target both through attenuating scar formation or modulating scar-associated inhibitory molecules (Bradbury and Burnside, 2019).

6.1 *In Vitro* Modelling of TSCI

The rationale for using collagen hydrogels as an *in vitro* system to model TSCI was that it is an easily available biomimetic substrate with intrinsic cell attachment motifs, possesses proven cytocompatibility with neural cells, and astrocytes maintain a non-reactive state over a prolonged period of time in them (East *et al.,* 2007, 2009; Kirk, 2018; Smith, 2016). Here, astrocytes remained viable in three-dimensional (3D) culture in collagen hydrogels over the 14-day time period of the study. The astrocytes were also maintained in a non-reactive state in the non-injured samples. 3D culture systems, such as hydrogels, were selected over 2D culture systems since stiff substrates, such as tissue culture plastic, have been shown to induce an astrogliosis response (East *et al.,* 2009; Georges *et al.,* 2006; Wilson *et al.,* 2016). *In vitro* models also allow greater control of experimental conditions compared to *in vivo* animal models of TSCI. Further, the cellular complexity of the spinal cord means that it would be difficult to isolate specific cellular effects, and cells may also influence each other behaviourally which is a confounding factor.

The *in vitro* model used in this project was adapted and enhanced from previous research at The University of Leeds to simulate clinically relevant contusion and distraction injury events, using the BOSE 5110 Electroforce BioDynamic (BOSE) materials testing machine, with independent control of input velocity and displacement depth/length. Similar models of the BOSE 5110 have previously been used to characterise the mechanical properties of hydrogels at low strain rates, and there is one published study using the BOSE TestBench™system to model contusion injury *in vivo* (Chapter 1; Section 1.8.2.1). However, the limitations of these studies are that the strain rates used are not clinically relevant, or errors of up to 73% in the velocity were measured for the *in vivo* study (Salegio *et al.,* 2016).

Kirk (2018) used the BOSE 5110 to overcome the technical limitations associated with the Infinite Horizons impactor in modelling contusion injury *in vitro*, namely the lack of independent control over displacement and velocity, and variable output force data. The aim of that study was to investigate the effects of extracellular matrix (ECM) stiffness on neural cell behaviour, and modelled focal contusion injury on primary astrocyte and microglia-seeded collagen hydrogels. Alterations in cellular metabolism and GFAP expression were observed, indicating the appropriateness of the BOSE for modelling TSCI *in vitro*. However, verification of the velocity and displacement

parameters was not fully performed.

Building on from this, the results in Chapter 3 in this study demonstrate more in-depth characterisation and verification of the accuracy and precision of the BOSE, under compressive and tensile configurations. Under compressive and tensile strains, the BOSE was accurate and precise, achieving the desired maximum input displacement value. A velocity of 1000 mm.s^{-1} was achievable under compression, which demonstrated that the input velocity of 3000 mm.s^{-1} used by Kirk (2018) was unlikely to have been achieved. Distraction injury has not been previously modelled using the BOSE, and work was undertaken to adapt an existing hydrogel mould which could be used to cast the hydrogel and loaded into the BOSE rig to have the distraction load applied. The distraction length range selected (10, 20, 30% of the gauge length, 8.25 mm) required a maximum distraction length of 2.475 mm (30%). Results from Chapter 3 showed that a maximum velocity of 300 mm.s^{-1} could be achieved at this distraction length. Because both the tensile grips were coupled to the mould, the distraction injury was effectively the entire stroke length available to accelerate. In contusion injury, only one platen was coupled to the sample; thus, the working distance was increased to allow the actuator to accelerate to the desired velocity. Therefore, although the velocity of both contusion and distraction injury modelled was within the range of those measured *in vivo* (Chapter 1 Table 1.5), a limitation of the distraction study in Chapter 5 was that the velocity modelled was towards the lower end of the range and only one velocity was tested.

Astrocytes, and other neural cells, are mechanosensitive cells and substrate stiffness has been shown to affect their reactivity, as mentioned previously. The mechanical properties of the collagen hydrogel used in this project (2 mg.mL $^{-1}$, First Link UK Ltd.) were previously evaluated by Smith (2016) at The University of Leeds (Chapter 1 Table 1.7). Using oscillatory rheometry, its elastic modulus was calculated to be 55.19 Pa (1% strain, 1 Hz, 2 x 10^6 p.mL^{-1} primary astrocytes). Other mechanical analyses of collagen hydrogels reported moduli ranging from 4 Pa to 1.5 MPa. There is large variation in these values due to the different concentrations of collagen, testing method, and testing parameters used such as strain and strain rate. The higher modulus values can also be attributed to modifications to the collagen hydrogels, such as incorporating plastic compression or functionalisation. The values for fully hydrated collagen hydrogels of the same concentration used in this project are substantially softer than the reported stiffness values of human (40.12 kPa – 1.40 MPa) spinal cord (Chapter 1 Section 1.3). The effects of matrix stiffness on the progression of astrogliosis *in vitro* is not fully known. Further, type-I collagen is not a major component of the CNS matrix, which is predominantly composed of glycosaminoglycans (GAGs) and proteoglycans (Chapter 1 Section 1.2.2). However, the collagen hydrogels used in this study supported cell attachment, low baseline astrocyte reactivity and survival, and similarly in other studies as well (East *et al.,* 2007, 2009; Georgiou *et al.,* 2013; Phillips *et al.,* 2005). In future, however, a more biologically and mechanically relevant substrate should be evaluated.

One of the aims of this project was to evaluate the relationship between injury

mechanisms and mechanics on astrocyte outcomes *in vitro*. Mechanical parameters did influence astrocyte reactivity: an increase in contusion velocity from 100 to 1000 mm.s^{-1} resulted in an increase in astrocyte reactivity, as measured via GFAP volume, sphericity and CSPG expression. Sparrey *et al.,* (2008) and Maikos and Shreiber (2007) both demonstrated velocity dependent disruption to the white matter and blood-spinal cord barrier (BSCB), respectively. Further, an increase in contusion displacement depth resulted in an increase in astrocyte reactivity at 100 mm.s^{-1} in this study, and other studies have also shown displacement related increases in SC damage (Pearse *et al.,* 2005).

However, interactive effects between displacement and velocity has been demonstrated by Lam *et al.,* (2014), which the other studies have not shown as both displacement and velocity were not varied independently. Lam *et al.,* (2014) showed that increasing contusion velocity from 8 to 800 mm.s^{-1} resulted in increased behavioural deficit and reduced tissue sparing but only at the higher displacement depths (1.5 mm), suggesting the lower displacement depth (0.9 mm) was below the threshold with which significant differences in increased velocity would be observed. In this study, an increase in contusion velocity resulted in increased astrocyte reactivity at all displacement depths, suggesting the depths used were great enough to elicit significant changes in astrocyte reactivity with increasing velocity.

Results from the contusion study here showed a step-wise increase in load with displacement depth and velocity (Chapter 4 and Appendix E Table 6.10). Despite the significant increase in load between 100 mm.s^{-1} – 75% and 1000 mm.s^{-1} – 25%, there was no significant difference in the energy applied. However, differences in astrocyte reactivity were observed between these two injury groups (Chapter 4 Table 4.2): astrocytes in the 1000 mm.s^{-1} – 25% group expressed a significantly larger volume of GFAP per cell. This could be attributed to the increased stiffness response of the hydrogel at higher velocities due to the viscoelastic nature of collagen hydrogels (Chandran and Barocas, 2004; Fratzl, 2008; Motte and Kaufman, 2013). At high strain rates the elastic response dominates, and the gel exhibits an increased elastic modulus. Since astrocytes are mechanosensitive cells, this increased stiffness may induce or contribute to the initiation of astrogliosis.

For distraction injury, only one velocity was tested: 100 mm.s^{-1} so it is difficult to determine whether velocity could be a dominant parameter. Load and energy applied increased significantly with an increase in distraction length. Displacement length had little influence on astrocyte GFAP volume and sphericity after Day 1 post-injury, but did influence CSPG release at all time points. It is still unclear precisely how each biomechanical parameter influences astrocyte reactivity and the interaction between them in different injury mechanisms, thus more research is required which includes testing more input velocities.

6.2   Mechanistic Insights into Astrogliosis

Astrogliosis comprises a spectrum of alterations that appear to be induced by both the type and severity of injury, and has been modelled using a variety of methods, including mechanical trauma and chemical stimuli. In this project, results showed that mechanical trauma induced a more severe astrogliosis response compared to TGF-β1 treated cells (10 ng.mL^{-1}), with more GFAP and CSPG being expressed particularly at the higher velocities and displacements (Chapters 4 and 5). A difference in viability was also observed between mechanically and chemically treated astrocytes: TGF-β1 treatment did not significantly affect cell viability, whereas both contusion and distraction injury induced a significant reduction in viability 24 hours post-injury.

Chemical induction of astrogliosis through the treatment of astrocytes with TGF-β1 has been used in multiple studies *in vitro* (Cullen *et al.,* 2007; East *et al.,* 2009; Kirk, 2018; Smith, 2016; Yu *et al.,* 2012) and *in vivo* (Logan *et al.,* 1994). All the studies showed that TGF-β treatment resulted in astrocyte responses considered as characteristic markers of astrogliosis, including increased GFAP expression, cellular hypertrophy, and scar formation. Cullen *et al.,* (2007) compared astrocyte-neuron co-cultures which had been treated with TGF-β1 (10 ng.mL^{-1}) or subjected to shear deformation at various strain rates. Both mechanisms induced astrocyte hypertrophy and increased GFAP and CSPG expression after 48 hours. However, viability was not adversely affected by TGF-β1 48 hours following treatment, which agrees with the results of this project. Other chemical inducers of astrogliosis, such as bacterial lipopolysaccharides (LPS) have also been shown to induce astrogliosis, but not affect viability (Acaz-Fonseca *et al.,* 2019; Brahmachari *et al.,* 2006; Guerra *et al.,* 2011; Kirk, 2018). This suggests that some chemicals considered inducers of astrogliosis may not activate cell death pathways, thus does not faithfully represent all aspects of astrogliosis.

Results in this project showed that an immediate morphological and biological change in astrocytes was observed in response to mechanical trauma, with an increase in GFAP volume occurring from Day 1 post-contusion and distraction. GFAP volume also significantly increased in TGF-β1-treated astrocytes, although never to an extent that was greater than mechanical injury. Other research has also suggested that astrocyte activation can occur within a matter of hours following injury, as shown by the increase in expression of multiple activation markers such as GFAP, CSPG, pSTAT3, and NF-κb (Brambilla *et al.,* 2005; O'Callaghan *et al.,* 2014). However, other research has suggested that severe injury results in delayed astrogliosis (Cullen *et al.,* 2007). At the higher strain rates (30 s^{-1}), cell viability decreased but with no concomitant increase in CSPG deposition or hypertrophic processes at 48 hours post-injury. One potential reason for this conflicting result is the lack of cellular complexity of the model used in this project. Signalling from other cell types, such as neurons and microglia could influence the temporal progression of astrogliosis.

Mechanical trauma is known to induce a robust and well-studied astrogliosis response and scar formation *in vivo*. However, few studies have directly compared astrocyte

responses to different mechanisms of TSCI. Choo *et al.,* (2008) modelled contusion, dislocation and distraction mechanisms in rats and observed increased GFAP immunoreactivity from 3 hours following injury.   Although there was a trend for increased GFAP area following contusion injury, this was not significantly different from the other mechanisms. Reactive astrocytes were largely confined to the lesion epicentre following contusion injury, whereas there was more rostral-caudal extension of reactive astrocytes following dislocation and distraction injury. As the contusion injury modelled in Chapter 3 was not a focal contusion, a defined lesion with a border was lacking and this limited the evaluation of the distribution of reactive astrocytes. It is important to note that although mechanical insult has induced multiple responses indicative of astrogliosis, in an isolated population of astrocytes, this is not fully representative of the whole process, which is a multicellular process.

It is also recognised that human SCI is likely to involve multiple types of strain- such as shear and compressive strains experienced during a dislocation SCI- which compounds the complexity of developing truly representative models of TSCI. Force and strain distribution to the spinal cord varies depending on the injury mechanism and it is difficult to directly compare physiological and behavioural outcomes of different injury mechanisms as they will likely be of varying severity as well. It would be a challenge to model different injury mechanisms with the same force distribution due to the experimental setup, particularly the closed column nature of distraction injury compared to the open nature (via laminectomy) of contusion *in vivo.* This has yet to be achieved, although Park *et al.,* (2016) attempted to accommodate for the differences of two contusion SCI devices- the New York University (NYU) impactor and the Infinite Horizon (IH) impactor- by determining their equivalent parameters.

Direct strain transfer to astrocytes in this study may be an initiating factor for astrogliotic alterations via mechanotransduction: the process by which cells convert mechanical stimuli into changes in intracellular signalling (Hamill and Martinac, 2001). When mechanical force is applied directly to the hydrogel, the resulting strain can be translated to the cells via focal adhesions which mediate cell attachment to the matrix (Ahearne, 2014; Bowman *et al.,* 1992). Mechanotransduction may be initiated in a variety of ways, such as through deformation of ion channels, changes in the cytoskeletal structure, and/or activation of integrin-mediated signalling pathways (Alenghat and Ingber, 2002; Cullen *et al.,* 2007). These signalling pathways can regulate changes in gene expression which ultimately modify cellular behaviour, such as migration and proliferation. Astrogliotic induction mechanisms may also involve biochemical processes, such as autocrine and paracrine signalling involving factors like glutamate or ATP (Ahmed *et al.,* 2000; Cullen *et al.,* 2007; Neary *et al.,* 2003).

Astrogliosis has been depicted as a finely regulated collection of processes along a gradient of severity, rather than an all-or-nothing event with a single threshold (Sofroniew, 2015). It can be broadly categorised ranging from mild to moderate, where cytoskeletal hypertrophy is initiated but with preservation of domains and without

proliferation, to severe diffuse astrogliosis which is characterised by significant GFAP upregulation, cytoskeletal hypertrophy, and some domain overlapping. Severe astrogliosis with scar formation comprises predominantly newly-proliferated astrocytes with extensive process overlapping to demarcate the area of damage (Khakh and Sofroniew, 2015; Sofroniew, 2015). There was no evidence of significant proliferation in this study, although this was not evaluated using a specific proliferation assay, and a global contusion was administered so there was no lesion epicentre with a border. This may suggest that the astrogliosis observed here was severe- as evidenced by GFAP upregulation, hypertrophy and domain overlapping- but not as severe as the scar forming level.

6.3 Heterogeneity of Astrocytes

Glial fibrillary acidic protein (GFAP) is one of the most commonly used markers for astrocytes *in vivo* and *in vitro*, and it is widely accepted that upregulation of GFAP occurs during astrogliosis (Eng and Ghirnikar, 1994; Hinkle *et al.,* 1997; Pekny and Nilsson, 2005; Sofroniew and Vinters, 2010). However, although upregulation of GFAP is a sensitive marker of reactive astrocytes, many astrocytes do not express detectable levels of GFAP in healthy tissue. Whilst this meant that there was not a way to verify the identity of these GFAP-negative cells as actually being astrocytes, the distinction between non-reactive and reactive astrocytes could be made through quantification of the change in GFAP volume expression. Hinkle *et al.,* (1997) modelled traumatic brain contusion injury in rats and assessed GFAP and S100β expression 96 hours post-injury (1 mm cortical displacement at 3.5 m.s^{-1}). Results showed that all S100β-positive astrocytes expressed largely undetectable levels of GFAP under native conditions. However, following a mild contusion injury, these astrocytes began expressing GFAP. This property of astrocytes was observed in this project, particularly of astrocytes that were seeded in 3D into the collagen hydrogels. Immunolabelling of astrocytes using a polyclonal antibody against GFAP revealed that the majority of astrocytes in the control samples (no injury) were GFAP-negative, despite verification of GFAP immunoreactivity in 2D.

GFAP does not appear to be essential for the normal appearance and function of astrocytes in the CNS since GFAP-deficient mice develop normally (Pekny *et al.,* 1995), but it has been shown to be essential for the pathogenesis of astrogliosis (Sofroniew and Vinters, 2010). The mechanisms governing GFAP expression and its role in astrogliosis is not fully understood but since it is a key component for the assembly of intermediate filaments in astrocytes, it is thought that GFAP upregulation is important for the process of hypertrophy and ramification (Yang and Wang, 2015). The presence of intermediate filaments may provide increased mechanical resistance, which is considered unnecessary under non-injurious circumstances as protection is already provided by the vertebrae, meninges and cerebrospinal fluid (CSF). However, the structural demands are increased following trauma when reactive astrocytes undergo hypertrophy (Pekny *et al.,* 1999; Wilhelmsson *et al.,* 2004).

The lack of GFAP immunoreactivity in this research may have limited the complete evaluation of astrocyte behaviour in response to mechanical trauma, as the population of GFAP-negative astrocytes may provide useful insights into astrocyte biology and their roles in astrogliosis. However, GFAP was deemed an appropriate structural marker in this project to monitor changes in astrocyte reactivity and morphology following mechanical injury. As a more broad marker of astrocytes, $S100\beta$ could have been used alongside GFAP to visualise the GFAP-negative population in the sample. Gene profiling of mouse forebrain astrocytes, neurons, and oligodendrocytes have also highlighted antigenic markers specific for astrocytes, such as Aldh1L1, with a broader pattern of expression compared to GFAP (Cahoy *et al.*, 2008). Other markers reported to be broad pan-astrocyte markers are GLAST (EAAT1), and GLT-1 (EAAT2).

In this research, both contusion and distraction resulted in an increase in GFAP volume per cell and values were of a similar magnitude, particularly between both injury mechanisms at 100 mm.s^{-1} (Figures 4.7 and 5.7). This may suggest a similar level of reactivity, but does not provide information on potential genomic or functional differences. Differences in gene expression profiles have been observed between astrocytes activated by inflammation or ischaemic stroke (Anderson *et al.*, 2014; Zamanian *et al.*, 2012). Although there were genes that were altered in astrocytes in response to both injury mechanisms, at least 50% of the genes were specific to the applied injury type (Zamanian *et al.*, 2012). Another consideration for this research is that astrocyte heterogeneity exists between species as well. Human astrocytes have been shown to be different to rodent astrocytes in terms of size and the complexity of processes, and it has been suggested that increased astrocyte complexity has contributed to the increased power and capacity of the human brain (Oberheim *et al.*, 2009). These potential functional differences in astrocytes between species may have implications for future testing of therapeutic interventions.

6.4   Verification and Validation of *In Vitro* Models of TSCI

Validation of the *in vitro* model and results of this project is a challenge that must be achieved in order to enable the accurate comparison of *in vitro* results with clinical results. A robust and valid model could better inform the design of preclinical models *in vivo* or even replace some aspects such as early stage testing of therapeutic interventions. This is a challenge due to the biological heterogeneity between human patients and animal models, the wide variety of outcome measures used even between animal models, and robustness of the *in vitro* model including hydrogel system, source of materials, and stability of components. In this project, verification of the output biomechanical measurements was performed against the input parameters and found to be accurate (Chapter 3). Reliability was established for the injury methodology since repeatable results were obtained over time using the same methodology. However, robust reliability testing would require another group to use the same methodology and evaluate the reproducibility of the study, which has not yet been achieved.

Validation relies on the establishment of the reliability of the methodology, and the interpretation of test results against the real world human system. The data needs to be interpreted in the context of human TSCI, since reliability does not guarantee its applicability. TSCI is difficult to study in humans due to the typically unexpected nature of the event, and practical and ethical limitations associated with human research. Much of the knowledge of human TSCI pathophysiology has been derived from animal models. As the most commonly used animal model of TSCI, there remain important differences between rodent and human physiology, which contributes to the difficulties in translating this research into effective treatments for humans. At a cellular level, morphological and functional differences have been observed between astrocytes of different species and even between and within different tissue regions of the same species (Miller, 2018; Sofroniew and Vinters, 2010; Vasile *et al.,* 2017). For instance, GFAP expression has been shown to be higher in the adult spinal cord relative to the brain (Yoon *et al.,* 2017).

The primary astrocytes used in this project were derived from cortical tissue of pre-weaner Wistar rats. The identity and purity of the astrocytes were verified using qualitative analysis of morphology and immunocytochemical staining methods, with a GFAP antibody (Chapter 3). However, since the expression of GFAP was shown to vary between 2D and 3D culture further validation of the cells will be required, such as gene or protein expression analysis. Further, although multiple aspects of astrogliosis were observed following mechanical injury in this project, further validation of the model by treating with interventions known to modulate the microenvironment and/or promote repair *in vivo* is needed. Digestion of CSPGs was briefly investigated but this did not appear to affect astrocyte morphology after 48 hours. CSPG modulation may be more appropriate when neurons are present as CSPGs are known to be inhibitors of neurite outgrowth (Siebert *et al.,* 2014; Yiu and He, 2006; Yu *et al.,* 2012).

Successful validation of the *in vitro* contusion and distraction models used in this study provide the basis for developing more informed TSCI models where the biomechanics and, therefore, pathophysiology of injury can be more faithfully replicated within a single system. As such, these are useful tools for pre-clinical studies where therapeutic interventions can be tested to better inform animal studies, addressing the principles of the Three Rs to replace, reduce and refine the use of animals in research. There is also scope for analysing astrocyte behaviour using multiple molecular and genetic assays within a single hydrogel sample through splitting the sample into multiple segments, which will provide a better understanding of the effects of injury biomechanics on astrogliosis. The injury model protocols can be adapted and used with different hydrogel systems or spinal cord tissue, or used to mechanically characterise and test interventions such as spinal cord conduits, depending on the research question(s) posed.

6.5   Future Investigations

The research in this project raised further areas of investigation, which could provide useful insights into neural cell biology and their roles in TSCI.

6.5.1   Mechanisms of TSCI

Given the complexity of human SCI, no one model can encompass all aspects of injury. Each model aims to generate a consistent and easily reproducible injury that replicates SCI pathology in humans. The contusion and distraction injury mechanisms modelled in this project were clinically relevant as they are commonly observed in humans. However, as previously mentioned, human SCI is often represented by a combination of different mechanisms and strain modalities. Contusion-compression mechanisms of injury are likely more clinically relevant than pure contusion injuries- in which the impact is transient- as persistent spinal canal occlusion and cord compression is common in fracture dislocations and burst fractures, where bony vertebral fragments remain impinging on the cord. Some of the contusion models are, in fact, contusion–compression models that comprise an acute injury, followed by prolonged compression of the cord (Joshi and Fehlings, 2002; Rivlin and Tator, 1978).

Modelling contusion-compression injuries *in vitro* using the current model would be feasible as additional dwell steps can be incorporated into the waveform setup of the BOSE software. Further, the capability of perfusing cell culture medium through the chamber means the environmental conditions of the cells can be maintained during the experiment. Dislocation SCI is considered the most common mechanism of TSCI, representing up to 58% of mechanisms (Sekhon and Fehlings, 2001; Tator, 1983), thus this would be an important mechanism to model. However, substantial adaptations to the BOSE and mould designs would need to be considered in order to model this injury.

6.5.2   Increasing Model Complexity

One limitation of this research was the lack of cellular complexity in the *in vitro* model. Whilst simplifying the biological milieu to include only one cell type enabled the evaluation of the direct impact of mechanical trauma on astrocyte biology, this removed important interactions between astrocytes and other cell types and their secreted molecules, which are likely to contribute to the dynamics of astrogliosis. As such, increasing the cellular complexity of the model will increase its biological relevance. Initially, different neural cell types- neurons, microglia, and oligodendrocytes- could be cultured in isolation to evaluate the effects of different TSCI mechanisms on their pathophysiology, followed by incorporating different cell types into co-cultures. Co-cultures of neural cells have previously been used to model mechanical trauma, including neurons and astrocytes (Cullen *et al.,* 2007; LaPlaca *et al.,* 2005).

Astrocytes are known to influence neuronal survival and behaviour, through providing trophic factors, regulating the synaptic environment, and supporting neurite outgrowth (Fields and Stevens-Graham, 2002; Tsacopoulos, 2002). By co-culturing

astrocytes in isolation, and with neurons in co-culture, the influence of astrogliosis on neurons and vice versa could be evaluated. For instance, since neurite outgrowth is impeded by the glial scar *in vivo*, the effects of different injury mechanisms and injury severity on neurite outgrowth could be assessed (McKeon *et al.,* 1991; Wanner *et al.,* 2008). Further, additional secondary injury events could be investigated, such as neurite outgrowth. In addition to cellular complexity, cytoarchitecture plays an important role in the functioning of the spinal cord. The spinal cord is highly organised, with the white matter containing the myelinated axons of neurons organised into bundles called tracts. Cellular alignment has been previously shown to guide axon outgrowth *in vitro* (East *et al.,* 2010), and can be achieved by tethering hydrogels at opposite ends. This causes the gel to contract as cells remodel the matrix and align along the axis of principal strain (Phillips *et al.,* 2005). The moulds used in the distraction study (Chapter 5) were based on the design by Phillips *et al.,* (2005) although alignment was not generated as it necessitated the use of TGF-β1, an inducer of astrogliosis but alignment would be a useful feature when evaluating neuronal behaviour in response to mechanical injury mechanisms.

6.5.3 Local Mechanical Changes Following Injury

An accurate *in vitro* model of TSCI would faithfully replicate not only the pathophysiological alterations, but also any potential mechanical alterations that occur following injury. Human tissues have a poor regenerative capacity and fibrosis often takes place following damage, a pathological wound healing process which results in scar tissue which has been found to be stiffer than healthy tissue (Swift *et al.,* 2013). In the CNS, damage also results in a scar (glial scar) through astrogliosis. Glial scars are described as rich in glial cells, non-neural cells such as meningeal cells, and various ECM components like CSPGs which create a dense network of cells and ECM chemically and mechanically non-permissive to neuroregeneration (Fawcett and Asher, 1999; Silver and Miller, 2004). Therefore, the concept of the glial scar being stiff was a natural assumption to make.

However, evidence has been presented for a softening of the microenvironment following injury, at the cellular level *in vitro* (Miller *et al.,* 2009) and tissue level *in vivo* (Moeendarbary *et al.,* 2017). Moeendarbary *et al.,* (2017) found that the increases observed in GFAP, vimentin, laminin, and collagen-IV following rat cortical stab injury and spinal cord crush injury was correlated with tissue softening. Since some differences in GFAP and CSPG expression were observed between contusion and distraction injury in this project, it would be interesting to evaluate whether there are mechanical differences too. Bulk mechanical properties can be evaluated using tools such as rheology, and local mechanical properties can be evaluated using AFM like Moeendarbary *et al.,* (2017). AFM would be more useful in contusion models, for instance, in which a focal injury is inflicted as this enables the measurement of elastic modulus in injured and uninjured regions of the same sample.

6.5.4 Inflammation

Following TSCI, disruption of the blood-spinal cord barrier (BSCB) leads to the recruitment of blood-borne leukocytes, as well as activation of the intrinsic glia, including astrocytes and microglia (Okada, 2016). The inflammatory response plays a major role in the pathophysiology of TSCI (Chapter 1) and astrocytes are also important mediators of inflammation through the release of numerous pro- and anti-inflammatory chemokines, cytokines and growth factors. Selective ablation of reactive astrocytes has been shown to exacerbate inflammation following SCI, amongst other degenerative effects (Bush *et al.,* 1999; Faulkner *et al.,* 2004) so astrogliosis does provide a protective role despite also being inhibitory to repair. It is difficult to demonstrate the release of cytokines, chemokines and ECM components specifically by astrocytes *in vivo* since other cell types secrete similar molecules (Kang and Hébert, 2011). Thus, using isolated cultures of astrocytes *in vitro* would be advantageous.

This study has demonstrated that astrocytes produce increased amounts of CSPGs in response to mechanical trauma (Chapters 5 and 6). ELISA analysis of cytokines in the cell culture medium was attempted, but detectable levels of the analyte could not be measured. Cytokine profiling for different injury mechanisms would provide insight into the potential differences in inflammatory response, which could indicate whether one injury mechanism environment could be better targeted with a particular treatment. For instance, if one injury mechanism results in the expression of significantly more IL-6, a key pro-inflammatory cytokine known to be expressed by reactive astrocytes (Garcia *et al.,* 2016), a receptor-neutralising antibody to IL-6 could be tested (Okada *et al.,* 2004). Increasing the cell density of each sample could enable a detectable level of cytokines to be measured, but this would increase the number of animals required. Cytokine arrays are also available to test for a wider range of cytokines which would provide a more detailed picture of the inflammatory profile of astrocytes in response to different injury mechanisms.

6.6   Conclusions

The aim of this project was to model two distinct mechanisms of traumatic spinal cord injury *in vitro*, contusion and distraction, using the BOSE Electroforce BioDynamic 5110 with a three-dimensional primary astrocyte-seeded collagen hydrogel, in order to evaluate the effects of differing injury biomechanics on astrocyte behaviour:

- The BOSE Electroforce BioDynamic 5110 materials testing machine is an appropriate tool for the application of clinically relevant strains and strain rates representing more than one mechanism of TSCI.

- Protocols were designed to simulate compressive and tensile forces representing contusion and distraction TSCI, using a range of different input velocities and displacement depths/lengths, which resulted in accurate and reproducible injuries being inflicted *in vitro* with hydrogels.

- A collagen hydrogel seeded in 3D with primary rat cortical astrocytes was developed for the application of experimental injury representing contusion and distraction TSCI.

- Contusion and distraction injury both induced a response in astrocytes which reflected multiple processes of astrogliosis, including increased GFAP and CSPG expression, astrocyte hypertrophy, ramification, and loss of domain preservation.

- Differences in astrocyte responses were observed in response to contusion and distraction injury *in vitro*, particularly temporal differences in GFAP volume and CSPG expression. Viability was reduced similarly for both injury mechanisms at Day 1 post-injury.

- Further investigations are required to probe in more depth the interactions between velocity and displacement and how these influence cellular behaviour and dynamics, extending to more cell types of the CNS.

References

Abu-Rub, M., McMahon, S., Zeugolis, D. I., Windebank, A., and Pandit, A. (2010). "Spinal cord injury in vitro: modelling axon growth inhibition". In: *Drug discovery today* 15.11-12, pp. 436–443.

Acaz-Fonseca, E., Ortiz-Rodriguez, A., Azcoitia, I., Garcia-Segura, L. M., and Arevalo, M.-A. (2019). "Notch signaling in astrocytes mediates their morphological response to an inflammatory challenge". In: *Cell death discovery* 5.1, pp. 1–14.

Agrawal, G., Kerr, C., Thakor, N. V., and All, A. H. (2010). "Characterization of graded MASCIS contusion spinal cord injury using somatosensory evoked potentials". In: *Spine* 35.11, p. 1122.

Ahearne, M., Yang, Y., and Liu, K. (2008). "Mechanical characterisation of hydrogels for tissue engineering applications". In: *Topics in tissue Engineering* 4.12, pp. 1–16.

Ahearne, M. (2014). "Introduction to cell–hydrogel mechanosensing". In: *Interface focus* 4.2, p. 20130038.

Ahmed, S. M., Rzigalinski, B. A., Willoughby, K. A., Sitterding, H. A., and Ellis, E. F. (2000). "Stretch-induced injury alters mitochondrial membrane potential and cellular ATP in cultured astrocytes and neurons". In: *Journal of neurochemistry* 74.5, pp. 1951–1960.

Alenghat, F. J. and Ingber, D. E. (2002). "Mechanotransduction: all signals point to cytoskeleton, matrix, and integrins". In: *Science Signaling* 2002.119.

Allen, A. R. (1911). "Surgery of experimental lesion of spinal cord equivalent to crush injury of fracture dislocation of spinal column: a preliminary report". In: *Journal of the American Medical Association* 57.11, pp. 878–880.

Aloisi, F. (2001). "Immune function of microglia". In: *Glia* 36.2, pp. 165–179.

Anderson, K. D., Sharp, K. G., and Steward, O. (2009). "Bilateral cervical contusion spinal cord injury in rats". In: *Experimental neurology* 220.1, pp. 9–22.

Anderson, M. A., Ao, Y., and Sofroniew, M. V. (2014). "Heterogeneity of reactive astrocytes". In: *Neuroscience letters* 565, pp. 23–29.

Antoine, E. E., Vlachos, P. P., and Rylander, M. N. (2015). "Tunable collagen I hydrogels for engineered physiological tissue micro-environments". In: *Plos one* 10.3, pp. 1–18.

Antoine, E. E., Vlachos, P. P., and Rylander, M. N. (2014). "Review of collagen I hydrogels for bioengineered tissue microenvironments: characterization of mechanics, structure, and transport". In: *Tissue Engineering Part B: Reviews* 20.6, pp. 683–696.

Ashammakhi, N., Kim, H.-J., Ehsanipour, A., Bierman, R. D., Kaarela, O., Xue, C., Khademhosseini, A., and Seidlits, S. K. (2019). "Regenerative therapies for spinal cord injury". In: *Tissue Engineering Part B: Reviews* 25.6, pp. 471–491.

Åström, K. J. and Hägglund, T. (1995). *PID controllers: theory, design, and tuning.* Vol. 2. Instrument society of America Research Triangle Park, NC.

Badhiwala, J. H., Wilson, J. R., Witiw, C. D., Harrop, J. S., Vaccaro, A. R., Aarabi, B., Grossman, R. G., Geisler, F. H., and Fehlings, M. G. (2020). "The influence of timing of surgical decompression for acute spinal cord injury: a pooled analysis of individual patient data". In: *The Lancet Neurology.*

Bain, A. C. and Meaney, D. F. (2000). "Tissue-level thresholds for axonal damage in an experimental model of central nervous system white matter injury". In: *J. Biomech. Eng.* 122.6, pp. 615–622.

Baker, B. M. and Chen, C. S. (2012). "Deconstructing the third dimension–how 3D culture microenvironments alter cellular cues". In: *Journal of cell science* 125.13, pp. 3015–3024.

Bar-Kochba, E., Scimone, M. T., Estrada, J. B., and Franck, C. (2016). "Strain and rate-dependent neuronal injury in a 3D in vitro compression model of traumatic brain injury". In: *Scientific reports* 6.1, pp. 1–11.

Bareyre, F. M. and Schwab, M. E. (2003). "Inflammation, degeneration and regeneration in the injured spinal cord: insights from DNA microarrays". In: *Trends in neurosciences* 26.10, pp. 555–563.

Barnabé-Heider, F., Göritz, C., Sabelström, H., Takebayashi, H., Pfrieger, F. W., Meletis, K., and Frisén, J. (2010). "Origin of new glial cells in intact and injured adult spinal cord". In: *Cell stem cell* 7.4, pp. 470–482.

Barnes, J. M., Przybyla, L., and Weaver, V. M. (2017). "Tissue mechanics regulate brain development, homeostasis and disease". In: *J Cell Sci* 130.1, pp. 71–82.

Barros, C. S., Franco, S. J., and Müller, U. (2011). "Extracellular matrix: functions in the nervous system". In: *Cold Spring Harbor perspectives in biology* 3.1, pp. 1–24.

Barson, A. (1970). "The vertebral level of termination of the spinal cord during normal and abnormal development." In: *Journal of anatomy* 106.Pt 3, p. 489.

Bartlett, R., Choi, D., and Phillips, J. (2016a). "A novel protocol to characterise the mechanical properties of spinal cord tissue and benchmark candidate biomaterials for CNS tissue-engineering". In: *European Cells and Materials* 31.1, p. 8.

Bartlett, R. D., Choi, D., and Phillips, J. B. (2016b). "Biomechanical properties of the spinal cord: implications for tissue engineering and clinical translation". In: *Regenerative medicine* 11.7, pp. 659–673.

Basso, D. M., Beattie, M. S., and Bresnahan, J. C. (1995). "A sensitive and reliable locomotor rating scale for open field testing in rats". In: *Journal of neurotrauma* 12.1, pp. 1–21.

Basso, D. M., Beattie, M. S., and Bresnahan, J. C. (1996). "Graded histological and locomotor outcomes after spinal cord contusion using the NYU weight-drop device versus transection". In: *Experimental neurology* 139.2, pp. 244–256.

Beattie, M. S., Hermann, G. E., Rogers, R. C., and Bresnahan, J. C. (2002). "Cell death in models of spinal cord injury". In: *Progress in brain research* 137, pp. 37–47.

Bhatnagar, T., Liu, J., Yung, A., Cripton, P. A., Kozlowski, P., and Oxland, T. (2016). "In vivo measurement of cervical spinal cord deformation during traumatic spinal cord injury in a rodent model". In: *Annals of Biomedical Engineering* 44.4, pp. 1285–1298.

Bilston, L. E. (2011). *Neural tissue biomechanics*. Vol. 3. Springer Science & Business Media.

Bilston, L. E. and Thibault, L. E. (1995). "The mechanical properties of the human cervical spinal cord In Vitro". In: *Annals of biomedical engineering* 24.1, pp. 67–74.

Bitar, M., Salih, V., Brown, R. A., and Nazhat, S. N. (2007). "Effect of multiple unconfined compression on cellular dense collagen scaffolds for bone tissue engineering". In: *Journal of Materials Science: Materials in Medicine* 18.2, pp. 237–244.

Boni, R., Ali, A., Shavandi, A., and Clarkson, A. N. (2018). "Current and novel polymeric biomaterials for neural tissue engineering". In: *Journal of biomedical science* 25.1, p. 90.

Boomkamp, S., McGrath, M., Houslay, M., and Barnett, S. (2014). "Epac and the high affinity rolipram binding conformer of PDE 4 modulate neurite outgrowth and

myelination using an in vitro spinal cord injury model". In: *British journal of pharmacology* 171.9, pp. 2385–2398.

BOSE (2015). *WinTest 7 Software Reference Manual*. English. Version Version 2. BOSE. 334 pp. 2015.

Bowman, C. L., Ding, J.-P., Sachs, F., and Sokabe, M. (1992). "Mechanotransducing ion channels in astrocytes". In: *Brain research* 584.1-2, pp. 272–286.

Bradbury, E. J. and Burnside, E. R. (2019). "Moving beyond the glial scar for spinal cord repair". In: *Nature communications* 10.1, pp. 1–15.

Bradbury, E. J., Moon, L. D., Popat, R. J., King, V. R., Bennett, G. S., Patel, P. N., Fawcett, J. W., and McMahon, S. B. (2002). "Chondroitinase ABC promotes functional recovery after spinal cord injury". In: *Nature* 416.6881, pp. 636–640.

Brahmachari, S., Fung, Y. K., and Pahan, K. (2006). "Induction of glial fibrillary acidic protein expression in astrocytes by nitric oxide". In: *Journal of Neuroscience* 26.18, pp. 4930–4939.

Brambilla, R., Bracchi-Ricard, V., Hu, W.-H., Frydel, B., Bramwell, A., Karmally, S., Green, E. J., and Bethea, J. R. (2005). "Inhibition of astroglial nuclear factor κB reduces inflammation and improves functional recovery after spinal cord injury". In: *The Journal of experimental medicine* 202.1, pp. 145–156.

Bresnahan, J. C., Beattie, M. S., Todd III, F. D., and Noyes, D. H. (1987). "A behavioral and anatomical analysis of spinal cord injury produced by a feedback-controlled impaction device". In: *Experimental neurology* 95.3, pp. 548–570.

Brody, D. L., Mac Donald, C., Kessens, C. C., Yuede, C., Parsadanian, M., Spinner, M., Kim, E., Schwetye, K. E., Holtzman, D. M., and Bayly, P. V. (2007). "Electromagnetic controlled cortical impact device for precise, graded experimental traumatic brain injury". In: *Journal of neurotrauma* 24.4, pp. 657–673.

Brown, R. A., Wiseman, M., Chuo, C.-B., Cheema, U., and Nazhat, S. N. (2005). "Ultrarapid engineering of biomimetic materials and tissues: Fabrication of nano-and microstructures by plastic compression". In: *Advanced Functional Materials* 15.11, pp. 1762–1770.

Bucz, Š. and Kozáková, A. (2018). "Advanced methods of PID controller tuning for specified performance". In: *PID Control for Industrial Processes*, pp. 73–119.

Burda, J. E. and Sofroniew, M. V. (2014). "Reactive gliosis and the multicellular response to CNS damage and disease". In: *Neuron* 81.2, pp. 229–248.

Busby, G. A., Grant, M. H., MacKay, S. P., and Riches, P. E. (2013). "Confined compression of collagen hydrogels". In: *Journal of biomechanics* 46.4, pp. 837–840.

Bush, T. G., Puvanachandra, N., Horner, C. H., Polito, A., Ostenfeld, T., Svendsen, C. N., Mucke, L., Johnson, M. H., and Sofroniew, M. V. (1999). "Leukocyte infiltration, neuronal degeneration, and neurite outgrowth after ablation of scar-forming, reactive astrocytes in adult transgenic mice". In: *Neuron* 23.2, pp. 297–308.

Bushong, E. A., Martone, M. E., Jones, Y. Z., and Ellisman, M. H. (2002). "Protoplasmic astrocytes in CA1 stratum radiatum occupy separate anatomical domains". In: *Journal of Neuroscience* 22.1, pp. 183–192.

Cahoy, J. D., Emery, B., Kaushal, A., Foo, L. C., Zamanian, J. L., Christopherson, K. S., Xing, Y., Lubischer, J. L., Krieg, P. A., Krupenko, S. A., Thompson, W. J., and Barres, B. A. (2008). "A transcriptome database for astrocytes, neurons, and oligodendrocytes: a new resource for understanding brain development and function". In: *Journal of Neuroscience* 28.1, pp. 264–278.

Cajal, S. R. (1909). "Histologie du Systeme Nerveux de l'Homme et des Vertebres". In: 2, pp. 832–835.

Caliari, S. R. and Burdick, J. A. (2016). "A practical guide to hydrogels for cell culture". In: *Nature methods* 13.5, pp. 405–414.

Cappozzo, A. (1983). "Compressive loads in the lumbar vertebral column during normal level walking". In: *Journal of orthopaedic research* 1.3, pp. 292–301.

Carulli, D., Rhodes, K. E., Brown, D. J., Bonnert, T. P., Pollack, S. J., Oliver, K., Strata, P., and Fawcett, J. W. (2006). "Composition of perineuronal nets in the adult rat cerebellum and the cellular origin of their components". In: *Journal of Comparative Neurology* 494.4, pp. 559–577.

Center, N. S. C. I. S. *et al.,* (2015). "Recent trends in causes of spinal cord injury". In: *Birmingham, AL: University of Alabama at Birmingham.*

Chandran, P. L. and Barocas, V. H. (2004). "Microstructural mechanics of collagen gels in confined compression: poroelasticity, viscoelasticity, and collapse". In: *J. Biomech. Eng.* 126.2, pp. 152–166.

Cheema, U., Rong, Z., Kirresh, O., MacRobert, A. J., Vadgama, P., and Brown, R. A. (2012). "Oxygen diffusion through collagen scaffolds at defined densities: implications for cell survival in tissue models". In: *Journal of tissue engineering and regenerative medicine* 6.1, pp. 77–84.

Chen, K., Liu, J., Assinck, P., Bhatnagar, T., Streijger, F., Zhu, Q., Dvorak, M. F., Kwon, B. K., Tetzlaff, W., and Oxland, T. R. (2016). "Differential histopathological and behavioral outcomes eight weeks after rat spinal cord injury by contusion, dislocation, and distraction mechanisms". In: *Journal of Neurotrauma* 33.18, pp. 1667–1684.

Chen, M. S., Huber, A. B., van der Haar, M. E., Frank, M., Schnell, L., Spillmann, A. A., Christ, F., and Schwab, M. E. (2000). "Nogo-A is a myelin-associated neurite outgrowth inhibitor and an antigen for monoclonal antibody IN-1". In: *Nature* 403.6768, pp. 434–439.

Cheng, S., Clarke, E. C., and Bilston, L. E. (2008). "Rheological properties of the tissues of the central nervous system: a review". In: *Medical engineering & physics* 30.10, pp. 1318–1337.

Cheriyan, T., Ryan, D., Weinreb, J. H., Cheriyan, J., Paul, J. C., Lafage, V., Kirsch, T., and Errico, T. J. (2014). "Spinal cord injury models: a review". In: *Spinal cord* 52.8, pp. 588–595.

Choo, A. M., Liu, J., Dvorak, M., Tetzlaff, W., and Oxland, T. R. (2008). "Secondary pathology following contusion, dislocation, and distraction spinal cord injuries". In: *Experimental Neurology* 212.2, pp. 490–506.

Choo, A. M., Liu, J., Lam, C. K., Dvorak, M., Tetzlaff, W., and Oxland, T. R. (2007). "Contusion, dislocation, and distraction: primary hemorrhage and membrane permeability in distinct mechanisms of spinal cord injury". In: *Journal of Neurosurgery: Spine* 6.3, pp. 255–266.

Choo, A. M., Liu, J., Liu, Z., Dvorak, M., Tetzlaff, W., and Oxland, T. R. (2009). "Modeling spinal cord contusion, dislocation, and distraction: characterization of vertebral clamps, injury severities, and node of Ranvier deformations". In: *Journal of Neuroscience Methods* 181.1, pp. 6–17.

Cukierman, E., Pankov, R., Stevens, D. R., and Yamada, K. M. (2001). "Taking cell-matrix adhesions to the third dimension". In: *Science* 294.5547, pp. 1708–1712.

Cullen, D. K. and LaPlaca, M. C. (2006). "Neuronal response to high rate shear deformation depends on heterogeneity of the local strain field". In: *Journal of neurotrauma* 23.9, pp. 1304–1319.

Cullen, D. K., Simon, C. M., and LaPlaca, M. C. (2007). "Strain rate-dependent induction of reactive astrogliosis and cell death in three-dimensional neuronal–astrocytic co-cultures". In: *Brain research* 1158, pp. 103–115.

Cullen, D. K., Vernekar, V. N., and LaPlaca, M. C. (2011). "Trauma-induced plasmalemma disruptions in three-dimensional neural cultures are dependent on strain modality and rate". In: *Journal of neurotrauma* 28.11, pp. 2219–2233.

Dabney, K. W., Ehrenshteyn, M., Agresta, C. A., Twiss, J. L., Stern, G., Tice, L., and Salzman, S. K. (2004). "A model of experimental spinal cord trauma based on computer-controlled intervertebral distraction: characterization of graded injury". In: *Spine* 29.21, pp. 2357–2364.

David, G., Mohammadi, S., Martin, A. R., Cohen-Adad, J., Weiskopf, N., Thompson, A., and Freund, P. (2019). "Traumatic and nontraumatic spinal cord injury: pathological insights from neuroimaging". In: *Nature Reviews Neurology*, pp. 1–14.

De Campos, D., Goerck, M. L., Ellwanger, J. H., Corbellini, R. O., Hoelscher, R. H., Souza, M. S., and Rieger, A. (2017). "Anatomy of the first spinal nerve–a review". In: *Journal of Morphological Sciences* 29.2.

Denis, F. (1983). "The three column spine and its significance in the classification of acute thoracolumbar spinal injuries." In: *spine* 8.8, pp. 817–831.

DeQuach, J. A., Yuan, S. H., Goldstein, L. S., and Christman, K. L. (2011). "Decellularized porcine brain matrix for cell culture and tissue engineering scaffolds". In: *Tissue Engineering Part A* 17.21-22, pp. 2583–2592.

Didangelos, A., Puglia, M., Iberl, M., Sanchez-Bellot, C., Roschitzki, B., and Bradbury, E. J. (2016). "High-throughput proteomics reveal alarmins as amplifiers of tissue pathology and inflammation after spinal cord injury". In: *Scientific Reports* 6, pp. 1–15.

Dinescu, S., Albu Kaya, M., Chitoiu, L., Ignat, S., Kaya, D. A., and Costache, M. (2018). "Collagen-based hydrogels and their applications for tissue engineering and regenerative medicine". In: *Cellulose-Based Superabsorbent Hydrogels. Polymers and Polymeric Composites: A Reference Series; Mondal, M., Ed*, pp. 1–21.

Dong, X.-x., Wang, Y., and Qin, Z.-h. (2009). "Molecular mechanisms of excitotoxicity and their relevance to pathogenesis of neurodegenerative diseases". In: *Acta Pharmacologica Sinica* 30.4, pp. 379–387.

Du, F., Qian, Z. M., Zhu, L., Wu, X. M., Qian, C., Chan, R., and Ke, Y. (2010). "Purity, cell viability, expression of GFAP and bystin in astrocytes cultured by different procedures". In: *Journal of cellular biochemistry* 109.1, pp. 30–37.

Duchen, L. (1992). "General pathology of neurons and neuroglia". In: *Greenfields neuropathology*, pp. 1–68.

Dumont, R. J., Okonkwo, D. O., Verma, S., Hurlbert, R. J., Boulos, P. T., Ellegala, D. B., and Dumont, A. S. (2001). "Acute spinal cord injury, part I: pathophysiologic mechanisms". In: *Clinical neuropharmacology* 24.5, pp. 254–264.

Dunham, K. A., Siriphorn, A., Chompoopong, S., and Floyd, C. L. (2010). "Characterization of a graded cervical hemicontusion spinal cord injury model in adult male rats". In: *Journal of Neurotrauma* 27.11, pp. 2091–2106.

East, E., de Oliveira, D. B., Golding, J. P., and Phillips, J. B. (2010). "Alignment of astrocytes increases neuronal growth in three-dimensional collagen gels and is maintained following plastic compression to form a spinal cord repair conduit". In: *Tissue engineering Part A* 16.10, pp. 3173–3184.

East, E., Golding, J., and Phillips, J. (2007). "Development of a 3-dimensional in vitro model to study reactive gliosis following nervous system injury". In: *Tissue Engineering* 13.7, pp. 1668–1778.

East, E., Golding, J. P., and Phillips, J. B. (2009). "A versatile 3D culture model facilitates monitoring of astrocytes undergoing reactive gliosis". In: *Journal of tissue engineering and regenerative medicine* 3.8, pp. 634–646.

Ellis, E., McKinney, J., Willoughby, K., Liang, S., and Povlishock, J. (1995). "A new model for rapid stretch-induced injury of cells in culture: characterization of the model using astrocytes". In: *Journal of neurotrauma* 12.3, pp. 325–339.

Eng, L. F. (1985). "Glial fibrillary acidic protein (GFAP): the major protein of glial intermediate filaments in differentiated astrocytes". In: *Journal of neuroimmunology* 8, pp. 203–214.

Eng, L. F. and Ghirnikar, R. S. (1994). "GFAP and astrogliosis". In: *Brain pathology* 4.3, pp. 229–237.

Faulkner, J. R., Herrmann, J. E., Woo, M. J., Tansey, K. E., Doan, N. B., and Sofroniew, M. V. (2004). "Reactive astrocytes protect tissue and preserve function after spinal cord injury". In: *Journal of Neuroscience* 24.9, pp. 2143–2155.

Fawcett, J. W. and Asher, R. A. (1999). "The glial scar and central nervous system repair". In: *Brain research bulletin* 49.6, pp. 377–391.

Feeney, C. J., Frantseva, M. V., Carlen, P. L., Pennefather, P. S., Shulyakova, N., Shniffer, C., and Mills, L. R. (2008). "Vulnerability of glial cells to hydrogen peroxide in cultured hippocampal slices". In: *Brain research* 1198, pp. 1–15.

Fields, R. D. and Stevens-Graham, B. (2002). "New insights into neuron-glia communication". In: *Science* 298.5593, pp. 556–562.

Fiford, R. J., Bilston, L. E., Waite, P., and Lu, J. (2004). "A vertebral dislocation model of spinal cord injury in rats". In: *Journal of Neurotrauma* 21.4, pp. 451–458.

Fiford, R. J. and Bilston, L. E. (2005). "The mechanical properties of rat spinal cord in vitro". In: *Journal of biomechanics* 38.7, pp. 1509–1515.

Figueiredo, L., Pace, R., d'Arros, C., Réthoré, G., Guicheux, J., Le Visage, C., and Weiss, P. (2018). "Assessing glucose and oxygen diffusion in hydrogels for the rational design of 3D stem cell scaffolds in regenerative medicine". In: *Journal of tissue engineering and regenerative medicine* 12.5, pp. 1238–1246.

Fitch, M. T. and Silver, J. (2008). "CNS injury, glial scars, and inflammation: Inhibitory extracellular matrices and regeneration failure". In: *Experimental neurology* 209.2, pp. 294–301.

Fleming, J. C., Norenberg, M. D., Ramsay, D. A., Dekaban, G. A., Marcillo, A. E., Saenz, A. D., Pasquale-Styles, M., Dietrich, W. D., and Weaver, L. C. (2006). "The cellular inflammatory response in human spinal cords after injury". In: *Brain* 129.12, pp. 3249–3269.

Floyd, C. L., Rzigalinski, B. A., Weber, J. T., Sitterding, H. A., Willoughby, K. A., and Ellis, E. F. (2001). "Traumatic injury of cultured astrocytes alters inositol (1, 4, 5)–trisphosphate-mediated signaling". In: *Glia* 33.1, pp. 12–23.

Fournely, M., Petit, Y., Wagnac, E., Laurin, J., Callot, V., and Arnoux, P.-J. (2018). "High-speed video analysis improves the accuracy of spinal cord compression measurement in a mouse contusion model". In: *Journal of Neuroscience Methods* 293, pp. 1–5.

Frantseva, M. V., Carlen, P. L., and El-Beheiry, H. (1999). "A submersion method to induce hypoxic damage in organotypic hippocampal cultures". In: *Journal of neuroscience methods* 89.1, pp. 25–31.

Frantz, C., Stewart, K. M., and Weaver, V. M. (2010). "The extracellular matrix at a glance". In: *Journal of cell science* 123.24, pp. 4195–4200.

Fratzl, P. (2008). *Collagen: structure and mechanics, an introduction.* Springer, pp. 1–13.

Friedl, P. and Bröcker, E.-B. (2000). "The biology of cell locomotion within three-dimensional extracellular matrix". In: *Cellular and molecular life sciences CMLS* 57.1, pp. 41–64.

Frostell, A., Hakim, R., Thelin, E. P., Mattsson, P., and Svensson, M. (2016). "A review of the segmental diameter of the healthy human spinal cord". In: *Frontiers in neurology* 7, p. 238.

Fukuda, S., Nakamura, T., Kishigami, Y., Endo, K., Azuma, T., Fujikawa, T., Tsutsumi, S., and Shimizu, Y. (2005). "New canine spinal cord injury model free from laminectomy". In: *Brain research protocols* 14.3, pp. 171–180.

Garcia, E., Aguilar-Cevallos, J., Silva-Garcia, R., and Ibarra, A. (2016). "Cytokine and growth factor activation in vivo and in vitro after spinal cord injury". In: *Mediators of inflammation* 2016.

Gaudet, A. D. and Fonken, L. K. (2018). "Glial cells shape pathology and repair after spinal cord injury". In: *Neurotherapeutics* 15.3, pp. 554–577.

Geddes, D. M., LaPlaca, M. C., and Cargill II, R. S. (2003). "Susceptibility of hippocampal neurons to mechanically induced injury". In: *Experimental neurology* 184.1, pp. 420–427.

Geddes-Klein, D. M., Schiffman, K. B., and Meaney, D. F. (2006). "Mechanisms and consequences of neuronal stretch injury in vitro differ with the model of trauma". In: *Journal of neurotrauma* 23.2, pp. 193–204.

Gensel, J. C., Tovar, C. A., Hamers, F. P. T., Deibert, R. J., Beattie, M. S., and Bresnahan, J. C. (2006). "Behavioral and histological characterization of unilateral cervical spinal cord contusion injury in rats". In: *Journal of Neurotrauma* 23.1, pp. 36–54.

Georges, P. C., Miller, W. J., Meaney, D. F., Sawyer, E. S., and Janmey, P. A. (2006). "Matrices with compliance comparable to that of brain tissue select neuronal over glial growth in mixed cortical cultures". In: *Biophysical journal* 90.8, pp. 3012–3018.

Georgiou, M., Bunting, S. C., Davies, H. A., Loughlin, A. J., Golding, J. P., and Phillips, J. B. (2013). "Engineered neural tissue for peripheral nerve repair". In: *Biomaterials* 34.30, pp. 7335–7343.

Ghasemlou, N., Kerr, B. J., and David, S. (2005). "Tissue displacement and impact force are important contributors to outcome after spinal cord contusion injury". In: *Experimental Neurology* 196.1, pp. 9–17.

Gray, H. (1985). "Anatomy of the human body 20th ed". In: *Philadelphia, Pa: Lea & Febiger*.

Greenberg, S. A. (2003). "The history of dermatome mapping". In: *Archives of Neurology* 60.1, pp. 126–131.

Griffith, C. K., Miller, C., Sainson, R. C., Calvert, J. W., Jeon, N. L., Hughes, C. C., and George, S. C. (2005). "Diffusion limits of an in vitro thick prevascularized tissue". In: *Tissue engineering* 11.1-2, pp. 257–266.

Gruner, J. A. (1992). "A monitored contusion model of spinal cord injury in the rat". In: *Journal of neurotrauma* 9.2, pp. 123–128.

Guerra, M. C., Tortorelli, L. S., Galland, F., Da Re, C., Negri, E., Engelke, D. S., Rodrigues, L., Leite, M. C., and Gonçalves, C.-A. (2011). "Lipopolysaccharide modulates astrocytic S100B secretion: a study in cerebrospinal fluid and astrocyte cultures from rats". In: *Journal of neuroinflammation* 8.1, p. 128.

Guo, Y., Hu, H., Wang, J., Zhang, M., and Chen, K. (2019). "Walking Function After Cervical Contusion and Distraction Spinal Cord Injuries in Rats". In: *Journal of experimental neuroscience* 13, pp. 1–12.

Hackett, A. R. and Lee, J. K. (2016). "Understanding the NG2 glial scar after spinal cord injury". In: *Frontiers in neurology* 7, p. 199.

Hadjipanayi, E., Mudera, V., and Brown, R. A. (2009). "Guiding cell migration in 3D: a collagen matrix with graded directional stiffness". In: *Cell motility and the cytoskeleton* 66.3, pp. 121–128.

Haggerty, A. E., Marlow, M. M., and Oudega, M. (2017). "Extracellular matrix components as therapeutics for spinal cord injury". In: *Neuroscience letters* 652, pp. 50–55.

Halford, J., Shen, S., Itamura, K., Levine, J., Chong, A. C., Czerwieniec, G., Glenn, T. C., Hovda, D. A., Vespa, P., Bullock, R., *et al.,* (2017). "New astroglial injury-defined biomarkers for neurotrauma assessment". In: *Journal of Cerebral Blood Flow & Metabolism* 37.10, pp. 3278–3299.

Hamill, O. P. and Martinac, B. (2001). "Molecular basis of mechanotransduction in living cells". In: *Physiological reviews* 81.2, pp. 685–740.

Hinkle, D. A., Baldwin, S. A., Scheff, S. W., and Wise, P. M. (1997). "GFAP and S100β expression in the cortex and hippocampus in response to mild cortical contusion". In: *Journal of neurotrauma* 14.10, pp. 729–738.

Hopkins, A. M., DeSimone, E., Chwalek, K., and Kaplan, D. L. (2015). "3D in vitro modeling of the central nervous system". In: *Progress in neurobiology* 125, pp. 1–25.

Hung, T.-K. and Chang, G.-L. (1981). "Biomechanical and neurological response of the spinal cord of a puppy to uniaxial tension". In: *Journal of biomechanichanical engineering* 103, pp. 43–47.

Hung, T.-K., Chang, G.-L., Chang, J.-L., and Albin, M. S. (1981a). "Stress-strain relationship and neurological sequelae of uniaxial elongation of the spinal cord of cats." In: *Surgical neurology* 15.6, pp. 471–476.

Hung, T.-K., Chang, G.-L., Lin, H.-S., Walter, F. R., and Bunegin, L. (1981b). "Stress-strain relationship of the spinal cord of anesthetized cats". In: *Journal of biomechanics* 14.4, pp. 269–276.

Ivancic, P. C., Pearson, A. M., Tominaga, Y., Simpson, A. K., Yue, J. J., and Panjabi, M. M. (2007). "Mechanism of cervical spinal cord injury during bilateral facet dislocation". In: *Spine* 32.22, pp. 2467–2473.

Jakeman, L. B., Guan, Z., Wei, P., Ponnappan, R., Dzwonczyk, R., Popovich, P. G., and Stokes, B. T. (2000). "Traumatic spinal cord injury produced by controlled contusion in mouse". In: *Journal of Neurotrauma* 17.4, pp. 299–319.

Jazayeri, S. B., Beygi, S., Shokraneh, F., Hagen, E. M., and Rahimi-Movaghar, V. (2015). "Incidence of traumatic spinal cord injury worldwide: a systematic review". In: *European spine journal* 24.5, pp. 905–918.

Jones, L. L., Margolis, R. U., and Tuszynski, M. H. (2003). "The chondroitin sulfate proteoglycans neurocan, brevican, phosphacan, and versican are differentially regulated following spinal cord injury". In: *Experimental neurology* 182.2, pp. 399–411.

Joshi, M. and Fehlings, M. G. (2002). "Development and characterization of a novel, graded model of clip compressive spinal cord injury in the mouse: Part 1. Clip design, behavioral outcomes, and histopathology". In: *Journal of Neurotrauma* 19.2, pp. 175–190.

Kang, W. and Hébert, J. M. (2011). "Signaling pathways in reactive astrocytes, a genetic perspective". In: *Molecular neurobiology* 43.3, pp. 147–154.

Karimi, A., Shojaei, A., and Tehrani, P. (2017). "Mechanical properties of the human spinal cord under the compressive loading". In: *Journal of chemical neuroanatomy* 86, pp. 15–18.

Kassmann, C. M. and Nave, K.-A. (2008). "Oligodendroglial impact on axonal function and survival–a hypothesis". In: *Current opinion in neurology* 21.3, pp. 235–241.

Katsuura, Y., Osborn, J. M., and Cason, G. W. (2016). "The epidemiology of thoracolumbar trauma: a meta-analysis". In: *Journal of Orthopaedics* 13.4, pp. 383–388.

Kayal, C., Moeendarbary, E., Shipley, R. J., and Phillips, J. B. (2020). "Mechanical response of neural cells to physiologically relevant stiffness gradients". In: *Advanced Healthcare Materials* 9.8, p. 1901036.

Kearney, P. A., Ridella, S. A., Viano, D. C., and Anderson, T. E. (1988). "Interaction of contact velocity and cord compression in determining the severity of spinal cord injury". In: *Journal of Neurotrauma* 5.3, pp. 187–208.

Kerschensteiner, M., Schwab, M. E., Lichtman, J. W., and Misgeld, T. (2005). "In vivo imaging of axonal degeneration and regeneration in the injured spinal cord". In: *Nature medicine* 11.5, pp. 572–577.

Kerstetter, A. E. and Miller, R. H. (2012). "Isolation and culture of spinal cord astrocytes". In: *Methods Mol Biol.* 814, pp. 93–104.

Khakh, B. S. and Sofroniew, M. V. (2015). "Diversity of astrocyte functions and phenotypes in neural circuits". In: *Nature neuroscience* 18.7, p. 942.

Kim, J. H., Tu, T.-W., Bayly, P. V., and Song, S.-K. (2009). "Impact speed does not determine severity of spinal cord injury in mice with fixed impact displacement". In: *Journal of Neurotrauma* 26.8, pp. 1395–1404.

Kirk, J. S. L. (2018). "Development of a 3D in vitro spinal cord injury model to investigate how the mechanical properties of the matrix affect CNS cell behaviour". PhD thesis. Mechanical Engineering.

Kjell, J. and Olson, L. (2016). "Rat models of spinal cord injury: from pathology to potential therapies". In: *Disease models & mechanisms* 9.10, pp. 1125–1137.

Koivisto, J. T., Joki, T., Parraga, J. E., Pääkkönen, R., Ylä-Outinen, L., Salonen, L., Jönkkäri, I., Peltola, M., Ihalainen, T. O., Narkilahti, S., *et al.,* (2017). "Bioamine-crosslinked gellan gum hydrogel for neural tissue engineering". In: *Biomedical materials* 12.2, p. 025014.

Koser, D. E., Moeendarbary, E., Hanne, J., Kuerten, S., and Franze, K. (2015). "CNS cell distribution and axon orientation determine local spinal cord mechanical properties". In: *Biophysical Journal* 108.9, pp. 2137–2147.

Kottis, V., Thibault, P., Mikol, D., Xiao, Z.-C., Zhang, R., Dergham, P., and Braun, P. E. (2002). "Oligodendrocyte-myelin glycoprotein (OMgp) is an inhibitor of neurite outgrowth". In: *Journal of neurochemistry* 82.6, pp. 1566–1569.

Krassioukov, A. V., Ackery, A., Schwartz, G., Adamchik, Y., Liu, Y., and Fehlings, M. G. (2002). "An in vitro model of neurotrauma in organotypic spinal cord cultures from adult mice". In: *Brain research protocols* 10.2, pp. 60–68.

Kuhn, P. L. and Wrathall, J. R. (1998). "A mouse model of graded contusive spinal cord injury". In: *Journal of Neurotrauma* 15.2, pp. 125–140.

Kuwazawa, Y., Bashir, W., Pope, M. H., Takahashi, K., and Smith, F. W. (2006). "Biomechanical aspects of the cervical cord: effects of postural changes in healthy volunteers using positional magnetic resonance imaging". In: *Clinical Spine Surgery* 19.5, pp. 348–352.

Lam, C. J., Assinck, P., Liu, J., Tetzlaff, W., and Oxland, T. R. (2014). "Impact depth and the interaction with impact speed affect the severity of contusion spinal cord injury in rats". In: *Journal of Neurotrauma* 31.24, pp. 1985–1997.

LaPlaca, M. C., Cullen, D. K., McLoughlin, J. J., and Cargill II, R. S. (2005). "High rate shear strain of three-dimensional neural cell cultures: a new in vitro traumatic brain injury model". In: *Journal of biomechanics* 38.5, pp. 1093–1105.

LaPlaca, M. C., Simon, C., Prado, G. R., and Cullen, D. (2007). "CNS injury biomechanics and experimental models". In: *Progress in brain research* 161, pp. 13–26.

Lappe-Siefke, C., Goebbels, S., Gravel, M., Nicksch, E., Lee, J., Braun, P. E., Griffiths, I. R., and Nave, K.-A. (2003). "Disruption of Cnp1 uncouples oligodendroglial functions in axonal support and myelination". In: *Nature genetics* 33.3, pp. 366–374.

Lau, N.-S. S., Gorrie, C. A., Chia, J. Y., Bilston, L. E., and Clarke, E. C. (2013). "Severity of spinal cord injury in adult and infant rats after vertebral dislocation depends upon displacement but not speed". In: *Journal of Neurotrauma* 30.15, pp. 1361–1373.

Lee, J. H. T., Jones, C. F., Okon, E. B., Anderson, L., Tigchelaar, S., Kooner, P., Godbey, T., Chua, B., Gray, G., Hildebrandt, R., Cripton, P., Tetzlaff, W., and Kwon, B. K. (2013). "A novel porcine model of traumatic thoracic spinal cord injury". In: *Journal of Neurotrauma* 30.3, pp. 142–159.

Lee, J. H., Streijger, F., Tigchelaar, S., Maloon, M., Liu, J., Tetzlaff, W., and Kwon, B. K. (2012). "A contusive model of unilateral cervical spinal cord injury using the infinite horizon impactor". In: *JoVE (Journal of Visualized Experiments)* 65, e3313.

Lemons, M. L., Howland, D. R., and Anderson, D. K. (1999). "Chondroitin sulfate proteoglycan immunoreactivity increases following spinal cord injury and transplantation". In: *Experimental neurology* 160.1, pp. 51–65.

Levine, J., Kwon, E., Paez, P., Yan, W., Czerwieniec, G., Loo, J. A., Sofroniew, M. V., and Wanner, I.-B. (2016). "Traumatically injured astrocytes release a proteomic signature modulated by STAT 3-dependent cell survival". In: *Glia* 64.5, pp. 668–694.

Li, J. and Lepski, G. (2013). "Cell transplantation for spinal cord injury: a systematic review". In: *BioMed research international* 2013.

Liu, B. P., Cafferty, W. B., Budel, S. O., and Strittmatter, S. M. (2006). "Extracellular regulators of axonal growth in the adult central nervous system". In: *Philosophical Transactions of the Royal Society B: Biological Sciences* 361.1473, pp. 1593–1610.

Logan, A., Berry, M., Gonzalez, A. M., Frautschy, S. A., Sporn, M. B., and Baird, A. (1994). "Effects of transforming growth factor β1, on scar production in the injured central nervous system of the rat". In: *European Journal of Neuroscience* 6.3, pp. 355–363.

Luna, C., Detrick, L., Shah, S. B., Cohen, A. H., and Aranda-Espinoza, H. (2013). "Mechanical properties of the lamprey spinal cord: uniaxial loading and physiological strain". In: *Journal of Biomechanics* 46.13, pp. 2194–2200.

Lutolf, M. and Hubbell, J. (2005). "Synthetic biomaterials as instructive extracellular microenvironments for morphogenesis in tissue engineering". In: *Nature biotechnology* 23.1, pp. 47–55.

Ma, M., Basso, D. M., Walters, P., Stokes, B. T., and Jakeman, L. B. (2001). "Behavioral and histological outcomes following graded spinal cord contusion injury in the C57Bl/6 mouse". In: *Experimental Neurology* 169.2, pp. 239–254.

Maikos, J. T. and Shreiber, D. I. (2007). "Immediate damage to the blood-spinal cord barrier due to mechanical trauma". In: *Journal of neurotrauma* 24.3, pp. 492–507.

Malas, S. and Panayiotou, E. (2013). "Adult spinal cord ependymal layer: a promising pool of quiescent stem cells to treat spinal cord injury". In: *Frontiers in physiology* 4, p. 340.

Mancall, E. L. and Brock, D. G. (2011). *Gray's Clinical Neuroanatomy: The Anatomic Basis for Clinical Neuroscience.* Saunders.

Mattucci, S., Speidel, J., Liu, J., Kwon, B. K., Tetzlaff, W., and Oxland, T. R. (2019). "Basic biomechanics of spinal cord injury—How injuries happen in people and how

animal models have informed our understanding". In: *Clinical biomechanics* 64, pp. 58–68.

Mazuchowski, E. L., Thibault, L. E., *et al.,* (2003). "Biomechanical properties of the human spinal cord and pia mater". In: *Summer Bioengineering Conference, Sonesta Beach Resort, Key Biscayne, FL, USA.*

Mazzone, G. L. and Nistri, A. (2014). "S100β as an early biomarker of excitotoxic damage in spinal cord organotypic cultures". In: *Journal of neurochemistry* 130.4, pp. 598–604.

McCarthy, K. D. and De Vellis, J. (1980). "Preparation of separate astroglial and oligodendroglial cell cultures from rat cerebral tissue." In: *The Journal of cell biology* 85.3, pp. 890–902.

McDaid, D., Park, A.-L., Gall, A., Purcell, M., and Bacon, M. (2019). "Understanding and modelling the economic impact of spinal cord injuries in the United Kingdom". In: *Spinal cord* 57.9, pp. 778–788.

McKeon, R. J., Jurynec, M. J., and Buck, C. R. (1999). "The chondroitin sulfate proteoglycans neurocan and phosphacan are expressed by reactive astrocytes in the chronic CNS glial scar". In: *Journal of Neuroscience* 19.24, pp. 10778–10788.

McKeon, R. J., Schreiber, R. C., Rudge, J. S., and Silver, J. (1991). "Reduction of neurite outgrowth in a model of glial scarring following CNS injury is correlated with the expression of inhibitory molecules on reactive astrocytes". In: *Journal of Neuroscience* 11.11, pp. 3398–3411.

McKerracher, L. a., David, S., Jackson, D., Kottis, V., Dunn, R., and Braun, P. (1994). "Identification of myelin-associated glycoprotein as a major myelin-derived inhibitor of neurite growth". In: *Neuron* 13.4, pp. 805–811.

McKinney, J., Willoughby, K., Liang, S., and Ellis, E. (1996). "Stretch-induced injury of cultured neuronal, glial, and endothelial cells: effect of polyethylene glycol–conjugated superoxide dismutase". In: *Stroke* 27.5, pp. 934–940.

McMurtrey, R. J. (2014). "Patterned and functionalized nanofiber scaffolds in three-dimensional hydrogel constructs enhance neurite outgrowth and directional control". In: *Journal of neural engineering* 11.6, p. 066009.

McMurtrey, R. J. (2016). "Analytic models of oxygen and nutrient diffusion, metabolism dynamics, and architecture optimization in three-dimensional tissue constructs with applications and insights in cerebral organoids". In: *Tissue Engineering Part C: Methods* 22.3, pp. 221–249.

Meletis, K., Barnabé-Heider, F., Carlén, M., Evergren, E., Tomilin, N., Shupliakov, O., and Frisén, J. (2008). "Spinal cord injury reveals multilineage differentiation of ependymal cells". In: *PLoS Biol* 6.7, e182.

Milbreta, U., von Boxberg, Y., Mailly, P., Nothias, F., and Soares, S. (2014). "Astrocytic and vascular remodeling in the injured adult rat spinal cord after chondroitinase ABC treatment". In: *Journal of neurotrauma* 31.9, pp. 803–818.

Miller, R. H. (2002). "Regulation of oligodendrocyte development in the vertebrate CNS". In: *Progress in neurobiology* 67.6, pp. 451–467.

Miller, S. J. (2018). "Astrocyte heterogeneity in the adult central nervous system". In: *Frontiers in cellular neuroscience* 12, p. 401.

Miller, W. J., Leventhal, I., Scarsella, D., Haydon, P. G., Janmey, P., and Meaney, D. F. (2009). "Mechanically induced reactive gliosis causes ATP-mediated alterations in astrocyte stiffness". In: *Journal of neurotrauma* 26.5, pp. 789–797.

Miron-Mendoza, M., Seemann, J., and Grinnell, F. (2010). "The differential regulation of cell motile activity through matrix stiffness and porosity in three dimensional collagen matrices". In: *Biomaterials* 31.25, pp. 6425–6435.

Moeendarbary, E., Weber, I. P., Sheridan, G. K., Koser, D. E., Soleman, S., Haenzi, B., Bradbury, E. J., Fawcett, J., and Franze, K. (2017). "The soft mechanical signature of glial scars in the central nervous system". In: *Nature communications* 8.1, pp. 1–11.

Moon, L., Asher, R., Rhodes, K., and Fawcett, J. (2002). "Relationship between sprouting axons, proteoglycans and glial cells following unilateral nigrostriatal axotomy in the adult rat". In: *Neuroscience* 109.1, pp. 101–117.

Motte, S. and Kaufman, L. (2013). "Strain stiffening in collagen I networks". In: *Biopolymers* 99.1, pp. 35–46.

Mukhamedshina, Y. O., Akhmetzyanova, E. R., Martynova, E. V., Khaiboullina, S. F., Galieva, L. R., and Rizvanov, A. A. (2017). "Systemic and local cytokine profile following spinal cord injury in rats: a multiplex analysis". In: *Frontiers in neurology* 8, p. 581.

Nam, S., Hu, K. H., Butte, M. J., and Chaudhuri, O. (2016). "Strain-enhanced stress relaxation impacts nonlinear elasticity in collagen gels". In: *Proceedings of the National Academy of Sciences* 113.20, pp. 5492–5497.

Neary, J. T., Kang, Y., Willoughby, K. A., and Ellis, E. F. (2003). "Activation of extracellular signal-regulated kinase by stretch-induced injury in astrocytes involves

extracellular ATP and P2 purinergic receptors". In: *Journal of Neuroscience* 23.6, pp. 2348–2356.

Neel, E. A. A., Cheema, U., Knowles, J. C., Brown, R. A., and Nazhat, S. N. (2006). "Use of multiple unconfined compression for control of collagen gel scaffold density and mechanical properties". In: *Soft matter* 2.11, pp. 986–992.

Nishi, R. A., Liu, H., Chu, Y., Hamamura, M., Su, M.-Y., Nalcioglu, O., and Anderson, A. J. (2007). "Behavioral, histological, and ex vivo magnetic resonance imaging assessment of graded contusion spinal cord injury in mice". In: *Journal of Neurotrauma* 24.4, pp. 674–689.

Noble, L. J. and Wrathall, J. R. (1989). "Correlative analyses of lesion development and functional status after graded spinal cord contusive injuries in the rat". In: *Experimental Neurology* 103.1, pp. 34–40.

Nógrádi, A. and Vrbová, G. (2006). "Anatomy and physiology of the spinal cord". In: *Transplantation of neural tissue into the spinal cord*. Springer, pp. 1–23.

Norenberg, M. D., Smith, J., and Marcillo, A. (2004). "The pathology of human spinal cord injury: defining the problems". In: *Journal of Neurotrauma* 21.4, pp. 429–440.

O'Callaghan, J. P., Kelly, K. A., VanGilder, R. L., Sofroniew, M. V., and Miller, D. B. (2014). "Early activation of STAT3 regulates reactive astrogliosis induced by diverse forms of neurotoxicity". In: *PloS one* 9.7, e102003.

O'Rourke, C., Lee-Reeves, C., Drake, R. A., Cameron, G. W., Loughlin, A. J., and Phillips, J. B. (2017). "Adapting tissue-engineered in vitro CNS models for high-throughput study of neurodegeneration". In: *Journal of tissue engineering* 8, p. 2041731417697920.

Oakland, R., Hall, R., Wilcox, R., and Barton, D. (2006). "The biomechanical response of spinal cord tissue to uniaxial loading". In: *Proceedings of the Institution of Mechanical Engineers, Part H: Journal of Engineering in Medicine* 220.4, pp. 489–492.

Oberheim, N. A., Takano, T., Han, X., He, W., Lin, J. H., Wang, F., Xu, Q., Wyatt, J. D., Pilcher, W., Ojemann, J. G., *et al.,* (2009). "Uniquely hominid features of adult human astrocytes". In: *Journal of Neuroscience* 29.10, pp. 3276–3287.

Ohtake, Y. and Li, S. (2015). "Molecular mechanisms of scar-sourced axon growth inhibitors". In: *Brain research* 1619, pp. 22–35.

Okada, S., Nakamura, M., Mikami, Y., Shimazaki, T., Mihara, M., Ohsugi, Y., Iwamoto, Y., Yoshizaki, K., Kishimoto, T., Toyama, Y., *et al.,* (2004). "Blockade of interleukin-6 receptor suppresses reactive astrogliosis and ameliorates functional

recovery in experimental spinal cord injury". In: *Journal of neuroscience research* 76.2, pp. 265–276.

Okada, S. (2016). "The pathophysiological role of acute inflammation after spinal cord injury". In: *Inflammation and regeneration* 36.1, p. 20.

Oxland, T. R., Bhatnagar, T., Choo, A. M., Dvorak, M. F., Tetzlaff, W., and Cripton, P. A. (2010). "Biomechanical aspects of spinal cord injury". In: *Neural Tissue Biomechanics*. Springer, pp. 159–180.

Oyinbo, C. A. (2011). "Secondary injury mechanisms in traumatic spinal cord injury: a nugget of this multiply cascade". In: *Acta Neurobiol Exp (Wars)* 71.2, pp. 281–99.

Ozawa, H., Matsumoto, T., Ohashi, T., Sato, M., and Kokubun, S. (2004). "Mechanical properties and function of the spinal pia mater". In: *Journal of Neurosurgery: Spine* 1.1, pp. 122–127.

Pampaloni, F., Reynaud, E. G., and Stelzer, E. H. (2007). "The third dimension bridges the gap between cell culture and live tissue". In: *Nature reviews Molecular cell biology* 8.10, pp. 839–845.

Pandamooz, S., Salehi, M. S., Zibaii, M. I., Safari, A., Nabiuni, M., Ahmadiani, A., and Dargahi, L. (2019). "Modeling traumatic injury in organotypic spinal cord slice culture obtained from adult rat". In: *Tissue and Cell* 56, pp. 90–97.

Panjabi, M. M., Oxland, T. R., Lin, R.-M., and McGowen, T. W. (1994). "Thoracolumbar burst fracture. A biomechanical investigation of its multidirectional flexibility." In: *Spine* 19.5, pp. 578–585.

Panjabi, M. M. and White, A. (1990). "Clinical biomechanics of the spine". In:

Parenteau-Bareil, R., Gauvin, R., Cliche, S., Gariépy, C., Germain, L., and Berthod, F. (2011). "Comparative study of bovine, porcine and avian collagens for the production of a tissue engineered dermis". In: *Acta biomaterialia* 7.10, pp. 3757–3765.

Park, J. H., Kim, J. H., Oh, S.-K., Baek, S. R., Min, J., Kim, Y. W., Kim, S. T., Woo, C.-W., and Jeon, S. R. (2016). "Analysis of equivalent parameters of two spinal cord injury devices: the New York University impactor versus the Infinite Horizon impactor". In: *The Spine Journal* 16.11, pp. 1392–1403.

Pearse, D. D., Lo Jr, T. P., Cho, K. S., Lynch, M. P., Garg, M. S., Marcillo, A. E., Sanchez, A. R., Cruz, Y., and Dietrich, W. D. (2005). "Histopathological and behavioral characterization of a novel cervical spinal cord displacement contusion injury in the rat". In: *Journal of neurotrauma* 22.6, pp. 680–702.

Pedersen, J. A. and Swartz, M. A. (2005). "Mechanobiology in the third dimension". In: *Annals of biomedical engineering* 33.11, pp. 1469–1490.

Pekny, M., Johansson, C. B., Eliasson, C., Stakeberg, J., Wallén, Å., Perlmann, T., Lendahl, U., Betsholtz, C., Berthold, C.-H., and Frisén, J. (1999). "Abnormal reaction to central nervous system injury in mice lacking glial fibrillary acidic protein and vimentin". In: *The Journal of cell biology* 145.3, pp. 503–514.

Pekny, M., Leveen, P., Pekna, M., Eliasson, C., Berthold, C.-H., Westermark, B., and Betsholtz, C. (1995). "Mice lacking glial fibrillary acidic protein display astrocytes devoid of intermediate filaments but develop and reproduce normally." In: *The EMBO journal* 14.8, pp. 1590–1598.

Pekny, M. and Nilsson, M. (2005). "Astrocyte activation and reactive gliosis". In: *Glia* 50.4, pp. 427–434.

Perale, G., Rossi, F., Sundstrom, E., Bacchiega, S., Masi, M., Forloni, G., and Veglianese, P. (2011). "Hydrogels in spinal cord injury repair strategies". In: *ACS chemical neuroscience* 2.7, pp. 336–345.

Persson, C., McLure, S. W., Summers, J., and Hall, R. M. (2009). "The effect of bone fragment size and cerebrospinal fluid on spinal cord deformation during trauma: an ex vivo study". In: *Journal of Neurosurgery: Spine* 10.4, pp. 315–323.

Phillips, J. B. (2014a). "Building stable anisotropic tissues using cellular collagen gels". In: *Organogenesis* 10.1, pp. 6–8.

Phillips, J. B. (2014b). "Monitoring neuron and astrocyte interactions with a 3D cell culture system". In: *In: Murray A. (eds) Axon Growth and Regeneration. Methods in Molecular Biology (Methods and Protocols)* 1162, pp. 113–124.

Phillips, J. B. and Brown, R. (2011). "Micro-structured materials and mechanical cues in 3D collagen gels". In: *3D Cell Culture.* Springer, pp. 183–196.

Phillips, J. B., Bunting, S. C., Hall, S. M., and Brown, R. A. (2005). "Neural tissue engineering: a self-organizing collagen guidance conduit". In: *Tissue engineering* 11.9-10, pp. 1611–1617.

Pineau, I. and Lacroix, S. (2007). "Proinflammatory cytokine synthesis in the injured mouse spinal cord: multiphasic expression pattern and identification of the cell types involved". In: *Journal of Comparative Neurology* 500.2, pp. 267–285.

Pogoda, K. and Janmey, P. A. (2018). "Glial tissue mechanics and mechanosensing by glial cells". In: *Frontiers in cellular neuroscience* 12, p. 25.

Prabhakar, V., Capila, I., Bosques, C. J., Pojasek, K., and Sasisekharan, R. (2005). "Chondroitinase ABC I from Proteus vulgaris: cloning, recombinant expression and active site identification". In: *Biochemical journal* 386.1, pp. 103–112.

Purves, D., Augustine, G., Fitzpatrick, D., Katz, L., LaMantia, A., McNamara, J., and Williams, S. (2001). *Neuroscience 2nd Edition.* Sinauer Associates, Sunderland (MA).

Ramo, N. L., Troyer, K. L., and Puttlitz, C. M. (2018). "Viscoelasticity of spinal cord and meningeal tissues". In: *Acta biomaterialia* 75, pp. 253–262.

Rao, S. S. and Winter, J. (2009). "Adhesion molecule-modified biomaterials for neural tissue engineering". In: *Frontiers in neuroengineering* 2, p. 6.

Rauch, U. (2007). *Brain matrix: structure, turnover and necessity.*

Rhodes, K. and Fawcett, J. (2004). "Chondroitin sulphate proteoglycans: preventing plasticity or protecting the CNS?" In: *Journal of anatomy* 204.1, pp. 33–48.

Rhodes, K., Raivich, G., and Fawcett, J. (2006). "The injury response of oligodendrocyte precursor cells is induced by platelets, macrophages and inflammation-associated cytokines". In: *Neuroscience* 140.1, pp. 87–100.

Rivlin A, S. and Tator, C. H. (1978). "Effect of duration of acute spinal cord compression in a new acute cord injury model in the rat." In: *Surgical Neurology* 10.1, pp. 38–43.

Rolls, A., Shechter, R., and Schwartz, M. (2009). "The bright side of the glial scar in CNS repair". In: *Nature Reviews Neuroscience* 10.3, pp. 235–241.

Russell, C. M., Choo, A. M., Tetzlaff, W., Chung, T.-E., and Oxland, T. R. (2012). "Maximum principal strain correlates with spinal cord tissue damage in contusion and dislocation injuries in the rat cervical spine". In: *Journal of Neurotrauma* 29.8, pp. 1574–1585.

Saari, A., Itshayek, E., and Cripton, P. A. (2011). "Cervical spinal cord deformation during simulated head-first impact injuries". In: *Journal of biomechanics* 44.14, pp. 2565–2571.

Sahlas, D. J., Bilbao, J. M., Swartz, R. H., and Black, S. E. (2002). "Clasmatodendrosis correlating with periventricular hyperintensity in mixed dementia". In: *Annals of neurology* 52.3, pp. 378–381.

Sakai, K., Fukuda, T., and Iwadate, K. (2013). "Beading of the astrocytic processes (clasmatodendrosis) following head trauma is associated with protein degradation pathways". In: *Brain injury* 27.13-14, pp. 1692–1697.

Sakka, L., Coll, G., and Chazal, J. (2011). "Anatomy and physiology of cerebrospinal fluid". In: *European annals of otorhinolaryngology, head and neck diseases* 128.6, pp. 309–316.

Salegio, E. A., Bresnahan, J. C., Sparrey, C. J., Camisa, W., Fischer, J., Leasure, J., Buckley, J., Nout-Lomas, Y. S., Rosenzweig, E. S., Moseanko, R., Strand, S., Hawbecker, S., Lemoy, M.-J., Haefeli, J., Ma, X., Nielson, J. L., Edgerton, V. R., Ferguson, A. R., Tuszynski, M. H., and Beattie, M. S. (2016). "A unilateral cervical spinal cord contusion injury model in non-human primates (Macaca mulatta)". In: *Journal of Neurotrauma* 33.5, pp. 439–459.

Sayıt, E., Aghdasi, B., Daubs, M. D., and Wang, J. C. (2015). "The occupancy of the components in the cervical spine and their changes with extension and flexion". In: *Global spine journal* 5.5, pp. 396–405.

Scheff, S. W., Rabchevsky, A. G., Fugaccia, I., Main, J. A., and Lumpp Jr, J. E. (2003). "Experimental modeling of spinal cord injury: characterization of a force-defined injury device". In: *Journal of Neurotrauma* 20.2, pp. 179–193.

Schwab, J. M., Brechtel, K., Mueller, C.-A., Failli, V., Kaps, H.-P., Tuli, S. K., and Schluesener, H. J. (2006). "Experimental strategies to promote spinal cord regeneration—an integrative perspective". In: *Progress in neurobiology* 78.2, pp. 91–116.

Schwartz, M. (2003). "Macrophages and microglia in central nervous system injury: are they helpful or harmful?" In: *Journal of Cerebral Blood Flow & Metabolism* 23.4, pp. 385–394.

Seifert, J., Bell, J., Elmer, B., Sucato, D., and Romero, M. (2011). "Characterization of a novel bidirectional distraction spinal cord injury animal model". In: *Journal of neuroscience methods* 197.1, pp. 97–103.

Sekhon, L. H. S. and Fehlings, M. G. (2001). "Epidemiology, demographics, and pathophysiology of acute spinal cord injury". In: *Spine* 26.24S, pp. 2–12.

Sharif-Alhoseini, M., Khormali, M., Rezaei, M., Safdarian, M., Hajighadery, A., Khalatbari, M. M., Meknatkhah, S., Rezvan, M., Chalangari, M., Derakhshan, P., and Rahimi-Movaghar, V. (2017). "Animal models of spinal cord injury: a systematic review". In: *Spinal Cord* 55.8, pp. 714–721.

Sharma, K., Selzer, M. E., and Li, S. (2012). "Scar-mediated inhibition and CSPG receptors in the CNS". In: *Experimental neurology* 237.2, pp. 370–378.

Shreiber, D. I., Hao, H., and Elias, R. A. (2009). "Probing the influence of myelin and glia on the tensile properties of the spinal cord". In: *Biomechanics and modeling in mechanobiology* 8.4, p. 311.

Shuman, S. L., Bresnahan, J. C., and Beattie, M. S. (1997). "Apoptosis of microglia and oligodendrocytes after spinal cord contusion in rats". In: *Journal of neuroscience research* 50.5, pp. 798–808.

Siebert, J. R., Conta Steencken, A., and Osterhout, D. J. (2014). "Chondroitin sulfate proteoglycans in the nervous system: inhibitors to repair". In: *BioMed research international* 2014.

Silva, N. A., Sousa, N., Reis, R. L., and Salgado, A. J. (2014). "From basics to clinical: a comprehensive review on spinal cord injury". In: *Progress in neurobiology* 114, pp. 25–57.

Silver, J. and Miller, J. H. (2004). "Regeneration beyond the glial scar". In: *Nature reviews neuroscience* 5.2, pp. 146–156.

Simons, M. and Trajkovic, K. (2006). "Neuron-glia communication in the control of oligodendrocyte function and myelin biogenesis". In: *Journal of cell science* 119.21, pp. 4381–4389.

Singh, A., Tetreault, L., Kalsi-Ryan, S., Nouri, A., and Fehlings, M. G. (2014). "Global prevalence and incidence of traumatic spinal cord injury". In: *Clinical epidemiology* 6, p. 309.

Sjovold, S. G., Mattucci, S. F., Choo, A. M., Liu, J., Dvorak, M. F., Kwon, B. K., Tetzlaff, W., and Oxland, T. R. (2013). "Histological effects of residual compression sustained for 60 minutes at different depths in a novel rat spinal cord injury contusion model". In: *Journal of Neurotrauma* 30.15, pp. 1374–1384.

Slovinska, L., Blasko, J., Nagyova, M., Szekiova, E., and Cizkova, D. (2016). "In vitro models of spinal cord injury". In: *Recovery of Motor Function Following Spinal Cord Injury.* IntechOpen.

Smith, J. T. (2016). "A 3D culture model to investigate cellular responses to mechanical loading in spinal cord injury". PhD thesis. Mechanical Engineering.

Snow, D. M., Lemmon, V., Carrino, D. A., Caplan, A. I., and Silver, J. (1990). "Sulfated proteoglycans in astroglial barriers inhibit neurite outgrowth in vitro". In: *Experimental neurology* 109.1, pp. 111–130.

Sobel, R. A. (1998). "The extracellular matrix in multiple sclerosis lesions". In: *Journal of Neuropathology & Experimental Neurology* 57.3, pp. 205–217.

Sofroniew, M. V. (2005). "Reactive astrocytes in neural repair and protection". In: *The Neuroscientist* 11.5, pp. 400–407.

Sofroniew, M. V. (2009). "Molecular dissection of reactive astrogliosis and glial scar formation". In: *Trends in neurosciences* 32.12, pp. 638–647.

Sofroniew, M. V. (2015). "Astrogliosis". In: *Cold Spring Harbor perspectives in biology* 7.2, a020420.

Sofroniew, M. V. and Vinters, H. V. (2010). "Astrocytes: biology and pathology". In: *Acta neuropathologica* 119.1, pp. 7–35.

Sparrey, C. J., Choo, A. M., Liu, J., Tetzlaff, W., and Oxland, T. R. (2008). "The distribution of tissue damage in the spinal cord is influenced by the contusion velocity". In: *Spine* 33.22, E812–E819.

Sparrey, C. J. and Keaveny, T. M. (2011). "Compression behavior of porcine spinal cord white matter". In: *Journal of biomechanics* 44.6, pp. 1078–1082.

Spillmann, A. A., Amberger, V. R., and Schwab, M. E. (1997). "High molecular weight protein of human central nervous system myelin inhibits neurite outgrowth: an effect which can be neutralized by the monoclonal antibody IN-1". In: *European Journal of Neuroscience* 9.3, pp. 549–555.

Stammers, A., Liu, J., and Kwon, B. (2012). "Expression of inflammatory cytokines following acute spinal cord injury in a rodent model". In: *Journal of neuroscience research* 90.4, pp. 782–790.

Stokes, B. T. and Jakeman, L. B. (2002). "Experimental modelling of human spinal cord injury: a model that crosses the species barrier and mimics the spectrum of human cytopathology". In: *Spinal Cord* 40.3, pp. 101–109.

Stoppini, L., Buchs, P.-A., and Muller, D. (1991). "A simple method for organotypic cultures of nervous tissue". In: *Journal of neuroscience methods* 37.2, pp. 173–182.

Sultan, I., Lamba, N., Liew, A., Doung, P., Tewarie, I., Amamoo, J. J., Gannu, L., Chawla, S., Doucette, J., Cerecedo-Lopez, C. D., *et al.,* (2020). "The safety and efficacy of steroid treatment for acute spinal cord injury: A Systematic Review and meta-analysis". In: *Heliyon* 6.2, e03414.

Sundstrom, L., Pringle, A., Morrison, B., and Bradley, M. (2005). "Organotypic cultures as tools for functional screening in the CNS". In: *Drug discovery today* 10.14, pp. 993–1000.

Swift, J., Ivanovska, I. L., Buxboim, A., Harada, T., Dingal, P. D. P., Pinter, J., Pajerowski, J. D., Spinler, K. R., Shin, J.-W., Tewari, M., *et al.,* (2013). "Nuclear lamin-A scales with tissue stiffness and enhances matrix-directed differentiation". In: *Science* 341.6149.

Szwedowski, D. and Walecki, J. (2014). "Spinal cord injury without radiographic abnormality (SCIWORA)–clinical and radiological aspects". In: *Polish journal of radiology* 79, p. 461.

Tator, C. H., Duncan, E. G., Edmonds, V. E., Lapczak, L. I., and Andrews, D. F. (1987). "Comparison of surgical and conservative management in 208 patients with acute spinal cord injury". In: *Canadian Journal of Neurological Sciences* 14.S1, pp. 60–69.

Tator, C. H. (1983). "Spine-spinal cord relationships in spinal cord trauma". In: *Neurosurgery* 30.CN_suppl_1, pp. 479–494.

Tator, C. H. (2006). "Review of treatment trials in humanspinal cord injury: issues, difficulties, and recommendations". In: *Neurosurgery* 59.5, pp. 957–987.

Tester, N. J., Plaas, A. H., and Howland, D. R. (2007). "Effect of body temperature on chondroitinase ABCs ability to cleave chondroitin sulfate glycosaminoglycans". In: *Journal of neuroscience research* 85.5, pp. 1110–1118.

Tomimoto, H., Akiguchi, I., Wakita, H., Suenaga, T., Nakamura, S., and Kimura, J. (1997). "Regressive changes of astroglia in white matter lesions in cerebrovascular disease and Alzheimer's disease patients". In: *Acta neuropathologica* 94.2, pp. 146–152.

Tronci, G., Grant, C. A., Thomson, N. H., Russell, S. J., and Wood, D. J. (2015). "Multi-scale mechanical characterization of highly swollen photo-activated collagen hydrogels". In: *Journal of the Royal Society Interface* 12.102, p. 20141079.

Tsacopoulos, M. (2002). "Metabolic signaling between neurons and glial cells: a short review". In: *Journal of Physiology-Paris* 96.3-4, pp. 283–288.

Tukmachev, D., Forostyak, S., Koci, Z., Zaviskova, K., Vackova, I., Vyborny, K., Sandvig, I., Sandvig, A., Medberry, C. J., Badylak, S. F., *et al.,* (2016). "Injectable extracellular matrix hydrogels as scaffolds for spinal cord injury repair". In: *Tissue Engineering Part A* 22.3-4, pp. 306–317.

Tunturi, A. R. (1978). "Elasticity of the spinal cord, pia, and denticulate ligament in the dog". In: *Journal of neurosurgery* 48.6, pp. 975–979.

Ullian, E. M., Sapperstein, S. K., Christopherson, K. S., and Barres, B. A. (2001). "Control of synapse number by glia". In: *Science* 291.5504, pp. 657–661.

Uriel, S., Labay, E., Francis-Sedlak, M., Moya, M. L., Weichselbaum, R. R., Ervin, N., Cankova, Z., and Brey, E. M. (2009). "Extraction and assembly of tissue-derived gels for cell culture and tissue engineering". In: *Tissue Engineering Part C: Methods* 15.3, pp. 309–321.

Vaccaro, A. R., Lehman Jr, R. A., Hurlbert, R. J., Anderson, P. A., Harris, M., Hedlund, R., Harrop, J., Dvorak, M., Wood, K., Fehlings, M. G., *et al.,* (2005). "A new classification of thoracolumbar injuries: the importance of injury morphology, the integrity of the posterior ligamentous complex, and neurologic status". In: *Spine* 30.20, pp. 2325–2333.

Vanický, I., Urdzíková, L., Saganová, K., Čízková, D., and Gálik, J. (2001). "A simple and reproducible model of spinal cord injury induced by epidural balloon inflation in the rat". In: *Journal of neurotrauma* 18.12, pp. 1399–1407.

Varma, A. K., Das, A., Wallace, G., Barry, J., Vertegel, A. A., Ray, S. K., and Banik, N. L. (2013). "Spinal cord injury: a review of current therapy, future treatments, and basic science frontiers". In: *Neurochemical research* 38.5, pp. 895–905.

Vasile, F., Dossi, E., and Rouach, N. (2017). "Human astrocytes: structure and functions in the healthy brain". In: *Brain Structure and Function* 222.5.

Volpato, F. Z., Führmann, T., Migliaresi, C., Hutmacher, D. W., and Dalton, P. D. (2013). "Using extracellular matrix for regenerative medicine in the spinal cord". In: *Biomaterials* 34.21, pp. 4945–4955.

Wadell, H. (1935). "Volume, shape, and roundness of quartz particles". In: *The Journal of Geology* 43.3, pp. 250–280.

Wang, H., Song, G., Chuang, H., Chiu, C., Abdelmaksoud, A., Ye, Y., and Zhao, L. (2018). "Portrait of glial scar in neurological diseases". In: *International Journal of Immunopathology and Pharmacology* 31, p. 2058738418801406.

Wang, J., Zhang, M., Guo, Y., Hu, H., and Chen, K. (2019). "Quantification of surviving neurons after contusion, dislocation, and distraction spinal cord injuries using automated methods". In: *Journal of Experimental Neuroscience* 13, p. 1179069519869617.

Wanner, I. B., Deik, A., Torres, M., Rosendahl, A., Neary, J. T., Lemmon, V. P., and Bixby, J. L. (2008). "A new in vitro model of the glial scar inhibits axon growth". In: *Glia* 56.15, pp. 1691–1709.

Watson, C., Paxinos, G., and Kayalioglu, G. (2009). *The spinal cord: a Christopher and Dana Reeve Foundation text and atlas*. Academic press.

Weightman, A. P., Pickard, M. R., Yang, Y., and Chari, D. M. (2014). "An in vitro spinal cord injury model to screen neuroregenerative materials". In: *Biomaterials* 35.12, pp. 3756–3765.

Wilcox, R., Allen, D., Hall, R., Limb, D., Barton, D., and Dickson, R. (2004). "A dynamic investigation of the burst fracture process using a combined experimental and finite element approach". In: *European Spine Journal* 13.6, pp. 481–488.

Wilcox, R., Boerger, T., Allen, D., Barton, D., Limb, D., Dickson, R., and Hall, M. (2003). "A dynamic study of thoracolumbar burst fractures". In: *The Journal of Bone and Joint Surgery* 85.11, pp. 2184–2189.

Wilcox, R., Boerger, T., Hall, R., Barton, D., Limb, D., and Dickson, R. (2002). "Measurement of canal occlusion during the thoracolumbar burst fracture process". In: *Journal of biomechanics* 35.3, pp. 381–384.

Wilhelmsson, U., Li, L., Pekna, M., Berthold, C.-H., Blom, S., Eliasson, C., Renner, O., Bushong, E., Ellisman, M., Morgan, T. E., *et al.,* (2004). "Absence of glial fibrillary acidic protein and vimentin prevents hypertrophy of astrocytic processes and improves post-traumatic regeneration". In: *Journal of Neuroscience* 24.21, pp. 5016–5021.

Wilson, C. L., Hayward, S. L., and Kidambi, S. (2016). "Astrogliosis in a dish: substrate stiffness induces astrogliosis in primary rat astrocytes". In: *RSC advances* 6.41, pp. 34447–34457.

Wilson, J. R., Vaccaro, A., Harrop, J. S., Aarabi, B., Shaffrey, C., Dvorak, M., Fisher, C., Arnold, P., Massicotte, E. M., Lewis, S., Rampersaud, R., Okonkwo, D. O., and Fehlings, M. G. (2013). "The impact of facet dislocation on clinical outcomes after cervical spinal cord injury: results of a multicenter North American prospective cohort study". In: *Spine* 38.2, pp. 97–103.

Wood, K. B., Li, W., Lebl, D. S., and Ploumis, A. (2014). "Management of thoracolumbar spine fractures". In: *The Spine Journal* 14.1, pp. 145–164.

Wu, J., Xue, J., Huang, R., Zheng, C., Cui, Y., and Rao, S. (2016). "A rabbit model of lumbar distraction spinal cord injury". In: *The Spine Journal* 16.5, pp. 643–658.

Yang, J. H., Suh, S. W., Modi, H. N., Ramani, E. T., Hong, J. Y., Hwang, J. H., and Jung, W. Y. (2013). "Effects of vertebral column distraction on transcranial electrical stimulation-motor evoked potential and histology of the spinal cord in a porcine model". In: *The Journal of Bone and Joint Surgery* 95.9, pp. 835–842.

Yang, Z. and Wang, K. K. (2015). "Glial fibrillary acidic protein: from intermediate filament assembly and gliosis to neurobiomarker". In: *Trends in neurosciences* 38.6, pp. 364–374.

Yiu, G. and He, Z. (2006). "Glial inhibition of CNS axon regeneration". In: *Nature Reviews Neuroscience* 7.8, pp. 617–627.

Yong, C., Arnold, P. M., Zoubine, M. N., Citron, B. A., Watanabe, I., Berman, N. E., and Festoff, B. W. (1998). "Apoptosis in cellular compartments of rat spinal cord after severe contusion injury". In: *Journal of neurotrauma* 15.7, pp. 459–472.

Yoon, H., Walters, G., Paulsen, A. R., and Scarisbrick, I. A. (2017). "Astrocyte heterogeneity across the brain and spinal cord occurs developmentally, in adulthood and in response to demyelination". In: *PLoS One* 12.7, e0180697.

Yu, P., Wang, H., Katagiri, Y., and Geller, H. M. (2012). "An in vitro model of reactive astrogliosis and its effect on neuronal growth". In: *Astrocytes.* Springer, pp. 327–340.

Zamanian, J. L., Xu, L., Foo, L. C., Nouri, N., Zhou, L., Giffard, R. G., and Barres, B. A. (2012). "Genomic analysis of reactive astrogliosis". In: *Journal of neuroscience* 32.18, pp. 6391–6410.

Zhang, D., Hu, X., Qian, L., O'Callaghan, J. P., and Hong, J.-S. (2010a). "Astrogliosis in CNS pathologies: is there a role for microglia?" In: *Molecular neurobiology* 41.2-3, pp. 232–241.

Zhang, J., O'Carroll, S. J., Wu, A., Nicholson, L. F., and Green, C. R. (2010b). "A model for ex vivo spinal cord segment culture—A tool for analysis of injury repair strategies". In: *Journal of neuroscience methods* 192.1, pp. 49–57.

Zhang, N., Fang, M., Chen, H., Gou, F., and Ding, M. (2014). "Evaluation of spinal cord injury animal models". In: *Neural regeneration research* 9.22, p. 2008.

Zhao, Y., Tang, F., Xiao, Z., Han, G., Wang, N., Yin, N., Chen, B., Jiang, X., Yun, C., Han, W., *et al.,* (2017). "Clinical study of NeuroRegen scaffold combined with human mesenchymal stem cells for the repair of chronic complete spinal cord injury". In: *Cell transplantation* 26.5, pp. 891–900.

Zhou, X., He, X., and Ren, Y. (2014). "Function of microglia and macrophages in secondary damage after spinal cord injury". In: *Neural regeneration research* 9.20, p. 1787.

Ziegler, J. G. and Nichols, N. B. (1942). "Optimum settings for automatic controllers". In: *trans. ASME* 64.11.

Appendices

Appendix A – Equipment and Reagents

Table 6.1: List of Equipment and Software Used

Equipment	Model	Supplier
General		
Analytical Balance	ABS-N/ ABJ-NM	Kern & Sohn. Balingen, Germany
Autoclave, oven		
Autoclave, steam		
Automatic pipette (Pipetteboy)		Starlab UK Ltd., Milton Keynes, UK
BOSE Electroforce BioDynamic	5110	TA Instruments, Newcastle, UK
Centrifuge Harrier 15/80	MSB080.CX1.5	Sanyo, Watford, UK
Centrifuge, refrigerated	220R	VWR International Ltd., Leicestershire, UK
Class II Laminar Flow Safety Cabinet	Herasafe	Heraeus, Germany
Freezer (-20 °C)		
Freezer (-80 °C)	MDF-U2086S	Sanyo Electric Biomedical Co. Ltd., Tokyo, Japan
Fridge, sparkfree		Labcold
Fume Hood		Whiteley Fume Extraction Ltd., York, UK
Haemocytometer	Neubauer	Sigma-Aldrich Ltd., Dorset, UK
Humidified CO_2 Incubator	MCO-20AIC	Sanyo Biomedical Europe, BV Amsterdam, Holland
Ice Maker	FM-150KE-50	Hoshizaki Europe Ltd., Telford, UK
Magnetic Flea		
Orbital shaker, 10 mm $\varnothing$	PSU-10i	Grant Instruments Ltd., Cambridgeshire, UK
pH Meter	Jenway 3510	Wolf Laboratories Ltd., York, UK

Continued on next page

Table 6.1 – *Continued from previous page*

Equipment	Model	Supplier
Pipettes	P2, P20, P200, P1000	Scientific Laboratory Supplies Ltd, Nottingham, UK
Plate Reader	Chameleon Plate	Hidex LabLogic Systems Ltd., Sheffield, UK
Refrigerant Gel Pack PolarPack TM		Fisher Scientific Ltd., Loughborough, UK
Rheometer	Malvern Kinexus Pro+	Malvern Instruments Ltd., Malvern, UK
Spatula	Various Sizes	VWR International Ltd., Leicestershire, UK
Water Bath		Grant Instruments Ltd., Cambridgeshire, UK
Dissection Equipment		
Dissecting Scissors, Curved (10 cm)		World Precision Instruments Ltd., Hertfordshire, UK
Dumont Tweezers (11 cm)	#55	World Precision Instruments Ltd., Hertfordshire, UK
Dumont Tweezers, Curved (11.5 cm)	#7	World Precision Instruments Ltd., Hertfordshire, UK
Fine Scissors ToughCut, Straight (9 cm)		Interfocus Ltd., Linton, UK
Mayo Scissors ToughCut, Straight (17 cm)		Interfocus Ltd., Linton, UK
Scalpel Handle (95 mm)	#3	Scientific Laboratory Supplies Ltd., Nottingham, UK
Springbow Curved Scissors (115 mm)		Scientific Laboratory Supplies Ltd., Nottingham, UK
Vannas Spring Scissors Straight (2.5 mm cutting edge)		Interfocus Ltd., Linton, UK
Surgical Scissors (16 cm)		World Precision Instruments Ltd., Hertfordshire, UK
Tweezers (11 cm)	#4, #5	TAAB Laboratories Equipment Ltd., Berkshire, UK
Microscopy		
Olympus Inverted Light Microscope	CK40	Olympus Optical Co. Ltd., UK
Zeiss Axio Imager.Z2 Upright Microscope (confocal scanning laser microscope)	LSM880	Carl Zeiss Ltd., Cambridge, UK
Zeiss Axio Upright Fluorescent microscope		Zeiss, Cambridge, UK

Table 6.1 – *Continued from previous page*

Equipment	Model	Supplier
Software		
(Fiji Is Just) ImageJ	v1.52k	National Institutes of Health, USA
GraphPad Prism 7	v7.01	GraphPad Software, USA
MikroWin 2000	v4.43	Mikrotek Laborsysteme GmbH
rSpace Rheology Software		Malvern Instruments Ltd., Malvern, UK
Volocity 3D Image Analysis Software		PerkinElmer; MA, USA
WinTest	v7.2	TA Instruments, Newcastle, UK
ZEN 2.3 SP1 FP1 (Black)	14.0.12.201	Carl Zeiss Microscopy GmbH, Germany
ZEN 2.5 (Blue)	2.5.75.0	Carl Zeiss Microscopy GmbH, Germany

Table 6.2: List of Consumables Used

Consumable	Supplier
Bijou (5 ml)	Scientific Laboratory Supplies Ltd., Nottingham, UK
Blade removers, non-surgical	VWR International Ltd., Leicestershire, UK
Blue Roll	Scientific Laboratory Supplies Ltd., Nottingham, UK
Cell Scrapers	Fisher Scientific UK Ltd., Loughborough, UK
Cell Strainers (40 µm)	Fisher Scientific UK Ltd., Loughborough, UK
Cryovial Tubes (2.0 ml)	Sarstedt Ltd., Leicester, UK
Falcon Conical Centrifuge Tubes (15 ml, 50 ml)	Sarstedt Ltd., Leicester, UK
FFP3 Valved Respirator	VWR International Ltd., Leicestershire, UK
Glass Cover Slips (22 x 22 mm)	Scientific Laboratory Supplies Ltd., Nottingham, UK
Maxisorp 96-well microplate (flat bottom)	Thermo Fisher Scientific, Paisley, UK
Microplate 96-well (polypropylene round bottom)	Fisher Scientific UK Ltd., Loughborough, UK
Nitrile Gloves, Ecoshield	Appleton Woods Ltd., Birmingham, UK
OptiPlate, 96-well	PerkinElmer Life & Analaytical Sciences, Bucks, UK
Petri Dish (60 x 15 mm)	Sigma-Aldrich Ltd., Dorset, UK
Petri Dish (90 x 16 mm)	Fisher Scientific UK Ltd., Loughborough, UK
Pipette tips (2 µl, 20 µl, 200 µl, 1000 µl)	Starlab, Ahrensburg, Germany
Plate Sealers, TopSeal-A PLUS	PerkinElmer Life & Analaytical Sciences, Bucks, UK
Serological pipettes (5 ml, 10 ml, 25 ml)	Sigma-Aldrich Ltd., Dorset, UK
Scalpel Blades (#10)	Fisher Scientific UK Ltd., Loughborough, UK
Single Edge Razor Blades (38.1 mm x 19 mm)	VWR International, Poole, UK
Sterile Pots (60 ml, 150 ml, 250 ml)	Fisher Scientific UK Ltd., Loughborough, UK
Superfrost Plus Slides	Fisher Scientific UK Ltd., Loughborough, UK
Syringe (10 ml)	
Syringe Filters (0.22 µm)	Sigma-Aldrich Ltd., Dorset, UK
Tethering Bars (Plastic Mesh, 10-count)	Darice, Amazon, UK

Continued on next page

Table 6.2 – *Continued from previous page*

Consumable	Supplier
Tissue Culture Flasks, Nunclon Delta (25 cm^2, 75 cm^2)	Thermo Fisher Scientific, Paisley, UK
Universal Tubes (30 ml)	Scientific Laboratory Supplies Ltd., Nottingham, UK
Weighing boats	Scientific Laboratory Supplies Ltd., Nottingham, UK
Well Plates, Nunclon Delta Surface Flat, (6, 48 well)	Thermo Fisher Scientific, Paisley, UK

Consumable	Supplier
Tissue Culture Flasks, Nunclon Delta (25 cm^2, 75 cm^2)	

Table 6.3: List of Reagents Used

Reagent	Supplier
General	
Bovine Serum Albumin	Sigma-Aldrich ltd., Dorset, UK
DAPI (4',6-diamidino-2-phenylindole)	Sigma-Aldrich Ltd., Dorset, UK
Dimethyl Sulfoxide (DMSO)	Sigma-Aldrich Ltd., Dorset, UK
Dulbecco's Phosphate Buffered Saline (PBS)	Sigma-Aldrich Ltd., Dorset, UK
Dulbecco's Phosphate Buffered Saline (PBS) Tablets	Fisher Scientific UK Ltd., Loughborough, UK
Ethanol	Fisher Scientific, UK Ltd., Loughborough, UK
Hydrochloric Acid (37% w/w, d=1.18)	Fisher Scientific UK Ltd., Loughborough, UK
OptiPrep^{TM} Density Gradient Medium	STEMCELL Technologies UK Ltd., Cambridge, UK
Paraformaldehyde (4%)	Insight Biotechnology Ltd., Wembley, UK
pH Buffer Solution (pH 4, 7, 10)	Scientific Laboratory Supplies Ltd., Nottingham, UK
Sodium Azide (1% w/v)	VWR International Ltd., Leicestershire, UK
Sodium Hydroxide Pellets	Fisher Scientific UK Ltd., Loughborough, UK
Triton X-100	Fisher Scientific UK Ltd., Loughborough, UK
Trypan Blue Solution	Sigma-Aldrich Ltd., Dorset, UK
Trypsin (3000 - 20 000 U.mg^{-1})	Sigma-Aldrich Ltd., Dorset, UK
Virkon	Fisher Scientific, Loughborough, UK
General Cell Culture	
Dulbecco's Modified Eagle's Medium (DMEM) High Glucose	Lonza Biological, Cambridge, UK
Foetal Bovine Serum (FBS)	Bio-Whittaker, Lonza, Verviers, Belgium
Hank's Balanced Salt Solution (HBSS) with Ca^{2+} and Mg^{2+}	Sigma-Aldrich Ltd., Dorset, UK
Hank's Balanced Salt Solution (HBSS) modified without Ca^{2+} and Mg^{2+}	Sigma-Aldrich Ltd., Dorset, UK
Laminin from Engelbreth-Holm-Swarm murine	Sigma-Aldrich Ltd., Dorset, UK
L-glutamine	Sigma-Aldrich Ltd., Dorset, UK
Penicillin/Streptomycin Solution	Sigma-Aldrich Ltd., Dorset, UK
Poly-D-lysine hydrobromide	Sigma-Aldrich Ltd., Dorset, UK
Trypsin-EDTA 1X	Sigma-Aldrich Ltd., Dorset, UK

Table 6.3 – *Continued from previous page*

Reagents	Supplier
Additional Primary Cell Culture Supplements	
Collagenase Type IV	Sigma-Aldrich Ltd., Dorset, UK
Cytosine β-D-arabinofuranoside	Sigma-Aldrich Ltd., Dorset, UK
Deoxyribonuclease I (DNase) from bovine pancreas (DNase), 2000 U.mg^{-1} Type IV	Sigma-Aldrich Ltd., Dorset, UK
5-Fluorodeoxyuridine	MP Biomedicals Europe, Cambridge, UK
Nerve Growth Factor (Recombinant Human β-NGF, animal free) expressed in E.coli	Biolegend Ltd., London, UK
Pierce Protease and Phosphatase Inhibitor Mini Tablets	Thermo Fisher Scientific, Paisley, UK
Soybean Trypsin Inhibitor from Glycine Max	Sigma-Aldrich Ltd., Dorset, UK
Transforming Growth Factor β–1, human	Cambridge Bioscience, Cambridge, UK
Uridine	MP Biomedicals Europe, Cambridge, UK
Assay Kits	
ATPlite Luminescence System	Perkin-Elmer Life & Analytical Sciences, Buckinghamshire, UK
LIVE/DEAD Viability/Cytotoxicity kit	Thermo Fisher Scientific, Paisley, UK
Rat IL-6 DuoSet ELISA kit	Bio-Techne, Abingdon, UK
Reagent Additive 1 (21 mL)	Bio-Techne, Abingdon, UK
Substrate Reagent Pack (8 vials Color A, 8 vials Color B)	Bio-Techne, Abingdon, UK
Collagen Hydrogel Reagents	
Collagen Type-I rat tail, >2 mg.ml^{-1} in 0.6% (v/v) acetic acid	First Link Ltd., Wolverhampton, UK
Minimum Essential Media, 10x (without alkali)	First Link Ltd., Wolverhampton, UK
Neutralising Solution	Lonza Biological, Cambridge, UK

Appendix B – Characterisation of the BOSE Electroforce BioDynamic 5110

B.1. Contusion

Table 6.4: Mean peak output displacement values under compression waveforms with or without the addition of a 100 ms dwell step and with or without PID tuning. Output displacement values were recorded, under waveforms of various combinations of input displacement and velocity parameters simulated in air. The peak output displacement values were selected and compared to the input displacement value. Data is presented as the mean $\pm$ SEM (% error). N=4.

Input Displacement (mm)	Mean Output Peak Displacement (mm)		
	100 mm.s^{-1}	1000 mm.s^{-1}	3000 mm.s^{-1}
$-$ Dwell $-$ PID			
1.000	0.642 ± 9.6 x 10^{-4} (35.85)	0.128 ± 4.1 x 10^{-4} (87.20)	0.064 ± 2.9 x 10^{-4} (93.65)
2.000	1.511 ± 1.2 x 10^{-3} (24.43)	0.471 ± 1.3 x 10^{-3} (76.44)	0.219 ± 6.5 x 10^{-4} (89.08)
4.000	3.571 ± 4.1 x 10^{-4} (10.73)	1.701 ± 5.8 x 10^{-4} (57.48)	0.699 ± 8.5 x 10^{-4} (82.52)
6.000	5.681 ± 8.5 x 10^{-4} (5.32)	3.470 ± 9.1 x 10^{-4} (42.17)	1.435 ± 4.8 x 10^{-4} (76.09)
8.000	7.659 ± 6.3 x 10^{-4} (4.26)	5.595 ± 4.8 x 10^{-4} (30.07)	2.601 ± 5.0 x 10^{-4} (67.49)
10.000	9.460 ± 6.3 x 10^{-4} (5.40)	7.763 ± 2.5 x 10^{-4} (22.37)	3.889 ± 7.5 x 10^{-4} (61.11)
$+$ Dwell $-$ PID			
1.000	0.999 ± 2.5 x 10^{-4} (0.13)	0.998 ± 4.8 x 10^{-4} (0.23)	0.999 ± 4.1 x 10^{-4} (0.10)
2.000	2.001 ± 6.3 x 10^{-4} (0.06)	2.001 ± 2.5 x 10^{-4} (0.04)	2.001 ± 4.8 x 10^{-4} (0.06)
4.000	4.002 ± 2.5 x 10^{-4} (0.04)	4.007 ± 4.1 x 10^{-4} (0.18)	4.007 ± 4.8 x 10^{-4} (0.18)
6.000	6.001 ± 5.0 x 10^{-4} (0.02)	6.014 ± 8.5 x 10^{-4} (0.24)	6.014 ± 2.5 x 10^{-4} (0.23)
8.000	8.004 ± 5.0 x 10^{-4} (0.04)	8.015 ± 4.8 x 10^{-4} (0.18)	8.038 ± 1.0 x 10^{-3} (0.47)
10.000	9.986 ± 5.0 x 10^{-4} (0.15)	9.989 ± 2.5 x 10^{-4} (0.11)	10.084 ± 7.5 x 10^{-4} (0.84)
$+$ Dwell $+$ PID			
1.000	1.089 ± 3.7 x 10^{-4} (8.92)	0.961 ± 5.1 x 10^{-4} (3.94)	
2.000	2.001 ± 3.7 x 10^{-4} (0.06)	1.974 ± 5.1 x 10^{-4} (1.32)	
4.000	4.069 ± 4.0 x 10^{-4} (1.72)	3.998 ± 4.0 x 10^{-4} (0.04)	
6.000	6.001 ± 4.5 x 10^{-4} (0.02)	6.002 ± 3.2 x 10^{-4} (0.03)	
8.000	8.003 ± 4.5 x 10^{-4} (0.04)	7.997 ± 5.8 x 10^{-4} (0.04)	
10.000	9.993 ± 5.5 x 10^{-4} (0.07)	10.236 ± 6.0 x 10^{-4} (2.36)	
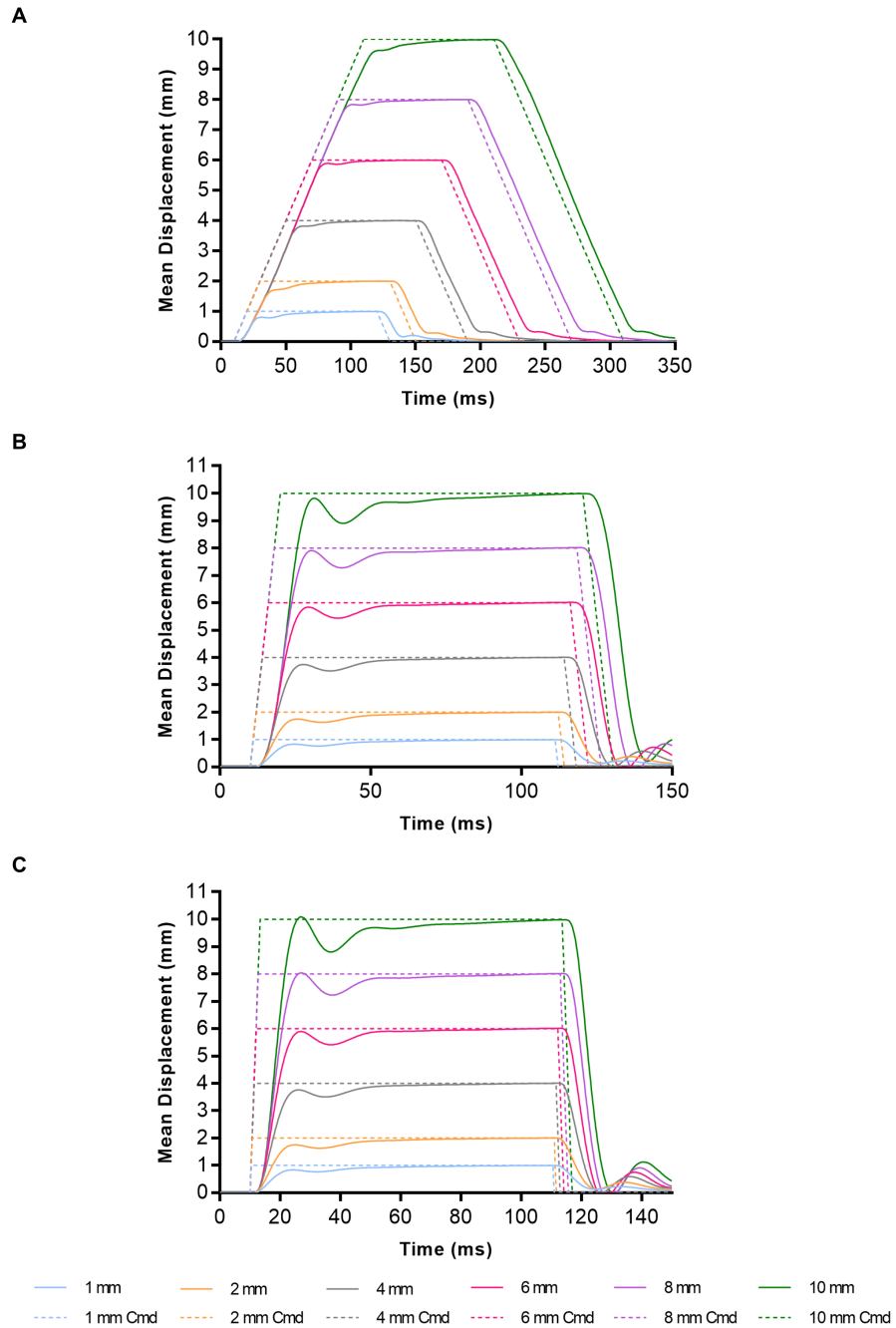
Figure 6.1: Comparison of input and output displacement profiles of a simulated contusion regime with the addition of a 100 ms dwell step. Dashed lines represent the output profiles; solid lines represent the input command. The simulated waveform was programmed as follows: dwell (10 ms), ramp (100, 1000, or 3000 mm.s^{-1} to the defined displacement depth) in compression, dwell (100 ms), and ramp (100, 1000, or 3000 mm.s^{-1}) to 0.000 mm.

Table 6.5: Mean peak output velocity values under compression waveforms with or without the addition of a 100 ms dwell step and with or without PID tuning. Output velocity values were recorded, under waveforms of various combinations of input displacement and velocity parameters simulated in air. The peak output velocity values were selected and compared to the input velocity value. Data is presented as the mean $\pm$ SEM (% error). N=4.

Input Displacement (mm)	Mean Output Peak Velocity (mm.s^{-1})		
	100 mm.s^{-1}	1000 mm.s^{-1}	3000 mm.s^{-1}
$-$ Dwell $-$ PID			
1.000	80.00 $\pm$ 0.00 (20.00)	45.00 $\pm$ 0.00 (95.50)	25.00 $\pm$ 0.00 (99.17)
2.000	91.25 $\pm$ 1.25 (8.75)	136.25 $\pm$ 1.25 (86.38)	77.50 $\pm$ 1.44 (97.42)
4.000	110.00 $\pm$ 0.00 (10.00)	365.00 $\pm$ 0.00 (63.50)	226.25 $\pm$ 1.25 (92.46)
6.000	112.50 $\pm$ 1.44 (12.50)	587.50 $\pm$ 1.44 (41.25)	420.00 $\pm$ 0.00 (86.00)
8.000	112.50 $\pm$ 1.44 (12.50)	795.00 $\pm$ 2.04 (20.50)	666.25 $\pm$ 1.25 (77.79)
10.000	113.75 $\pm$ 2.50 (13.75)	918.75 $\pm$ 1.25 (8.13)	897.50 $\pm$ 1.44 (70.08)
$+$ Dwell $-$ PID			
1.000	82.50 $\pm$ 1.44 (17.50)	110.00 $\pm$ 0.00 (89.00)	111.25 $\pm$ 1.25 (96.29)
2.000	90.00 $\pm$ 0.00 (10.00)	221.25 $\pm$ 1.25 (77.88)	226.25 $\pm$ 1.25 (92.46)
4.000	110.00 $\pm$ 0.00 (10.00)	440.00 $\pm$ 0.00 (56.00)	458.75 $\pm$ 1.25 (84.71)
6.000	111.25 $\pm$ 1.25 (11.25)	647.50 $\pm$ 1.44 (35.25)	703.75 $\pm$ 2.39 (76.54)
8.000	111.25 $\pm$ 1.25 (11.25)	810.00 $\pm$ 0.00 (19.00)	947.50 $\pm$ 1.44 (68.42)
10.000	111.25 $\pm$ 1.25 (11.25)	927.50 $\pm$ 1.44 (7.25)	1176.25 $\pm$ 3.15 (60.79)
$+$ Dwell $+$ PID			
1.000	117.00 $\pm$ 0.94 (17.00)	125.00 $\pm$ 0.00 (87.50)	
2.000	94.00 $\pm$ 0.61 (6.00)	254.00 $\pm$ 0.61 (74.60)	
4.000	118.00 $\pm$ 1.22 (18.00)	545.00 $\pm$ 0.00 (45.50)	
6.000	108.00 $\pm$ 0.50 (8.00)	768.50 $\pm$ 0.61 (23.15)	
8.000	107.50 $\pm$ 0.00 (7.50)	943.00 $\pm$ 1.22 (5.70)	
10.000	110.00 $\pm$ 0.00 (10.00)	1031.00 $\pm$ 1.00 (3.10)	

Table 6.6: PID values determined for each combination of displacement and velocity parameters.

Displacement (mm)	Input Velocity (mm.s^{-1})	P Value	I Value	D Value
1.000	100	0.658196	0.019039	-2.81748
	1000	0.536222	0.004389	-2.17659
2.000	100	0.658196	0.009272	-2.81748
	1000	0.536222	0.005305	-2.23762
4.000	100	0.322592	0.008357	-2.26814
	1000	0.231037	0.004694	-2.57333
6.000	100	0.658296	0.009272	-2.81748
	1000	0.627777	0.007441	-2.81748
8.000	100	0.658296	0.009272	-2.81748
	1000	0.658296	0.007746	-2.81748
10.000	100	0.658296	0.009272	-2.81748
	1000	0.505703	0.008051	-2.39022

Table 6.7: Mean peak output displacement and velocity values under compression waveforms with or without the presence of a hydrogel. Acellular gels 300 µl in volume were compressed to 25, 50, or 75% of their calculated height at 100 or 1000 mm.s^{-1} with the peak displacement and velocities achieved reported. Control tests refer to the corresponding waveform simulated in air. Data is presented as the mean $\pm$ SEM (% error). Two-way ANOVA with Tukey's post-hoc test performed. N=4.

	100 mm.s^{-1}		1000 mm.s^{-1}	
	Ctrl	**Gel**	**Ctrl**	**Gel**
Peak Output Displacement (mm)				
25%	0.376 ± 0.02 (0.05)	0.376 ± 0.02 (0.05)	0.351 ± 0.02 (0.04)	0.351 ± 0.02 (0.04)
50%	0.768 ± 0.02 (0.04)	0.770 ± 0.02 (0.06)	0.733 ± 0.06 (0.04)	0.717 ± 0.03 (0.02)
75%	1.018 ± 0.20 (0.03)	1.049 ± 0.10 (0.05)	1.152 ± 0.04 (0.06)	1.156 ± 0.04 (0.02)
Peak Output Velocity (mm.s^{-1})				
25%	115.00 ± 0.00 (15.00)	115 ± 0.00 (15.00)	902.50 ± 32.56 (9.75)	900.00 ± 33.35 (10.00)
50%	115.00 ± 0.00 (15.00)	115.00 ± 0.00 (15.00)	955.00 ± 0.00 (4.50)	957.50 ± 1.44 (4.25)
75%	115.00 ± 0.00 (15.00)	115.00 ± 0.00 (15.00)	967.50 ± 1.44 (3.25)	966.25 ± 1.25 (3.38)

B.2. Distraction

Table 6.8: Mean peak output displacement and velocity values under tensile loads with or without PID tuning in air. Data is presented as the mean ± SEM (% error). Two-way ANOVA with Tukey's post-hoc test performed. N=3.

	100 mm.s^{-1}		1000 mm.s^{-1}	
	− PID	+ PID	− PID	+ PID
Peak Output Displacement (mm)				
2.000 mm	2.004 ± 3.3 x 10^{-4} (0.22)	2.008 ± 6.7 x 10^{-4} (0.42)	2.143 ± 6.7 x 10^{-4} (7.17)	2.022 ± 3.3 x 10^{-4} (1.08)
4.000 mm	3.997 ± 5.8 x 10^{-4} (0.08)	4.004 ± 3.3 x 10^{-4} (0.09)	4.189 ± 8.8 x 10^{-4} (4.73)	4.006 ± 5.8 x 10^{-4} (0.15)
6.000 mm	5.947 ± 6.7 x 10^{-4} (0.88)	5.995 ± 0.001 (0.08)	6.221 ± 8.8 x 10^{-4} (3.69)	6.008 ± 3.3 x 10^{-4} (0.13)
Peak Output Velocity (mm.s^{-1})				
2.000 mm	111.67 ± 1.67 (11.67)	111.67 ± 1.67 (11.67)	253.33 ± 1.67 (74.67)	333.33 ± 1.67 (66.67)
4.000 mm	111.67 ± 1.67 (11.67)	111.67 ± 1.67 (11.67)	491.67 ± 1.67 (50.83)	628.33 ± 1.67 (37.17)
6.000 mm	110.00 ± 0.00 (10.00)	115.00 ± 2.89 (15.00)	703.33 ± 1.67 (29.67)	856.67 ± 1.67 (14.33)

Table 6.9: Mean peak output displacement and velocity values under tensile loads with or without collagen hydrogels. Gels were distracted to lengths ranging from 10 – 30%, then repeated in air (ctrl) with peak displacement and velocity calculated. Data is presented as the mean $\pm$ SEM (% error). Two-way ANOVA with Tukey's post-hoc test performed. N=3.

	100 mm.s^{-1}	
	Ctrl	**Gel**
Peak Output Displacement (mm)		
10%	0.857 ± 0.005 (3.84)	0.858 ± 0.005 (3.96)
20%	1.654 ± 6.7 x 10^{-4} (0.22)	1.658 ± 0.003 (0.46)
30%	2.480 ± 8.8 x 10^{-4} (0.22)	2.482 ± 5.7 x 10^{-4} (0.28)
Peak Output Velocity (mm.s^{-1})		
10%	111.67 ± 1.67 (11.67)	90.00 ± 0.00 (10.0)
20%	111.67 ± 1.67 (11.67)	115.00 ± 0.00 (15.0)
30%	111.67 ± 1.67 (11.67)	115.00 ± 0.00 (15.0)
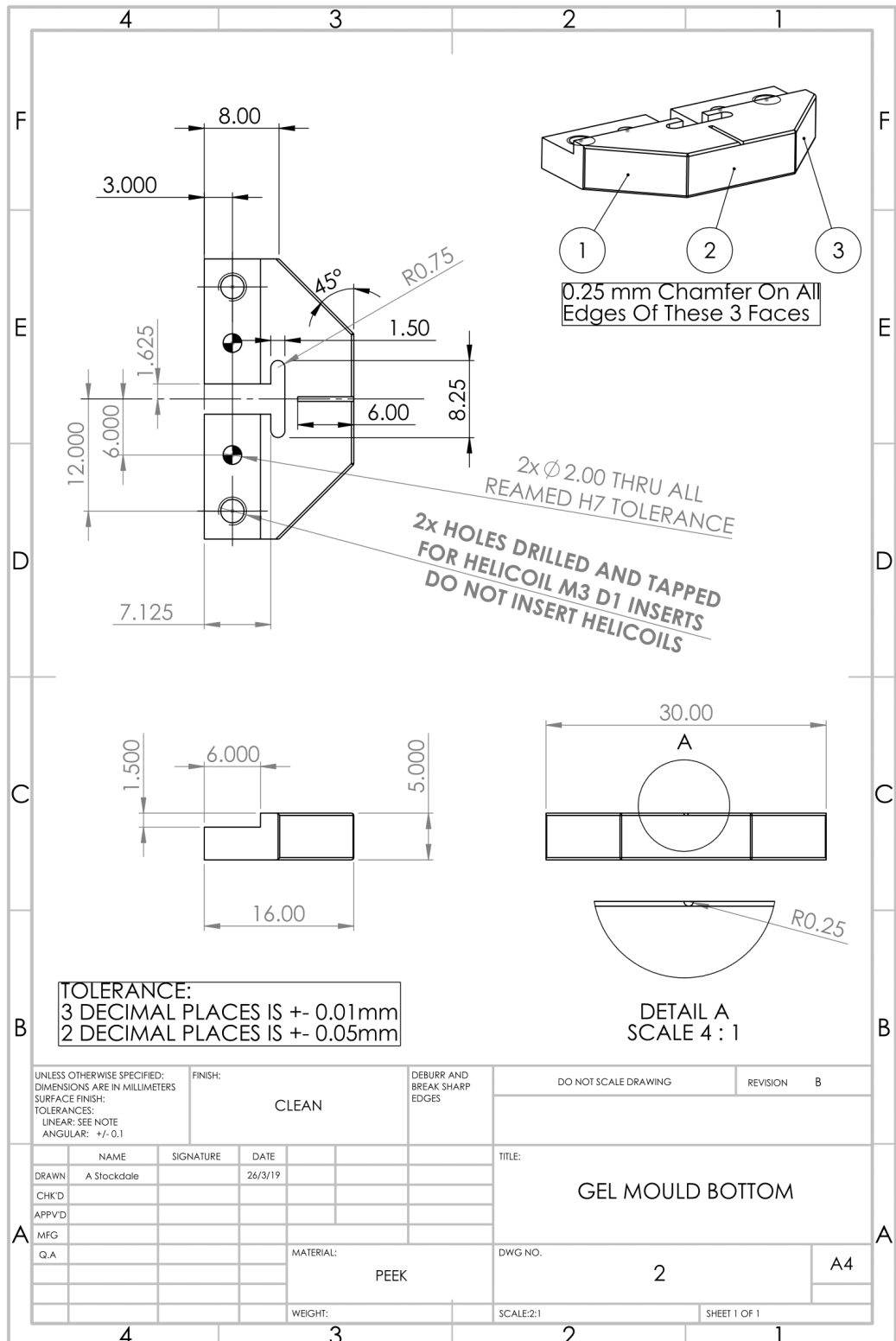
Figure 6.2: CAD drawing of the bottom piece of the distraction mould.
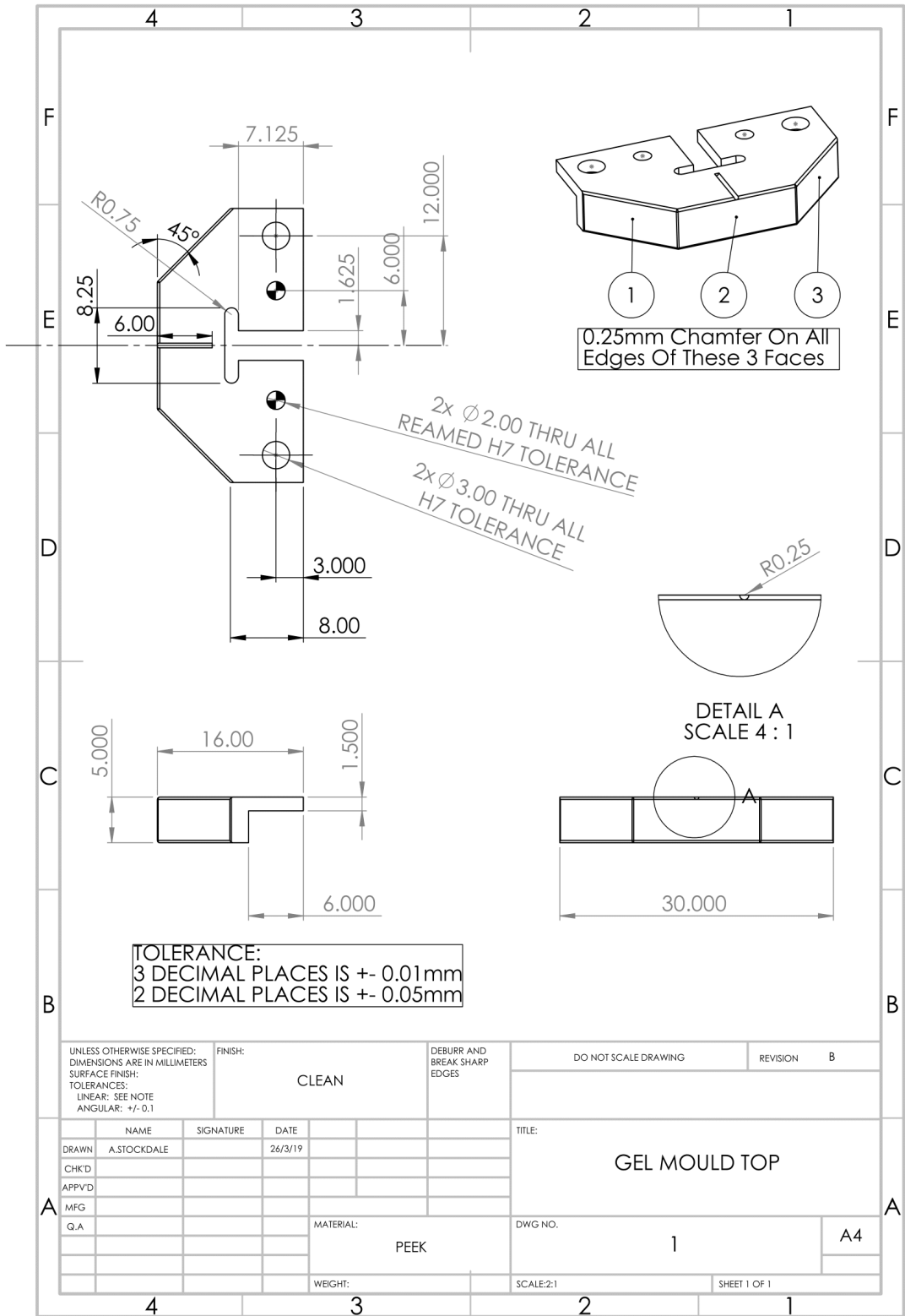
Figure 6.3: CAD drawing of the top piece of the distraction mould.

45 DEGREE CHAMFER @ 0.25mm

10.00

⌀2.50

4.75

0.50

45 DEGREE CHAMFER @ 0.50mm

M3 x 0.5 Thread

Grooves x6
Equidistant Around
Central Axis

R2.50

R1.50

3.75

	NAME	SIGNATURE	DATE			TITLE:		
DRAWN	A.STOCKDALE		26/3/19				GEL MOULD SCREW	
CHK'D								
APPV'D								
MFG								
Q.A				MATERIAL: 316 SS		DWG NO. 4		A4

UNLESS OTHERWISE SPECIFIED:
DIMENSIONS ARE IN MILLIMETERS
SURFACE FINISH:
TOLERANCES:
 LINEAR: +/- 0.05
 ANGULAR: +/- 0.1

FINISH:

CLEAN

DEBURR AND
BREAK SHARP
EDGES

DO NOT SCALE DRAWING

REVISION   B

WEIGHT: SCALE:5:1   SHEET 1 OF 1

Figure 6.4: CAD drawing of the screw piece of the distraction mould.

R2.50

3.75

R1.50

Grooves x6 Equidistant Around
Central Axis

0.25mm 45 DEGREE CHAMFER x 2

5

4.75

R0.25

∅2 ±0.010

UNLESS OTHERWISE SPECIFIED: DIMENSIONS ARE IN MILLIMETERS SURFACE FINISH: STANDARD TOLERANCES: LINEAR: 0.05 UNLESS STATED ANGULAR: +/- 0.1	FINISH: CLEAN		DEBUR AND BREAK SHARP EDGES		DO NOT SCALE DRAWING	REVISION	B

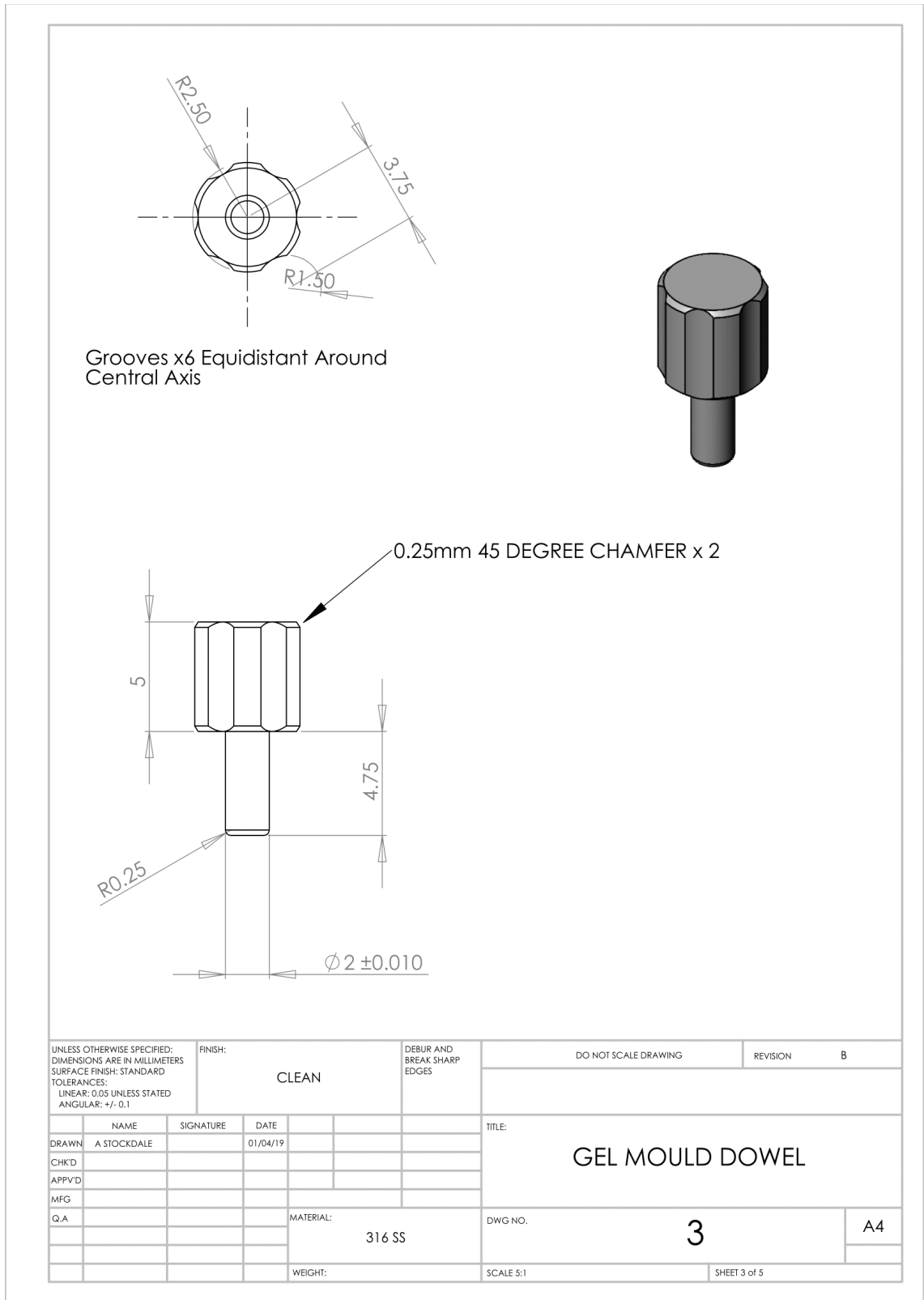|	NAME	SIGNATURE	DATE			TITLE:		
DRAWN	A STOCKDALE		01/04/19					
CHK'D						**GEL MOULD DOWEL**		
APPV'D								
MFG								
Q.A			MATERIAL: 316 SS		DWG NO. **3**		A4
			WEIGHT:		SCALE 5:1	SHEET 3 of 5	

Figure 6.5: CAD drawing of the dowel piece of the distraction mould.

230

Appendix D – Modelling Contusion SCI *In Vitro*

D.1. Kinetic Outputs

Table 6.10: **Kinetic Outputs Following Simulated Contusion Injury.** Data presented as the mean ± SEM. N = 12 per condition.

	Peak Displacement (mm)	Impact Velocity (mm.s^{-1})	Peak Velocity (mm.s^{-1})	Peak Load (N)	Energy Applied (mJ)
100 mm.s^{-1}					
25%	0.386 ± 0.01	95.00 ± 1.0	115.42 ± 0.4	0.722 ± 0.02	0.150 ± 0.008
50%	0.770 ± 0.01	98.33 ± 0.7	115.00 ± 0.00	1.064 ± 0.07	0.506 ± 0.03
75%	1.140 ± 0.05	99.58 ± 1.0	115.00 ± 0.00	1.586 ± 0.1	0.945 ± 0.08
1000 mm.s^{-1}					
25%	0.361 ± 0.01	605.00 ± 26	825.00 ± 19	3.948 ± 0.3	0.954 ± 0.05
50%	0.737 ± 0.02	642.92 ± 29	871.67 ± 22	4.722 ± 0.2	1.836 ± 0.03
75%	1.159 ± 0.02	760.00 ± 4	967.08 ± 0.7	5.562 ± 0.05	3.709 ± 0.1

D.2. Astrocyte Responses Following Contusion Injury

Table 6.11: Mean volume of GFAP expressed per cell following simulated contusion injury *in vitro*. Data presented as the mean ± SEM. N = 3.

	Mean volume of GFAP per cell (μm^3)				
	Ctrl	**25%**	**50%**	**75%**	**TGF-β1**
100 mm.s^{-1}					
Day 1	427.67 ± 41	758.73 ± 41	959.92 ± 71	979.40 ± 56	901.40 ± 47
Day 7	873.92 ± 31	939.13 ± 97	1452.22 ± 78	1564.38 ± 117	1435.41 ± 78
Day 14	867.08 ± 48	1064.99 ± 79	1386.62 ± 83	1834.90 ± 128	1983.05 ± 133
1000 mm.s^{-1}					
Day 1	787.73 ± 47	2455.26 ± 221	2738.87 ± 158	2579.48 ± 183	904.91 ± 60
Day 7	1157.70 ± 104	3041.29 ± 243	2872.04 ± 259	2844.02 ± 193	1381.26 ± 57
Day 14	859.17 ± 54	2650.82 ± 132	2808.04 ± 108	3110.02 ± 232	1886.33 ± 150

Appendix E – Modelling Distraction SCI *In Vitro*

E.1. Kinetic Outputs

Table 6.12: Kinetic Outputs Following Simulated Distraction Injury. Data presented as the mean ± SEM. N = 9 per condition.

	Peak Displacement (mm)	Peak Velocity (mm.s^{-1})	Peak Load (N)	Energy Applied (mJ)
100 mm.s^{-1}				
10%	0.852 ± 0.005	107.22 ± 2	0.127 ± 0.009	0.057 ± 0.003
20%	1.656 ± 0.001	115.56 ± 1	0.146 ± 0.007	0.108 ± 0.006
30%	2.482 ± 0.0003	115.56 ± 1	0.196 ± 0.03	0.143 ± 0.01

E.2. Astrocyte Responses Following Distraction Injury

Table 6.13: Mean volume of GFAP expressed per cell following simulated distraction injury *in vitro*. Data presented as the mean ± SEM. N = 3.

	Mean volume of GFAP per cell (μm^3)				
	Ctrl	**10%**	**20%**	**30%**	**TGF-β1**
100 mm.s^{-1}					
Day 1	546.77 ± 61	1134.42 ± 36	1322.40 ± 61	1781.22 ± 86	874.37 ± 61
Day 7	535.50 ± 44	1568.49 ± 89	1754.67 ± 54	1773.31 ± 61	1606.30 ± 69
Day 14	700.91 ± 40	2120.09 ± 101	2400.30 ± 108	2408.57 ± 119	2142.00 ± 94